



**HAL**  
open science

## Membranes in cells: transport and identity

Serge Dmitrieff

► **To cite this version:**

Serge Dmitrieff. Membranes in cells: transport and identity. Biological Physics [physics.bio-ph]. Université Pierre et Marie Curie - Paris VI, 2011. English. NNT : . pastel-00733626

**HAL Id: pastel-00733626**

**<https://pastel.hal.science/pastel-00733626>**

Submitted on 19 Sep 2012

**HAL** is a multi-disciplinary open access archive for the deposit and dissemination of scientific research documents, whether they are published or not. The documents may come from teaching and research institutions in France or abroad, or from public or private research centers.

L'archive ouverte pluridisciplinaire **HAL**, est destinée au dépôt et à la diffusion de documents scientifiques de niveau recherche, publiés ou non, émanant des établissements d'enseignement et de recherche français ou étrangers, des laboratoires publics ou privés.

# Membranes in cells : transport and identity

## THÈSE

présentée et soutenue publiquement le 29 Septembre 2011

Pour l'obtention du

**Doctorat de l'université Pierre et Marie Curie - PARIS VI**  
( Spécialité Physique)

par

Serge Dmitrieff

### Composition du jury

*Rapporteurs* : M. Luis BAGATOLLI  
M. Peter OLMSTED

*Examineurs* : M. Bruno GOUD  
M. Jean-François JOANNY  
M. Rob PHILLIPS  
M. Pierre SENS



# Contents

<b>Table of contents</b>	<b>iv</b>
<b>Remerciements</b>	<b>vii</b>
<b>Introduction</b>	<b>ix</b>
<b>1 Lipid receptors mediated pathogenic invasion.</b>	<b>1</b>
Introduction . . . . .	1
1.1 Introduction to membrane Physics . . . . .	4
1.2 Adsorption of a particle on a membrane . . . . .	9
1.3 Formation of aggregates . . . . .	12
1.4 Comparison with experiments . . . . .	18
1.5 Conclusion . . . . .	19
1.6 Typical values of the parameters . . . . .	20
1.7 Article . . . . .	20
<b>2 Transport in the Golgi apparatus</b>	<b>29</b>
Introduction . . . . .	29
2.1 Building a transport equation . . . . .	33
2.2 Solutions of the Fokker Planck equation . . . . .	37
2.3 Results . . . . .	41
2.4 Beyond constant rates of transport . . . . .	47
2.5 Microscopic origin of the parameters . . . . .	52
Conclusion . . . . .	55
2.6 Appendix A : diffusion coefficient in the Golgi apparatus . . . . .	56
2.7 Appendix B : analytical approaches to solving the diffusion-convection equation . . . . .	58
2.8 Appendix C : Discretization of the convection-diffusion equation . . . . .	61
<b>3 Maintenance of identity in cellular compartments</b>	<b>65</b>
Introduction . . . . .	65
3.1 Stationary compartment differentiation in a closed system . . . . .	68
3.2 Compartment differentiation in an open system . . . . .	78
3.3 Consequence of cooperative transport for protein maturation . . . . .	80
3.4 Conclusion and outlook . . . . .	85
3.5 Appendix : From transport rates to an energy landscape . . . . .	86

<b>4 Building differentiated compartments</b>	<b>91</b>
Introduction . . . . .	91
4.1 Thermodynamics of phase separation in a membrane . . . . .	94
4.2 Kinetics of domain growth . . . . .	100
4.3 Kinetics of domain growth with maturation . . . . .	107
4.4 Discussion . . . . .	113
Conclusion . . . . .	115
<b>Conclusion</b>	<b>117</b>
<b>Bibliography</b>	<b>119</b>

---

“ ... a PhD thesis typically contains obscure epigraphs and nonsensical dicta loosely connected, or sometimes completely unrelated, to the issue at hand”

---

Mike Slackenerny, **The Hitchhiker's guide to the PhD**



# Remerciements

*A ma nièce*

Ce travail a été réalisé au sein du laboratoire de Physico-Chimie Théorique de l'unité de recherche Gulliver. Je remercie donc leurs directeurs respectifs, M. Tony Maggs et M. Elie Raphael, de leur chaleureux accueil.

Je souhaite sincèrement remercier mes examinateurs, M. Jean-François Joanny pour avoir accepté de présider le jury, M. Luis Bagatolli et M. Peter Olmsted pour avoir accepté de rapporter cette thèse, et M. Rob Phillips et M. Bruno Goud pour faire partie du jury. Je les remercie pour leur intérêt, leur lecture de ce manuscrit, et leurs commentaires.

J'adresse des remerciements tout particuliers à mon directeur de thèse, Pierre Sens, pour avoir accepté de me prendre en thèse tout d'abord, et pour m'avoir guidé tout au long de cette thèse. Pendant trois ans, j'ai appris non seulement beaucoup sur la physique, mais plus encore sur comment faire de la physique. Son attention et son soutien ont été précieux tout au long de la thèse et particulièrement pendant la rédaction. Je le remercie aussi de m'avoir fait confiance pour aborder un sujet ouvert et riche en surprises. J'ai aussi eu l'opportunité de découvrir un large aperçu de la communauté scientifique mondiale grâce aux collaborations que nous avons eu, et aux conférences auxquelles j'ai été. Je souhaite notamment remercier nos collaborateurs à l'institut Curie : Patricia Bassereau et Ludwig Berland chez les physiciens ainsi que Ludger Johannes et Winfried Roemer chez les biologistes. Je voudrais aussi remercier nos collaborateurs à l'étranger, Madan Rao à Bangalore, Nir Gov à Rehovot et Rob Phillips à Pasadena.

Je me suis aussi senti soutenu par tout le laboratoire pendant cette thèse. Je tiens cependant à remercier particulièrement Falko Ziebert, qui m'a toujours poussé à douter et à aller chercher encore plus loin, Michael Schindler qui m'a (entre autres) initié à Python, le meilleur langage de scripting qui soit, et Antoine Blin, pour avoir pensé à mon bronzage quand j'en avais besoin. Merci aussi à David Lacoste, Florent Krzakala, Tony Maggs, Elie Raphael et Ken Sekimoto pour leur présence et les discussions scientifiques que nous avons eu. Il me faut aussi bien sûr remercier Gabrielle Fridelance pour son aide et sa patience pendant trois ans, ainsi que Khadija Fartasse. Enfin, je remercie tous les membres de l'UMR Gulliver où ma thèse s'est déroulée dans un contexte scientifique passionnant, et dans la bonne humeur.

C'est avec grand plaisir que je remercie ceux auprès de qui j'ai appris la physique. Marie-Agnès Sautière d'abord, qui m'a enseigné la physique en classe préparatoire, alors que je me destinais à devenir biologiste. Je remercie aussi Bill Gelbart qui m'a chaleureusement accueilli à Los Angeles, ainsi que tout le Virus Group.

Je remercie ensuite tout naturellement ma famille qui m'a beaucoup soutenu. Tout d'abord, mes parents, sans qui je n'aurais pu rêver d'un si beau parcours, qui ont largement stimulé ma curiosité tout en me laissant une grande liberté. Je remercie ma sœur, qui a eu un rôle incommensurable dans ma vie. Et la famille plus ou moins éloignée, parce qu'en Bretagne il est difficile de tracer précisément la limite. Je remercie notamment Eric et Marc, qui ont eu un grand rôle dans mon éducation scientifique. Merci aussi à tous mes cousins et mes cousines de Bretagne et d'ailleurs !

Au tour des amis maintenant. Je me suis senti très soutenu par tous pendant ma thèse, et je ne peux pas remercier chacun individuellement. Je voudrais cependant adresser des remerciements particuliers à mes collocataires qui m'ont supporté et ont égailé la rue Barbès ! Je remercie aussi tout le gang Marais-Ripoche-Montreuil, dont tous les membres n'ont pas encore été appréhendés, et leurs complices à l'international. Merci aux lillois aussi, en particulier ceux qui m'ont hébergé et nourri à maintes occasions. Je veux aussi souligner le rôle des musiciens pendant ces trois ans, que ce soit ceux qui ont essayé de m'apprendre des choses ou ceux avec qui j'ai joué. Merci aussi à ceux qui n'entrent dans aucune catégorie, qu'ils me croient en Afghanistan, aient été courir au Luxembourg, qu'ils aient occupés mon appartement ou m'aient hébergé dans de lointaines contrées... Et un remerciement tout particulier à Marie et Marie.

Enfin, je remercie Pauline Lafille, pour m'avoir supporté avant et pendant ma thèse, et qui continue à le faire malgré les tentacules de la dérégulation. Et pour tout.

“ If you want to gamble, I tell you I'm  
your man,  
You win some, lose some, it's all the  
same to me ”

---

Lemmy Killmister **An introduction  
to Monte Carlo methods**

# Introduction

Cells, by definition, are distinct from their environment. All the cells we know are separated from the outside by at least a lipid bilayer, sometimes supplemented by a cell wall or an extracellular matrix. Obviously, the chemical and physical properties of the separation will dictate how the cell will respond to its environment. We will focus on Eukaryotic cells ("ευ": true, "καρυον" : cell), the definition of which is the existence of inner compartments (as illustrated in figure 1). Eukaryotic cells are usually separated from their environment by a single lipid bilayer. The inner compartments (called organelles) are themselves separated from their outside (the inside of the cell, called cytoplasm) by a lipid membrane. Just as each cell type has a specific function, each organelle has a very specific in the physiology of the cell.

The cell, and its compartments, have to exchange molecules with their environment. First, the sinews of war, energy has to be taken in, commonly by importing reduced molecules (e.g. sugars) which will yield energy after oxidation. Many other molecules have of course to be taken in to build the proteins, lipids, sugars, DNA, and all the components of a living cell. But the cells are dynamical systems that respond to their environment, and signals from the outside must also be integrated. In particular, chemical signals have to be either detected by receptors on the cell membrane, or taken into the cell. The other way round, molecules can be exported by the cell, for instance to communicate with other cells. The compartments in the cell also have to export their products to various locations in the cell. Because of the specialization of cells and organelles, each organelle and each cell type will exchange different molecules with its environment, and this is made possible by the difference in their interface with their environment, which is the lipid membrane.

We can define the notion of membrane identity : the identity of a membrane is the sum of its physical and chemical properties that are accessible to its environment. Interestingly, each organelle in a cell has a distinct identity, and different cells have different identities, i.e. the compositions of their plasma membrane are different from one another, allowing specific interactions with the environment. Moreover, molecules are often exchanged between organelles, and exported from the cell, by the means of membrane-based carriers, vesicles and tubules, which also have specific identities, allowing them to carry out a target-specific transport. Those vesicles are transported in the cell along microtubules, a component of the cytoskeleton spanning the whole cytoplasm. The microtubules are therefore often called the "highways" of cellular transport. In this thesis, we will rather focus of the role of membranes in transport, though the study of the microtubular network offers exiting perspectives.

We will be especially interested in one compartment, the Golgi apparatus (G.A.), at the center cellular trafficking. Proteins, and many lipids, are synthesized in the Endoplasmic Reticulum (E.R.), but are usually not synthesized in their final form, the one which will enable them to fulfill their function. Most have to be matured, i.e. chemically transformed (e.g. by modification of the head groups of lipids, and addition or deletion

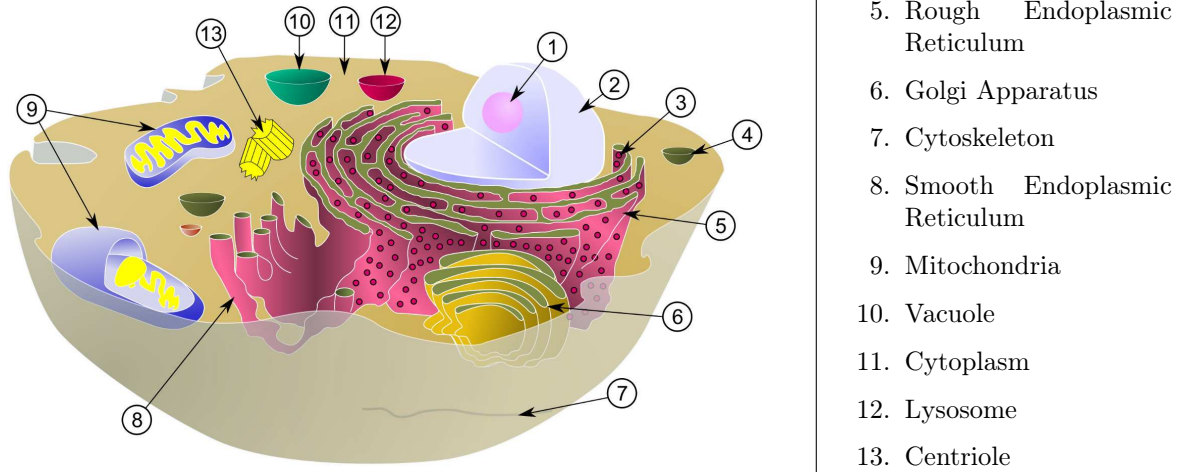


**Figure 1:** Diagram of a typical Eukaryote cell, of size  $\approx 10\mu m$ . The cytoskeleton actually spans through the whole cells, and vesicles are present throughout the cytoplasm, and particularly along microtubules, a component of the cytoskeleton.

of glycans in proteins), and sometimes physically transformed (by an accurate folding in the case of proteins). While folding usually takes place in the E.R., many chemical steps of maturation take place in the Golgi Apparatus. In mammals, and most upper Eukaryotes, the Golgi apparatus is a stack of five to seven sub-compartments, flat disc-shaped vesicles called cisternae, as illustrated in figure 1. Each cisterna has a radius of the order of 500 nanometers ( $nm$ ), a thickness of the order of  $30nm$ , and is constantly exchanging molecules with its neighbors, by direct tubular connections or through vesicular transport. In striking contrast, the Golgi apparatus of Yeast and some lower Eukaryotes is unstacked, and is constituted of rather autonomous cisternae disseminated throughout the cell.

The stacked structure of the Golgi apparatus has been shown to be very robust, by experiments in which the microtubule network is destroyed by nocodazole (a drug which prevents microtubule polymerization). After disruption of the microtubule network, the Golgi apparatus is dispersed throughout the cell. Golgi apparatus are then formed *de novo*, and keep the same structure as the Golgi apparatus in the absence of nocodazole, although with smaller lateral dimensions. Therefore, the Golgi apparatus can be seen as a self-organizing organelle, which builds up to its known stacked structure from the flux exported by the ER. Such self-organization is a beautiful illustration of the complex interplays between the structural and the dynamical properties in biological systems.

In this thesis, we will first study the entry of pathogens such as viruses or toxins in cells. We showed how the chemical and physical properties of the cell membrane, i.e. its identity, can control the entry of molecules or bodies by controlling their adhesion and aggregation on the membrane. It is a first illustration on the role of membrane identity of transport.

In the second chapter, we will focus on transport in the Golgi apparatus. We will see that by an adequate formulation of transport in the Golgi, we can give an accurate

interpretation of existing experimental data. Once again, we will realize that differences of identity between the cisternae can drive anterograde or retrograde transport, and allow the localization of molecules in one cisterna of the Golgi stack.

In the third chapter of this thesis we will consider the maintenance of identity in organelles. Though organelles are constantly exchanging molecules with the rest of the cell, they manage to keep their own identity. We will see that we can write general requirements on the transport processes to enable the heterogeneity of compartments. We will show that this requirements may have dramatic functional consequences on transport. There is hence a feedback between transport, which maintain identity, and identity, which control transport.

Eventually, as another illustration of the consequences of membrane identity, we will study the building of new compartments in the cell. We will consider one membrane compartment, which we can see as the precursor of the Golgi apparatus, in which the membrane lipids undergo a chemical reaction and are transformed into another lipid species (as occurs in the Golgi apparatus). There can be a competition between the kinetics of phase separation and the kinetics of the chemical reaction, and we will see how this competition may control the structure of the compartment. It is an illustration of self-organization and shows how membrane identity (the lipid composition) can control the structure of an organelle.



# Chapter 1

## Lipid receptors mediated pathogenic invasion.

### Introduction

As mentioned in the introduction, the cell membrane acts as an interface between the cell and its outside. It has however to be selectively permeable, so as to really separate the cell from the outside and yet to enable the cell to exchange with its environment : the cell has to intake molecules (whether for its metabolism, or as signals), and also to export various molecules. While small molecules (water, salts, sugars) can go through the membrane either using the permeability of the membrane bilayer, or by using channels, this is not possible for larger bodies (macromolecular aggregates, pathogens such as viruses for instance). The processes by which large molecules or bodies are engulfed in the cell are regrouped under the term endocytosis. Endocytosis has been abundantly studied (see for instance [1, 2]), and occurs by forming large membrane invaginations which eventually close on themselves. This results in a vesicle, called endosome, entering the cell.

There are various biochemical pathways to the formation of endosomes. They are usually described like a stepwise process, the prototype of which is the clathrin-mediated endocytosis, illustrated in figure 1.1 . The steps of this pathway are [3] :

- Receptors on the cell membrane bind to ligands outside the cell
- The receptors cause the local recruiting of clathrin proteins
- Clathrin deforms the membrane into pits of radius of order 100 nm.
- The invaginations are pinched off and enter the cell

This mechanism is energy-dependent as the disassembly of clathrin shells requires the consumption of ATP [4]. This pathway enables the cell to intake molecules from the environment, with selectivity and efficiency, as the molecules are recognized by specific receptors. As many pathways in the cell, it can be hijacked by pathogens such as

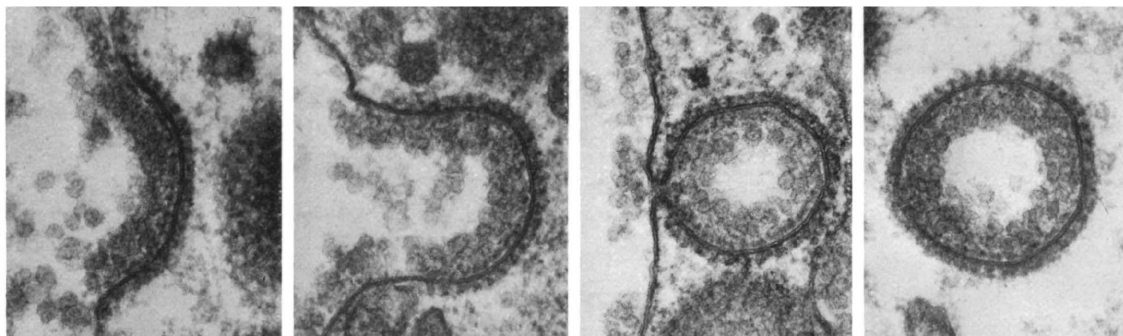


**Figure 1.1:** Electron microscopy images of clathrin endocytosis. The radius of a clathrin-coated vesicle is 150nm. Taken from M.M Perry and A.B. Gilbert, 1979 [9].

viruses [5, 6], and even bacteria [7]. More generally, endocytosis is the gateway to the cell for invasive pathogens [8].

It was shown that this clathrin pathway is not the only infection pathway for cells : viruses and toxins may also enter the cell by creating membrane invaginations if clathrin is knocked out [10] . It has been shown that toxins, such as the Shiga toxin (responsible for dysentery, and found in the tragically famous enterohemorrhagic *E. coli*), and viruses (such as SV40 virus, a polyomavirus known to cause tumors) use this clathrin-free pathway. In fact, they both invade cells after interaction with lipid receptors : GM1 for SV40 [11] and Gb3 for the Shiga toxin [12].

It was observed [13] that the formation of protein-enriched membrane tubules (of radius  $\approx 25nm$ ) throughout the cell (illustrated in fig. 1.2) was highly correlated to cell invasion. Interestingly, tubule formation and cell infection did not require energy input (by hydrolysis of ATP molecules). Tubules were actually much more numerous in the absence of ATP hydrolysis. This lead to the proposal that membrane tubulation results from passive aggregation of proteins adsorbed on the cell membrane, while active mechanisms played a role in severing the tubules, which enable them to enter the cell. We therefore assumed that tubulation was the first step towards pathogen entry, and used the theory of membrane mechanics to study this tubulation.

The adhesion of viruses on the membrane has been studied theoretically [14, 15, 16], and numerically [17], though the formation of tubules of small radius was seldom considered. In those studies, the tension of the membrane was not always considered, and the presence of lipid receptors in the membrane was not taken into account. Recent experiments [18] showed however that the membrane tension and the presence of lipid receptor were crucial factors to the formation of tubules and the infection of cells. Therefore, the precise mechanisms of tubule formation by those pathogens were still unknown. We focused on the SV40 virus because our collaborators could change various experimental parameters. For instance they could either work with full grown viral capsids depleted of DNA, called virus-like particles (VLPs), or with the unit building block of those capsids, protein pentamers of a much smaller size. They could also tune the physical properties of the receptors, by changing the length or the saturation of the acyl chain. Moreover, they could work on living cells to study infection or on giant vesicles of better-defined physical properties to study the membrane deformations induced by pentamers and VLPs.

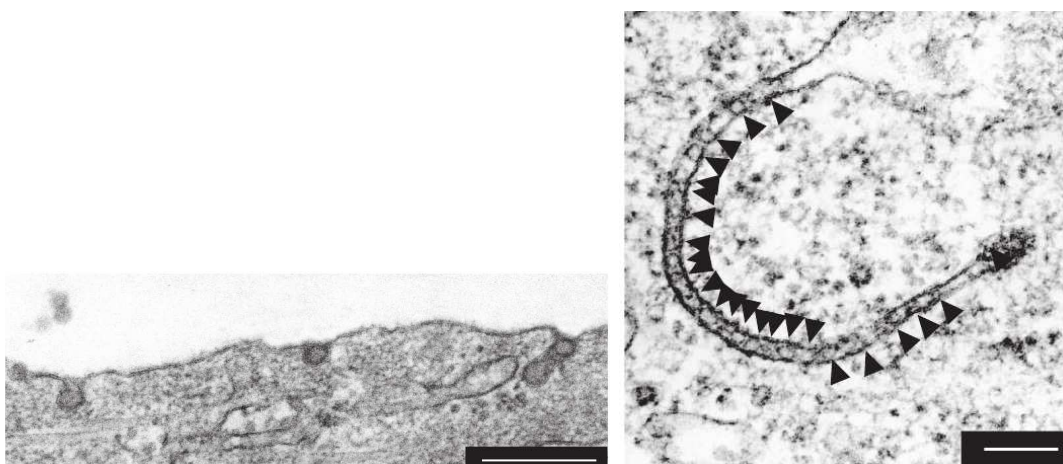


**Figure 1.2:** Electron microscopy images of (left) adsorbed viruses on the membrane and (right) tubules formed by viruses in a cell. In both pictures, individual viruses can be seen (arrowheads). Scale bar : 200 nm.

By comparing experimental results to membrane physics theory, we were able to understand the mechanisms of tubule formation by such pathogens. We showed that the physics of tubulation is dominated by the competition between the tension of the membrane and a line energy due to the aggregation of lipid receptors beneath the adsorbed particles. Therefore, in contrast with clathrin-mediated endocytosis, tubulation does not require the recruitment of membrane proteins, but can be studied as a temperature-activated process, using mostly equilibrium thermodynamics tools.

## 1.1 Introduction to membrane Physics

To know if VLPs and pentamers may adsorb on the membrane and form tubules, allowing the invasion of the cell, we need to study the physics of membranes. In this section, we will describe some of the various energies involved in membrane physics. Let us first consider the energies associated with the mechanical deformations (bending and stretching) of the membrane. Then, we will consider the energies associated with the composition of the membrane.

### 1.1.1 Membrane Mechanics

The standard tools for studying membrane mechanics were introduced by Helfrich [19]. When deforming a membrane, there are two main contributions in the energies :

- $\mathcal{H}_\kappa$  The bending of the membrane
- $\mathcal{H}_\gamma$  The tension of the membrane

The bending energies reads :

$$\mathcal{H}_\kappa = \int_S \left[ \frac{1}{2} \kappa (C_1 + C_2 - C_0)^2 + \kappa_G C_1 C_2 \right] d^2s \quad (1.1)$$

In which  $C_1$  and  $C_2$  are two principal curvatures of the surface,  $C_0$  is the spontaneous curvature of the surface,  $\kappa$  is the bending modulus and  $\kappa_G$  is the elastic modulus of the Gaussian curvature. In a uniform membrane, for any change in the membrane shape conserving the topology of the membrane, the Gaussian contribution in this energy does not change. Therefore, we will usually consider only the first term of this Hamiltonian.

There is another energetic penalty when deforming a membrane due to the tension  $\gamma$  of the membrane. It reads :

$$\mathcal{H}_\gamma = \int_S \gamma ds \quad (1.2)$$

This term expresses the energy cost of increasing the membrane surface area. In an infinite membrane,  $\gamma$  does not depend on the deformation, yielding an energy penalty  $\Delta E = \gamma \Delta S$  after an increase  $\Delta S$  of the surface area. In a finite membrane,  $\gamma$  however depends on the stretching of the membrane. It depends on a combination of molecular and entropic elasticity [20, 21]. In the following, we will work at constant tension, which is reasonable if the deformations are much smaller than the membrane area.

Let us consider a lightly deformed membrane : its shape can be represented by a height  $h$  as a function of planar coordinates  $(x, y) = \mathbf{r}$ . This is called the Monge representation. In the limit of small deformations (i.e. small values of  $\nabla h$ ), the energy  $\mathcal{H}_\kappa + \mathcal{H}_\gamma$  can be expanded in powers of  $\nabla h$  and  $\Delta h$ . The Hamiltonian then writes

$$\mathcal{H}_{\kappa,\gamma} \approx \int_S \frac{1}{2} [\kappa (\nabla^2 h)^2 + \gamma (\nabla h)^2] d^2r \quad (1.3)$$

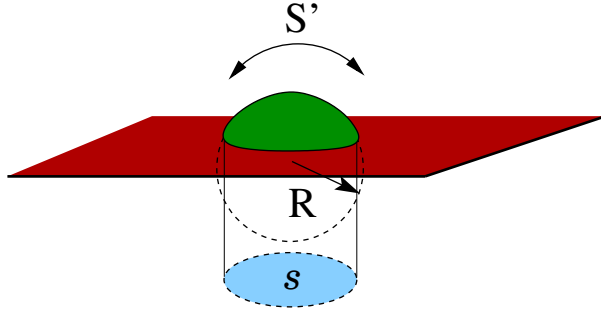


**Figure 1.3:** Cartoon of a partial bud (green) on a membrane (red).  $S'$  is the total surface area of the bud while  $s$  is the surface actually occupied by the bud on the membrane and  $R$  is the radius of curvature of the bud.

Using the Euler-Lagrange equation on  $\mathcal{H}_{\kappa,\gamma}$  let a characteristic length scale  $\lambda = \sqrt{\kappa/\gamma}$  appear. Deformations on scales larger than  $\lambda$  will be dominated by the effect of  $\gamma$ , whereas deformations at smaller scales will yield a penalty dominated by  $\kappa$ . Using values presented in section 1.6 ( $\kappa \sim 20k_B T$ ,  $\gamma = 10^{-6} - 10^{-3}$ ), we find  $5nm \leq \lambda \leq 300nm$ .

### 1.1.2 Application : the cost of budding

Let us now use those energies to compute how much energy is required to form a bud on a flat membrane, as illustrated in figure 1.3. Let us consider a partial bud of radius of curvature  $R$ , which occupies a surface  $s = \pi r^2$  on the membrane. Simple geometry shows that  $s$  can be expressed as a function of the surface  $S'$  of the partial bud :

$$s = S' \left( 1 - \frac{S'}{4\pi R^2} \right) \quad (1.4)$$

From then on, it can be shown easily that the total variation in surface area  $\Delta S = S' - s$  is :

$$\Delta S = \frac{S'^2}{4\pi R^2} \quad (1.5)$$

Using equations 1.1, 1.2, we find that the variation of energy  $\Delta E_{loc}$  upon forming a bud is :

$$\Delta E_{loc} = \gamma \frac{S'^2}{4\pi R^2} + \frac{1}{2} \kappa S' \left( \frac{2}{R^2} - \frac{1}{R_0} \right)^2 - \kappa \frac{s}{2R_0^2} \quad (1.6)$$

in which  $R_0$  is the spontaneous curvature of the membrane. However, there cannot be a discrete boundary between the bud and the flat membrane, otherwise the local curvature would be infinite and the bending energy (Eq. 1.1) would diverge. Therefore, there must be a region around the bud where the membrane is deformed, as shown in figure 1.4. This region is called the tail, and also contributes in the energy.

This contribution has been studied theoretically [15, 16, 22], and an analytical expression can be found in the limit of small deformations, using Monge representation. We recall the usual Helfrich Hamiltonian in Monge representation (equation 1.3) :

$$\mathcal{H}_{\kappa,\gamma} \approx \int_{S_{tail}} \frac{1}{2} [\kappa(\nabla^2 h)^2 + \gamma(\nabla h)^2] d^2r \quad (1.7)$$

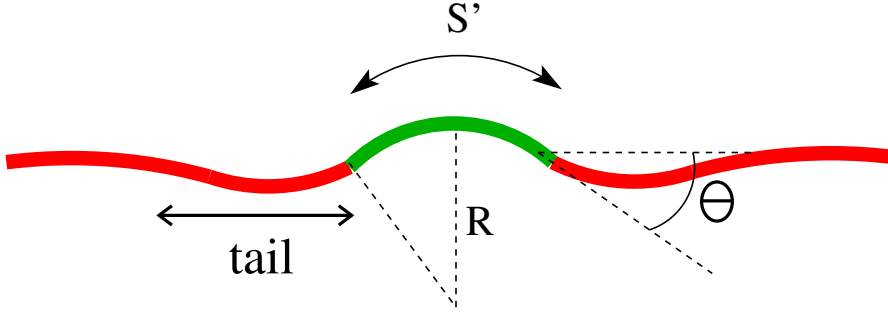


**Figure 1.4:** Schematic cutaway of a partial bud (in green) of surface  $S'$  and radius of curvature  $1/R$  on a membrane (red). The angle the bud makes with the membrane plane is called  $\theta$ . Because of the bending energy, the bud has to be connected to the rest of the membrane by a region of finite curvature. Hence, there must exist a tail around the bud, which will also contribute to the deformation energy. In the case of a well-formed bud ( $\theta > \pi/2$ ), this energy includes the cost of a zone of high curvature at the neck of the bud.

As mentioned in section 1.1.1, the minimization of this energy gives a typical length  $\lambda = \sqrt{\frac{\kappa}{\gamma}}$ , of the order of  $10 - 300nm$  in typical membranes. We can define a contact angle  $\theta$ , illustrated in figure 1.4. In the limit  $\theta \ll 1$ , we find :

$$E_{tail}(S') \approx \pi\kappa \frac{\sqrt{S'}}{\lambda} \theta^2 \frac{K_0(\frac{\sqrt{S'}}{\lambda})}{K_1(\frac{\sqrt{S'}}{\lambda})} \quad (1.8)$$

Where  $K_0$  and  $K_1$  are modified Bessel functions of the second kind. Of course  $\theta$  is known when  $S'$  and  $R$  are known : with  $\Omega$  being the solid angle corresponding to  $S'$ , it is easy to see that  $\cos \theta = 1 - \Omega/2\pi$ , therefore  $\cos \theta = 1 - \frac{S'}{2\pi R^2}$ , and  $\theta \approx \frac{S'}{\pi R^2}$ . For small domains  $S' \ll \lambda$ , using this expression for  $\theta$  in equation 1.8, we find :

$$E_{tail}(S') \approx \gamma \frac{S'^2}{4\pi R^2} \quad (1.9)$$

Which is of the same order as the membrane tension energy of the bud itself (as long as  $\theta \ll 1$ ).

For large angles (i.e. well formed buds) the analytical expression for the energy is much harder to calculate. However, we can find an order of magnitude for the tail energy. We know that this deformation takes place on a length scale  $\lambda$ , since larger deformations are prevented by  $\gamma$  and smaller deformations are prevented by  $\kappa$ . Therefore, we expect a surface of deformation around the bud of order  $S_{tail} \approx \sqrt{s}\lambda$ . Because the tail energy results in the minimization of the bending energy and the surface tension energy, both terms should contribute equally and the tail energy can be expected to scale as :

$$E_{tail} \sim \gamma \sqrt{s}\lambda = \sqrt{s\kappa\gamma} \quad (1.10)$$

For still larger angles (i.e. complete buds, as cartooned in figure 1.1.4), the tail energy will however not tend to zero, there will exist a region of high curvature at the neck of the bud. As we discussed in this section, deformations on scales smaller than  $\lambda$  are prevented by  $\kappa$  whereas deformation at larger scales are prevented by  $\gamma$ . Therefore, we can assume

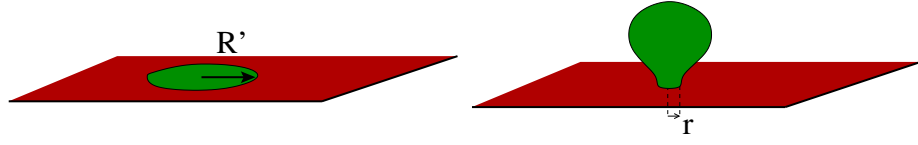


**Figure 1.5:** Cartoon of the budding (right) of an initially flat circular domain of radius  $R'$  and surface  $S' = 4\pi R'^2$  (left). Line tension  $\sigma$  may cause the domain to bud, up to a complete bud in certain conditions, the neck of which has a radius  $r$  much smaller than  $R'$ .

the minimum length of the bud interface to be of the order of  $\lambda$ , and we find :

$$E_{tail} \sim \gamma \lambda^2 \sim \kappa \quad (1.11)$$

Therefore, the tail energy when forming a bud scales like the bending energy of the bud itself.

In biological membranes, membrane buds often have a different lipid composition than the rest of the membrane. This includes an additional contribution to the bud energy. More generally, energetic terms due to membrane composition have to be taken into account.

### 1.1.3 Composition energy and line tension

One can generically expect the existence of gradients of concentration in the membrane to be penalized energetically [23]. We will describe this contribution in more details in chapter 4. As of now, let us assume that domains of distinct composition have an energy proportional to the length  $\mathcal{L}$  of their interface (in the case of well-defined domains) and hence the energy penalty to the existence of a domain writes approximately:

$$\mathcal{H}_\sigma = \sigma \mathcal{L} \quad (1.12)$$

in which  $\mathcal{L}$  is the contour length of the domain, and  $\sigma$  is called line tension and depends on the lateral energy between the lipid molecules. Its order of magnitude is typically  $\sigma \sim 0.1 k_B T / nm$  [24]. Since we will be considering the aggregation of receptors beneath a virus or a protein, we must mention the entropy cost in aggregating isolated lipid molecules. We will use a perfect gas approximation for the entropy [25], and therefore, the cost to aggregating  $N$  lipid molecules, assuming the overall density  $\phi_R$  is unchanged (i.e. there is a reservoir of lipids), reads :

$$\Delta S_N = -kN \log \phi_R \quad (1.13)$$

### 1.1.4 An illustration : line tension induced budding

Let us consider a flat membrane with a domain of distinct chemical composition from the membrane bulk. The interface energy is proportional to the contour length  $\mathcal{L}$  of the domain, and the domain will tend to be circular as this shape minimizes  $\mathcal{L}$ . If we now allow the membrane to bend, the line energy is minimal when the domain forms a bud (represented in figure 1.5), though as we mentioned in section 1.1.2 , this has a cost in bending energy

and in surface tension energy. For a circular domain of radius  $R'$ , the energy gain in forming a complete spherical bud is of order  $E_\sigma \sim 2\pi\sigma R'$ , whereas membrane deformation penalty is of order  $E_\kappa \sim 8\pi\kappa$  for the membrane bending energy (assuming a spherical shape for the bud),  $E_\gamma \sim 4\pi\gamma R'^2$  for the surface tension energy, and a tail energy  $E_{tail}$  at the neck of the bud. While it is not easy to compute the neck energy, we estimated it to scale like  $\kappa$  in section 1.1.2 :

$$E_{tail} \propto \gamma\lambda^2 \sim \kappa \quad (1.14)$$

This energy does not depend on the domain size, and just adds to the bending energy. Therefore, this energy has to be taken into account. It could be for instance modeled by an effective bending modulus  $\kappa' > \kappa$ . We can now compare the line tension energy  $E_\sigma$  to the energy of membrane deformation :  $E'_\kappa + E_\gamma$ . We find that a complete spherical bud, assuming  $R' \gg \lambda$ , will form if :

$$4\frac{\kappa'}{\sigma} < R' < 2\frac{\sigma}{\gamma} \quad (1.15)$$

Using typical values for the parameters (i.e.  $\kappa' \sim \kappa \sim 10k_B T$ ,  $\sigma \sim 0.4pN \sim 0.1k_B Tnm^{-1}$ ,  $\gamma \sim 10^{-6} - 10^{-3} J.m^{-2}$ , as indicated in section 1.6) we find that budding may occur if :

$$400nm < R' < 2.10^{-3} - 2\mu m \quad (1.16)$$

Since  $\lambda \approx 10 - 300nm$ , the approximation  $R > \lambda$  is verified for typical budding conditions (Eq. 1.16) and the equation 1.15 will usually be valid. This is however a rough estimate in the case of a full spherical bud. A more complete and exact phase diagram can be obtained as shown in [26] and [27], including the possibility for incomplete or non-spherical buds. The simplified analysis presented here will however be sufficient for most of the work presented in this thesis, and we will merely use the scaling of equation 1.15.

We can now use the tools from membrane physics to study the adsorption of viruses and toxins on the membrane of cells or vesicles in order to understand under which conditions particles can adsorb on membrane, and the mechanisms with which adsorbed particles may aggregate into tubules.

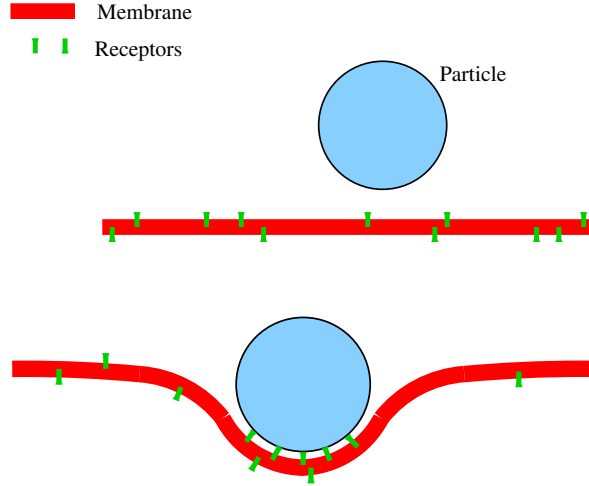


**Figure 1.6:** Cartoon of the adsorption (bottom) of a particle (for instance, a VLP) initially in the bulk (top). Adsorption involves the adhesion of the particles to lipid receptors (green), that regroup below the particle.

## 1.2 Adsorption of a particle on a membrane

In this chapter, we are interested in the aggregation of adsorbed particles, either full grown viruses (or virus-like particles, VLPs, i.e. viral capsids depleted of their genomes), or pentamers of the proteins constituting the viral capsids. In our case of interest, the VLPs are spheroid aggregates of 72 pentamers. The radius of each pentamer is about 5 nanometers, and the radius of a VLPs is 25 nm [28].

To understand their aggregation, we first need to understand their adsorption on the membrane, cartooned in figure 1.6. The pentamers adsorb on the membrane by interacting with specific lipids, called GM1. Each pentamer recruits up to five GM1, hence generating a local accumulation of the lipid receptors. Let us call  $N$  the number of GM1 molecules recruited by one particle (pentamer or VLP). Because of the long acyl chains of those lipids, the membrane is very ordered locally beneath the particles, and an interface forms with the membrane bulk, yielding a line tension  $\sigma$ . Let us call  $\epsilon$  the energy gained when a lipid is recruited (which includes a term of interaction with the particle and a term due to the interaction with the surrounding membrane environment).

The variation of the compositional free energy upon aggregating  $N$  lipids under a particle is therefore (assuming  $N$  to be much smaller than the total number of receptors in the membrane):

$$\Delta F_\sigma(N) = 2\pi\sigma r(N) - N(\epsilon + kT \log \phi_R) \quad (1.17)$$

in which  $r(N)$  is the radius of the domain interface (depending upon the domain geometry). Since the interface length  $2\pi r$  of  $N$  aggregated lipids is smaller than the interface length of  $N$  isolated lipids, we have  $2\pi\sigma r(N) - N\epsilon < 0$ . Therefore only the entropy may prevent the aggregation of the lipids, and lipids will aggregate under a particle if  $\phi_R > e^{-\epsilon/k_B T}$ .

Alternatively, we may write the variation of free energy as a function of the adsorbed surface  $S'$  :

$$\Delta F_\sigma(S') = 2\pi\sigma r(S') - S'\omega \quad (1.18)$$

in which  $\omega$  is the energy per unit surface of adhesion, i.e.  $(\epsilon + k_B T \log \phi_R)$  multiplied by the number of recruited lipids per unit surface. In the case of SV40 adhesion to membranes with GM1 lipids,  $\omega$  is typically of the order of  $10^{-3} J.m^{-2}$  [29].

However, other energies have to be taken into account. The compaction of the lipid heads beneath the particles [18] can induce a spontaneous curvature in the membrane. This curvature can cause the bending of the membrane, which will give rise to an energetic contribution of the surface tension (because there is a local increase of membrane surface compared to a flat membrane). Moreover, because the membrane shape is continuous, there must be a contribution in bending energy and surface tension energy around the adsorbed particle, which we mentioned, the tail energy (see fig 1.4).

Therefore, we must compute the total membrane energy (including membrane mechanics and composition) to know whether a particle will adsorb on the membrane. Let us consider the adhesion of one partially spherical particle of radius  $R$ , with a contact surface area  $s$  with the membrane, with an adhesive energy per surface area  $w$ . We call  $1/R_0$  the spontaneous curvature of the underlying membrane due to the aggregation of the lipid receptors below the particle. We regroup all the contributions from the membrane below the particle in the term  $F_{loc}$ . The situation is described in fig. 1.6.

The variation of free energy associated with such an adhesion reads :

$$\Delta F_{ad}^1(S', R, R_0) = \Delta F_{loc}^1(S', R, R_0) + E_{tail}^1(S', R, R_0) \quad (1.19)$$

We assume the membrane to have no spontaneous curvature outside of the area of adsorption. On the surface of adsorption  $s$ , the membrane has a spontaneous curvature  $R_0$ , that may or may not correspond to  $R$ . Let us detail  $F_{loc}^1$ , using equation 1.6 and equation 1.18 :

$$\Delta F_{loc}^1(S', R, R_0) = 2\pi r \sigma - S' \left( \omega - \frac{1}{2} \kappa \left( \frac{1}{R} - \frac{1}{R_0} \right)^2 - \gamma \frac{S'}{4\pi R^2} \right) \quad (1.20)$$

We may define  $\bar{\omega}$  such as :

$$\bar{\omega} = \omega - \frac{1}{2} \kappa \left( \frac{1}{R} - \frac{1}{R_0} \right)^2 \quad (1.21)$$

And therefore :

$$\Delta F_{ad}^1(S', R, R_0) = 2\pi r \sigma - S' \bar{\omega} + \gamma \frac{S'^2}{4\pi R^2} + E_{tail}^1(S', R, R_0) \quad (1.22)$$

We now need to know the sign of  $\Delta F_{adh}^1$  as a function of  $S', R$  and  $R_0$  to know whether a particle will adsorb. We can see from equation 1.21 that the membrane bending cost in  $\bar{\omega}$  plays no role as long as  $R \gg \sqrt{\kappa/\omega} \sim 1nm$ . Since we are considering membrane curvatures of the order of 50nm, we find  $\bar{\omega} \sim \omega$ . We know that  $r$  has  $\sqrt{S'/\pi}$  for upper bound, and therefore  $2\pi r \sigma - S' \bar{\omega} < 0$  as long as  $S' > (\sigma/\omega)^2$ , i.e. as long as  $S' > 1nm^2$ .

Therefore, the term  $2\pi r \sigma - S' \bar{\omega}$  always favors adsorption in the case of monomers and viruses and decreases linearly with the adsorbed surface  $S'$ . We mentioned earlier that

in the limit of small deformations, the tail energy grows like  $S'^2$  and is equal to the local surface tension energy beneath the particle :

$$E_{tail}^1(S', R, R_0) = \gamma \frac{S'^2}{4\pi R^2} \quad (1.23)$$

By comparing the linear (proportional to  $\bar{\omega}$ ) and the quadratic term (due to the surface tension energy beneath the particle, and  $E_{tail}^1$ ), we find that, in the small deformation regime there exists a optimal adhesion surface area  $S^*$  that minimizes the total adhesion energy. Using the small deformations approximation for  $E_{tail}^1$ , we find :

$$S^* \approx \pi R^2 \frac{\bar{\omega}}{2\gamma} \quad (1.24)$$

The adsorption of a particle is therefore the result of a competition between the effective adhesion energy per surface  $\bar{\omega}$  and the surface tension. Assuming  $R$  to be the radius of a virus, and using the numerical values of the parameters mentioned in appendix, we find that  $S^*$  is of the order of the size of a virus, or larger. Because the approximations we used are valid only for small deformations, we may only conclude that pentamers will be fully adsorbed on the membrane. Though we cannot with certainty conclude that the viruses will be fully adsorbed (that would be out of the range of validity of our approximations), we still have a good indication that viruses should be at least partially wrapped by the membrane. This was confirmed experimentally, as shown in figure 1.2. More precise modeling [16] shows that as long as  $\omega > \omega^* = 2\kappa/R^2$ , the wrapping of a virus is controlled by the ratio  $2\omega/\gamma$ . Using  $\kappa \sim 20k_B T$  and  $R \approx 25nm$ , we find  $\omega^* < 10^{-4} J.m^{-2}$  i.e.  $\omega \gg \omega^*$ . Therefore, VLPs will be strongly largely wrapped if  $\omega > \gamma$ , i.e. if  $\gamma \leq 10^{-3} J.m^{-2}$ .

Now we understand under which conditions pentamers and viruses will be well adsorbed, we need to know whether they will form tubules, which we assume to be the first step towards the infection of the cell.

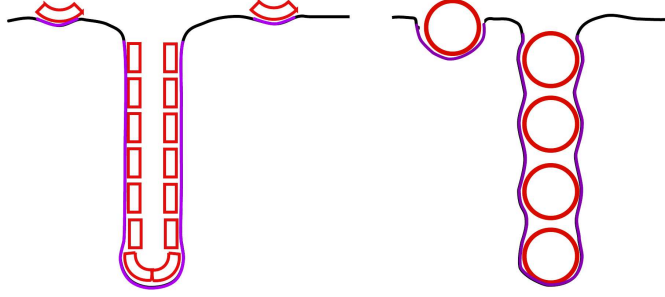


**Figure 1.7:** Schematic of the aggregation of (left) small particles such as capsid proteins pentamers and (right) large particles such as VLPs. The tail energy is concentrated at the neck of the tube and its apex.

### 1.3 Formation of aggregates

Using the formalism we previously described, we can study particle aggregation on the membrane. There are two conditions for observing membrane invagination by aggregation of monomers: it has to be energetically favorable, and it has to be done in a reasonable time (i.e. the energy barrier must be small enough). This is why we need to study the energetics and dynamics of formation of aggregates of such particles on the membrane.

#### 1.3.1 General considerations

As shown in [30], the aggregation of adsorbed particles on a membrane can be described as a diffusion on a free energy landscape [31]. Let us call  $\Delta F(l)$  the difference in free energy between an aggregate of  $l$  particles and  $l$  isolated particles. Tubulation may be observed experimentally under two conditions :

- Forming tubules must be energetically favorable ( $\exists l > 1$  ,  $\Delta F(l) < 0$ ).
- The time to form such tubules must be within experimental limits

In our case, the free energy difference writes, with  $\phi_1$  the density of adsorbed particles on the membrane :

$$\Delta F(l) = E_{tail}(l) + F_{loc}(l) - l [E_{tail}^1 + F_{loc}^1 - k_B T \log \phi_1] \quad (1.25)$$

For aggregates,  $E_{tail}(l > 1)$  and  $F_{loc}(l > 1)$  differ widely from  $E_{tail}^1$  and  $F_{loc}^1$ , because the aggregates are not circular, but may take more complex shapes to minimize their energy. We will see later how to compute these energies in some simple cases. In general, as schematized in fig. 1.8, the energy will grow for small  $l$  (because of the formation of a cap) and decrease at large  $l$  if tubules are energetically favorable, or keep on increasing otherwise [30].

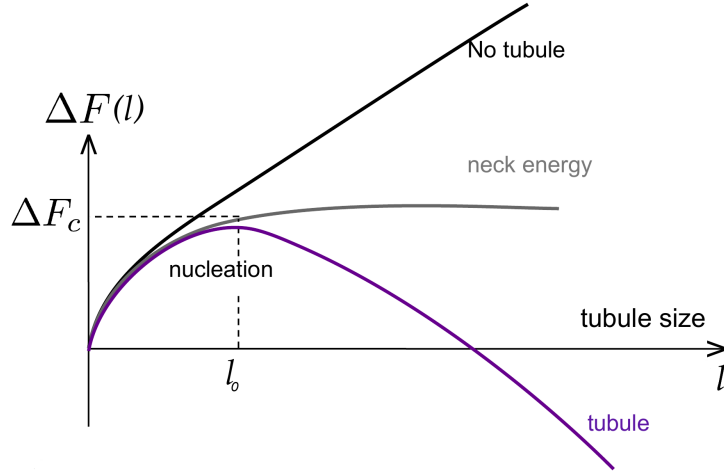


**Figure 1.8:** Expected behavior of the free energy of membrane tubules formed by aggregation of adsorbed particles.  $l_0$  is the number of particles required to form a tubule that will grow, and  $\Delta F_c$  is the corresponding variation in free energy.

Let us now consider the dynamics of aggregation. We call  $n(l)S$  the number of aggregates of size  $l$ , and  $j$  the aggregation current, such as :

$$\partial_t n(l) = -\partial_l j(l) \quad (1.26)$$

$$j(l) = -kn_1 \left( \partial_l n(l) + \frac{n(l)}{kT} \partial_l \Delta F(l) \right) \quad (1.27)$$

Let us call  $A$  the surface area of the membrane.  $1/k = A/D$  is a typical diffusion time. We can write the flux in equation 1.27 in a slightly different way :

$$j(l) = -k' \phi_1 \left( \partial_l n(l) + \frac{n(l)}{kT} \partial_l \Delta F(l) \right) \quad (1.28)$$

in which  $k' = D/S'$ . We can give a rough estimate of  $k'$ . In the case of pentamers,  $S' \approx 25\pi nm^2$ . With  $D \simeq 10^{-13} m^2 s^{-1}$ , we come up with  $k' \simeq 10^4 s^{-1}$ .

If the energy  $\Delta F(l)$  has an energy barrier for a given size  $l_0$ , as depicted in figure 1.8, the growth of large tubules will be controlled by the rate of crossing of the energy barrier. As small protein aggregates form stochastically on the membrane, most of them will evaporate in the membrane bulk, and only a few will reach the nucleation size because of thermal fluctuations. The rate at which this happens can be computed by calculating the flux  $j$  of nuclei that cross the cap. Because there are few nucleated aggregate passing the barrier, we can assume quasi-stationarity, i.e.  $\partial_l j = 0$  in equation 1.27. The exact solution depends upon  $E_{cap}(l)$ , but for most shapes of the cap energy, we find the same scaling for  $j$ , and thus for  $\tau_N$ , the nucleation time :

$$\tau_N \propto \frac{1}{k' \phi_1} e^{\frac{\Delta F_{l_0}}{kT}} \quad (1.29)$$

Using  $\phi_1 \sim 10^{-3}$ , a (rather arbitrary) nucleation condition ( $\tau_N \leq 1min$ ) yields  $\Delta F_l \leq 3 - 4k_B T$ .

We now have an expression of the energies for isolated adsorbed particles on a membrane. We can study three limit cases.

- Flat pentamers of capsid proteins.
- Curved pentamers of capsid proteins (illustrated in figure 1.7, left).
- Full VLPs (capsids depleted of DNA), as illustrated in figure 1.7, right.

In each case, we will be interested in the control of tubulation by the surface tension  $\gamma$  as it can be actively controlled by the cell (for instance by regulating its volume), and can be controlled (with various degrees of precision) experimentally.

### 1.3.2 Flat pentamers of capsid proteins

In this section, we assume the adsorbed pentamers to lay flat on the membrane, i.e. the pentamers are not curved and do not induce spontaneous curvature. This means taking the limits  $R \rightarrow \infty$  and  $R_0 \rightarrow \infty$  in equation 1.21. In this case, pentamers are well adsorbed as long as there are enough GM1 receptors on the membrane (i.e. if  $\phi_1 > \exp(\pi a^2 \omega / k_B T)$ ). Because there is no spontaneous curvature, the tail energy is null and therefore the variation of free energy in aggregating  $l$  pentamers of radius  $a$  just depends on the line tension, and we would be tempted to write it :

$$\Delta F(l) = \sigma \mathcal{L} - l [2\pi\sigma a + k_B T \log \phi_1] \quad (1.30)$$

in which  $\phi_1$  is the density of adsorbed pentamers on the membrane and  $\mathcal{L}$  is the contour length of the domain. For a flat circular domain,  $\mathcal{L} \simeq 2\pi a \sqrt{l}$ . As  $l \geq 1$ , aggregates will grow as long as  $2\pi\sigma a - k_B T \log \phi_1 > 0$ . This is actually not exact as we do not know the precise organization of the membrane below the adsorbed pentamers in an aggregate and for isolated pentamers. For instance, if the aggregate is not perfectly packed, we can expect the presence of other lipids to fill the gaps. Therefore the gain in surface tension energy when aggregating a monomer is slightly lower than the surface tension of one isolated monomer, and equation 1.30 should be written, with  $\sigma' \leq \sigma$  :

$$\Delta F(l) = \sigma \mathcal{L} - l [2\pi\sigma' a + k_B T \log \phi_1] \quad (1.31)$$

We then find that there is a critical value of  $l$ ,  $l_0 \sim (\sigma/\sigma')^2$  above which it is favorable for flat aggregates to grow. We expect  $l_0$  to be of the order of a few units as we do not expect  $\sigma$  and  $\sigma'$  to be too different. Therefore, flat pentamers should rapidly form flat aggregates because of line tension.

However, those domain might not remain flat as the line tension term tends to decrease the interface length. By comparing the line tension term  $2\pi\sigma R$  to the bending energy  $8\pi\kappa$ , one finds that spontaneous budding will occur for domains of radius  $R > R^*$ ,  $R^* = 4\kappa/\sigma \approx 400nm$  (section 1.1.4).  $R^*$  is much larger than the radius of tubules observed experimentally, and there must be an other cause to the formation of tubules of small radius.

### 1.3.3 Pentamers of capsid proteins - with spontaneous curvature

Let us consider pentamers adsorbed on a vesicle. If the pentamers have a curvature and are rigid, the membrane below pentamers will bend to the same curvature to maximize

the adhesion surface. Moreover, the pentamers are adsorbed on one face of the membrane, and, because this adsorption recruits GM1 lipids below the pentamers, the membrane is locally asymmetric. Adsorption compacts lipids head groups below the proteins, which can cause a spontaneous curvature. To ease the comparison with capsid shells, we will assume this spontaneous curvature  $R_0$  to be equal to the radius of a viral capsid, i.e.  $R_0 \approx R$ .

We showed earlier that such particles were fully adsorbed on the membrane, because their size  $a \approx 5nm$  is much below the limit adsorption size (i.e.  $\pi a^2 \leq S^*$ , see equation 1.24). Moreover, the adhesion energy per surface  $\omega$  is the same for proteins in a tube and for isolated proteins. The contribution of the surface tension, however, is not the same. For isolated proteins, the membrane tension energy  $E_\gamma^1$  is approximately equal to the tail energy of isolated pentamers (given by the limit of 1.8 for  $s/\lambda \rightarrow 0$ ) :

$$E_\gamma^1 \approx E_{tail}^1 \propto \gamma \frac{a^4}{R^2} \quad (1.32)$$

This is negligible compared to the surface tension energy of the protein in a tube :

$$E_\gamma^{tube}(1) = \pi\gamma a^2 \quad (1.33)$$

The driving force to making tubes is hence not the tail energy of individual pentamers, which is overwhelmed by the surface tension of pentamers in a tube.

In large enough tube, for which the neck and apex have a fixed shape, the total energy is proportional to the length of the tube, and hence to the number of particles in the tube, in addition to a constant term corresponding to the deformation of the membrane at the neck and the apex of the tube. Therefore, the variation of free energy resulting from the aggregation of  $l$  adsorbed particle in tubular domain of contour length  $\mathcal{L}$  is :

$$\Delta F(l) = \sigma \mathcal{L}(l) + E_{tail}(l) + E_{apex}(l) - l (2\pi\sigma' a - \pi\gamma a^2 + k_B T \log \phi_1) \quad (1.34)$$

in which  $\mathcal{L}(l)$ ,  $E_{tail}(l)$  (the neck energy) and  $E_{apex}(l)$  tend to constants when  $l$  is large. In this scenario, tubes will be energetically favorable if adding one adsorbed pentamer to the tube decreases the energy and hence if  $2\pi\sigma' a - \pi\gamma a^2 + k_B T \log \phi_1 > 0$ .

Therefore, the thermodynamic condition to the formation of tubules by pentamers (assuming a large excess of pentamers) is

$$\gamma < 2\frac{\sigma'}{a} \sim 2\frac{\sigma}{a} \quad (\sim 10^{-4} J.m^{-2}) \quad (1.35)$$

If this condition is satisfied, there is a critical monomer density  $\phi_1^*$  allowing tubule formation :

$$\phi_1^* = e^{\frac{\gamma\pi a^2 - 2\pi\sigma a}{k_B T}} \quad (1.36)$$

Let us now consider the dynamic condition, i.e. let us find for which range of parameters the energy barrier is small enough for tubes to form in a reasonable time. Let us consider a hemispherical aggregate of pentamers. The bending energy contribution to the apex energy is zero if  $R = R_0$ , that which we assumed. The neck energy grows like  $R\sqrt{\kappa\gamma}$  as found in section 1.1.2. The free energy variation for a hemispherical aggregate hence is

$$\Delta F(l) = 2\pi\sigma R + R\sqrt{\kappa\gamma} - l \left( 2\pi\sigma a - \frac{1}{2}\pi\gamma a^2 + k_B T \log \phi_1 \right) \quad (1.37)$$

In the intermediate situation between small domains and large tubes, the minimization of the energy does not actually yield a hemispherical shape, and computing the shape of the aggregate is not an easy task. However equation 1.37 gives the scaling of this energy. If  $l < (R/a)^2$ , we can use the approximation  $R \sim a\sqrt{l}$ , and the energy barrier  $\Delta E(l)$  to overcome is :

$$\frac{\lambda}{a} < l < \left(\frac{R}{a}\right)^2 \quad : \quad \Delta E(l) \approx 2\pi a\sqrt{l}(\sigma + \sqrt{\kappa\gamma}) \quad (1.38)$$

$$(1.39)$$

The cost in surface tension energy when adding a pentamer to an aggregate has an upper bound  $\gamma\pi a^2$  (the surface tension energy for a pentamer to enter a tube). Therefore the energy gain  $\mu$  per aggregated monomer has a lower bound :

$$\mu > 2\pi a\sigma' - \pi\gamma a^2 + k_B T \log \phi_1 \quad (1.40)$$

Let us call  $l_0$  the critical nucleation size (as illustrated in figure 1.8), defined by the number of pentamers that need to be aggregated for the energy barrier to be crossed, i.e.  $\Delta E(l_0) = l_0\mu$ . Using equations 1.38 and 1.40, we find that the critical nucleation size  $l_0$  scales like :

$$l_0 \approx \left( \frac{2\pi a (\sigma + \sqrt{\kappa\gamma})}{2\pi a\sigma' - \pi\gamma a^2 + k_B T \log \phi_1} \right)^2 \quad (1.41)$$

in which the denominator is non-zero because we assumed that there was an energy maximum, i.e.  $\mu < 0$ . The nucleation energy is  $\Delta E(l_0)$  and therefore the nucleation time reads :

$$\tau_N \propto \frac{1}{n_1} \tau_D e^{\frac{2\pi a(\sigma' + \sqrt{\kappa\gamma})\sqrt{l_0}}{kT}} \quad (1.42)$$

Even if the thermodynamic condition to forming tubes are satisfied, the nucleation time can be prohibitively long, due to the energy barrier. We showed in section 1.3.1 that this energy barriers start playing an important role ( $\tau_N > 1\text{min}$ , say) for  $\Delta E(l_0) > 4k_B T$ . Using  $\sigma' \approx \sigma \sim 0.1k_B T.nm^{-1}$ ,  $\kappa \approx 20k_B T$  and  $a \approx 5nm$ , we find that the nucleation time will be prohibitively long if  $\gamma > 2.10^{-3}k_B T.nm^{-2} \approx 10^{-5}J.m^{-2}$ .

In this section, we showed that even if the formation of tubes by adsorbed pentamers is thermodynamically favorable ( $\gamma < 10^{-4}J.m^{-2}$ ) surface tension might strongly limit the existence of tubes, except for very low surface tensions ( $\gamma < 10^{-5}J.m^{-2}$ ), because of the kinetics of domain formation. We can now investigate the adhesion and aggregation of VLP particles.

### 1.3.4 Aggregation of virus-like particles

VLP might not be fully wrapped by the membrane if, for instance, the surface tension is too high. The degree of wrapping around the VLP is of order  $\min(1, \bar{\omega}/\gamma)$ , as shown in

section 1.2. We will consider the situation of high wrapping since it has been observed experimentally by our collaborators, as shown in fig. 1.2. For well-wrapped VLPs, the surface tension energy does not change whether the VLP is in a tubule or isolated, whereas the neck energy of a tubule and the neck energy of an isolated VLP is about the same, corresponding to  $E_{tail}$ . Therefore one could write naively :

$$\Delta F_l = E_{tail}(1) + E_\sigma(1) - l\mu \quad (1.43)$$

$$\mu = (E_{\sigma'}(1) + E_{tail}(1) + k_B T \log n_1) \quad (1.44)$$

The energy gain per monomer is actually smaller than expected from naive arguments since the wrapping in a tube is imperfect at two poles of one VLP whereas the wrapping of a single VLP is imperfect at only one pole. Therefore, the tail energy might play a role in the aggregation, but its role will be reduced by the wrapping energy lost when a capsid enters a tubules. In contrast, the line tension energy will always favor the formation of tubules for  $l > (\sigma/\sigma')^2$ .

We only showed that line tension definitely promotes aggregation. More complex modeling could be done to study the role of the tail energy in the aggregation of VLPs, and previous results indicate that it does enable tubulation [17, 15]. However, this argument shows that is favorable to grow tubules of VLP as long as they are well adsorbed, i.e. as long as  $\gamma < \bar{\omega} \approx 10^{-3} J.m^{-2}$ .

## 1.4 Comparison with experiments

We showed that the aggregation of small toxins or pentamers is promoted by line tension, but the formation of tubules of small radius ( $\approx 50nm$ ) requires a bending of the membrane below the pentamer, i.e. a spontaneous curvature of the pentamers imposed to the membrane. This spontaneous curvature can be due to the shape of the pentamers or to the asymmetric distribution of lipids in the bilayer, caused by the particle adsorption on one face of the membrane. Tubules of pentamers cannot form in cells or vesicles if  $\gamma > 2\sigma/a \approx 10^{-4}J.m^{-2}$  and nucleation is expected to be very slow for  $\gamma > 4\mu^2/\kappa \approx 10^{-5}J.m^{-2}$ .

In the case of the VLPs, the spherical shape of the capsids necessarily impose a curvature to the membrane. The adhesion of VLPs on the membrane results from a competition between surface tension  $\gamma$  and the effective adhesion energy  $\bar{\omega}$ . A large adhesion of VLP requires  $\gamma > \bar{\omega} \approx 10^{-3}J.m^{-2}$ . Aggregation of capsids will be driven by line tension and facilitated by the tail energy of the adsorbed particles. In the case of strong wrapping ( $\theta \geq \pi/2$ ) the tail contribution can amount to a sizable contribution to the overall line tension of the membrane, and drive aggregation of the adhered VLPs.

Our results can be qualitatively compared to experiments performed by collaborators. They could change the length of the acyl chains of the viral receptor, GM1, and they showed that smaller chains did not enable the formation of tubules by capsids or pentamers. Long acyl chains length are known to promote liquid ordered phase ( $l_o$ ). We can thus expect the acyl chain length of receptors to have a strong effect on the line tension  $\sigma$ . In particular, we expect that decreasing this chain length decreases the line tension  $\sigma$ . The experimental observation that GM1 with shorter acyl chains did not allow such tubulation therefore suggests that line tension is an important driving force to the formation of protein aggregates, as predicted by our model. As VLP binding to the membrane is not hindered by GM1 with shorter acyl chains [13], this effect is indeed a line tension effect.

Our collaborators also showed that GM1 with unsaturated chains did not enable the tubulation by pentamers. The existence of unsaturations of the acyl chains will decrease the membrane order (hence decreasing the line tension), and will increase the ability of acyl chains to interpenetrate, hence decreasing the spontaneous curvature of the membrane below the particles by the lipid compaction mechanism described in [18]. This observation therefore confirms the importance of the spontaneous curvature of the membrane below the adsorbed proteins in the formation of tubules by pentamers, as was predicted by our model.

Eventually, our collaborators showed that membrane tension may prevent the tubulation of pentamers but does not seem to affect VLP-induced tubulation. This is in agreement with our theory, which predicts pentamer tubulation to be much more sensitive to surface tension than tubulation by VLPs.

The full article with experimental results is shown in the appendix of this chapter.

## 1.5 Conclusion

In this first chapter, we showed that the heterogeneities in the membrane composition can trigger membrane deformations and, in our case, enable transport. In the case of viruses, the cell metabolism is hijacked and after infection, the viruses will use the cell machinery to duplicate themselves. In addition to creating thousands of capsid proteins and hundreds of copies of their DNA, the viruses will act in various ways on the gene expression of the host cell. The properties of host membrane, for instance, may be changed to promote the release of new viruses. This is an example of feedback of the transported molecules on the transport properties.

One very interesting case of virus having a feedback of its own transport is the vesicular stomatitis virus (VSV). This virus enters the cell via the clathrin pathway, and encodes in its RNA genome the code for a protein, called VSV protein G (or VSVG), which is integrated in the plasma membrane after being transported and altered in the secretion pathway of the cell. Once in the plasma membrane, it facilitates the infection of the cell by other VSV virus. VSVG is now a very widely used tool to study the transport in the secretion pathway.

In the case of toxins, they are transported after their entrance in the cell to their destination of action. This transport can use various means. It has been shown that some toxin use the secretion pathway in a backward fashion, in a process called retrograde trafficking. In the next chapter, we will study transport in a particular organelle in the center of the secretion pathway : the Golgi apparatus. We will gain some understanding of some mechanisms of protein localization in the cell, and we will have precious hints on the physical basis of anterograde and retrograde transport in the secretion pathway.

## 1.6 Typical values of the parameters

To have a better understanding of the approximations, we need an idea of the numerical values of the different parameters. We took the values from [13], [11], [29] and [28].

	Physical parameter	Energy scale for	
		Monomer (radius $a = 5nm$ )	Capsid (radius $R = 25nm$ )
Adhesion energy	$\omega = 10^{-3} J.m^{-2}$	$\pi a^2 \omega \approx 20k_B T$	$4\pi R^2 \omega \approx 2000k_B T$
Bending energy	$\kappa = 10 - 20k_B T$	$2\pi \kappa a^2 / R^2 \approx 5k_B T$	$8\pi \kappa \approx 500k_B T$
Line tension	$\sigma \approx 0.4pN \approx 0.1k_B T/nm$	$2\pi a \sigma \approx 3kT$	$2\pi R \sigma \approx 15k_B T$
Surface tension	$\gamma \approx 10^{-6} - 10^{-3} J.m^{-2}$	$\pi a^2 \gamma \approx 0.02 - 20k_B T$	$4\pi R^2 \gamma \approx 2 - 2000k_B T$
Deformation line tension	$\sigma_\lambda = \sqrt{\kappa \gamma} \approx 0.1 - 2pN$	$2\pi a \sqrt{\kappa \gamma} \approx 2 - 11k_B T$	$2\pi R \sqrt{\kappa \gamma} \approx 70 - 350k_B T$
Membrane decay length	$\lambda = \sqrt{\frac{\kappa}{\gamma}} \approx 10 - 300nm$	$a \approx 0.02 - 0.5\lambda$	$R \approx 0.1 - 3\lambda$

## 1.7 Article

# GM1 structure determines SV40-induced membrane invagination and infection

Helge Ewers<sup>1,12,14</sup>, Winfried Römer<sup>2,3,14</sup>, Alicia E. Smith<sup>1</sup>, Kirsten Bacia<sup>4,13</sup>, Serge Dmitrieff<sup>5</sup>, Wengang Chai<sup>6</sup>, Roberta Mancini<sup>1</sup>, Jürgen Kartenbeck<sup>1,7</sup>, Valérie Chambon<sup>2,3</sup>, Ludwig Berland<sup>8,9</sup>, Ariella Oppenheim<sup>10</sup>, Günter Schwarzmann<sup>11</sup>, Ten Feizi<sup>6</sup>, Petra Schwille<sup>4</sup>, Pierre Sens<sup>5</sup>, Ari Helenius<sup>1,15,16</sup> and Ludger Johannes<sup>2,3,15</sup>

Incoming simian virus 40 (SV40) particles enter tight-fitting plasma membrane invaginations after binding to the carbohydrate moiety of GM1 gangliosides in the host cell plasma membrane through pentameric VP1 capsid proteins. This is followed by activation of cellular signalling pathways, endocytic internalization and transport of the virus via the endoplasmic reticulum to the nucleus. Here we show that the association of SV40 (as well as isolated pentameric VP1) with GM1 is itself sufficient to induce dramatic membrane curvature that leads to the formation of deep invaginations and tubules not only in the plasma membrane of cells, but also in giant unilamellar vesicles (GUVs). Unlike native GM1 molecules with long acyl chains, GM1 molecular species with short hydrocarbon chains failed to support such invagination, and endocytosis and infection did not occur. To conceptualize the experimental data, a physical model was derived based on energetic considerations. Taken together, our analysis indicates that SV40, other polyoma viruses and some bacterial toxins (Shiga and cholera) use glycosphingolipids and a common pentameric protein scaffold to induce plasma membrane curvature, thus directly promoting their endocytic uptake into cells.

SV40 is a non-enveloped DNA virus of the polyoma family. The capsid is 45 nm in diameter, and composed of 72 icosahedrally organized VP1 pentamers<sup>1</sup> that each bear five binding sites highly specific for GM1 (refs 2, 3), its glycolipid receptor for infection<sup>4</sup>. Incoming SV40 virions attach to several GM1 molecules<sup>5,6</sup> in the exoplasmic leaflet of the plasma membrane and quickly become immobilized by the cortical actin cytoskeleton<sup>7,8</sup>. Cholesterol-dependent entry<sup>7</sup> occurs after kinase signalling<sup>7,9</sup> via small, tight-fitting indentations<sup>10</sup>, most of which are devoid of caveolin-1 (Cav-1; ref. 11). Internalized vesicles are transported via microtubules to the smooth endoplasmic reticulum<sup>12</sup> where the protein folding and retrotranslocation machineries are involved in SV40 export into the cytosol<sup>13</sup> for infection.

How the binding of a virion to glycolipids in the exoplasmic leaflet leads to cell entry and infection is not clear. Several other multivalent glycolipid ligands are also internalized by clathrin-independent endocytosis<sup>14–16</sup>, suggesting that the reorganization of specific lipids into membrane domains<sup>17,18</sup> is important for the uptake process<sup>19–21</sup>. Indeed, binding of the pentavalent cholera toxin to GM1 induces the formation of membrane domains *in vitro*<sup>22</sup>, and multivalent binding is required for

efficient endocytosis<sup>23</sup>. By binding to up to 15 Gb3 glycolipid molecules, Shiga toxin drives curvature changes of cell and model membranes<sup>24</sup>. Whether multivalent binding and glycolipid structure mediate the process of cell infection by colloidal viral particles is not known.

Here, we investigate the role of the hydrocarbon chain structure of the GM1 receptor molecule in SV40 endocytosis and infection. Based on experimental work with cells and liposomal membranes and on theoretical considerations, a physical model for the formation of SV40-induced membrane invaginations is derived. Our results indicate that the tight organization of GM1 molecules with specific hydrocarbon chain structures is required for membrane mechanical processes leading to endocytosis and infection by SV40.

## RESULTS

### Dependence of SV40 infection on GM1 hydrocarbon chain structure

To test how critical the structure of the GM1 hydrocarbon chain is for cellular uptake and infection, we took advantage of a mutant mouse melanoma cell

<sup>1</sup>ETH Zurich, Institute of Biochemistry, HPM E, Schafmattstrasse 18, 8093 Zurich, Switzerland. <sup>2</sup>Institut Curie, Centre de Recherche, Laboratoire Trafic, Signalisation et Ciblage Intracellulaires, 75248 Paris Cedex 05, France. <sup>3</sup>CNRS UMR144, France. <sup>4</sup>Institute for Biophysics, TU Dresden, BIOTEC, Tatzberg 47-51, D-01307 Dresden, Germany. <sup>5</sup>UMR Gulliver CNRS-ESPCI 7083, 10 rue Vauquelin, 75231 Paris Cedex 05, France. <sup>6</sup>Glycosciences Laboratory, Imperial College London, Harrow, Middlesex, HA1 3UJ, UK. <sup>7</sup>M010, German Cancer Research Center (DKFZ), D-69120 Heidelberg, Germany. <sup>8</sup>Institut Curie, Centre de Recherche, Laboratoire Physico-Chimie, 75248 Paris Cedex 05, France. <sup>9</sup>Université P. et M. Curie/CNRS UMR168, France. <sup>10</sup>Department of Hematology, The Hebrew University-Hadassah Medical School, Ein Kerem, Jerusalem 91120, Israel. <sup>11</sup>LIMES, Membrane Biology and Lipid Biochemistry Unit c/o Kekulé-Institut für Organische Chemie und Biochemie der Universität Bonn, 53123 Bonn, Germany. <sup>12</sup>Current address: ETH Zurich, Laboratory for Physical Chemistry, HCI F, Wolfgang-Pauli Strasse 10, 8093 Zurich, Switzerland. <sup>13</sup>Current address: University of California at Berkeley, Department of Molecular and Cell Biology, Berkeley, CA 94720, USA.

<sup>14</sup>These authors contributed equally to this work.

<sup>15</sup>These authors contributed equally to this work.

<sup>16</sup>Correspondence should be addressed to A.H. (e-mail: ari.helenius@bc.biol.ethz.ch).

Received 16 September 2009; accepted 24 November 2009; published online 20 December 2009; DOI: 10.1038/ncb1999

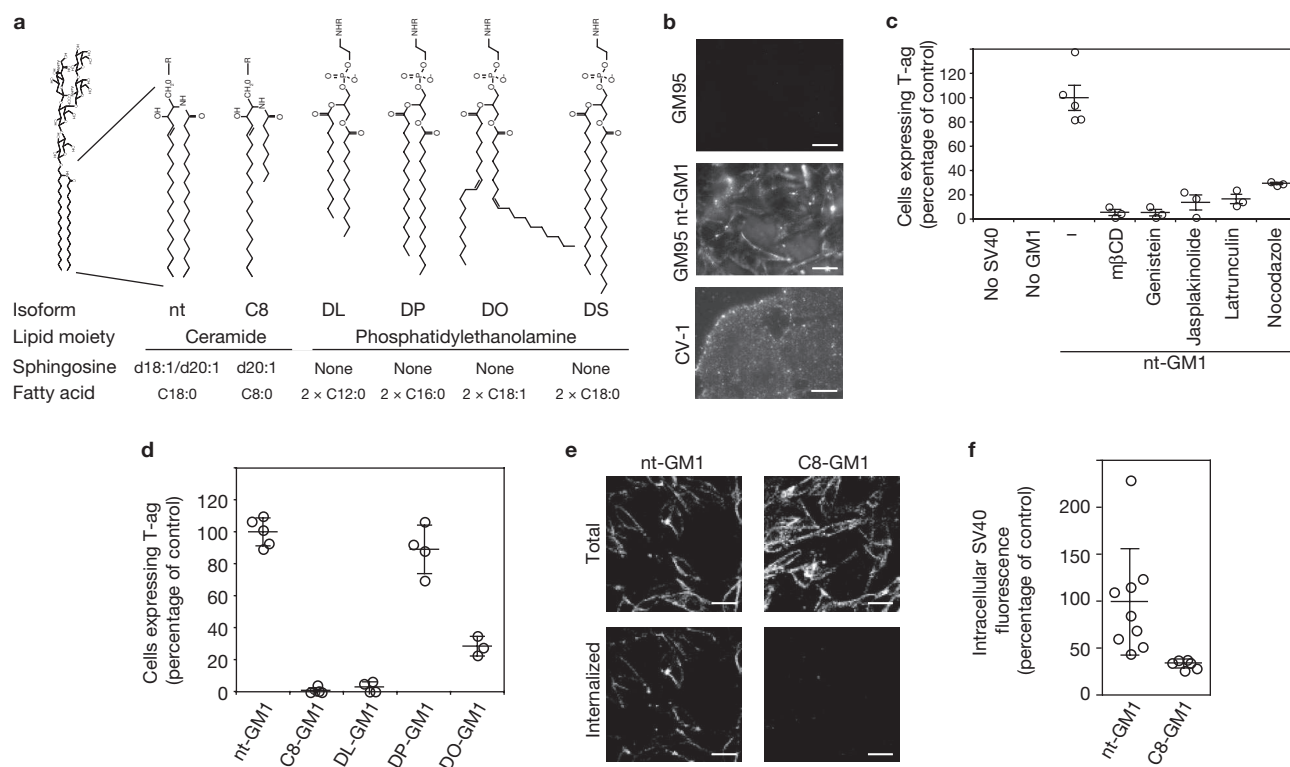


**Figure 1** SV40 infection and endocytosis depend on GM1 hydrocarbon chain structure. **(a)** Structures of nt-GM1 and the chemically synthesized GM1 species used in this study. The native (nt-GM1) species is shown on the left next to C8-GM1, which has an 8-carbon short-chain fatty acid. For other species, the GM1 pentasaccharide was attached to the amino groups of phosphatidylethanolamine (PE) glycerophospholipid species bearing different fatty acid chains: di-lauroyl-PE (DL-GM1), di-palmitoyl-PE (DP-GM1), di-oleoyl-PE (DO-GM1) and di-stearoyl-PE (DS-GM1). **(b)** Fluorescence microscopy images of Cy5-labelled SV40 (SV40-Cy5) incubated with GM1-deficient GM95 cells, GM95 cells that were supplemented with nt-GM1, or CV-1 cells naturally expressing GM1. **(c)** SV40 infection in GM95 cells that were supplemented or not with nt-GM1, as indicated. nt-GM1-supplemented cells were mock treated (–) or pre-incubated for 1 h with methyl- $\beta$ -cyclodextrin (m $\beta$ CD, 5 mM), genistein (0.1 mM), nocodazole (1  $\mu$ M), latrunculin (0.1  $\mu$ M) or jasplakinolide (0.1  $\mu$ M). Inhibitors were maintained during the experiment. Infection was

scored by immunofluorescence detection of nuclear SV40 T-antigen (T-ag) expression after Hoechst staining and data were normalized to expression in nt-GM1-supplemented GM95 cells. Data are the mean  $\pm$  s.d. of at least three independent experiments,  $P < 0.01$  for all inhibitors compared with nt-GM1-supplemented cells (Student's *t*-test). **(d)** SV40 infection in GM95 cells supplemented with the indicated GM1 species. Infection was scored and plotted as in **c**. Data are the mean  $\pm$  s.d.,  $P < 0.01$  for C8-GM1 and DL-GM1 compared with nt-GM1 cells (Student's *t*-test). **(e)** Confocal images of atto-488-biotin dual-labelled SV40-VLPs after 2 h incubation at 37°C with GM95 cells supplemented with nt-GM1 (left) or C8-GM1 (right). Total atto-488 fluorescence of SV40-VLPs (top) and specific detection of intracellular SV40-VLPs through the biotin label by indirect immunofluorescence (bottom). **(f)** Quantification of intracellular SV40-biotin-VLPs after immunofluorescence detection of internalized particles as in **e**. Fluorescence intensity was normalized to that of cells supplemented with nt-GM1. Data are the mean  $\pm$  s.d.,  $P < 0.001$  (Student's *t*-test). Scale bars, 10  $\mu$ m.

line, GM95, that lacks all glucose-based glycolipids<sup>25</sup>. We incorporated GM1 species with differing lipid chain compositions<sup>26,27</sup> into these cells. GM1 with C18:1/C20:1 sphingosine molecules and C18:0 fatty acids (native, nt-GM1, Fig. 1a) was used as a control. After GM95 cell reconstitution with nt-GM1, the lipid was evenly distributed in the plasma membrane, as judged by the homogeneous appearance of fluorescently labelled cholera toxin B-subunit (CTxB-FITC; Supplementary Information, Fig. S1a), another natural GM1 ligand<sup>28</sup>. This situation was similar to the one found on cells that naturally express GM1 (data not shown). Fluorescence recovery after photobleaching (FRAP) demonstrated that the GM1-bound CTxB-FITC was mobile in the plane of the membrane (Supplementary Information, Fig. S1a). Moreover, confocal microscopy showed that CTxB was efficiently internalized by endocytosis (data not shown). We concluded that nt-GM1 was integrated as a functional component of the plasma membrane, as demonstrated previously by electron spin resonance<sup>27</sup>.

Whereas Cy5-labelled SV40 failed to associate with untreated GM95 cells (Fig. 1b), it bound to nt-GM1-supplemented cells to a similar extent

as to wild-type murine cells (Fig. 1b). In contrast to untreated cells that were totally resistant to infection, up to 76% of the cells supplemented with nt-GM1 were infected, as indicated by T-antigen expression. The level of infection depended on the amounts of GM1 and SV40 used (Supplementary Information, Fig. S1b, c). As in normal host cells, infection was inhibited by extraction of cellular cholesterol (m $\beta$ CD), inhibition of tyrosine kinase activity (genistein), disruption of microtubulules (nocodazole) and interference with the dynamics of the actin cytoskeleton (jasplakinolide and latrunculin A; Fig. 1c)<sup>2,29</sup>. By supplementing cells with GM1, we could thus reconstitute the normal, productive entry pathway of SV40 in GM95 cells.

Next, GM95 cells were supplemented with GM1 species with differing tail structures. One was a GM1 molecule with short fatty acid chains (C8), and the others (DL, DP and DO) were glycerophospholipids with differing saturation levels and lengths of lipid chains to which the GM1 pentasaccharide was conjugated through the amino group of the phosphatidylethanolamine (Fig. 1a; Methods)<sup>27,30</sup>. By measuring CTxB-Cy5 binding to GM95 cells, we first determined the amount of each lipid

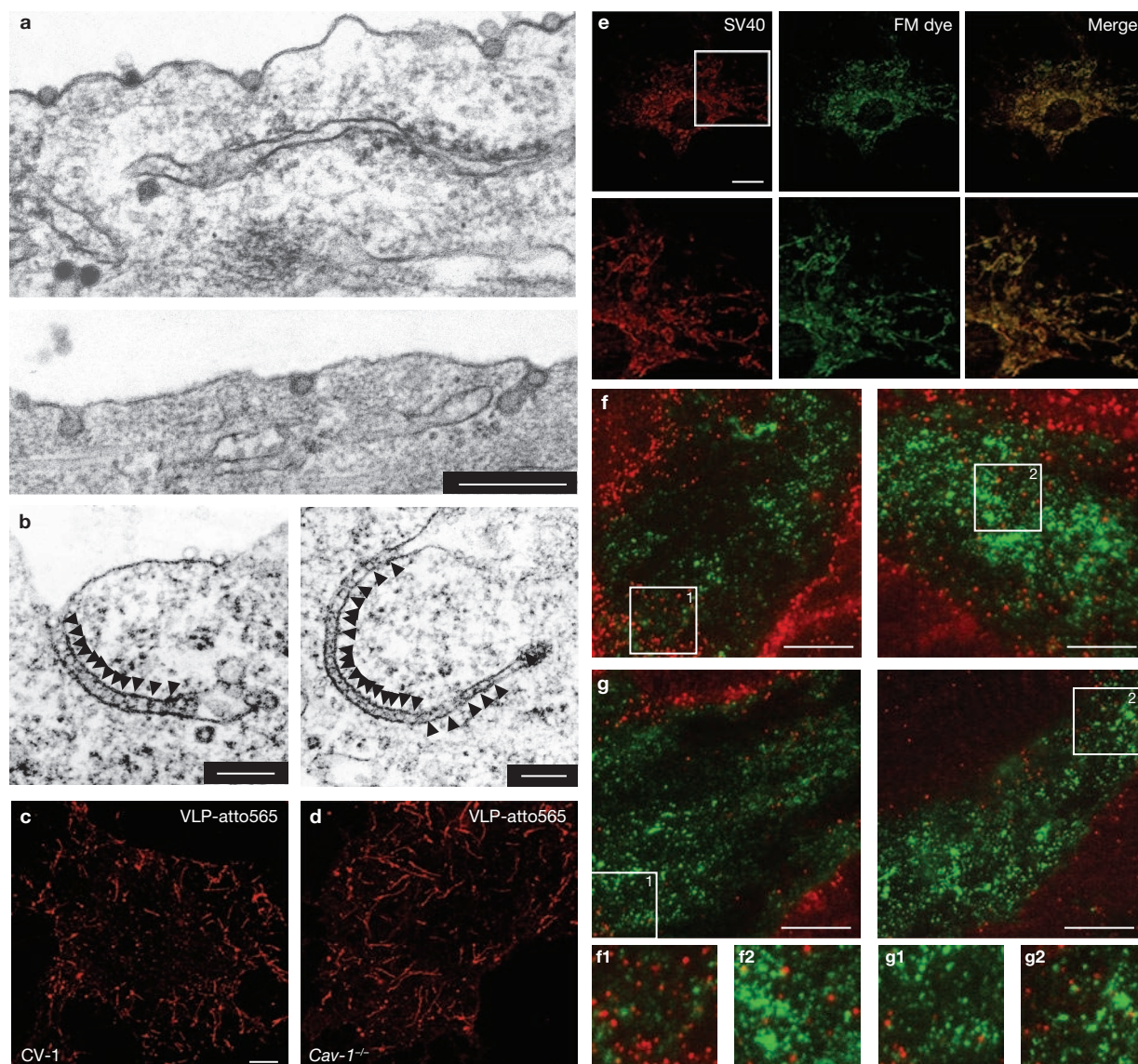


**Figure 2** SV40 binding induces caveolin-independent membrane invagination in cells. **(a)** Electron micrographs of CV-1 cells that were incubated for 7 min with SV40. Note the tight-fitting membrane under SV40 particles. **(b)** Electron micrograph of polyomavirus VLPs after 30 min incubation with cells. The VLPs line the lumen of tubular membrane invaginations like beads on a string (arrowheads). Scale bars, 200 nm. **(c–d)** Confocal images of fluorescence-labelled SV40-VLPs after 30 min incubation with energy-depleted CV-1 cells **(c)** or *Cav-1*<sup>-/-</sup> cells **(d)**. Scale

bars, 5  $\mu$ m. **(e)** Confocal images of fluorescence labelled SV40-VLPs (red) and the membrane dye FM 43 FX (green) after 30 min incubation with energy-depleted *Cav-1*<sup>-/-</sup> cells (top panels). Scale bar, 10  $\mu$ m. A magnified region of the cell is shown in the bottom panels. **(f, g)** TIRF microscopy images of fluorescence-labelled SV40-VLPs a few minutes after binding to the bottom surface of untreated **(f)** or energy-depleted **(g)** Cav-1-GFP-expressing cells. Magnified regions of the cells are shown in the bottom panel. Scale bars, 10  $\mu$ m.

species needed to result in a level of binding comparable to that found on cells supplemented with nt-GM1 (Supplementary Information, Fig. S1d). To make sure that the different lipid species were properly inserted into the plasma membrane, lateral CTxB-FITC mobility was confirmed under all conditions by FRAP analysis (data not shown).

We then analysed the binding of SV40 to these reconstituted cells using virus-like particles (VLPs), which are recombinant capsids composed exclusively of VP1 proteins<sup>31,32</sup>. VLPs behave as intact virus with respect to receptor binding and endocytosis, but are devoid of viral DNA as well as internal capsid proteins. SV40-VLP binding was similar between cells reconstituted with the different GM1 species (Supplementary Information, Fig. S1e, f). However, only GM1 species with long acyl chains, DP- and

DO-GM1, supported SV40 infection (Fig. 1d). The levels of infection were  $88.9 \pm 15.1\%$  and  $26.8 \pm 7.4\%$ , respectively, compared with nt-GM1 supplemented cells. In contrast, infection in cells that were supplemented with short chain species was close to background levels (Fig. 1d). We concluded that a ceramide base structure was not an absolute requirement for glycolipid receptor function, but acyl chain length was critical.

To determine which step in the infectious entry programme required a receptor lipid with long acyl chains, GM95 cells were supplemented with either nt-GM1 or C8-GM1. The latter was chosen to represent a non-permissive receptor species. Confocal microscopy after indirect immunofluorescence labelling of internalized particles showed that only nt-GM1 supported efficient endocytosis of the virus (Fig. 1e). SV40-VLP

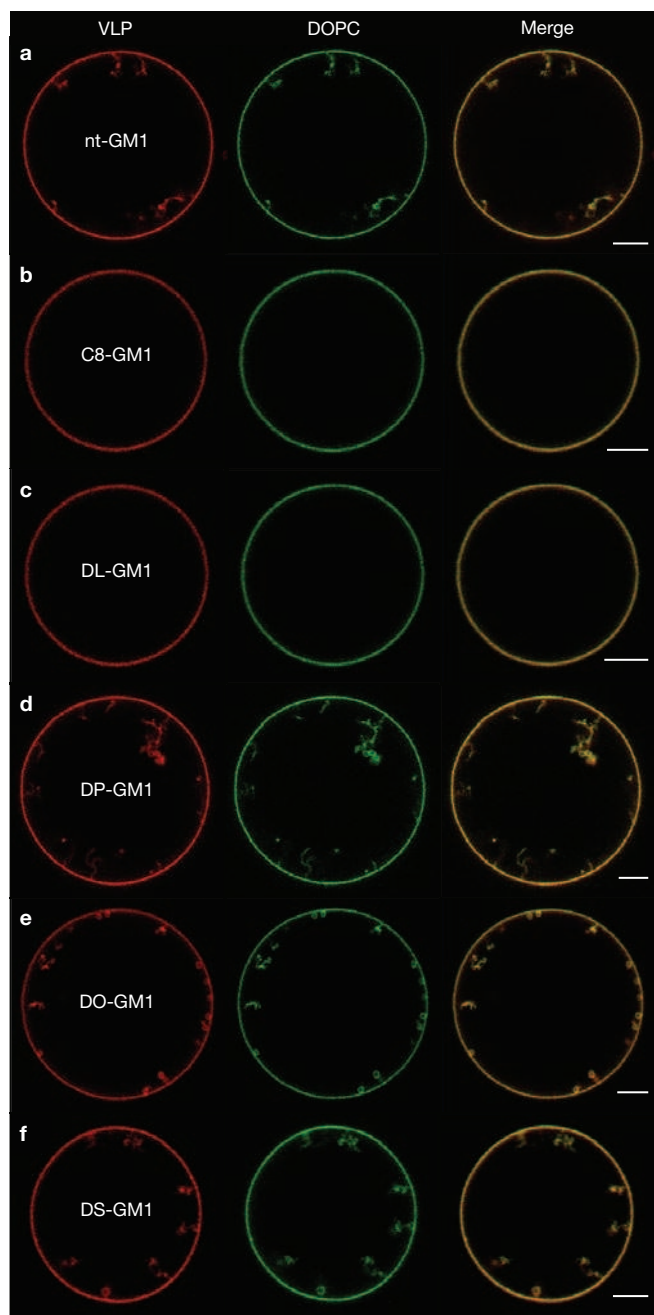


**Figure 3** SV40-induced membrane invagination on model membranes is dependent on GM1 hydrocarbon chain structure. (a–f) Confocal sections in the equatorial plane of GUVs made from a mixture of 68 mol% DOPC, 30 mol% cholesterol, 1 mol% BodipyFl-C5-HPC (green) and 1 mol% of nt-GM1 (a), C8-GM1 (b), DL-GM1 (c), DP-GM1 (d), DO-GM1 (e) or DS-GM1 (f). Fluorescence-labelled SV40-VLPs are shown in red. Scale bars, 5  $\mu$ m.

internalization in C8-GM1-supplemented cells was reduced to  $34.4 \pm 1.5\%$  when compared with nt-GM1 supplemented cells (Fig. 1f), probably representing particles taken up by non-infectious pathways.

#### Caveolin-independent membrane invagination in cells

A few minutes after binding to CV-1 cells, transmission electron microscopy showed SV40 particles in small invaginations that sometimes extended to enclose few virions (Fig. 2a) and in tight-fitting early

endocytic vesicles lacking sub-membrane, electron-dense material<sup>10,12</sup>. The close contact between virus and the plasma membrane and the formation of tight-fitting indentations differentiates SV40 and other polyomavirus family members from most other viruses. When high VLP doses of mouse polyomavirus, a closely related virus with a similar structure<sup>33</sup>, ganglioside receptor<sup>4,26</sup> and endocytic pathway<sup>8,34,35</sup>, were used, even longer tubular structures were observed that extended from the plasma membrane and contained a continuous row of particles (Fig. 2b, arrowheads). These thin (50–60-nm diameter) tubules could thus penetrate the cortical actin meshwork, which has a mesh size of 200–300 nm (ref. 36).

Electron microscopy images indicated an inward-directed budding process, as if the virus particles directly participated in the induction of membrane curvature by binding to gangliosides. To test this possibility, we blocked active cellular processes, such as coat dynamics and membrane traffic, in CV-1 and HeLa cells by using metabolic inhibitors to deplete energy. We hypothesized that this treatment would abolish abscission of VLP-containing invaginations from the plasma membrane. Starting 20–30 min after addition to such cells, fluorescently labelled SV40-VLPs were found to induce numerous tubular, virus-containing structures of variable length that in some cases reached several microns into the cytoplasm and contained the majority of SV40 particles (Fig. 2c; Supplementary Information, Fig. S2a). These tubules did not form in the absence of virus (data not shown), and using the membrane dye FM-1-43 FX, it was found that they were connected to the plasma membrane (Fig. 2e). Incubation of SV40-VLPs with Cav-1-negative mouse embryonic fibroblasts led to the formation of identical tubular structures (Fig. 2d). Furthermore, tubules in wild-type cells did not colocalize with endogenous Cav-1 immunostaining (Supplementary Information, Fig. S2c) and, even before tubule formation, SV40-VLPs rarely colocalized with Cav-1-GFP in normal (Fig. 2f) or energy-depleted cells (Fig. 2g), as observed by total internal reflection fluorescence (TIRF) microscopy. These findings are consistent with previously published immuno-electron microscopy experiments in which only 13–20% of viruses on the cell surface were associated with anti-Cav-1 gold<sup>37</sup>, and confocal microscopy experiments on Cav-1-expressing cells in which only about 1 out of ten viruses associated with Cav-1, and few entered together with Cav-1 (ref. 11). We concluded that SV40 induces the formation of membrane invaginations without the help of active cellular machinery or caveolar coats.

Interference with the actin cytoskeleton, depletion of cholesterol or inhibition of tyrosine kinases in non energy-depleted cells also led to SV40-VLP-induced tubule formation (Supplementary Information, Fig. S2b), suggesting that these factors have a role in the scission process. On the other hand, treatment of cells with the dynamin-inhibitor dynasore did not result in tubule formation (Supplementary Information, Fig. S2b), indicating that the budding of SV40 binding-induced membrane invaginations is dynamin-independent, which is consistent with previous reports<sup>11</sup>.

#### SV40 binding-induced membrane invaginations — properties of GM1

To test whether SV40 binding to GM1 was sufficient to induce membrane invagination, we incubated fluorescently labelled VLPs with GUVs made of a mixture of 1,2-dioleoylphosphatidylcholine (DOPC; 68 mol%; spiked with 1 mol% BodipyFl-C5-HPC), cholesterol (30 mol%) and nt-GM1 (1 mol%). The VLPs bound to the GUVs, and within a few

seconds membrane invaginations were formed that contained the VLPs (Fig. 3a; Supplementary Information, Movie 1). These invaginations had a similar morphology to those observed in cells and their formation did not require the presence of cholesterol in the lipid mixture (data not shown). Mouse polyomavirus-VLPs also induced tubular invaginations on GUVs containing the ganglioside GD1a (Supplementary Information, Fig. S3a), the polyomavirus cellular receptor<sup>4,26,38</sup>.

When the different GM1 species were incorporated into GUVs, addition of SV40-VLPs led to efficient binding in all cases. However, VLPs failed to induce invaginations in GUVs that contained the two short chain species C8 and DL (Fig. 3b, c). In contrast, lipid species with longer acyl chains (DP, DO and DS — di-stearoyl-GM1, which could not be incorporated into cells at non-toxic concentrations) supported the formation of invaginations, independently of their saturation status (Fig. 3d–f). These observations demonstrated that the structure of receptor lipid tails was essential for the virus-induced formation of invaginations on GUVs, as observed for endocytosis and infectivity in cells.

### SV40 binding-induced membrane invaginations — properties of SV40

In virus particles and VLPs, the VP1 molecules provide a surface with 360 regularly spaced binding sites for the GM1 glycan moiety. To test whether the number and colloidal topology of binding sites was critical for tubule formation, we expressed and purified recombinant VP1 pentamers that are incapable of assembly into VLP capsids<sup>39</sup>. When fluorescence-labelled and incubated with energy-depleted CV-1 cells, such VP1 proteins induced long invaginations (Fig. 4a). CTxB, whose five GM1-binding sites are arranged in an identical geometry to that found on the SV40 VP1 pentamer<sup>2</sup>, also induced invaginations (Fig. 4b). In contrast, an antibody against cell-bound GM1 failed to induce invaginations, even when crosslinked by a secondary antibody (Fig. 4c).

These results indicated that the spatial organization of the GM1-binding sites was critical for tubule formation. Crosslinking of GM1 via antibodies did not allow tubule formation, which required the pentavalent organization of binding sites, as found in VP1 and CTxB molecules. This was confirmed on GUVs containing nt-GM1. VP1 and CTxB induced invaginations (Fig. 4d, e), whereas the crosslinked anti-GM1 antibody did not (Fig. 4f). Interestingly, VP1-induced tubule formation was also sensitive to lipid structure in that tubules failed to form on GUVs that were made with C8-GM1 (Fig. 4g). This result is similar to that observed for infection (Fig. 1d), endocytosis (Fig. 1e, f) and VLP-induced tubule formation on GUVs (Fig. 3a, b).

Some differences could be observed between isolated VP1 pentamers or CTxB proteins and intact, colloidal viral capsids. The time lag between ligand addition to GUVs and the formation of invaginations was much longer for isolated pentamers (minutes) than for SV40-VLPs (seconds). When we repeated these experiments in nt-GM1 containing GUVs that were made from a lipid mixture that generates a more rigid, liquid-ordered ( $L_o$ ) phase (40.7 mol% brain SM, 13.6 mol% cholesterol, 40.7 mol% DOPC and 5 mol% GM1), SV40-VLPs were still able to induce membrane invaginations (Fig. 5a). However, CTxB failed to form tubules under these conditions. Furthermore, SV40-VLPs induced tubules on GUVs with a high membrane tension (data not shown), in contrast to CTxB (data not shown) and Shiga toxin B-subunit<sup>24</sup>. We concluded that the pre-curved colloidal organization of GM1-binding sites on the virion was not necessary for membrane deformation and tubulation, but it made

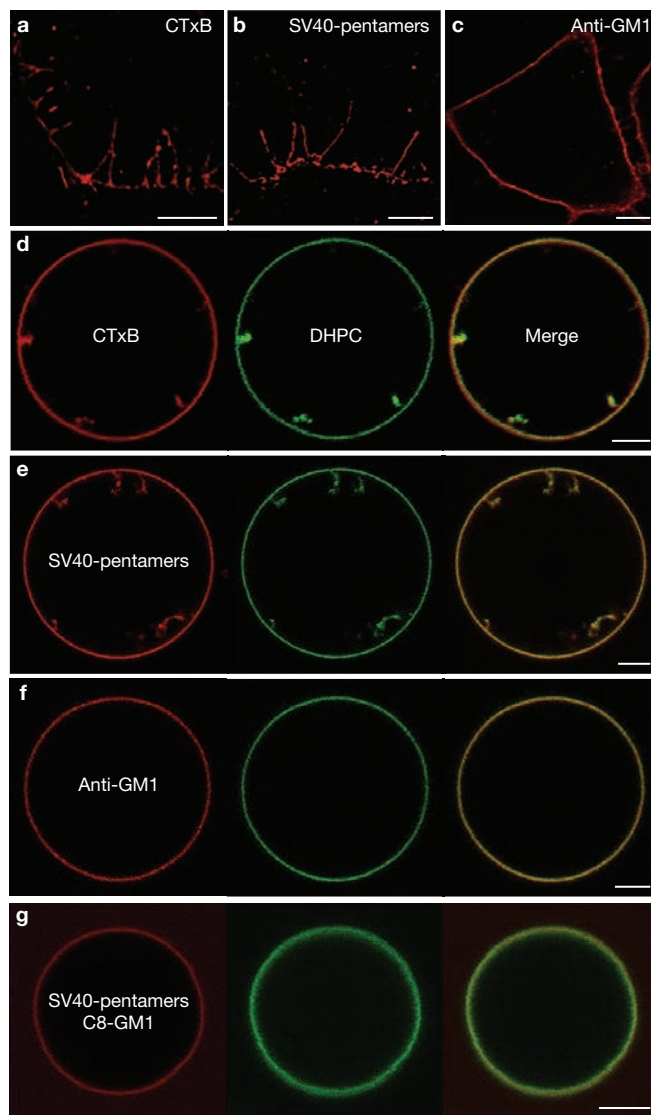


**Figure 4** Induction of membrane invaginations by GM1-binding pentamer units. (a–c) Confocal microscopy images of energy-depleted CV-1 cells incubated for 30 min with fluorescence-labelled SV40 VP1 pentamers (a), CTxB (b) or an anti-GM1 antibody crosslinked with a fluorescence-labelled secondary antibody (c). (d–f), Confocal sections of equatorial planes of GUVs made from a mixture of 68 mol% DOPC, 30 mol% cholesterol, 1 mol% BodipyFl-C5-HPC (green) and 1 mol% of nt-GM1. GUVs were incubated with fluorescence-labelled (red) CTxB (d), SV40 VP1 pentamers (e) or an anti-GM1 antibody crosslinked with a fluorescent secondary antibody (f). (g) Confocal section of a GUV made from a mixture of 64 mol% DOPC, 30 mol% cholesterol, 1 mol% BodipyFl-C5-HPC (green) and 5 mol% C8-GM1. GUVs were incubated with fluorescence labelled SV40 pentamers (red). Scale bars, 5  $\mu$ m.

the process more efficient, enabling it to overcome high membrane tension and rigidity.

In a previous study, we found that the pentameric Gb3 glycolipid-binding Shiga toxin B-subunit (STxB) can induce tubule formation in cells and GUVs with kinetics similar to the kinetics of tubule induction by SV40 pentamer and CTxB<sup>24</sup>. Like SV40 capsids, STxB required glycosphingolipid receptor species with long acyl-chains for tubule formation. However, for STxB-induced membrane tubulation, the Gb3 acyl-chains needed to be unsaturated, suggesting a difference in the underlying physical mechanism between the spherical capsids and the pentameric proteins.

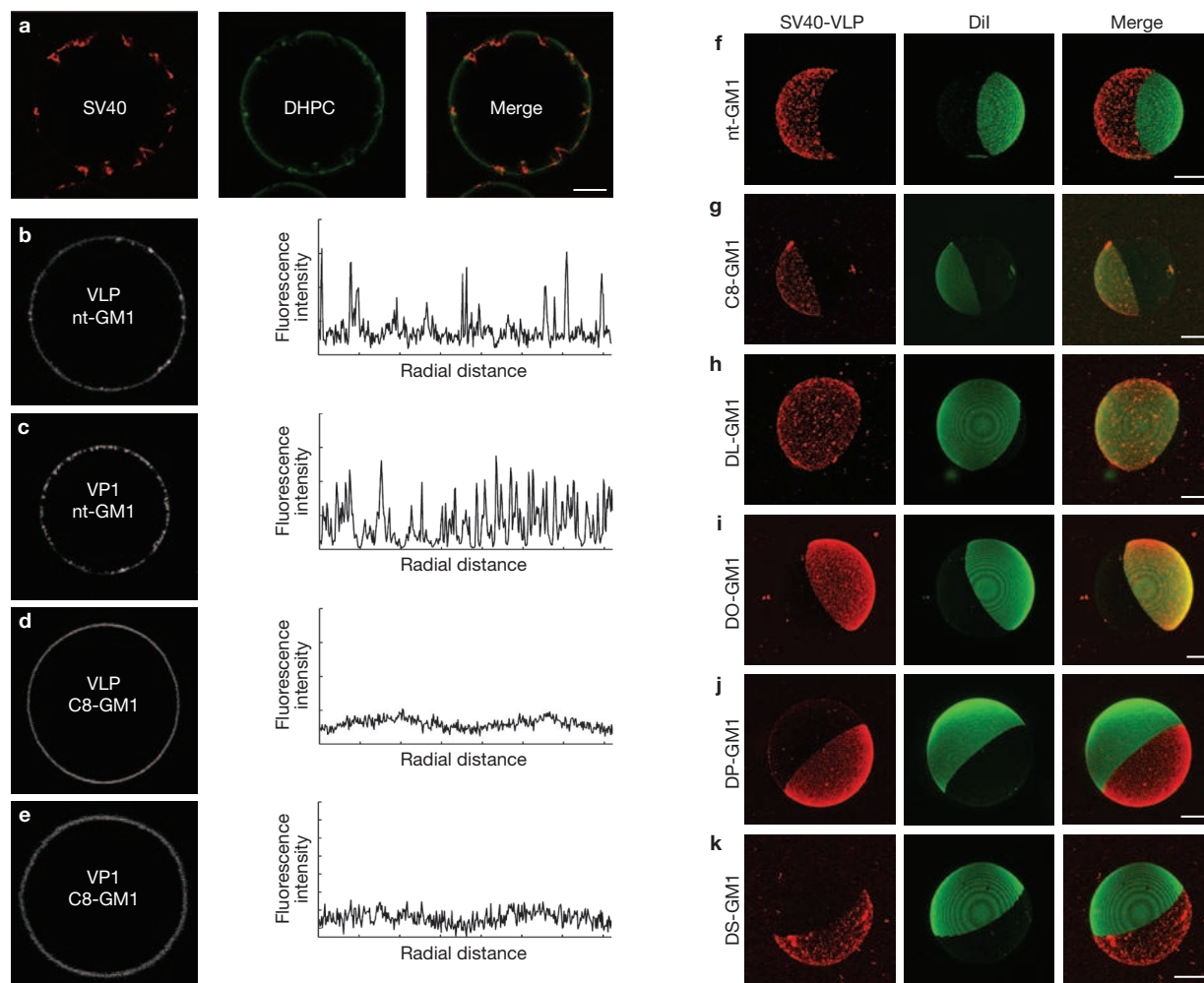


**Figure 5** Clustering and domain formation analysis. (a) Confocal sections in the equatorial plane of GUVs made from a mixture of 40.7 mol% brain-sphingomyelin, 13.6 mol% cholesterol, 40.7 mol% DOPC, 1 mol% BodipyFI-C5-HPC (green) and 5 mol% of nt-GM1. Under these conditions, GUV membranes are in a homogeneous liquid-ordered state. Fluorescence-labelled SV40-VLPs are shown in red. Scale bar, 10  $\mu\text{m}$ . (b–e) Confocal sections in the equatorial plane of GUVs made from a mixture of 68 mol% DOPC, 30 mol% cholesterol, 1 mol% BodipyFI-C5-HPC (green) and 1 mol% of either nt-GM1 (b, c) or C8-GM1 (d, e). Fluorescence intensity profiles of the GUV membranes are plotted on the right. Peaks indicate areas of relative enrichment of VLP or VP1 fluorescence. (f–k) 3D projections of GUVs formed from a lipid mixture of

33 mol% stearoyl-sphingomyelin, 33 mol% DOPC and 33 mol% cholesterol that undergoes phase separation. The lipid analogue Dil (pseudocoloured green, middle columns) was incorporated into the lipid mixture at 0.1 mol% to specifically label the liquid-disordered ( $l_d$ ) phase and the nt-GM1 or variant-GM1 species were incorporated at 0.1 mol% to investigate the phase preference of bound fluorescence-labelled SV40-VLPs (pseudocoloured red, left columns). While in GUVs containing nt-GM1 (f), DP-GM1 (j) and DS-GM1 (k), bound SV40-VLPs localized to the unlabelled liquid-ordered ( $l_o$ ) phase, in GUVs containing C8-GM1 (g), DL-GM1 (h) or DO-GM1 (i) bound SV40-VLPs localized to the Dil-labelled  $l_d$  phase as evident from the merged images (right columns). Scale bars, 10  $\mu\text{m}$ .

### A physical model for SV40 binding-induced membrane deformation

The formation of membrane tubules by the aggregation of membrane-bound monomers (which may either be small proteins such as toxins or VP1 pentamers, or large spherical capsids, Fig. 6a) can be understood from a generic physical model that couples the thermodynamics of phase separation to the mechanics of membrane deformation (Supplementary Information, Theoretical model). Tubule nucleation and growth is controlled by the free energy difference,  $\Delta F_N = E_{neck} - N(\Delta\epsilon + kT \log \phi_1)$ , between  $N$  species being either aggregated in a tubule or isolated on the membrane. Here,  $E_{neck}$  is the energy of the toroidal neck connecting the tubule to the membrane (Fig. 6b), and  $\Delta\epsilon$  and  $kT \log \phi_1$  are the energy gain and entropy loss, respectively, when a species joins a growing tubule ( $\phi_1$  is the surface fraction, concentration  $\times$  species area, of the isolated

species on the membrane and  $kT \sim 2.5 \text{ kJ mol}^{-1}$  is the thermal energy). Tubules can form if the energetic gain overcomes the entropic loss, which requires a sufficiently high species density on the membrane:  $\phi_1 > e^{-\Delta\epsilon/kT}$ . Tubules nucleate in a typical time controlled by a free energy barrier  $\Delta F_c$  (Fig. 6b), which is strongly influenced by the cost of membrane deformation in the tubule neck (Supplementary Information, Theoretical model). The insensitivity of spherical VLP-induced tubule formation to membrane tension and other factors such as the lipid tail saturation, as opposed to what is observed for individual proteins, stems directly from the properties of the energy difference  $\Delta\epsilon$ , as discussed below.

Because of their intrinsic curvature, large spherical VLPs imprint a close to tubular shape onto the membrane to which they adhere. Membrane tension can influence the virus-induced membrane deformation and tubulation only to the extent that it prevents the membrane

wrapping around the capsids, which requires tensions in the order of the high adhesion energy; about  $10kT$  per GM1 molecule<sup>40</sup>, or  $10^{-3} \text{ J m}^{-2}$ . Individual pentameric proteins on the other hand are fully bound to the membrane, whether in tubules or not. Membrane tubulation is in this case not driven by protein–lipid adhesion, but is the result of protein clustering due to the existence of a line tension  $\mu \sim 0.5 \text{ pN}$  between lipid-domains of different composition and ordering<sup>41</sup>. Individual pentamers or toxins should not be able to form tubules if the membrane tension is larger than the ratio of the line tension to the particle size ( $\gamma \sim \mu/a$ , Supplementary Information, Theoretical model), which we estimate to be in the order of  $10^{-4} \text{ J m}^{-2}$ . Furthermore, the kinetics of tubule nucleation is largely controlled by the tension-dependent energy of the tubule neck, and we expect tubule nucleation to be slow when the line energy associated with membrane deformation is larger than the line tension of the clustered domain ( $\sqrt{\kappa\gamma} > \mu$ , with membrane bending rigidity in the order of  $\kappa \sim 20kT$ , Supplementary Information, Theoretical model), which we estimate to be about  $10^{-5} \text{ J m}^{-2}$  (or smaller when the membrane is in the more rigid  $l_o$ -state and Shiga toxin fails to induce membrane invaginations)<sup>42</sup>.

These considerations explain a number of experimental findings. SV40-VLPs can induce tubules even on GUVs with a membrane tension in the order of  $10^{-3} \text{ J m}^{-2}$ , close to the lysis tension of a bilayer. In contrast, individual VP1 pentamers and toxins only form tubules in relatively ‘floppy’ vesicles with tensions in the order of  $10^{-5} \text{ J m}^{-2}$ . Furthermore, these observations clarify why several minutes are required for tubule nucleation by pentamers and CTxB, which is similar to what is observed with the Shiga toxin system<sup>24</sup>, in comparison to seconds with SV40 capsids.

The structure of the receptor tail can influence two important membrane properties: the degree of lipid ordering, related to the line tension of glycolipid receptor-enriched membrane domains, and mechanical properties, expressed by the bending rigidity and spontaneous curvature. Whereas the former property is crucial to the aggregation process of both individual proteins (pentamers or toxins) and spherical VLP capsids, the latter should only influence the tubulation induced by individual proteins, as adhesion of VLPs onto membranes is by itself sufficient to create strong curvature. Our findings show that long acyl chains are required for the induction of tubules by both capsids and individual pentamers, strongly suggesting that the effect is mediated by line tension. Indeed, both SV40-VLPs and VP1 pentamers form lateral aggregates shortly after binding to nt-GM1-containing GUVs (Fig. 5b, c), whereas such aggregates were not detectable in C8-GM1-containing GUVs (Fig. 5d, e). Receptor tail length should also have a strong influence on the nucleation of membrane phase separation. In agreement with this prediction, SV40 was found in  $l_o$  phase membranes when associated with saturated long chain GM1 molecules, and in the  $l_d$  phase when GUVs were made with short chain GM1 species (Fig. 5f). Saturated receptor chains were found to prevent membrane invagination by shiga toxin<sup>24</sup>, but did not modify the ability of the capsid to induce tubules. A likely explanation is that tail saturation strongly couples to spontaneous negative curvature, possibly by amplifying a head group compaction and chain splaying effect. This property is crucial for membrane tubulation induced by small proteins<sup>24</sup>, but dispensable in the case of intrinsically curved spherical capsids.

The picture emerging from the arguments summarized above and detailed in the Supplementary Information is that although pentamers and capsids share a common aspect related to lipid organization and line tension for their clustering, the mechanisms that drive membrane

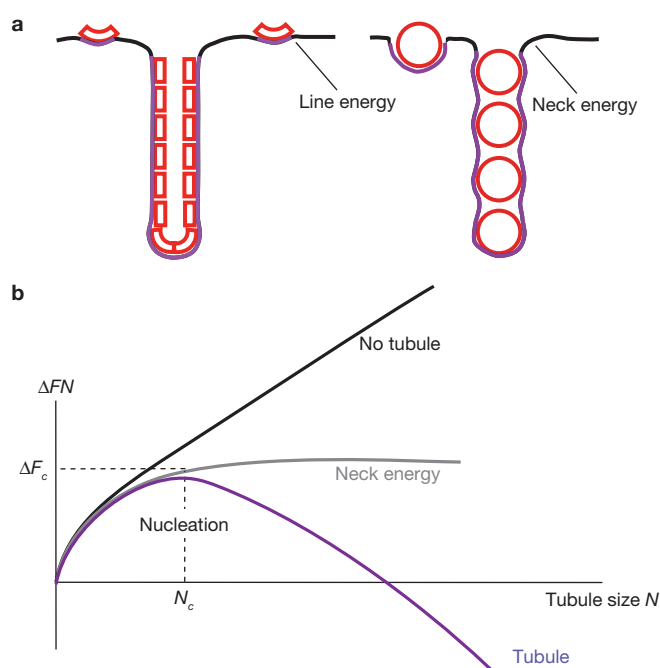


**Figure 6** Physical parameters controlling membrane invagination by SV40. (a) Sketch of membrane invaginations and tubules induced by large spherical capsids (right) and by the aggregation of small proteins (left) after multivalent binding to glycolipid receptors. The lipid receptors are specifically enriched in the contact area and thereby create an interface between the receptor-enriched membrane (lilac) and the adjacent cellular membrane. In the case of the viral particle, it is the shape of the membrane-bound surface that drives the formation of an indentation and the minimization of neck energy promotes tubule formation. (b) Free energy difference between a tubule containing  $N$  particles and  $N$  independent particles. Tubules grow if this energy decreases with  $N$ . The energy of forming a tubular membrane neck around the tubule provides a barrier ( $\Delta F_c$ ) that slows tubule nucleation. Tubules form if the driving force overcomes the loss of entropy and the forces opposing membrane deformation.

deformation are different. Capsids imprint membrane curvature through adhesion, whereas small proteins must promote the emergence of a spontaneously curved membrane organisation.

## DISCUSSION

From our study it seems that, unlike other viruses that rely on cell-driven processes, SV40 initiates its internalization process by inducing membrane curvature itself from the extracellular side of the membrane through multivalent binding of its VP1 pentamers to cell surface GM1. The association with caveolae, which is occasionally observed for SV40 but is not essential for entry or infection<sup>11,37,43,44</sup>, probably reflects a preferred localization of the virus to membrane environments with appropriate curvature radii, and does not seem to have a role in the invagination process described here. Indeed, while Cav-1 expression does not influence the infection efficiency of SV40, the structure of the hydrocarbon chain of GM1 does so significantly (Fig. 1). Hence, what we describe here is the infectious pathway of SV40. In cellular and artificial membranes, the binding of SV40 to GM1 alone suffices to induce the formation of invaginations. The subsequent membrane scission reaction to form an endocytic vesicle depends on signal transduction and active cellular fusion factors<sup>7,9,29</sup>. If this scission reaction does not occur,

membrane invagination can proceed to the formation of tubules. The capacity of the virus to induce membrane invaginations is shared with other polyomaviruses and with some bacterial toxins (Shiga and cholera toxins). As they all bear a remarkably similar pentameric organization for association with glycan moieties of glycosphingolipids, we suggest that they exploit a common mechanism that integrates precise requirements in the hydrocarbon chains of the glycolipid receptors and a compact organization of receptor binding sites within the pentameric protein scaffolds. These pentamers serve as nanoscale lipid-clustering devices for membrane mechanical processes leading to the coat-independent formation of endocytic membrane invaginations. □

## METHODS

Methods and any associated references are available in the online version of the paper at <http://www.nature.com/naturecellbiology/>.

Note: Supplementary Information is available on the Nature Cell Biology website.

## ACKNOWLEDGEMENTS

This work was funded by the Swiss SystemsX.ch initiative, grant LipidX-2008/011 (to A.H.), the Human Frontier Science Program (to A.E.S., L.J. and P.S.), a FEBS fellowship (to H.E.), a CNRS fellowship (to W.R.), the Israel Science Foundation (Grant # 604/07 to A.O.), the Delegation Generale pour l'Armement (to L.B.), the Wellcome Trust (to W.C. and T.F.), Deutsche Forschungsgemeinschaft (to G.S.) and the European Regional Development Fund grant # 4212/04-01 (to K.B. and P.S.). H.E. thanks D. Choquet for his patience and support. The authors thank M. Abdel-Latif for the preparation of VLPs and pentamers.

## AUTHOR CONTRIBUTIONS

H.E. and A.E.S. designed and performed the experiments involving infectious SV40; W.R. and V.C. designed and performed tubulation experiments in cells; A.E.S., J.K. and R.M. performed electron microscopy experiments; W.R., L.B., K.B. and Pe.S. designed and performed GUV experiments; W.C., G.S. and T.F. provided GM1 species; A.O. provided SV40 VLPs; S.D. and P.S. performed theoretical analysis; H.E., P.S., L.J. and A.H. wrote the manuscript; A.H. and L.J. supervised the work.

## COMPETING FINANCIAL INTERESTS

The authors declare no competing financial interests.

Published online at <http://www.nature.com/naturecellbiology/>

Reprints and permissions information is available online at <http://npg.nature.com/reprintsandpermissions/>

- Liddington, R. C. *et al.* Structure of simian virus 40 at 3.8-Å resolution. *Nature* **354**, 278–284 (1991).
- Neu, U., Woellner, K., Gauglitz, G. & Stehle, T. Structural basis of GM1 ganglioside recognition by simian virus 40. *Proc. Natl Acad. Sci. USA* **105**, 5219–5224 (2008).
- Campanero-Rhodes, M. A. *et al.* N-glycolyl GM1 ganglioside as a receptor for simian virus 40. *J. Virol.* **81**, 12846–12858 (2007).
- Tsai, B. *et al.* Gangliosides are receptors for murine polyoma virus and SV40. *EMBO J.* **22**, 4346–4355 (2003).
- Kukura, P., Ewers, H., Müller, C., Renn, A., Helenius, A. & Sandoghdar, V. High-speed nanoscopic tracking of the position and orientation of a single virus. *Nature Methods* **6**, 923–927 (2009).
- Ewers, H. *et al.* Label-free optical detection and tracking of single virions bound to their receptors in supported membrane bilayers. *Nano Lett.* **7**, 2263–2266 (2007).
- Pelkmans, L., Puntener, D. & Helenius, A. Local actin polymerization and dynamical recruitment in SV40-induced internalization of caveolae. *Science* **296**, 535–539 (2002).
- Ewers, H. *et al.* Single-particle tracking of murine polyoma virus-like particles on live cells and artificial membranes. *Proc. Natl Acad. Sci. USA* **102**, 15110–15115 (2005).
- Richards, A. A., Stang, E., Pepperkok, R. & Parton, R. G. Inhibitors of COP-mediated transport and cholera toxin action inhibit simian virus 40 infection. *Mol. Biol. Cell* **13**, 1750–1764 (2002).
- Hummeler, K., Tomassini, N. & Sokol, F. Morphological aspects of the uptake of simian virus 40 by permissive cells. *J. Virol.* **6**, 87–93 (1970).
- Damm, E. M. *et al.* Clathrin- and caveolin-1-independent endocytosis: entry of simian virus 40 into cells devoid of caveolae. *J. Cell Biol.* **168**, 477–488 (2005).
- Kartenbeck, J., Stukenbrok, H. & Helenius, A. Endocytosis of simian virus 40 into the endoplasmic reticulum. *J. Cell Biol.* **109**, 2721–2729 (1989).
- Schelhaas, M. *et al.* Simian virus 40 depends on ER protein folding and quality control factors for entry into host cells. *Cell* **131**, 516–529 (2007).
- Torgersen, M. L., Skretting, G., van Deurs, B. & Sandvig, K. Internalization of cholera toxin by different endocytic mechanisms. *J. Cell Sci.* **114**, 3737–3747 (2001).
- Sandvig, K. *et al.* Pathways followed by ricin and Shiga toxin into cells. *Histochem. Cell Biol.* **117**, 131–141 (2002).
- Gilbert, J. *et al.* Ganglioside GD1a restores infectibility to mouse cells lacking functional receptors for polyomavirus. *J. Virol.* **79**, 615–618 (2005).
- Jacobson, K., Mouritsen, O. G. & Anderson, R. G. Lipid rafts: at a crossroad between cell biology and physics. *Nature Cell Biol.* **9**, 7–14 (2007).
- Hancock, J. F. Lipid rafts: contentious only from simplistic standpoints. *Nature Rev. Mol. Cell Biol.* **7**, 456–462 (2006).
- Mayor, S. & Pagano, R. E. Pathways of clathrin-independent endocytosis. *Nature Rev. Mol. Cell Biol.* **8**, 603–612 (2007).
- Lencer, W. I. & Saslow, D. Raft trafficking of AB5 subunit bacterial toxins. *Biochim. Biophys. Acta* **1746**, 314–321 (2005).
- Parton, R. G. & Richards, A. A. Lipid rafts and caveolae as portals for endocytosis: new insights and common mechanisms. *Traffic* **4**, 724–738 (2003).
- Hammond, A. T. *et al.* Crosslinking a lipid raft component triggers liquid ordered-liquid disordered phase separation in model plasma membranes. *Proc. Natl Acad. Sci. USA* **102**, 6320–6325 (2005).
- Wolf, A. A. *et al.* Attenuated endocytosis and toxicity of a mutant cholera toxin with decreased ability to cluster ganglioside GM1 molecules. *Infect. Immun.* **76**, 1476–1484 (2008).
- Romer, W. *et al.* Shiga toxin induces tubular membrane invaginations for its uptake into cells. *Nature* **450**, 670–675 (2007).
- Ichikawa, S., Nakajo, N., Sakiyama, H. & Hirabayashi, Y. A mouse B16 melanoma mutant deficient in glycolipids. *Proc. Natl Acad. Sci. USA* **91**, 2703–2707 (1994).
- Smith, A. E., Lilie, H. & Helenius, A. Ganglioside-dependent cell attachment and endocytosis of murine polyomavirus-like particles. *FEBS Lett.* **555**, 199–203 (2003).
- Schwarzmann, G., Hoffmann-Bleihauer, P., Schubert, J., Sandhoff, K. & Marsh, D. Incorporation of ganglioside analogues into fibroblast cell membranes. A spin-label study. *Biochemistry* **22**, 5041–5048 (1983).
- Merritt, E. A. *et al.* Crystal structure of cholera toxin B-pentamer bound to receptor GM1 pentasaccharide. *Protein Sci.* **3**, 166–175 (1994).
- Dangoria, N. S., Breaux, W. C., Anderson, H. A., Cisek, D. M. & Norkin, L. C. Extracellular simian virus 40 induces an ERK/MAP kinase-independent signalling pathway that activates primary response genes and promotes virus entry. *J. Gen. Virol.* **77** (Pt 9), 2173–2182 (1996).
- Chai, W., Stoll, M. S., Galustian, C., Lawson, A. M. & Feizi, T. Neoglycolipid technology: deciphering information content of glycome. *Methods Enzymol.* **362**, 160–195 (2003).
- Sandalon, Z. & Oppenheim, A. Self-assembly and protein-protein interactions between the SV40 capsid proteins produced in insect cells. *Virology* **237**, 414–421 (1997).
- Kosukegawa, A. *et al.* Purification and characterization of virus-like particles and pentamers produced by the expression of SV40 capsid proteins in insect cells. *Biochim. Biophys. Acta* **1290**, 37–45 (1996).
- Yan, Y., Stehle, T., Liddington, R. C., Zhao, H. & Harrison, S. C. Structure determination of simian virus 40 and murine polyomavirus by a combination of 30-fold and 5-fold electron-density averaging. *Structure* **4**, 157–164 (1996).
- Richterova, Z. *et al.* Caveolae are involved in the trafficking of mouse polyomavirus virions and artificial VP1 pseudocapsids toward cell nuclei. *J. Virol.* **75**, 10880–10891 (2001).
- Gilbert, J. M. & Benjamin, T. L. Early steps of polyomavirus entry into cells. *J. Virol.* **74**, 8582–8588 (2000).
- Kusumi, A. *et al.* Paradigm shift of the plasma membrane concept from the two-dimensional continuum fluid to the partitioned fluid: high-speed single-molecule tracking of membrane molecules. *Annu. Rev. Biophys. Biomol. Struct.* **34**, 351–378 (2005).
- Stang, E., Kartenbeck, J. & Parton, R. G. Major histocompatibility complex class I molecules mediate association of SV40 with caveolae. *Mol. Biol. Cell* **8**, 47–57 (1997).
- Stehle, T., Yan, Y., Benjamin, T. L. & Harrison, S. C. Structure of murine polyomavirus complexed with an oligosaccharide receptor fragment. *Nature* **369**, 160–163 (1994).
- Roitman-Shemer, V., Stokrova, J., Forstova, J. & Oppenheim, A. Assemblages of simian virus 40 capsid proteins and viral DNA visualized by electron microscopy. *Biochem. Biophys. Res. Commun.* **353**, 424–430 (2007).
- Turnbull, W. B., Precious, B. L. & Homans, S. W. Dissecting the cholera toxin-ganglioside GM1 interaction by isothermal titration calorimetry. *J. Am. Chem. Soc.* **126**, 1047–1054 (2004).
- Baumgart, T., Hess, S. T. & Webb, W. W. Imaging coexisting fluid domains in biomembrane models coupling curvature and line tension. *Nature* **425**, 821–824 (2003).
- Windschiegel, B. *et al.* Lipid reorganization induced by Shiga toxin clustering on planar membranes. *PLoS ONE* **4**, e6238 (2009).
- Pelkmans, L., Kartenbeck, J. & Helenius, A. Caveolar endocytosis of simian virus 40 reveals a new two-step vesicular-transport pathway to the ER. *Nature Cell Biol.* **3**, 473–483 (2001).
- Anderson, H. A., Chen, Y. & Norkin, L. C. Bound simian virus 40 translocates to caveolin-enriched membrane domains, and its entry is inhibited by drugs that selectively disrupt caveolae. *Mol. Biol. Cell* **7**, 1825–1834 (1996).

## Chapter 2

# Transport in the Golgi apparatus

### Introduction

The Golgi apparatus is a fascinating organelle in Eucaryotic cells, by its highly organized (and self-organizing) structure, by its role of central dispatch station in cellular trafficking, and because its physiology is still mysterious. As mentioned in the introduction, it is located between the endoplasmic reticulum, situated at the periphery of the nucleus, and the outer cell membrane. Molecules synthesized in the E.R. transit to the Golgi apparatus, where they can be chemically altered, in a process called maturation (for instance, glycans can be added to lipids and proteins [32]). They are then exported selectively to their preferred location in the cell [33]. The Golgi apparatus usually has a polarity, with a *cis*-side facing the E.R. and the *trans*-side facing the plasma membrane.

We show a simplified diagram of the Golgi apparatus in figure 2.1. In mammals, and most upper Eukaryotes, the Golgi is a stack of sub-compartments (called cisternae), flat disc-shaped vesicles about  $1\mu m$  wide and  $50nm$  thick. Each cisternae is delimited by lipid membrane and, in some cases, tubular connections connecting neighboring cisternae have been observed, and are usually associated with large trafficking events [34]. Interestingly, the membranes of each cisterna have different chemical and physical properties [35], i.e. different identities [36]. There are different protein markers in the *cis*, medial and *trans* Golgi, which are embedded in membranes of different composition (the *cis* Golgi is richer in ceramids whereas the *trans* Golgi is enriched in cholesterol and sphingolipids), and different thickness (the membrane thickness grows from the *cis* Golgi to the *trans*-Golgi). Because of this structure we will call the *cis* to *trans* Golgi direction the "main axis" of the Golgi apparatus. As we mentioned, there is a gradient of chemical composition, and therefore of physical properties, along this axis.

It has been documented [37] that newly synthesized molecules from the ER are exported to the *cis* face of the Golgi apparatus, and, after transiting through the stack, they are exported at the *trans* face of the Golgi apparatus, the boundaries of which are not necessarily well defined. The boundary between the ER and the *cis* Golgi is a complex tubulo-vesicular membrane structure called ERGIC (E.R. to Golgi intermediate compartment). On the other hand, material exported from the *trans* Golgi joins another complex

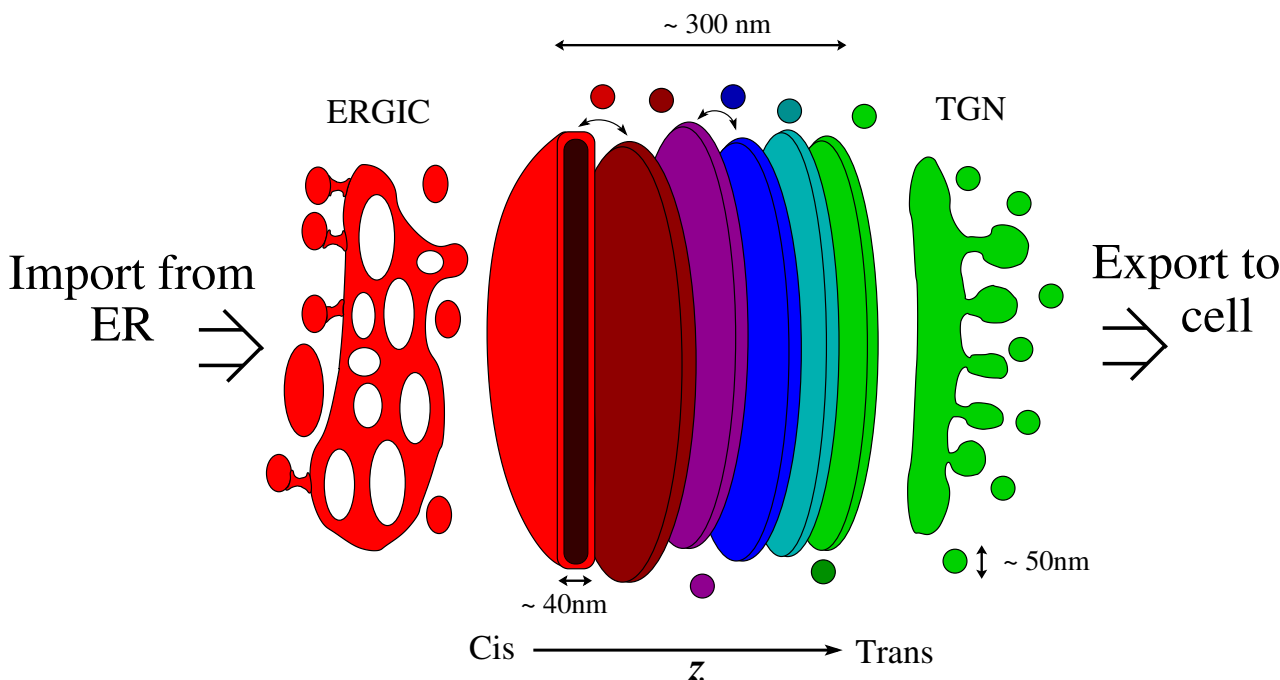


**Figure 2.1:** Cartoon of a Golgi apparatus with six cisternae (showing a cutaway of the first cisterna). The cis- to trans-Golgi axis will be called  $Oz$ , or main axis. The small spheres represents vesicles budding from cisternae (in greater number than represented here), and tubules (not shown here) may connect the cisternae. The different colors represent the different chemical composition.

intermediate compartment, the trans Golgi network (TGN), where the lipids and proteins are dispatched to the cell. This transport from the E.R. to the cell through the Golgi apparatus is called anterograde transport. A retrograde transport, in the opposite direction, has also been reported. Retrograde transport is used to recycle proteins to the E.R. [38], and by some products of endocytosis [39], including pathogens such as the Shiga toxin [40]. A last class of molecules keep constant average position in the Golgi stack, and are found preferentially in the cis, medial or trans Golgi. For instance, there are Golgi maturation enzymes responsible for glycosylation of proteins which are mainly distributed in one region of the Golgi apparatus, and are hence called resident Golgi enzymes [41]. A striking fact is that the glycosylation enzymes are located from cis to trans in the order they act on a molecule [42]. Therefore, a newly synthesized molecule from the E.R. has to be transported through the stack, from cis Golgi to trans Golgi, to be correctly matured. However, it has been shown that some proteins can actually bypass the Golgi apparatus, for instance virus proteins [43] or storage proteins in plants [44].

Various experiments have been performed (which we will discuss later), revealing typical anterograde transit times of 10-20 minutes for proteins to go through the Golgi apparatus. Given the volume of the Golgi apparatus (of the order of  $\approx 1\mu m^3$ ), this is much slower than bulk diffusion in the same volume. Two models (fig. 2.2) have been competing to explain transport of molecules through the Golgi apparatus [45].

The first model, called vesicular transport, assumes that cisternae have a fixed position in the stack, and that molecules are carried between neighboring cisternae by transport vesicles. The involved vesicles are thought to be vesicles coated by specific proteins (for

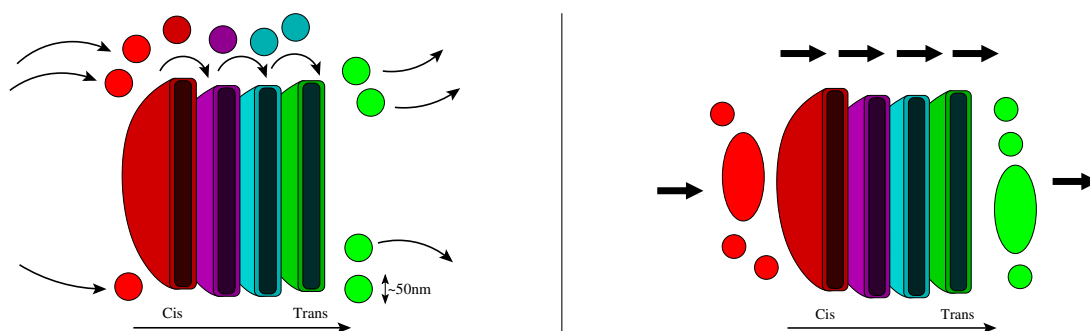


**Figure 2.2:** LEFT : Illustration of the vesicular transport model in which proteins and lipids are loaded at the cis face of the Golgi and are exchanged between fixed cisternae by vesicles. RIGHT : Cisternal progression model, in which cisternae are generated at the trans-face, progress through the stack, and are disassembled at the trans face.

instance COPI could be involved in retrograde transport), and to have a size of the order of  $50nm$ . However, this model failed at explaining the transport of large molecular aggregates such as scales or large collagen fibers. Another model (though not incompatible with vesicular transport), called cisternal progression (or cisternal maturation), proposed that individual cisternae advance through the stack, with cisternae being assembled at the cis face and disassembled at the trans-face, after a tread milling process. During this process, it is assumed that the identity of each cisterna changes with time, from a typical cis Golgi identity to a trans Golgi identity.

The later model predicts that molecules entering the Golgi stack at a given time will exit from the stack after a delay, the time needed for a cisterna in the cis Golgi to progress to the trans Golgi. Though cisternal progression explains many experimental data, the predicted delay in export was not observed in recent experiments [46], which seem to indicate that molecules entering the Golgi apparatus can be exported with little or no lag.

Confronted to these contradicting results, we wanted to know what information the experimental data actually contained. There are few existing quantitative studies of transport in the Golgi apparatus [47, 46], involving great mathematical complexity [47] or an excessively large parameter space (36 parameters of microscopic origin in [46]), and those studies do not enable a quantitative and simple distinction between the two existing models.

Therefore, we compared experimental results to a basic transport equation, to obtain model-independent transport coefficients, and then confronted them to predictions from the various models. We extended this framework to include localization of resident proteins (which, on average, keeps a constant position in the Golgi stack).

## Golgi by the numbers

Some typical values of the Golgi dimensions and transport rates will be mentioned in this chapter. Let us first have a quick outlook of the numerical values.

Quantity		Value
Radius of a cisterna	$R$	600 nm [48], 450 nm [46, 49]
Mean distance between two cisternae	$h$	30 nm [46], 40 nm [48, 34]
Radius of a connecting tubule	$a$	25 nm [34]
Thickness of the Golgi	$L$	200-300 nm [48, 46, 34]
Transit time	$\tau$	15-30 min [48, 46]
VSVG Diffusion coefficient	$D_2$	$0.14 \mu\text{m}^2/\text{s}$ [50, 51]

## 2.1 Building a transport equation

### 2.1.1 Biased diffusion

To build a simple formulation of transport in the Golgi apparatus, let us consider one transmembrane protein inserted in the membrane of one cisterna (as shown in figure 2.3). This protein diffuses laterally on the cisterna with a diffusion coefficient  $D_2$ , typically of order  $0.1\mu m^2.s^{-1}$  [50, 51]. During this diffusion, it may find a tube or a spot of vesicle budding, and thus be carried to a neighbouring cisterna. Therefore, the protein is moving forward or backward on the  $z$  axis as it encounters tubes connected with the next or previous cisterna respectively (or vesicles merging to the next or previous cisterna).

The movement of this protein, projected on the  $Oz$  axis, is therefore akin to diffusion, possibly biased by a different number of tubes on each face of the cisterna, different tube properties, or by a preferred direction of vesicular transport. In the following, unless mentioned otherwise, we will not distinguish between transport through tubes or by vesicles, since the effect of both types of transport intermediates on the overall transport may be described in a single mathematical framework.

Let us assume linear transport kinetics, i.e. let us neglect cooperative effects between proteins (the cooperative effects in transport being the focus of chapter 3). Let us call  $k_n$  the rate of jump, for a protein  $A$ , from the  $n$ -th cisterna to the cisterna  $n+1$ , and  $k'_n$  the rate of jump from the cisterna  $n$  to the cisterna  $n-1$ . Here, the rates  $k_n, k'_n$  include the time for a protein  $A$  to encounter a transport intermediate and the probability to be effectively transported by the intermediate. They are not restricted to processes involving protein-coated vesicles, but may include contributions from any fragment that detach from a cisterna and fuse with a neighboring cisterna, or, as we mentioned, the use of tubular connections between cisternae. As the transport processes may require energy input (e.g. from ATP hydrolysis), these rates do not, in general, obey detail balance.

The net flux between the  $n$ -th and the  $(n+1)$ -th cisterna will be called  $J_{n+\frac{1}{2}}$  (because it is the net flux through a fictive plane located between  $n$  and  $n+1$ ), and hence can be written :

$$J_{n+\frac{1}{2}} = k_n A_n - k'_{n+1} A_{n+1} \quad (2.1)$$

Let us also consider the possibility for proteins to enter the stack (by an incoming flux  $J_n^0$ ) or to exit from the stack (for instance by joining a vesicle exiting to the rest of cell), with a rate  $r_n$ . The master equation for the concentration  $A$  of a given species  $A$  therefore reads :

$$\partial_t A_n(t) = J_n^0 + J_{n-\frac{1}{2}} - J_{n+\frac{1}{2}} - r_n A_n \quad (2.2)$$

As we mentioned, the rates  $k_n$  and  $k'_n$  result in a (possibly biased) diffusion. We can find explicit expressions for the transport coefficients as a function of  $k_n$  and  $k'_n$  by mapping this discrete transport to a continuous transport, described by a Fokker-Planck equation.

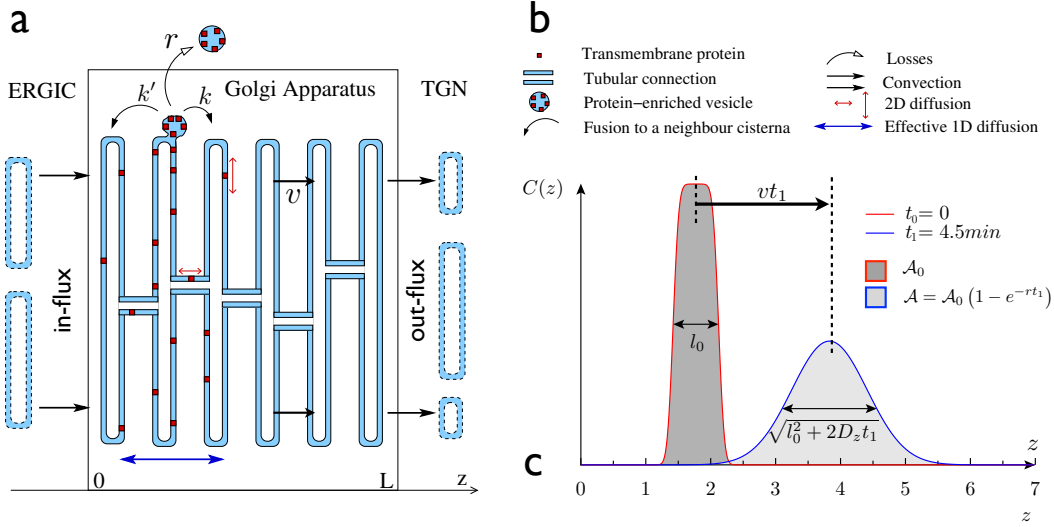


**Figure 2.3:** Schematic of the Golgi apparatus. **(a)** Sketch of the Golgi apparatus as a stack of connected cisternae exchanging material. **(b)** Relevant transport processes, including cisternal progression, diffusion through connecting membrane tubules and vesicular transport. **(c)** Spatiotemporal evolution of an initially narrow protein distribution (as produced by a pulse-chase experimental procedure). Pure convection produces a uniform translation of the peak, diffusion broadens the peak, and loss causes an exponential decrease of the protein content.

### 2.1.2 Transport rates

Discretizing a continuous equation has been abundantly described as it is a first step to numerical analysis of many systems (see [52, 53], and discussion in appendix C). Various arbitrary choices have to be made during discretization, and, the other way round, choices must be made to make our transport equation continuous. Starting from rates of exchange between discrete cisternae, we will make all choices in order to find a continuous equation that can be written as a Fokker-Planck equation, i.e. :

$$\partial_t A = \partial_z (D \partial_z A - vA) \quad (2.3)$$

Omitting the external fluxes (which we will reintroduce later), the discrete transport equation reads, with  $n$  the index of one cisterna :

$$\partial_t A_n = -(k_n + k'_n)A_n + k'_{n+1}A_{n+1} + k'_{n-1}A_{n-1} \quad (2.4)$$

We want to compare this equation to a discrete version of the Fokker-Planck equation (Eq. 2.3), in order to map the values of the  $\{k\}, \{k'\}$  to a velocity and a diffusion coefficient. The velocity here will not include the progression of cisternae through the stack and only results from the exchanges between the cisternae. Therefore, we will consider the Fokker-Planck equation in the reference frame of the cisternae, and we will call  $v^e$  the velocity associated to the exchange of material between cisternae.

Let us discretize 2.3. The discrete derivative of  $A$  with respect to  $z$  can be written as :

$$\frac{\partial A}{\partial z} = \frac{A(z + \delta z) - A(z - \delta z)}{2\delta z} \quad (2.5)$$

In which  $\delta z$  is the discrete spatial step. This can also be written, with the notation  $A_n = A(n \delta z)$  :

$$\frac{\partial A}{\partial z} = \frac{1}{\delta z} \frac{\partial A}{\partial n} = \frac{1}{\delta z} \frac{A_{n+1} - A_{n-1}}{2} \quad (2.6)$$

Since we want to map a discrete Fokker-Planck equation to the transport between cisternae (Eq. 2.4), we must take  $\delta z$  to be the distance between cisternae. Let us define  $A_{n+1/2}$  and write alternatively the derivative of  $X$ :

$$A_{n+1/2} = \frac{A_n + A_{n+1}}{2} \quad (2.7)$$

$$\left. \frac{\partial A}{\partial n} \right|_n = A_{n+\frac{1}{2}} - A_{n-\frac{1}{2}} \quad (2.8)$$

Let us note that equation 2.8 yields the usual (discrete) formulation for the second derivative :

$$\left. \frac{\partial^2 A}{\partial n^2} \right|_n = A_{n+1} + A_{n-1} - 2A_n \quad (2.9)$$

Discretizing the Fokker-Planck equation, using Eqs. 2.8,2.7,2.6 yields :

$$\begin{aligned} \partial_t A_n = & \frac{1}{\delta z^2} D_{n+\frac{1}{2}} (A_{n+1} - A_n) - \frac{1}{\delta z^2} D_{n-\frac{1}{2}} (A_n - A_{n-1}) \\ & - \frac{1}{2\delta z} v_{n+\frac{1}{2}} (A_{n+1} + A_n) + \frac{1}{2\delta z} v_{n-\frac{1}{2}} (A_n + A_{n-1}) \end{aligned} \quad (2.10)$$

Let us note that we did not discretize the time derivative, and hence this is not an explicit Euler discretization scheme, which we show to be unstable in appendix C). In the following, we will call  $v^e$  the effective velocity due to the exchange between cisternae, in order to make a distinction with the progression speed which we will introduce later. Identifying Eqs. 2.10 and 2.4 yields :

$$D_{n+\frac{1}{2}} = \frac{k_n + k'_{n+1}}{2} \delta z^2 \quad (2.11)$$

$$v_{n+\frac{1}{2}}^e = \delta z (k_n - k'_{n+1}) \quad (2.12)$$

In order to write  $D$  and  $v^e$  as rates (since they originate from rates of transport), we normalize all distances by  $\delta z$ , the distance between two adjacent cisternae, and we find :

$$D_{n+\frac{1}{2}} = \frac{k_n + k'_{n+1}}{2} \quad (2.13)$$

$$v_{n+\frac{1}{2}}^e = k_n - k'_{n+1} \quad (2.14)$$

A rate  $r$  of exit throughout the Golgi, which may represent recycling to the E.R. or direct export, can be added and is written the same way in a continuous or a discrete formalism :  $\partial_t A_n = -r A_n$ .

It is capital here to note that a unidirectional transport ( $\forall n, k'_n = 0, k_n > 0$ ) does not yield a zero diffusion coefficient : equations 2.13,2.14 show that, in this case,  $D = \frac{1}{2} v^e$ . More generally, for any transport by vesicles or tubes, the speed has an upper bound given by the diffusion coefficient :

$$v^e \leq 2D \quad (2.15)$$

Let us define the Peclet number  $Pe = Lv/D$ , a dimensionless quantity which quantifies the importance of convection relative to diffusion, in which  $L$  is the size of the system. In the absence of cisternal progression, the statement of equation 2.15 also writes, in term of the Peclet number  $Pe$  :

$$Pe < \frac{N-1}{2} \quad (2.16)$$

In which  $N$  is the number of cisternae in a Golgi stack, such as  $L = (N-1)\delta z$ .

These transport equations, and the conclusions, are valid in the reference frame of the cisternae. But as we mentioned in the introduction, the cisternae themselves, might be progressing through the stack, according to the cisternal progression model (fig. 2.2, right). In the reference frame of the cell, assuming a constant progression speed  $v_p$  through the stack, the continuous transport equation now reads :

$$\frac{\partial A(z)}{\partial t} = \frac{\partial}{\partial z} \left( D \frac{\partial A(z)}{\partial z} - v \cdot A(z) \right) - r \cdot A(z) + J_0(z) \quad (2.17)$$

With  $v = v_p + v^e$

Changing the reference frame shows that there is a simple addition of the progression speed with the speed of biased diffusion. Let us recall that  $v^e \leq 2D$  (Eq. 2.15). Therefore any experimental result indicating  $v > 2D$  would show unambiguously that cisternal progression exists. Because both models can result in a convection-diffusion equation, there is no other quantitative evidence of cisternal progression from the kinetics of transport through the Golgi apparatus.

The next step is therefore to analyse experimental data with a Fokker-Planck equation to find out if there are quantitative evidences for cisternal progression.

## 2.2 Solutions of the Fokker Planck equation

Since we can map both models to a general Fokker-Planck equation, it is of high interest to know how to solve this equation. Let us recall the expression of the time-derivative of the concentration  $A$  :

$$\frac{\partial A(z)}{\partial t} = \frac{\partial}{\partial z} \left( D \frac{\partial A(z)}{\partial z} - v.A(z) \right) - r.A(z) \quad (2.18)$$

This expression is not sufficient to find a unique solution : one has to know the initial concentration profile  $A(z, t = 0)$  and the boundary conditions.

In our case, the boundary conditions are dictated by the microscopic situation : if we call  $A_1$  and  $A_N$  the concentrations in  $A$  in the first and last cisterna respectively, molecules escape from the Golgi with a flux  $k'_1 A_1$  at the cis face and a flux  $k_N A_N$  at the trans-face. In the continuous formalism, the fluxes  $J^{out}$  exiting the Golgi because of the rates  $k'_0$  and  $k_N$  write :

$$J^{out}(0) = \frac{k'_1}{\delta z} A(0) \quad (2.19)$$

$$J^{out}(L) = \frac{k_N}{\delta z} A(L) \quad (2.20)$$

In which we kept the  $\delta z$  for clarity, but we can recall that we chose to set  $\delta z = 1$ .

In addition to those fluxes, in the case of cisternal progression, molecules in the last cisterna with exit the stack as the last compartment disassemble (with a speed  $v_p$ ). Finally, the incoming flux  $J^0$  to the Golgi can be put in the boundary conditions if we assume the incoming flux from the E.R. to only enter at the cis face, yielding a term  $J_{in}$ . Eventually, the boundary conditions read :

$$J(0) = -k'_1 A(0) + J_{in} \quad (2.21)$$

$$J(L) = (k_N + v_p) A(L) \quad (2.22)$$

If the initial concentration profile  $A(z, t = 0)$  is known, equations 2.18,2.21,2.22 allow us to find a unique solution  $A(z, t)$ . However, because of the variety of boundary conditions, solving explicitly those equations may turn out to be very difficult. As shown in the appendix, usual methods of solutions require at least some degree of numerical computations, because of the boundary conditions. We therefore chose to numerically solve the whole Fokker-Planck equation, which can be very straightforward under certain assumptions. In the following, we show how stationary solutions can be found analytically, and how the time-dependent solution can be found numerically.

### 2.2.1 Stationary solutions

The stationary solution of Eq. 2.18 for the protein distribution in the Golgi under a constant in-flux  $J_{in}$ , with an exiting flux  $J(L) = v_{off} A(L)$  may be found by setting

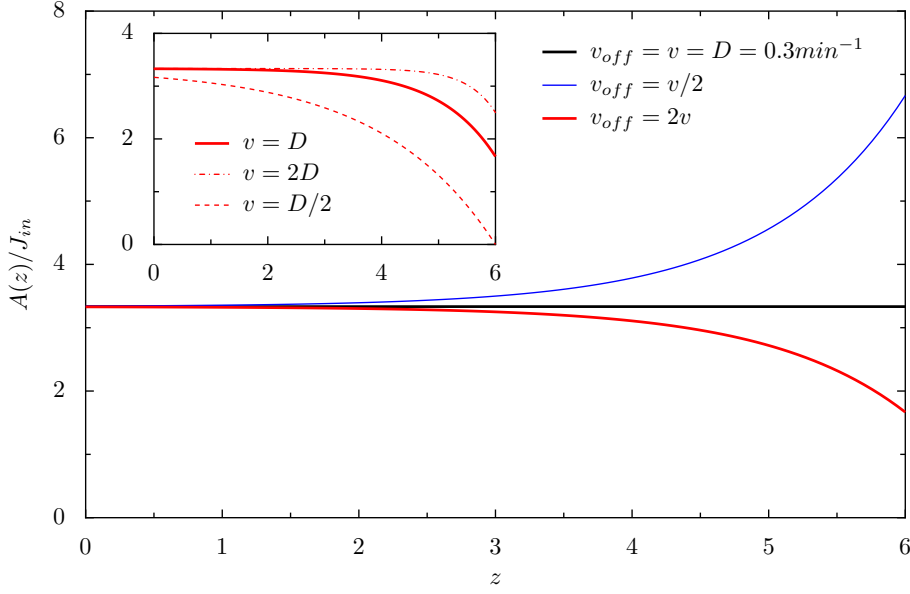


**Figure 2.4:** Stationary solutions of the Fokker-Planck equation (Eq. 2.17) under a constant influx  $J_{in}$  and an out flux  $J_{out} = v_{off}A(L)$ , for  $L = 6$  (i.e. seven cisternae) and  $D = 0.3 \text{ min}^{-1}$ . Main plot : concentration profiles  $A(z)$  for different exit rates  $v_{off}$ , the outflux at  $z = L$  being  $J(L) = v_{off}A(L)$ . If  $v_{off} > v$ , molecules exit faster at  $z = L$  than they are convected and the concentration decreases with  $z$  (red curve). Insert : concentration profiles for  $D = 0.3 \text{ min}^{-1}$ ,  $v_{off} = 2v$  and various values of  $v$ . The larger  $v$ , the smaller the zone in which the concentration decreases.

$\partial_t A = 0$  for all  $n$ , leading to :

$$A(z) = \alpha(z, J_{in}) \left( e^{\lambda_+ z} + \beta e^{\lambda_- z} \right) \quad (2.23)$$

$$\lambda_{\pm} = \frac{v}{2D} \left( 1 \pm \sqrt{1 + \frac{4rD}{v^2}} \right) \quad (2.24)$$

In which  $\alpha(z, J_{in})$  and  $\beta$  are found by applying the boundary conditions. A particular example of interest is when  $r = 0$ . In such case, we find :

$$A(z) = J_{in} \left[ \left( \frac{1}{v_{off}} - \frac{1}{v} \right) e^{\frac{v}{D}(z-L)} + \frac{1}{v} \right] \quad (2.25)$$

This result is illustrated in figure 2.4. We can see that if  $v_{off} > v$ , molecules exit faster at  $z = L$  than they are convected and the concentration decreases with  $z$ . Otherwise, if  $v_{off} < v$ , molecules exit slower at  $z = L$  than they are convected and the concentration increases with  $z$ . This concentration profile has been found from the continuous transport equation. We can compute the typical length scale at which the concentration changes, and if this length scale is smaller than the spatial step  $\delta z = 1$ , then the continuous equation is a poor approximation to the discrete equation.

Equation 2.25 shows that the characteristic length scale is  $\lambda = D/v$ . Recalling that the size of the system is  $L = N - 1$ , we find :

$$\lambda = \frac{N - 1}{Pe} \quad (2.26)$$

For the continuous approximation to be valid, we need  $\lambda > 1$ . In the absence of cisternal progression, we showed that  $Pe < \frac{N-1}{2}$ , and in this case  $\lambda > 2$ . In the presence of cisternal

progression, we might find larger velocities compared to the diffusion coefficient. In section 2.3, we find  $Pe < 3$  (and hence  $\lambda > 2$ ) from experimental data, which confirms that a continuous equation is a good tool even for a 7-compartments system. We show some concentration profiles for  $\lambda = \frac{1}{2}$ ,  $\lambda = 1$  and  $\lambda = 2$  in figure 2.4.

### 2.2.2 Numerical simulations

To describe the experiments, we use a numerical simulation of the Fokker-Planck equation. In the particular case in which the speed is constant with space, we can use a simple explicit Euler implementation of the diffusion in the moving frame of the cisternae, in order to have an accurate simulation (discretization schemes are discussed in appendix C, and practical algorithms are detailed in [52]).

Let us introduce  $dz$ , the unit spatial step,  $dt$ , the time step for diffusion, and  $\Delta t$ , the time step for convection. During each convection time step, there are  $N_d$  diffusion step. Those parameters are linked by the relations :

$$v\Delta t = dz \quad (2.27)$$

$$\frac{dz^2}{dt} = mD \quad m \gg 1 \quad (2.28)$$

$$N_d = \frac{\Delta t}{dt} \quad N_d \gg 1 \quad (2.29)$$

In which  $m$  is arbitrary, and the larger  $m$ , the better the accuracy.

During each convection step  $\Delta t$ , the whole system is moved to the right by a distance  $dz = v\Delta t$ , some material exiting at the right face while new material enters at the left face with a concentration  $A_0$ . In the simulations, the concentration is described by an array  $A[0 : L_z]$  containing the concentration in each unit length  $dz$  (and therefore  $L_z = L/dz$ ).

The algorithm can be written as follows :

```

while t<Tf:
    #New convection step
    t=t+Dt
    #The whole system is translated
    A[1:Lz]=A[0:Lz-1]
    #New material enters at z=0
    A[0]=A0
    #Many steps of diffusion are simulated
    for k=1 to N:
        #The concentration at the edges is stored
        AL=A[1]
        AR=A[Lz-1]
        #Diffusion is implemented by a Euler scheme
        A[1:Lz-1]=A[1:Lz-1]*(1-2/n-r*dt) + A[0:Lz-2]/n + A[2:Lz]/n
        #The boundary conditions are applied
        A[0]=A[0]*(1-1/n-kL*dt/dx)+AL/n+Jon*dt
        A[Lz]=A[Lz]*(1-1/n-kR*dt/dx)+AR/n

```

Using this simulation, we could compute the speed and diffusion coefficient using previously published experimental data.

## 2.3 Results

The Golgi apparatus occupies a volume of the order of  $1\mu m^3$ . Therefore, it may be seen in optical microscopy, and (as described later in this section) fluorescent assays allow experimentalists to track the kinetics of exit from the Golgi apparatus in a living cell. However, those experiments do not yield the spatial distribution of the molecules in the Golgi apparatus, hence limiting the information available from such assays. Other assays were therefore designed to track the localization of molecules in the stack by electron microscopy. Electron microscopy cannot be performed on living cells and hence the progression of molecules through the stack can only be reconstituted after successive experiments on many cells, thus yielding both tedious manipulations and large error bars. There are therefore few quantitative experimental results available to compare our simulations to, sometimes with low accuracy, and all on different cell lines and experimental conditions. Despite these difficulties, we believe that our approach is the only rigorous way to extract transport properties from experimental data, as we rely on few microscopic hypotheses and on a limited number of parameters.

In this section, we will not attempt to find a unique value for  $D$  and  $v$  in all cells, because of the reasons mentioned above. Rather, we will attempt to find likely values of the kinetic parameters for each experiment.

### 2.3.1 Optical microscopy assays

Recent experiments [46] casted doubts on the cisternal maturation model. In those optical microscopy experiments, various molecules (VSV protein G, a transmembrane protein, and procollagen, a large soluble protein that tends to form very large aggregates) could be tagged by fluorescent markers, while the Golgi apparatus was tagged with a different fluorescent marker. By selectively bleaching the fluorescent markers inside or outside the Golgi apparatus, they could observe the kinetics of import or export of fluorescent molecules. The experimental procedure is sketched in figure 2.5.

**Fig. 2.5,#1** : Various molecules were tagged with fluorescent markers, which were bleached outside the Golgi apparatus at  $t = 0$ . As molecules entering the Golgi at  $t > 0$  are not fluorescent, the fluorescence in the Golgi area decreases as fluorescent molecules leave the Golgi apparatus. Hence, the average kinetics of exit from the G.A. can be observed experimentally. They observed that the fluorescence, and hence the concentration of tagged molecules, decayed exponentially with time. Results are shown in figure 2.6,(c).

Since this experiment does not yield direct information on the kinetics inside the Golgi, many sets of parameters may be used to fit the data, and this experiment mainly yields a time scale of 16 minutes. A second experiment was performed to better understand the transport kinetics.

**Fig. 2.5,#2** : In a second experiment, fluorescently labeled VSV protein G was used. The Golgi apparatus itself was bleached at  $t = -5\text{min}$ , and at  $t = 0$ , the outside of the Golgi apparatus was bleached. The fluorescent VSVG molecules were thus allowed to enter only for five minutes, which is less than the mean transport time in the Golgi. Therefore,

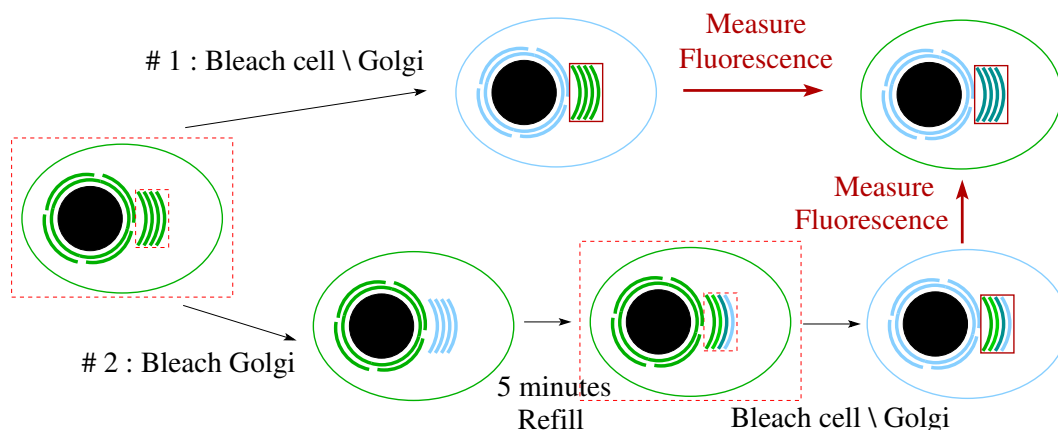


**Figure 2.5:** An illustration of the optical microscopy experiments performed by Patterson et al. [46]. The black disc represents the nucleus, which is surrounded by the endoplasmic reticulum (E.R.). The E.R. synthesizes fluorescent proteins. In the first experiment (#1), the fluorescence (represented in green) is bleached in the whole cell except the Golgi apparatus, and the fluorescence in the region corresponding to the Golgi apparatus (scarlet frame) is measured. In the second experiment (#2), the fluorescence in the Golgi apparatus is bleached. During five minutes, the fluorescence in the Golgi increases because of import from the E.R., and hence the cis Golgi is expected to have more fluorescent molecules than the trans Golgi. The rest of the cell is then bleached and the fluorescence in the Golgi region is measured.

fluorescence should be limited to the cis Golgi. They observed a similar exponential decay of the fluorescence as in the first experiment. Whereas a convective model with exit only at the trans face would predict a delay in export, because molecules have to be convected from the cis Golgi to the trans Golgi,. No such lag was observed, as shown in figure 2.6,(a).

The numerical analysis of those experiments have to be considered with caution for two reasons. Firstly, even using the second experiment, a large set of parameters can be used to fit the data. Secondly, the zone of observation does not necessarily match the real, microscopic, boundaries of the Golgi apparatus because of the optical resolution of the microscope. The observation zone could in particular include part of the ERGIC and TGN, in which transport processes could be very different than in the Golgi stack. To reduce the set of fitting parameters, we turned to electron microscopy assays.

### 2.3.2 Electronic microscopy assays

**Fig. 2.6, (d)** In 1998, a quantitative experiment quantitative assay to determine the kinetics inside the Golgi apparatus was performed by Bonfanti et al. [48]. They used electron microscopy to directly observe large aggregates of procollagen, and they could observe the number of aggregates as the function of the position in the stack (cis or trans) for different time intervals. They performed the so called "incoming wave" protocol, in which a temperature shift at  $t = 0$  suppresses the incoming flux from the E.R. to the Golgi apparatus. While the quantity of procollagen aggregates immediately decrease in the cis-Golgi, it decreases in the trans-Golgi only after a lag of about 30 minutes. This clearly shows the existence of a convection. It was considered a proof of cisternal progression by the authors as procollagen cannot enter small, protein-coated (COP) vesicles thought to

be responsible for vesicular transport in the Golgi apparatus.

**Fig. 2.6, (b)** Another experiment was done by Trucco et al. in 2004, in which VSVG proteins are tagged with gold beads, which are easily seen in electron microscopy. By using temperature blocks, they create a pulse of VSVG, that they observe as it progresses through the Golgi stack.

Though those experiments give more information, because they include the spatial distribution inside the stack, they produce few data with high uncertainty, because each electron microscopy assay at each time interval has to be done on a different cell.

### 2.3.3 Numerical solutions

The comparison of numerical simulations with experiments are shown in figure 2.6. We assumed constant values for the velocity  $v$ , the diffusion coefficient  $D$  and the exit rate  $r$  throughout the stack, because, as we mentioned, we cannot expect enough accuracy from the data to fit the experiments with an larger parameter space. Moreover, assuming spatially constant  $v$ ,  $D$  and  $r$  enables us to draw straightforward conclusions.

We mentioned in section 2.2 that the out fluxes at the boundaries of Golgi apparatus could be written :

$$J(0) = J_{in} - k'_1 A(0) \quad (2.30)$$

$$J(L) = (k_N + v_p) A(L) \quad (2.31)$$

When solving the Fokker-Planck equation to mimic experimental results, we do not have the microscopic information on  $\{k_n\}$ ,  $\{k'_n\}$  and  $v_p$ , and therefore we cannot implement such boundary conditions. We can write the boundary conditions more generically, in the form :

$$J(0) = J_{in} - k^- A(0) \quad \text{with} \quad k^- = k'_1 \quad (2.32)$$

$$J(L) = (k^+ + v) A(L) \quad \text{with} \quad k^+ = k_N + v_p - v \quad (2.33)$$

In which  $v$  is the total velocity and  $k^+$  is an effective rate of exit that can be negative (for instance,  $k^+ = -v^e$  if  $k_N = 0$ , i.e. no exit by vesicular transport) or positive. We mentioned that we cannot give a direct microscopical interpretation of  $k^+$  since we do not have enough independent information on  $v_p$  and  $\{k_n\}$ ,  $\{k'_n\}$ , but can make a few comments however. Since we assumed  $D$  and  $v$  to be constant in the Golgi apparatus, we know that the rates  $\{k_n\}$ ,  $\{k'_n\}$  are constant throughout the Golgi apparatus (except for  $k'_1$  and  $k_N$ ), and we will call their value  $k_n$  and  $k'_n$  respectively. Because of the definition of  $v$  ( $v = v_p + v^e$ ) and of  $v^e$  ( $v^e = k_n - k'_{n+1}$ ), equation 2.33 can be re-written as :

$$k_N = k_n + (k^+ - k'_n) \quad (2.34)$$

Therefore :

$$k_N \leq k_n \Leftrightarrow k^+ - k'_n \leq 0 \quad (2.35)$$

In particular,

$$k^+ \leq 0 \Rightarrow k_N \leq k_n \quad (2.36)$$

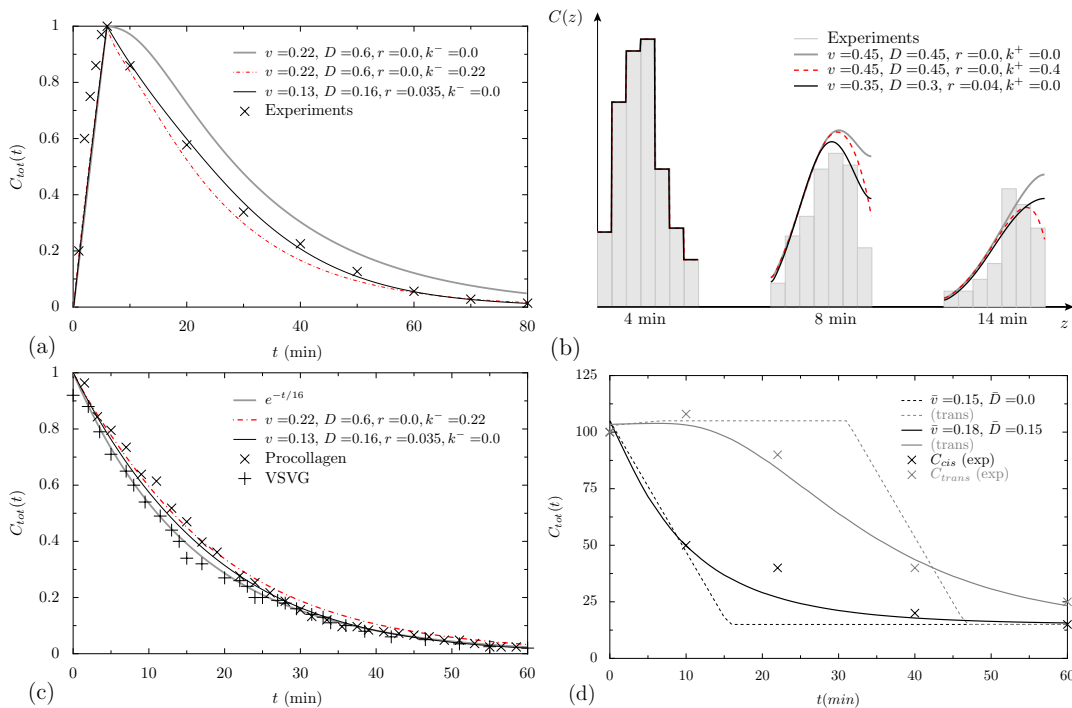


**Figure 2.6:** Quantitative analysis of data from different experimental protocols through numerical resolution of Eq.2.17. **(a,c)** Optical microscopy assays. **(a)** Exit of a short pulse of secretion of a tagged small transmembrane protein (VSVG). **(c)** Exit of a steady-state distribution (at  $t = 0$ ) of a large soluble protein aggregate (procollagen) and a small transmembrane protein (VSVG) [46]. Both experiments exhibit an almost exponential decay with a typical time of 16 minutes. **(b,d)** Electron microscopy assays. **(b)** Pulse chase experiment using VSVG [54] clearly shows a combination of translation, broadening and decay of the peaked concentration distribution. **(d)** Evolution of the concentration of a procollagen in the *cis* (black) and *trans* (grey) face of the Golgi upon sudden blockage of ER secretion [48]. Data suggests the presence of diffusion, corresponding to inter-cisternal exchange. In addition to experimental data, the various curves represent numerical results of equation 2.3 with relevant sets of parameters. Unless mentioned otherwise, we used by default  $k^+ = 0$  and  $k^- = 0$ , with  $J(0) = -k^- A(0)$  and  $J(L) = (k^+ + v)A(L)$ .

Which means that the exit from the trans face of the Golgi by vesicular transport is slower than vesicular transport all along the stack if  $k^+ < 0$ . On the other hand  $k^- = k'_1$  and has a direct interpretation : there is a retrograde flux from the cis Golgi to the E.R. if  $k^- > 0$ . The loss rate  $r$  is unspecified and can include retrograde flux to the E.R. and/or a flux to the cell.

We optimized  $v$ ,  $D$ ,  $k^+$ ,  $k^-$  and  $r$  by minimizing the difference between the simulations and the experimental results, for each set of experimental data. As we can see in figure 2.6 , sometimes several sets of  $(v, D, k, r)$  could yield similar results, and we represented here the most significant sets.

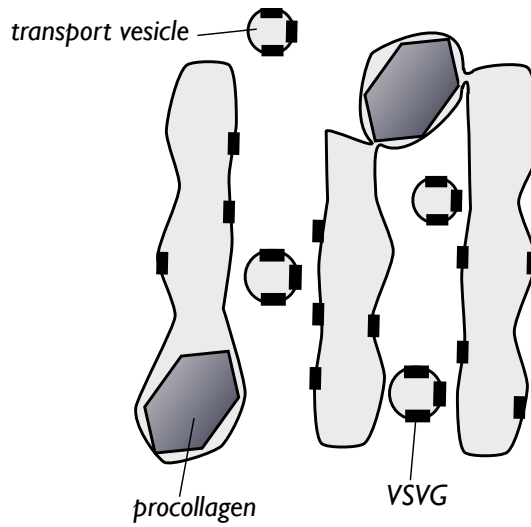


**Figure 2.7:** An illustration of the proposed mechanism of transport of large molecule in the Golgi : large fractions of cisternae can be translocated and merge with an adjacent cisterna.

### 2.3.4 Discussion

The analysis of experimental data by numerical simulations lead us to strong conclusions.

- Most importantly, figures 2.6,(a,b,c,d) show that in all experiments, we find  $v < \frac{1}{2}D$ , which means that there is no quantitative experimental data showing unambiguously cisternal progression.
- From figures 2.6,(a,b), we also learn that there is either a retrograde flux of VSVG to the E.R. at the cis face (if  $k^- > 0$ ), or VSVG exits throughout the stack ( $r > 0$ ). Otherwise see that export from the Golgi apparatus exhibits a delay that does not exist in experiments, even for very high values of diffusion with respect to convection ( $D \sim 3v$ ), much higher than observed in electron microscopy experiments (figure 2.6,(b) shows  $v \sim D$ ).
- Surprisingly, even procollagen exhibits a large diffusion coefficient compared to its velocity (2.6,(c,d)), despite the claim that procollagen cannot enter COP vesicles.

Those results show with certainty that cisternal progression is at best an incomplete model. Since  $v < \frac{1}{2}D$ , we find  $Pe < 3$ , and hence the convective transport, whatever its nature, never dominates over diffusion. If we accept the claim that procollagen cannot be transported by COP vesicles, then the only model we can come to is that large fractions of cisternae, containing large molecular aggregates, can be translocated and merge with an adjacent cisterna, as illustrated in figure 2.7. This model makes cisternal progression unnecessary as most known features of transport in the Golgi apparatus can be explained. However, as the exchange of large fractions of cisternae can be symmetric, the "large chunks" model is not incompatible with cisternal progression. Such large transporters have been observed in the E.R. to Golgi transport, as well as in transport from the Golgi

apparatus to the plasma membrane [55]. However, due to the interconnected structure of the Golgi stack, such large carriers could be difficult to identify in the Golgi apparatus. A conceptual model including a very similar mechanism has been proposed recently [56].

Our formulation enabled us to quantitatively analyse experimental results and yield conclusions on the transport of cargo in the Golgi apparatus. By allowing the rates  $k_n$  and  $k'_n$  to vary spatially, we may now consider the description of more complex transport.

## 2.4 Beyond constant rates of transport

In the previous section, we were interested in constant rates of transport  $v$ ,  $D$ , and  $r$ , in order to better understand the anterograde trafficking of newly synthesized molecules in the Golgi apparatus. As we mentioned in the introduction, there are other types of trafficking in the Golgi apparatus : some molecules move in a retrograde fashion (from trans to cis), while some other keep a constant averaged position. Resident Golgi enzymes, responsible for the maturation of lipids and proteins (for instance by adding glycans) are one particularly interesting example as they are crucial to the function of the Golgi apparatus.

It has been shown that these resident Golgi proteins are also transported in and around the Golgi apparatus [57]. Since they have a preferred localization in the Golgi apparatus, their transport rates cannot be constant, and have to be non-monotonous. Therefore, in this section, we will be interested in a Golgi apparatus in which the rates of transport  $v$  and  $D$  are not constant along  $Oz$ , corresponding to non-constant values of  $\{k_n\}$  and  $\{k'_n\}$ . In continuity with the other chapters this thesis, we are very interested in describing transport processes as a diffusion along an energy landscape, as it yields an intuitive description of transport in complex systems. Wells in the energy landscape, depending upon the physical properties of the transported proteins, could be a way to trap molecules at a given location in the Golgi apparatus, and hence enable the existence of resident Golgi proteins, characteristic of a given Golgi localization. On the other hand, a molecule on a monotonous energy landscape will be driven in a constant direction. One shortcoming of this description is the implicit assumption that detailed balance is satisfied, which is not guaranteed in transport processes involving energy input. If detailed balance is not satisfied, more complex descriptions, such as the existence of two distinct protein states [58] can be envisioned (in the issue at hand the two states of a protein distinguish if the protein is in a compartment in a carrier).

### 2.4.1 Diffusion in an energy landscape

In the previous section we assumed the transport rates  $k_n$  and  $k'_n$  to be independent of the cisternal number  $n$ . However, transport through the Golgi apparatus is most likely biased by the fact that, whether they move or not, different cisternae are not chemically and physically equivalent, so forward and backward transition rates between cisternae need not be equal ( $k_n \neq k'_n$ ), nor uniform through the Golgi ( $\partial_n k_n \neq 0$ ).

Let us write the energy landscape  $E_n$ , which reflects the interaction between a given protein and the local environment of the  $n$ -th cisterna . We want a thermodynamically consistent definition of  $E_n$ , so that, at equilibrium, the probability for a molecule to be in the  $n$ -th cisterna is :

$$P(n) \propto e^{-E_n} \quad (2.37)$$

All energies are defined here with respect to the reference energy available from the environment to perform the transition (the thermal energy  $k_B T$  for thermally activated processes, and of order  $20k_B T$  for processes optimally utilizing the energy hydrolysis of

one ATP molecule).

We assume the proteins to move only to neighboring cisternae (i.e. only the transitions  $n \rightarrow n + 1$  and  $n \rightarrow n - 1$  are allowed), and we assume all moves to be reversible (i.e. if  $n \rightarrow n + 1$  is allowed, so is  $n + 1 \rightarrow n$ ). Under those assumptions, any stationary solution satisfies detailed balance, and we can write :

$$k'_{n+1} = k_n e^{\partial_n E|_{n+\frac{1}{2}}} \quad (2.38)$$

From equations 2.13,2.13, we deduce :

$$D_{n+\frac{1}{2}} = \frac{1}{2} k_n \left( 1 + e^{\partial_n E|_{n+\frac{1}{2}}} \right) \quad (2.39)$$

$$v^e_{n+\frac{1}{2}} = k_n \left( 1 - e^{\partial_n E|_{n+\frac{1}{2}}} \right) \quad (2.40)$$

To go further, we need to assume that the differences in energy between the cisternae are small. We can then expand in  $\partial_n E$ . At first order, we find :

$$D_{n+\frac{1}{2}} \simeq k_n \left( 1 + \frac{1}{2} \partial_n E|_{n+\frac{1}{2}} \right) \quad (2.41)$$

$$v^e_{n+\frac{1}{2}} \simeq -D \partial_n E|_{n+\frac{1}{2}} \quad (2.42)$$

The term  $k_n$  in  $D$  does not come from a difference in energies between cisternae, but can be related to an energy barrier. By analogy with thermally activated processes, where rates are exponentials of energy differences, it is useful to define a protein-dependant energy barrier  $\Delta E$ . We call  $\Delta E(n + \frac{1}{2})$  the energy barrier to overcome to go from the  $n$ -th cisterna to the  $(n + 1)$ -th cisterna, such as :

$$k_n = k_0 e^{-\Delta E(n+\frac{1}{2})} \quad (2.43)$$

In which  $k_0$  is a constant rate, and can be seen as the frequency at which a molecule tries to overcome the energy barrier  $\Delta E$ . Eventually, we can write in shorthand :

$$D \simeq k_0 e^{-\Delta E} \left( 1 + \frac{1}{2} \partial_n E \right) \quad (2.44)$$

$$v^e = -D \partial_n E \quad (2.45)$$

This expresses the fact that  $v^e$  and  $D$  results from similar processes (transport between cisternae), but that unlike  $D$ ,  $v^e$  is entirely controlled by the gradient of cisternae properties. Note that, because of our assumptions, the relationship between  $v^e$  and  $D$  is an analogous to Einstein's relation, an example of the fluctuation-dissipation theorem [59].

As of now, in this section, we considered transport in the reference frame of cisternae. The global velocity appearing in the Fokker-Planck equation (Eq.2.17) (and the one measured experimentally) also includes the constant velocity of cisternal progression. From equations 2.44,2.45, we can see that cisternal progression can be included in the energy landscape formalism by adding a linear term  $nv_p/D$  in the energy.

Hence, we can describe transport in the reference frame of the laboratory by using an effective energy  $\tilde{E}$  including a linear term describing progression. We can identify the reference frame of the laboratory to the reference frame of fictive immobile cisternae, and the transport equations now read :

$$\partial_t A_n = \partial_n(D\partial_n A - vA) \quad (2.46)$$

$$v = -D\partial_n \tilde{E} \quad (2.47)$$

$$\tilde{E}_n = E_n - n\frac{v_p}{D} \quad (2.48)$$

It should be noted that the “energy landscape” picture is very general, and not restricted to, *e.g.*, differences of chemical potential in different cisternae. It can in particular capture at a phenomenological level the existence of differences in vesicle secretion in different cisternae or in the two faces of a given cisterna.

### 2.4.2 Dynamics of resident Golgi proteins

We mentioned that resident Golgi proteins are preferentially located in a given region of the Golgi apparatus [60]. Even in the presence of convection, the residency of such proteins may be accounted for by adding to the (linear) convective potential a term promoting protein localization, the simplest form of which is quadratic:  $\frac{K}{2}(n - n_0)^2$ . Such a potential favors protein localization around the  $n_0$ -th cisternae, with a stiffness  $K$ . This type of energy profile could in principle describe the transport of proteins moving in a retrograde or anterograde fashion ( $n_0 < 1$  and  $n_0 > N$ , respectively), as well as Golgi resident proteins preferentially localized in a particular cisternae ( $1 < n_0 < N$ ). The two former situations differ little from a purely convective picture, although with non-uniform velocity. The latter on the other hand yields interesting predictions concerning the residence time of resident Golgi proteins.

We can use equations 2.41,2.42,2.3 to write the Fokker-Planck equation in the energy landscape formalism :

$$\partial_t A = \partial_n j - rA \quad \text{with : } j = -(D\partial_n A - vA) \quad (2.49)$$

$$v = -D\partial_n \tilde{E} \quad (2.50)$$

Even if  $\tilde{E}$  has a minimum, the proteins have a finite probability to reach the Golgi boundaries by diffusion, and hence resident proteins have a finite lifetime in the Golgi. For completeness, we should take into account the possibility of  $r$  depending upon  $n$ . However, this cannot be included in the flux  $j$  in 2.49, and thus cannot be mapped on the energy landscape. Therefore, there is no simple general solution of 2.49 if  $r$  depends on the position. In the following, we will assume  $r$  to be constant, but we can keep in mind that a  $r$  depending upon  $n$  could be an additional way to influence protein transport, and hence another tool to locate resident Golgi proteins.

Let us compute this lifetime in the case of a strongly confining potential,  $\tilde{E}_n = \frac{K}{2}(n - n_0)^2$ , in the absence of global convection. If the outward flux  $J^{out}$  is small enough, the concentration in the Golgi is quasi static, (*i.e.* it is close to the stationary solution). In

the limit  $J^{out} \rightarrow 0$ , the stationary distribution of proteins is :

$$A \simeq A_0 e^{-\frac{K}{2}(n-n_0)^2} \quad (2.51)$$

Where  $A_0$  is proportional to the total concentration  $\mathcal{A}$  :  $A_0 \simeq \mathcal{A} \sqrt{\frac{K}{2\pi}}$ . Because the fluxes are linear in  $A$  in equation 2.49, the stationary distribution does not depend on  $r$  in the limit  $J^{out} \rightarrow 0$ . The exit fluxes from the Golgi apparatus write :

$$J_1^{out} = k'_1 A_1 \quad (2.52)$$

$$J_N^{out} = k_N A_N \quad (2.53)$$

We can compute the characteristic exit times  $\tau_1$  and  $\tau_n$  from the cis-most cisterna and the trans-most cisterna respectively :

$$\tau_1 = \frac{\mathcal{A}}{J_1^{out}} = \frac{1}{k'_1} \sqrt{\frac{2\pi}{K}} e^{\frac{K}{2}(1-n_0)^2} \quad (2.54)$$

$$\tau_N = \frac{\mathcal{A}}{J_N^{out}} = \frac{1}{k_N} \sqrt{\frac{2\pi}{K}} e^{\frac{K}{2}(N-n_0)^2} \quad (2.55)$$

$$(2.56)$$

Because all the fluxes are linear in  $A$ , the lifetime  $\tau_0$  of resident Golgi proteins is :

$$\tau_0 = \frac{1}{r + \frac{1}{\tau_1} + \frac{1}{\tau_N}} \quad (2.57)$$

Let us now compute the effect of convection on the lifetime of a resident protein. A velocity  $v$  can be modeled as a potential  $E'_n = -vn/D$ , and the new energy landscape  $\tilde{E}' = \tilde{E} + E'$  can be written :

$$\tilde{E}'_n = \frac{K}{2} (n - (n_0 + \delta n))^2 + \tilde{E}'_{n_0 + \delta n} \quad (2.58)$$

$$\delta n = \frac{v}{KD} \quad (2.59)$$

The location of the energy minimum is therefore shifted from  $n_0$  by a distance  $\delta n$  in the direction of the convection, and the fluxes at the boundary are modified accordingly. The situation is illustrated in figure 2.8. If  $v$  corresponds to cisternal progression, the exit rate at cis face is unchanged. If  $v$  is due asymmetric vesicular transport, we will assume the rates  $\{k'_n\}$  to be unchanged (i.e.  $v$  comes from an increase of the  $\{k_n\}$ ). In both scenarios, it is reasonable to assume the fluxes, in the presence of convection, to be :

$$J_1(\tilde{E}') = -k'_1 A_1 \quad (2.60)$$

$$J_N(\tilde{E}') = (k_N + v) A_N \quad (2.61)$$

By replacing  $n_0$  by  $n_0 + \delta n$  in equation 2.54,2.55, we can now compare the mean exit times  $\tau'_1$  and  $\tau'_N$  with convection to their equivalent in the absence of convection. We assume that  $\delta n$  is small compared to  $N$ , so that minimum of is energy is not drastically changed, and  $n_0 + \delta n$  is still far enough from the boundaries for the quasi-stationary approximation to be valid. At first order in  $\delta n$ , we find :

$$\frac{\tau'_1}{\tau_1} \simeq e^{-\frac{v}{D}(1-n_0)} \quad (2.62)$$

$$\frac{\tau'_N}{\tau_N} \simeq \frac{k_N}{k_N + v} e^{-\frac{v}{D}(L-n_0)} \quad (2.63)$$

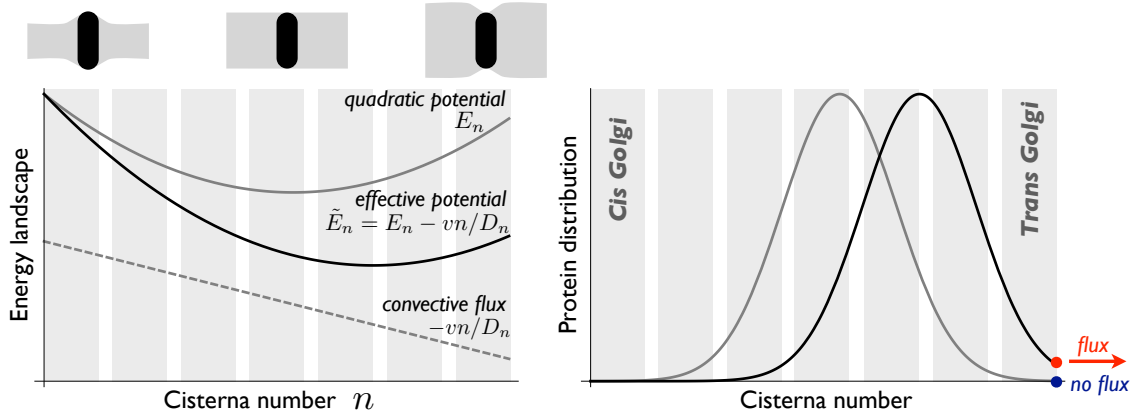


**Figure 2.8:** Convective flux affect the life-time of Golgi resident proteins. Proteins localized in particular cisternae by a quadratic energy possibly originating from hydrophobic mismatch as sketched (see section 2.5.3) between the protein transmembrane domain and the cisterna membrane (sketch) may be driven out of the Golgi by the convective flux imposed by cisternae maturation.

The lifetime of resident Golgi proteins is dominated by the smallest lifetime, as shown in equation 2.57. Let us consider the case in which the exit time is dominated by the flux at the trans face  $n = N$  (because  $k_N \gg k'_1$  or because  $n_0 > N/2$  and  $k_N \sim k'_1$ ). In this case the ratio of the exit time with convection  $\tau_v$  over the exit time in the absence of maturation  $\tau_0$  reads :

$$\frac{\tau_v}{\tau_0} \simeq \frac{1}{1 + \frac{v}{k_N}} e^{-Pe(1 - \frac{n_0}{N})} \quad (2.64)$$

$$Pe = \frac{Lv}{D} \quad (2.65)$$

This is an interesting result : the ratio of residency times does not depend upon the stiffness  $K$  of the potential well, but depends highly on the Peclet number and the position of the well. The further from the trans edge a resident protein is, the more its residency time will be sensitive to convection (because of the shape of the quadratic potential), as illustrated in figure 2.8.

A (dimensionless) confining potential of order of order  $E_{conf} (= KN^2/2) \sim 3$  increases the protein residency time by more than an order of magnitude (from twenty minutes to about four days) compared to pure diffusion, Eq.2.54. Protein localization under convective flux thus requires a stronger potential than in the absence of convection. Confinement within a particular cisterna is maintained against the flux if  $\delta n < 1$ , or  $K > v/D$  ( $\simeq 1$  according to our estimates, Fig.2.6), and confinement within the Golgi is only possible if  $\delta n < N$ , or  $K > \frac{v}{ND}$  ( $\simeq 0.15$ , giving a total confining energy  $E_{conf} \gtrsim 3.5$ ). Furthermore, Eq.2.64 yields the experimentally testable prediction that, all other things being equal, resident proteins located in the *trans* region should have an exponentially lower residency time than proteins located in the *medial* and *cis* regions of the Golgi stack.

We now have a functional formalism to describe transport and localization of proteins in the Golgi apparatus. To better understand our results, we now have to focus on the actual microscopic origin of the parameters.

## 2.5 Microscopic origin of the parameters

### 2.5.1 Diffusion coefficient

As we mentioned in the beginning of this chapter, physical transport between cisternae is thought to involve two possible carriers : vesicles secreted by one cisterna and merging with the other, and tubules connecting the two cisternae [34] (Fig.2.3). Both could in principle permit unidirectional and bidirectional transport, and both involve the diffusive search for a "hot spot" (the entrance of a tubule or a spot of vesicle secretion), possibly followed by activated processes (vesicle scission and fusion). In Eq.2.43, the diffusive search is characterized by the reference rate  $k_0$ , while the activated processes are described as an effective energy barrier  $\Delta E$ .

The time  $\tau$  needed for a molecule to find a hot spot by diffusion in a cisterna of radius  $R$  is related to the *microscopic* diffusion coefficient  $D_2$  of the molecule by  $1/k_0 \sim R^2/D_2$ . The effective diffusion coefficient is hence  $D = h^2/2\tau$ , in which  $h$  is the distance between two adjacent cisternae. We show in the appendix that the effective diffusion coefficient along  $Oz$  of a transmembrane protein like VSVG traveling between cisternae of radius  $R$  in a process limited by the diffusive search for one hot spot of size  $a$  is approximately :

$$D \approx \frac{1}{2 \log \left( \frac{R^2}{a^2} \right)} D_2 \frac{h^2}{R^2} \quad (2.66)$$

A microscopic diffusion coefficient  $D_2 \sim 0.15 \mu^2/s$  was found experimentally for VSVG, [50] and other transmembrane proteins [51]. Using a typical radius of the cisterna  $R = 450 \text{nm}$  as measured experimentally [46, 49]), we find :

$$D \approx 5 \text{min}^{-1} \quad (2.67)$$

Which is about 10 to 20 times larger than the diffusion coefficient obtained from the propagating pulse fitting method described above ( $D \sim 0.3/\text{min}$ ). We identify two possible causes for this large difference :

*i)* Transport between cisternae is not limited by diffusion, but by activation barriers such as vesicle scission and fusion or protein entry into tubules

*ii)* Transport is indeed limited by diffusion, but with a much smaller effective diffusion coefficient.

Support for the latter possibility comes from the observation that a large fraction of membrane proteins (about 95%) does not appear to diffuse laterally [46, 50], possibly because of its segregation within membrane domains and/or membrane-cytoskeleton interaction. Protein diffusion is only effective in the mobile state, so the effective diffusion coefficient (for all proteins) should only be about 5% of the microscopic one, leading to an inter-cisternal transport rate of  $0.25 \text{min}^{-1}$ , close to the fitted value for VSVG.

It is however also reasonable to expect that membrane diffusion goes unhindered but that there exists an energy barrier  $\Delta E$  for proteins entering the hot spot to be actually

transported. One can expect the effective diffusion coefficient with a such barrier to be of order  $D \sim k_0 e^{-\Delta E}$ , and a modest energy barrier of order  $\Delta E = 2 - 3$  (in units of  $k_B T$  if transport is thermally activated, in units of the activation energy otherwise) would be sufficient to reconcile the microscopic model with the fitted value of the parameters.

In the next sections, we discuss the possible origins of the energies mentioned in this chapter.

### 2.5.2 Energy barriers

The membrane curvature at the edges of cisternae, in the tubules connecting two cisternae, and at the neck of a budding vesicle (see chapter 1) is fairly high (of order  $\pm 1/30 \text{ nm}^{-1}$ , see [34, 54]) and some membrane proteins may find such highly curved environments unfavorable. As an illustration, it has been shown that lipid membranes with several components had different compositions in areas of different curvature, both in vivo [61], in vitro [62, 63], and theoretically [64]. Such an effect is difficult to quantify precisely and generically *a priori*, but using our knowledge of the bending energy of the membrane (equation 1.1), we can find a *very* rough estimate. The bending energy of a protein of radius  $a$ , of preferred curvature  $C_0$  and of bending modulus  $\kappa_p$  to enter a zone of curvature  $C$  is :

$$\Delta E \simeq \frac{1}{2} \kappa_p \pi a^2 (C - C_0)^2 \quad (2.68)$$

Using  $C - C_0 \approx 1/20 \text{ nm}^{-1}$  [34] and  $a \approx 3 \text{ nm}$  [65], one finds  $\Delta E \approx \frac{1}{25} \kappa_p$ . The bending modulus is not well defined at this scale and for one unique protein. However, since the typical bending modulus of membranes is of the order of  $20 k_B T$ , it is probably much higher in a protein, and it is reasonable to think that the energy scale for a protein to enter the tube is of the order of a few  $kT$ .

Since we do not expect diffusion in the membrane plane to be activated (it is rather the severing of vesicles, and the transport of membranes themselves that consumes energy) this barrier of a few  $k_B T$  is sufficient to explain the slow diffusion (on the  $Oz$  axis) encountered in the Golgi apparatus, and the assumption of a diffusion slowed down by energy barriers is reasonable.

### 2.5.3 Energy landscape

Let us now consider the whole energy landscape, i.e. the term  $\tilde{E}$  in equations 2.49, 2.50. Since the membrane composition and physical properties change along the  $Oz$  axis of the Golgi stack, one good candidate to provide for a potential energy along  $Oz$  is the insertion energy of a protein, i.e. how much the localization of this protein in one place is energetically favorable.

It has been shown that the dominant signal which determines the localization of resident trans-Golgi enzymes is the length transmembrane domain (see [66] for a review), and that the transmembrane domain does play a role in the localization of some med- and cis-Golgi proteins [67, 68]. One well-known contribution to the insertion energy of a molecule in a

membrane is the cost of having molecules with different hydrophobic chain lengths brought together, called hydrophobic mismatch [69], and illustrated in figure 2.8.

Hydrophobic mismatch between transmembrane proteins and the surrounding membrane has therefore been suggested as a good candidate for protein retention in the Golgi [70, 71] (see Fig.2.8). The membrane thickness of organelles is known to continuously increase along the secretory pathway from about 37 Å in the ER to 42 Å at the plasma membrane [72] and the path followed by a given protein is known to be affected by the length of its transmembrane domain [73, 74].

We can estimate the energy cost of the hydrophobic mismatch between a protein of radius  $a \sim 3\text{nm}$  and its environment. Let us call  $\beta$  the bilayer stretching modulus (of order  $0.2\text{J}/\text{m}^2$  [21]), and  $\lambda_m$  the decay length of the mismatch in the membrane (of order 1nm [75]),  $h_0$  the preferred thickness of the protein and  $h$  the thickness of the membrane. The hydrophobic mismatch energy reads [75] :

$$E_m \approx \pi a \lambda_m \beta \left( \frac{h - h_0}{h_0} \right)^2 \quad (2.69)$$

We can now write this energy as a function of the position  $n$  in the stack. For simplicity, we assume a linear profile of the membrane thickness :  $h(n) = h(0) + (n - n_0)\alpha$ . As we mentioned, the membrane thickness increases from about 37 Å to 42 Å and hence  $\alpha \approx 1\text{Å}$ . We can therefore write :

$$E_m(n) = \frac{1}{2} K (n - n_0)^2 \quad (2.70)$$

$$K = 2\pi \lambda_m a \beta \left( \frac{\alpha}{h_0} \right)^2 \approx \frac{1}{2} k_B T \quad (2.71)$$

We find that the stiffness of the potential is of order  $\frac{1}{2}k_B T$ , and hence the well energy on the whole Golgi apparatus is of the order of  $10k_B T$ . From the discussion of the previous section (section 2.4.2 , Eqs.2.55,2.63), we see that hydrophobic mismatch is in principle able to localize resident proteins in the Golgi apparatus, in a region spanning a few cisternae. There must be supplementary mechanisms to allow a more precise localization in the Golgi apparatus, and it was shown that the cytoplasmic domains of resident Golgi enzymes also played a role in enzyme localization. We can suspect that these domains are responsible for the interaction with various molecules, which could change the transport properties of the enzyme and enable more accuracy in its localization. One way achieve a better localization is to have an exit rate  $r_n$  which depends upon  $n$ .

## Conclusion

In this chapter, we developed a formalism to quantitatively study the experimental data available on the transport in the Golgi apparatus. Though we could not conclude definitively on the controversy opposing the cisternal progression model to the vesicular transport model, we did come to the conclusion that the existing data does not quantitatively favor one model, though they do show the existence of some amount of diffusion-like transport on the main axis, even for large protein complexes, imputable to inter-cisternal exchange. We agree with recent propositions that this exchange could be due to the fission and fusion of large fractions of cisternae, possibly in addition to cisternal progression. We showed that this one-dimensional diffusion normal to the membrane plane could emerge from a process including the two-dimensional diffusion in the membrane plane to find a hopping hot spot, the overcoming of an energy cap, and the hopping to an adjacent cisterna. Numbers seem coherent with the assumption that this energy cap results from the crossing of a highly curved membrane region such as a tubule or a vesicle bud.

The diffusion-convection formalism can be extended to a full Fokker-Planck equation including the transport of molecules along an energy landscape. In particular, the localization of resident enzymes could be explained by a well in the energy landscape, whereas proteins undergoing retrograde transport seem to encounter an energy monotonously increasing with  $z$ . We showed that hydrophobic mismatch is a well-suited candidate for the localization of resident Golgi enzymes within a few cisternae.

In this work, we only considered linear laws of transport, i.e. we neglected any feedback of the concentration of one protein on the energy landscape. In the case of hydrophobic mismatch, this can be shown to be inaccurate at high concentration, since the proteins will change the local thickness of the hydrophobic layer and make it closer to their own favored hydrophobic layer thickness : transported molecules will change the membrane identity and hence, alter the local transport properties. This will be the next level of complexity we want to tackle : in the next section, we will study the feedbacks between identity and transport.

## 2.6 Appendix A : diffusion coefficient in the Golgi apparatus

In this section, we aim at finding  $D$ , the effective diffusion coefficient on the  $Oz$  axis. It is different from  $D_2$ , the bidimensional diffusion coefficient in the membrane plane, though they are related.

It has been observed that there exist direct continuities between cisternae, and their surface is much smaller ( $\approx 2.10^{-3}\mu m^2$  [34]) than the surface of a cisternae ( $\approx \mu m^2$ ). It is logical to assume that finding a connection is the rate-limiting step in diffusing on the  $z$  axis. Let us call  $a$  and  $b$  the two faces of a cisternae. Let  $\tau$  be the mean first passage time of a protein located initially on the tube on face  $i$  to a the tube on face  $j$ , and let us assume the typical diffusion time in a tube to be small compared to  $\tau$ . We can now model diffusion along  $Oz$  as a random walk on discrete sites of size  $h$  with a constant rate of jumps  $1/\tau$ . In the continuous limit, this model gives :

$$D = \frac{h^2}{2\tau} \quad (2.72)$$

To reach the tube on face  $i$  when starting from the tube on face  $j$ , a protein has to reach the border of the cisterna (assumed circular) and find the tube on face  $j$ . Let us call  $\tau^+$  and  $\tau^-$  the mean first passage times from a tube to the border and from the border to a tube respectively. If we assume the faces  $i$  and  $j$  to be identical, each time a protein reaches the border, it has a probability  $1/2$  to switch face. Therefore, the mean first passage time from one cisterna to another is :

$$\tau = 2(\tau^- + \tau^+) \quad (2.73)$$

To compute these mean first passage times, we can use the backward Chapman-Kolmogorov differential equation for the probability  $P(\mathbf{r}_0, 0|\mathbf{r}, s)$  to be at time  $t = 0$  at position  $\mathbf{r}_0$  for the first time, given a position  $\mathbf{r}$  at time  $t = s$  (where  $s$  is negative) [76, 77, 78]. This equation reads :

$$-\partial_s P(\mathbf{r}_0, 0|\mathbf{r}, s) = \int d^2\boldsymbol{\rho} \left[ W(\boldsymbol{\rho}|\mathbf{r}, s) (P(\mathbf{r}_0, 0|\boldsymbol{\rho}, s) - P(\mathbf{r}_0, 0|\mathbf{r}, s)) + \frac{1}{2}D_2\Delta_r P(\mathbf{r}_0, 0|\mathbf{r}, s) \right] \quad (2.74)$$

In which  $W(\boldsymbol{\rho}|\mathbf{r}, s)$  is the jump probability density from position  $\mathbf{r}$  to position  $\boldsymbol{\rho}$  at time  $s$ . In this continuous formulation, the only possibility of a jump is when the seeker finds the target, i.e. when it is in a tube (when calculating  $\tau^-$ ) or a border (when calculating  $\tau^+$ ). For a tube at position  $\mathbf{r}_0$  and of radius  $a$ , we assume:

$$W(\boldsymbol{\rho}|\mathbf{r}, s)^- = k^- \theta(a - |\mathbf{r} - \mathbf{r}_0|) \delta(\boldsymbol{\rho} - \mathbf{r}_0) \quad (2.75)$$

In which  $\theta$  is the Heaviside step function. This assumption means that the tube is entered with a rate  $k^-$  by a protein located at a distance smaller than  $a$  from the center of the tube, whereas a molecule further away cannot enter the tube. In the following, we will assume that the tube is at the position  $\mathbf{r}_0 = \mathbf{0}$ .

Similarly, for a border of width  $b$  located at a radius  $R$  :

$$W(\boldsymbol{\rho}|\mathbf{r}, s)^+ = k^+ \theta(|\mathbf{r}| + b - R) \delta(|\boldsymbol{\rho}| - R) \quad (2.76)$$

Which means that the border is crossed with a rate  $k^+$  by a molecule at a distance  $b$  from the border, whereas a molecule further away cannot cross the border.

Because of the assumed circularity of the cisternae, the only relevant space variable will be  $r$ , the distance of the protein to the center the cisternae. Let us define the mean first passage times  $\tau^-(r)$  and  $\tau^+(r)$  using  $P(r_0, 0|r, s)$  :

$$\tau^-(r) = - \int_{-\infty}^0 sP(0, 0|r, s)ds \quad (2.77)$$

$$\tau^+(r) = - \int_{-\infty}^0 sP(R, 0|r, s)ds \quad (2.78)$$

By averaging the backward Chapman-Kolmogorov differential equation over all orientations (to have  $P(r, 0|r, s)$  instead of  $P(\mathbf{r}_0, 0|\mathbf{r}, s)$ ), and by multiplying by  $s$  and integrating over  $s$  from  $-\infty$  to  $0$ , we find :

$$-1 = \frac{1}{2}D_2\Delta\tau^-(r) - k^-\tau^-(r)\theta(a-r) \quad (2.79)$$

$$-1 = \frac{1}{2}D_2\Delta\tau^+(r) - k^+\tau^+(r)\theta(r+b-R) \quad (2.80)$$

The boundary conditions we assume for  $\tau^-$  are  $\tau^-(r \leq a) = 1/k^-$  (absorbing boundary) and  $\partial_r\tau^-|_R = 0$  (so-called reflective boundary condition, coming from the symmetry of the two face of a cisterna), and for  $\tau^+$  we assume  $\tau^+(r \geq R-b) = 1/k^+$  (absorbing boundary) and  $\partial_r\tau^+|_0 = 0$  (reflective boundary condition, coming from the axisymmetric structure of cisternae). The absorbing boundary conditions rely on the hypothesis  $\lambda^\pm \rightarrow \infty$ . Otherwise, they have to be computed self-consistently.

We can then solve equation 2.79,2.80 using these boundary conditions, and we find :

$$\tau^-(r) = \frac{R^2}{D_2} \log \frac{r}{a} + \frac{1}{k^-} + \frac{a^2 - r^2}{2D_2} \quad (2.81)$$

$$\tau^+(r) = \frac{b^2}{D_2} \log \frac{r}{R} + \frac{1}{k^+} + \frac{R^2 - r^2}{2D_2} \quad (2.82)$$

When a protein crosses a tube, its new position is  $r = a$  (we assumed the tubes to be centered), whereas after crossing a boundary, its new position is  $R - b$ . Therefore, the mean first passage time from a tube to another is  $\tau = \tau^+(a) + \tau^-(R - b)$ . As mentioned, the size of a tube and the width of the boundaries are much smaller than  $R$ , the radius of a cisterna, and we can take the limit  $R \gg a$ ,  $R \gg b$ . Moreover, in this section we are interested in computing the diffusion coefficient on  $Oz$  resulting from the time needed to find a tube. The consequences of energy barriers to cross the borders or the tube are discussed in the section 2.5.2, and do not need to be taken into account here. Therefore, it is consistent to assume  $\lambda^+ \rightarrow +\infty$  and  $\lambda^- \rightarrow +\infty$ . Under those assumptions, we find :

$$\tau \approx \frac{R^2}{D_2} \log \frac{R^2}{a^2} \quad (2.83)$$

$$D = \frac{h^2}{2\tau} \approx \frac{1}{2 \log \frac{R^2}{a^2}} D_2 \frac{h^2}{R^2} \quad (2.84)$$

In usual conditions, we have  $R \approx 500\text{nm}$ ,  $h \approx a \approx 50\text{ nm}$  and  $k \approx a^2/D_2$ , and hence  $D$  is about eight hundred times smaller than  $D_2$ . Using these values, we find a typical transport time of one minute, which is one order of magnitude less than observed experimentally.

## 2.7 Appendix B : analytical approaches to solving the diffusion-convection equation

In this appendix, we will see a few approaches to solving the convection-diffusion equation with an example of boundary conditions. The equation reads :

$$\partial_t C = -\partial_x J \quad (2.85)$$

$$J = -D\partial_x C + vC \quad (2.86)$$

We can take  $v = 1$  (if  $v \neq 0$ ) because of normalization, but let us keep it for a while for the sake of clarity and generality. A more interesting normalization is to renormalize distances by the system size  $L$ . Let us choose some relevant boundary conditions, as an example :

$$J(x=0) = J_0 = vC_i \quad (2.87)$$

$$\partial_x C \Big|_1 = 0 \quad (2.88)$$

In which  $C_i$  is a constant representing the concentration of the material coming in the system at  $x = 0$ . The second boundary condition is equivalent to setting the output flux to be  $vC(1)$ .

### 2.7.1 Fourier Transform

In this case the concentration is not defined outside the boundaries. If we assume a concentration  $C_i$  at  $x < 0$ , then the concentration will not be continuous at  $x = 0$ , which is not convenient. Therefore we have to integrate between the boundaries. We find :

$$\phi(q, t) = \int_0^1 C(x, t) e^{iqx} dx \quad (2.89)$$

$$\partial_t \phi(q, t) = iq v \phi(q, t) - vC(1, t) e^{iq} \quad (2.90)$$

$$+ vC(0, t) - iq D (C(1, t) e^{iq} - C(0, t)) - q^2 D \phi(q, t) \quad (2.91)$$

Here the presence of  $C(1, t)$  and  $C(0, t)$  implies an integral equation which has to be solved numerically.

### 2.7.2 Laplace Transform

We can think about using Laplace transforms to solve the equation :

$$\tilde{C}(x, s) = \int_0^{+\infty} e^{-st} C(x, t) dt \quad (2.92)$$

$$0 = \partial_x^2 \tilde{C}(x, s) - \frac{v}{D} \partial_x \tilde{C}(x, s) - \frac{s}{D} \tilde{C}(x, s) + \frac{C(x, 0)}{D} \quad (2.93)$$

Let us introduce the eigenvalues  $\lambda_{\pm}$  to solve this linear differential equation for  $\tilde{C}(x, s)$  :

$$\lambda_{\pm} = \frac{v}{2D} \pm \frac{1}{2} \sqrt{\frac{v^2}{D^2} + 4\frac{s}{D}} \quad (2.94)$$

$$\tilde{C}(x, s) = \frac{1}{s} C(x, 0) + \alpha e^{\lambda_+ x} + \beta e^{\lambda_- x} \quad (2.95)$$

We will make two assumptions to simplify our problem, in order to decrease the complexity. Those assumptions are :

$$(\partial_x C(x, 0))_{x=0} = 0 \quad (2.96)$$

$$C(0, 0) = 0 \quad (2.97)$$

With our boundary conditions, we find :

$$\beta = \frac{-J_0}{\lambda^- D - v + \frac{\lambda^-}{\lambda^+} (v - D\lambda^+) e^{-\sqrt{\frac{v^2}{D^2} + 4\frac{s}{D}}}} \quad (2.98)$$

$$\alpha = -\beta \frac{\lambda^-}{\lambda^+} e^{-\sqrt{\frac{v^2}{D^2} + 4\frac{s}{D}}} \quad (2.99)$$

Unfortunately, we could not inverse this transform analytically.

### 2.7.3 Green Functions

We know the Green function of the diffusion-convection equation. Let us try to apply it to our case. Consider the differential equation :

$$(\partial_t - D\Delta_x + v\partial_x)f(x, t) = 0 \quad (2.100)$$

$$\Phi_{t,x} = (\partial_t - D\Delta_x + v\partial_x) \quad (2.101)$$

Let us consider the associated Green function  $K$  and operators  $\Psi$  :

$$(\partial_s - D\Delta_y - v\partial_y)K(x - y, t - s) = \delta(t - s)\delta(x - y) \quad (2.102)$$

$$\Psi_x^\pm = (D\Delta_x \mp v\partial_x) \quad (2.103)$$

One can write  $f$  as :

$$f(x, t) = \int_0^{+\infty} ds \int_V f(y, s) \delta(x - y) \delta(t - s) \quad (2.104)$$

The product of the deltas can be re-written thanks to equation 2.102 and one finds :

$$f(x, t) = \int_0^{+\infty} ds \int_V f(y, s) (-\partial_s K(x - y, t - s) - \Psi_y^- K(x - y, s - t)) \quad (2.105)$$

We can expand and simplify these integrals and we find, using our boundary conditions :

$$f(x, t) = \int_0^L dy f(y, 0) K(x - y, t) \quad (2.106)$$

$$-2v \int_0^t [f(L, s) K(x - L, t - s) - f(0, s) K(x - 0, t - s)] ds \quad (2.107)$$

$$-D \int_0^t \left[ f(L, s) (\partial_y K(x - y, t - s))_{y=L} - f(0, s) (\partial_y K(x - y, t - s))_{y=0} \right] ds \quad (2.108)$$

$$+ \int_0^t (J_0 - v f(0, s)) K(x, t - s) ds \quad (2.109)$$

Moreover,  $K$  is the green function for diffusion-convection and is known :

$$K(x - y, t - s) = \frac{1}{\sqrt{4\pi^2 D(t - s)}} e^{-\frac{(x - y - v(t - s))^2}{4D(t - s)}} \quad (2.110)$$

We find a pair of coupled integral equations :

$$g_X(t) = \int_0^L dy f(y, 0) K(X - y, t) + \int_0^t J_0 K(X, t - s) ds \quad (2.111)$$

$$f(L, t) = g_L(t) - \int_0^t \left[ 2vK(0, t - s) + D(\partial_y K(y, t - s))_{y=0} \right] f(L, s) ds \quad (2.112)$$

$$+ \int_0^t \left[ vK(L, t - s) + D(\partial_y K(y, t - s))_{y=L} \right] f(0, s) ds \quad (2.113)$$

$$f(0, t) = g_0(t) - \int_0^t \left[ 2vK(-L, t - s) + D(\partial_y K(y, t - s))_{y=L} \right] f(L, s) ds \quad (2.114)$$

$$+ \int_0^t \left[ vK(0, t - s) + D(\partial_y K(y, t - s))_{y=0} \right] f(0, s) ds \quad (2.115)$$

Those coupled differential equations can be solved numerically, but are not trivial analytically.

## 2.8 Appendix C : Discretization of the convection-diffusion equation

The equivalency between a discrete and a continuous formalism for convection and diffusion is not necessarily straightforward. For instance,  $A_n^{t+1} = A_n^t - v(A_n - vA_{n-1})$  is not equivalent to  $\partial_t A = -v\partial_x A$  as will be shown further. Here, the equivalencies between formalisms are discussed, as well as the consequences of the choice of one formalism against the others. For simplicity, in the following, we will consider only *explicit* algorithms, i.e. relating the concentrations at the (discrete) time  $t + 1$  to the concentrations at the time  $t$ .

### 2.8.1 Diffusion

Diffusion can be written, in the continuous formalism :

$$\partial_t A = D\nabla^2 A \quad (2.116)$$

The naive Euler discretization reads :

$$A_n^{t+1} = A_n^t + D\Delta t \frac{A_{n+1} + A_{n-1}^t - 2A_n}{\Delta x^2} \quad (2.117)$$

In which  $\Delta x$  is the space step and  $\Delta t$  is the time step. To know whether this algorithm is stable, we can perform a Von Neumann analysis of the discretization presented in Eq. 2.117. The Von Neumann analysis consists in studying the stability of eigenvectors, which we write :

$$A_n^t = \zeta(k)^t e^{ikn\Delta x} \quad (2.118)$$

The values of  $A^t$  follow a (complex) geometric progression. Any stable solution has no divergent modes and therefore any algorithm is unstable if there is one  $k_0$  such as

$$\|\zeta(k_0)\| > 1 \quad (2.119)$$

We inject equation 2.118 in equation 2.117, and we find :

$$\zeta(t) = 1 + \frac{2D\Delta t}{\Delta x^2} (\cos(k\Delta x) - 1) \quad (2.120)$$

Therefore, Euler algorithm for diffusion is stable if :

$$\frac{2D\Delta t}{\Delta x^2} < 1 \quad (2.121)$$

Let us now consider discretization schemes for convection.

### 2.8.2 Convection

Convection can be written, in a continuous view :

$$\partial_t A = -\nabla \cdot (\mathbf{v}A) \quad (2.122)$$

If the initial condition reads  $A(x, t = 0) = f(x)$  and if  $v$  is constant, then the solution writes  $A(x, t) = f(x - vt)$ . Therefore, in this formalism, a delta function or a step function is propagated without broadening.

## Euler algorithms

Let us write the most naive discretization of equation 2.122 :

$$A_n^{t+1} = A_n^t - \Delta t \frac{v_{n+1}A_{n+1}^t - v_{n-1}A_{n-1}^t}{2\Delta x} \quad (2.123)$$

This is called the symmetric Euler algorithm (which we will refer to as Euler 2). To know whether it is stable, let us inject Eq. 2.118 in Eq. 2.123. This yields :

$$\zeta(k) = 1 - i \frac{v\Delta t}{\Delta x} \sin k\Delta x \quad (2.124)$$

Here  $\|\zeta(k)\|$  is almost always superior to one, and the naive symmetric Euler integration is hence unstable and should not be used, as shown in figure 2.9.

We can discretize convection in a slightly different way, using the so-called counter wind algorithm :

$$A_n^{t+1} = A_n^t - \Delta t \frac{v_n A_n^t - v_{n-1} A_{n-1}^t}{\Delta x} \quad (2.125)$$

In which  $\Delta x$  is the spatial step and  $\Delta t$  is the unit time step. We can see that it is merely an asymmetric Euler discretization. However, we can see in figure 2.9 that is not equivalent to a "true" (continuous) convection as a step function profile of the concentration broadens. Furthermore, this implementation is fundamentally asymmetric, and becomes absurd for  $v < 0$ . Despite that, this algorithm is frequently used because discontinuous initial conditions yield no instability. We can see that this algorithm is stable by performing a Von Neuman analysis. We find that the asymmetric Euler algorithm is stable provided  $\frac{v\Delta t}{2\Delta x} < 1$ , but also provided  $v > 0$ . Once again, this condition on  $v$  shows that the algorithm is fundamentally asymmetric and should not be trusted under all conditions.

## Other algorithms

A commonly used algorithm was designed by Lax. The trick is to use replace the values of  $A_n$  in the temporal derivative by the mean of  $A_{n-1}$  and  $A_{n+1}$  :

$$A_n^t = \frac{1}{2} (A_{n-1}^t + A_{n+1}^t) \quad (2.126)$$

And the new discretization writes (compare eq 2.125) :

$$A_n^{t+1} = \frac{1}{2} (A_{n-1}^t + A_{n+1}^t) + c\Delta t \frac{A_{n-1}^t - A_{n+1}^t}{2\delta x} \quad (2.127)$$

Injection 2.118 into 2.127 yields :

$$\zeta(k) = \cos(k\Delta x) - i \frac{c\Delta t}{\Delta x} \sin(k\Delta x) \quad (2.128)$$

And the stability condition is :

$$\frac{c\Delta t}{\Delta x} < 1 \quad (2.129)$$

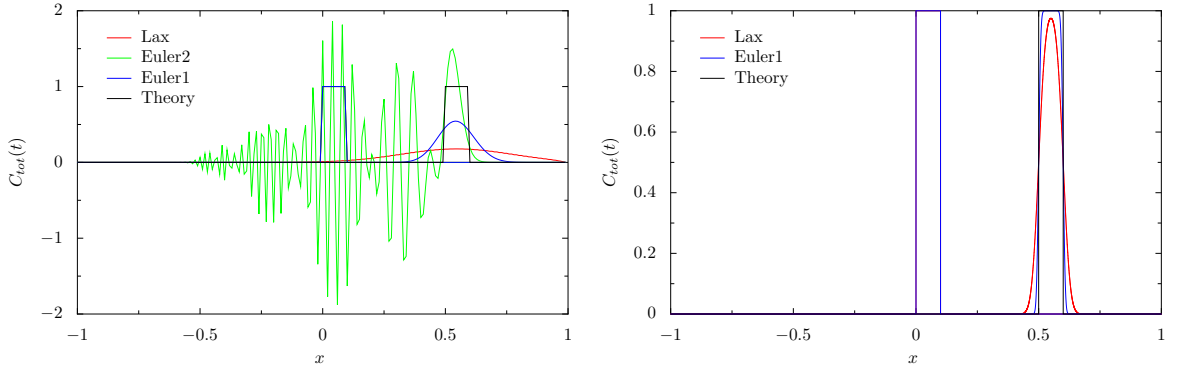


**Figure 2.9:** Comparison of the results of the Euler algorithm, symmetric (2) and asymmetric (1), the Lax algorithm, and the exact solution. Solutions are shown for  $\Delta x = 10^{-2}$  (left) and  $\Delta x = 10^{-4}$  (right). In both cases  $\Delta x = 10v\Delta t$  and  $v = 1$ . The solution found with a moving frame algorithm may not be distinguished from the exact solution in this case.

Which is also called the Courant condition. The issue with the Lax algorithm is that it actually is a Euler algorithm to which was added a diffusion coefficient. Indeed, it may straightforwardly be written :

$$A_n^{t+1} = A_n^t - c\Delta t \frac{A_{n+1}^t - A_{n-1}^t}{2\Delta x} + \frac{1}{2} (A_{n+1}^t + A_{n-1}^t - 2A_n^t) \quad (2.130)$$

Therefore, the effective diffusion coefficient introduced by Lax is :

$$D_{Lax} = \frac{\Delta x^2}{2\Delta t} \quad (2.131)$$

This diffusion makes it stable, but computationally heavier : to minimize the effect of diffusion, one has to minimise  $\Delta x$  while keeping the Courant condition (eq 2.129) satisfied, and hence the time step decreases, and the number of computational steps increases like  $1/\Delta x^2$ .

Similarly, the asymmetric Euler ("counter-wind") algorithm has an effective diffusion coefficient, since the algorithm may also be written :

$$A_n^{t+1} = A_n^t - c\Delta t \frac{A_{n+1}^t - A_{n-1}^t}{2\Delta x} + \frac{c\Delta t}{2\Delta x} (A_{n+1}^t + A_{n-1}^t - 2A_n^t) \quad (2.132)$$

Therefore, the effective diffusion coefficient is :

$$D_{E1} = \frac{1}{2}v\Delta x \quad (2.133)$$

As demonstrated in section 2.1, we clearly show this diffusion contribution in the model of transport by vesiculation in the Golgi apparatus, but it is not a desirable effect in a numerical resolution. Its effect is show in figure 2.9.

Eventually, let us note that one does not have to explicitly implement a constant convection when working in a moving frame. If so, the localization of the boundaries has to be changed with time, but the numerical solution can be as good as the solution of pure diffusion. However, this solution is easy to implement only for constant velocities throughout the system.

As a conclusion, fig 2.9 shows a comparison between the results of the different algorithms. It is possible to decrease arbitrarily the contribution of the effective diffusion added by the Lax or counter-wind algorithms by making  $\Delta x$  arbitrarily small (and decreasing  $\Delta t$  enough to satisfy Courant's condition). However, if  $\Delta x$  is fixed (in this chapter, it is the size of a cisterna in the Golgi apparatus), this is not possible and effective diffusion might be large.

## Chapter 3

# Maintenance of identity in cellular compartments

### Introduction

In the previous chapter, we did not consider the influence of transported molecules on membrane properties, and therefore any feedback was discarded. But any transported molecules will alter its environment. For instance the addition of transmembrane proteins in a membrane will change the identity (i.e. characteristic chemical composition) of this membrane, and thus will change the way this membrane senses its environment and how the membrane is felt by the environment.

Let us consider the case of SNARE proteins : they are pairs of complementary transmembrane proteins that act as specific anchors [79]. For instance, having one kind of SNARE proteins on a vesicle and the complementary kind on the plasma membrane will favor the fusion of the vesicle with the plasma membrane. This process is schematized in figure 3.1. During this fusion, the lipids and transmembrane proteins of the vesicle will be integrated in the plasma membrane, thus altering its identity by adding new anchors which will change the ability of the membrane to merge with vesicles. This provides a feedback between transport and membrane properties.

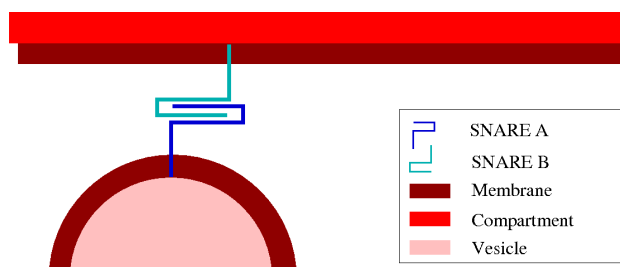


**Figure 3.1:** Cartoon of the role of SNARE proteins in cells. SNARE A and SNARE B are complementary and facilitate recognition and fusion of the vesicle with a compartment.

In this chapter, we will be particularly interested in the secretion pathway, and more

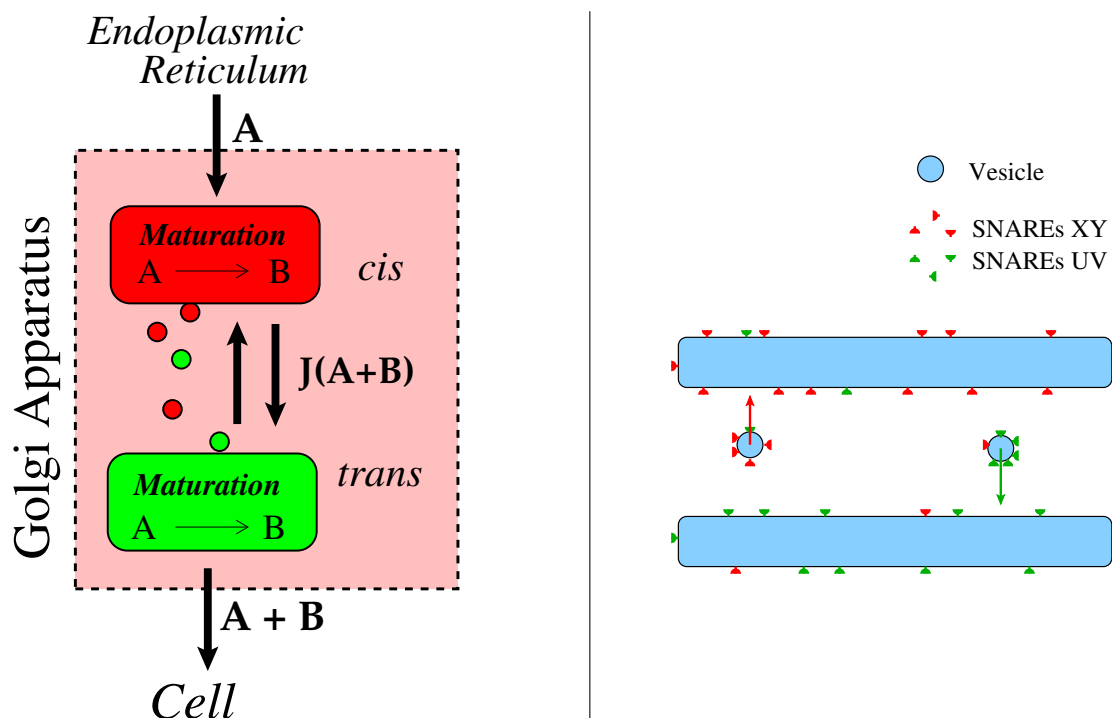


**Figure 3.2:** LEFT : Cartoon of the physiology of the Golgi apparatus. Molecules enter at the cis face of the Golgi apparatus, are exchanged between the cis Golgi and the trans Golgi, and exported from the trans Golgi. In the cis and trans Golgi, they can be chemically altered in a process called maturation. RIGHT : an illustration of cooperativity. Because of molecular recognition between the vesicles and the compartments, vesicles will more likely merge with compartments with similar chemical compositions. XY and UV are non-interacting pair of snares.

so in the Golgi apparatus. As we mentioned in the previous chapter, the G.A. intakes immature proteins and lipids and exports them [80], after processing them to their mature state. Famous examples of this maturation are the ceramids, converted to sphingolipids in the cis-Golgi, and VSV protein G, the sugars of which are gradually remove during its transit in the Golgi apparatus. A very simplified illustration of the Golgi physiology is shown in figure 3.2.

Let us consider the transport between compartments in this secretion pathway. While they constantly exchange molecules [81], they keep their own identity (namely, their chemical composition) unchanged [60]. In a system where fluxes are linearly related to concentration differences (*i.e.* satisfying Fickian diffusion), stationary concentration gradients can only be maintained by external fluxes. Fluctuations of the fluxes yield fluctuations of the local composition, and robust compartment identity (namely the existence of stationary concentration heterogeneities) is not to be expected. There must therefore exist some mechanism preventing the cell to become homogeneous, as would happen if the molecules were freely diffusing in the cell. The SNARE proteins we mentioned are one way [82] for the membrane composition to influence transport, because they enable a molecular recognition between the organelles and the vesicles, as illustrated in figure 3.2. There are many existing pairs of SNAREs, and because they influence transport, they are an essential component of organelle identity, and fluorescently tagged SNAREs are used experimentally to identify organelles and to make a distinction between cis and trans Golgi [83]. We will call

---

*cooperativity* the ability for transporters (for instance vesicles) and recipients (compartments such as the cis and trans region of the Golgi) to recognize each other. Of course, identity is not limited to SNAREs, and results from a complex interplay of networks of molecules. For instance, Rab GTPases [36] are important markers of membrane identity, and, interestingly, they are also involved in transport processes as they can recruit motors and tethering factors [84].

Recently, there has been an effort [85, 86, 87] to build models of vesicular transport including cooperative effects. In those models, the fusion rate of a vesicle with a compartment is controlled by the SNARE composition of the vesicle with respect to the SNARE composition of the target compartment. This specific vesicle fusion has been shown to enable the emergence of different identities in the different compartments (i.e. those compartments ended with different stationary SNARE compositions), because specificity introduced nonlinearities in the transport. However, this did not give a general understanding of the analytical requirements on transport for heterogeneous identities to be maintained, and neither did the existing work address the functional consequences of such non-linear transport. Indeed, as illustrated in figure 3.2, the Golgi apparatus is a dynamical organelle and we have to study if the requirements on transport to maintain compartment identity are compatible with biological activity.

In this chapter, we attempted to describe as generally as possible the conditions under which compartments exchanging material may maintain different identities. We find that the relation between the transport properties and membrane composition must be non-linear and have specific features. Based on this approach, we can study the consequences of the mechanisms of identity maintenance on the transport properties of organelles, and discuss their influence on the biological function of organelles.

We discuss below both the case of a closed system, and the case of an open system with incoming and outgoing fluxes. By including chemical transformation of the transported species, we show that cooperative transport can strongly increase the accuracy of a system responsible for protein maturation and sorting.

### 3.1 Stationary compartment differentiation in a closed system

We first consider a single protein species distributed between two compartments constantly exchanging material, and we later indicate how these results might be extended to a multicomponent system.

#### 3.1.1 One species system

We assume below that the total mass of the system (and the mass of each compartment) is maintained constant by an unspecified regulatory mechanism, so that the evolution of the concentration  $C_1$  in compartment 1 can generically be described by the Master equation [88] :

$$\partial_t C_1 = I_1 - J_{1 \rightarrow 2} + J_{2 \rightarrow 1} \quad (3.1)$$

with a similar expression for compartment 2 obtained by the transformation  $1 \leftrightarrow 2$ .

Here,  $J_{1 \rightarrow 2}(C_1, C_2)$  is the mean flux from compartment 1 to compartment 2 (with concentrations  $C_1$  and  $C_2$ , respectively), and  $J_{2 \rightarrow 1}(C_2, C_1)$  is the mean flux from the second compartment to the first. Compartments will naturally reach different concentrations if they follow different exchange rules. We focus on the more interesting case where  $J_{1 \rightarrow 2}(C, \bar{C}) = J_{2 \rightarrow 1}(C, \bar{C})$ , i.e. there is no structural difference between the two compartments. The source and sink term  $I_1$  in Eq. 3.1 may include both external fluxes in and out of compartment 1 and chemical transformation within this compartment.

The transport of cargo between organelles may be separated into three distinct steps; *step 1* : cargo packaging inside a membrane-based carrier, such as a small protein-coated vesicle or a membrane tubule [89], *step 2* : the actual transport between secreting and receiving compartments, often involving molecular motors moving along cytoskeletal filaments [90, 91], and *step 3* : fusion of the carrier with the receiving organelle (see [92] for a review). Each of these steps may permit molecular recognition and sorting ; through specific interaction with coat proteins at the vesicle membrane [89], with molecular motors [93, 94], or with highly specific fusion proteins such as the SNAREs [82]. For *step 1*, we call  $J_s$  the total flux of material secreted by a compartment, and  $S$  the fraction of this flux (a number between 0 and 1) occupied by the species of interest. We first assume *step 2* to be infinitely fast, and show below that a model with finite transport time can be mapped to the present model. Therefore any vesicle secreted by compartment 1 immediately merges (*step 3*) either with compartment 2, with a probability  $P_{1 \rightarrow 2}$ , or back with compartment 1 (with probability  $P_{1 \rightarrow 1} = 1 - P_{1 \rightarrow 2}$ ). The mean flux from compartment 1 to compartment 2 may thus be written :

$$J_{1 \rightarrow 2}(C_1, C_2) = J_s(C_1)S(C_1)P_{1 \rightarrow 2}(C_1, C_2) \quad (3.2)$$

For a closed system with fixed concentration  $C_{\text{tot}} = C_1 + C_2$  (no source and sink term), the symmetric state :  $C_1 = C_2 = C_{\text{tot}}/2$  is a trivial stationary solution ( $\partial_t C_1 = \partial_t C_2 = 0$ ). Linear stability analysis [88] shows that the symmetric solution is *unstable* provided

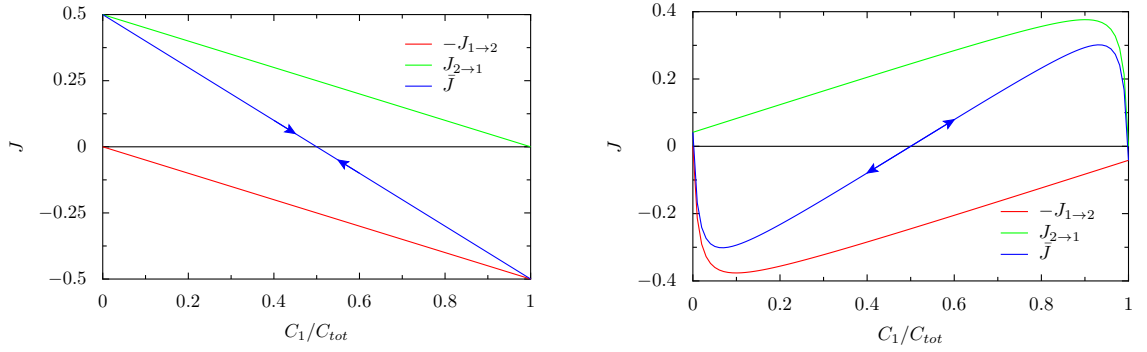


**Figure 3.3:** LEFT : Fluxes between compartments in a closed system with linear transport (such as diffusion), as a function of  $C_1/C_{tot}$ , the proportion of molecules in the first compartment.  $J_{1 \rightarrow 2}$  is the flux from the first to the second compartment,  $J_{2 \rightarrow 1}$  is the flux from the second to the first compartment, and  $\bar{J}$  is the net flux to the first compartment. The sign of  $\partial_{C_1} \bar{J}(C_1 = \frac{1}{2} C_{tot})$  shows that any perturbation from the symmetric state ( $C_1 = \frac{1}{2} C_{tot}$ ) will be unstable and the system will go back to the symmetric state. RIGHT : Fluxes between compartments in a closed system with our model of cooperative transport (equations 3.2 to 3.4) for  $C_s = 10^{-2} C_{tot}$  and  $C_f = \frac{1}{2} C_{tot}$ . The sign of the net flux  $\bar{J}$  shows that any perturbation from the symmetric state will lead the system to an asymmetric state.

$(\partial_{C_1} J_{1 \rightarrow 2})_{C_1=C_2=C_{tot}/2} < 0$ , as illustrated in 3.3. The case of particles randomly entering transport vesicles which are secreted at constant rate and fuse non-specifically with either compartment corresponds to a linear flux ( $J_{1 \rightarrow 2} \propto C_1$ ) (akin to passive diffusion) and leads to identical compartments. Spontaneous compartment differentiation can only occur if the flux reaching the second compartment *decreases* with increasing concentration in the first one, and this requires non-linear transport (i.e. cooperativity).

Let us assume the fluxes to have two rather universal types of non-linearity as a function of concentration. Firstly, the out-going flux of a given species should saturate at high species concentrations. This can be due to the limited capacity of transport vesicles, the limited availability of vesicle-coating proteins, or the formation of aggregates inapt for transport in a compartment beyond a critical concentration. For simplicity, we choose to keep the flux of secreted vesicles constant (and write it  $J_s \equiv K_0 C_s$ ), although direct interactions between cargoes and coat proteins are known to exist [89]. The packaging fraction  $S$  is assumed to saturate beyond a concentration  $C_s$  following a Michaelis-Menten saturation [95] :

$$S(C_1) = \frac{C_1}{C_1 + C_s} \quad (3.3)$$

Secondly, vesicle fusion is known to be strongly regulated by specific molecular interactions, including, but not restricted to, interactions between matching pairs of SNAREs[82]. Quantitative models have shown the importance of this step for the generation and maintenance of non-identical compartments, using fairly detailed mathematical modeling of the different pairs of SNAREs [85, 86] and/or extensive numerical simulations [87]. Numerous factors can however influence the delivery of transport vesicles, including specific interactions between the cargo and molecular motors [94]. Here, we adopt a very generic treatment of specific fusion, where the fusion probability  $P_{1 \rightarrow 2}$  deviates from its nonspecific value because of two-body interactions between constituents of the vesicle and the

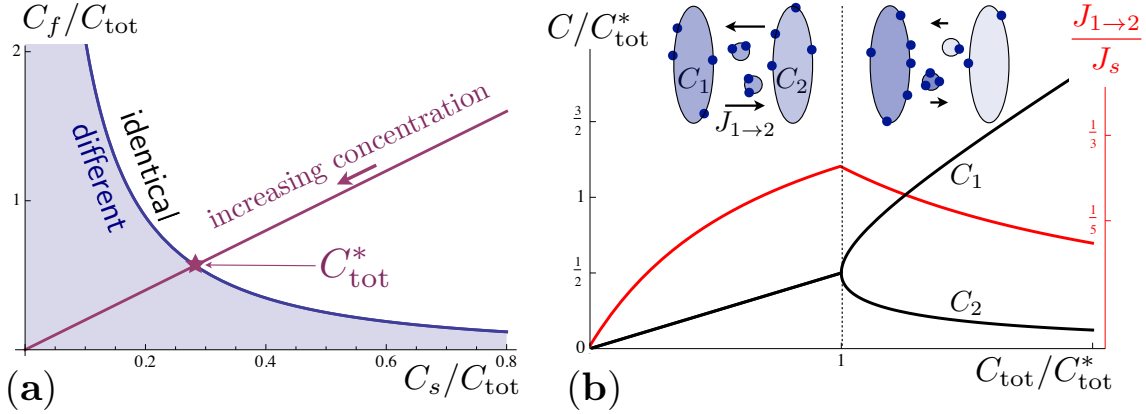


**Figure 3.4:** (a) Location of the critical region in the parameter space  $\{C_s/C_{\text{tot}}, C_f/C_{\text{tot}}\}$  where stationary compartment differentiation occurs in a closed system (shaded blue, Eq.3.5). Increasing the total concentration  $C_{\text{tot}}$  moves the system along the red line (arrow). (b) : Variation of the stationary compositions (black) and flux (red) with the total concentration, showing the breaking of symmetry for  $C_{\text{tot}} > C_{\text{tot}}^*$  (Eq.3.5).

receiving compartment :  $P_{1 \rightarrow 2} - 1/2 \sim S(C_1)C_2$ . After normalization, the probability may be written :

$$P_{1 \rightarrow 2} = \frac{C_f + S(C_1)C_2}{2C_f + S(C_1)(C_1 + C_2)} \quad (3.4)$$

where  $C_f$  is the typical concentration beyond which specific fusion becomes relevant. Within the description outlined in Eqs.(3.3,3.4), linear transport corresponds to both characteristic concentrations being very large :  $C_s, C_f \gg C_{\text{tot}}$ .

Spontaneous symmetry breaking (enrichment of one compartment at the expense of the other) occurs when  $(\partial_{C_1} J_{1 \rightarrow 2})_{C_{\text{tot}}/2} < 0$ . As shown in Fig.3.4a, this always happens at high enough concentration  $C_{\text{tot}} > C_{\text{tot}}^*$ , with

$$C_{\text{tot}}^*{}^3 = 4C_s C_f (C_s + C_{\text{tot}}^*) \quad (3.5)$$

Beyond this threshold, any small perturbation from the symmetric state brings the compartments into a stable asymmetric steady-state. As a consequence, the concentration of the least concentrated compartment (compartment 2, say) and the flux  $J_{1 \rightarrow 2}$  of material exchanged between compartments both decrease with increasing concentration when  $C_{\text{tot}} > C_{\text{tot}}^*$ , as shown in Fig.3.4b. At high concentration, the asymptotic solution reads  $C_2 \sim 2C_f C_s / C_{\text{tot}}$ .

Although the actual location of the critical line defined by Eq.3.5 depends on the model (Eqs.(3.3,3.4)) for the exchange flux  $J_{1 \rightarrow 2}$  (Eq.3.2), its existence does not. This critical behaviour is very general and stems from the presence of two competing effects : cooperative fusion promotes protein enrichment (and increases with decreasing  $C_f$ ), while saturation of protein packaging (beyond a composition  $C_s$ ) limits transport. Including the presence of different types of coat and fusion proteins does not fundamentally alter this picture [85].

### 3.1.2 Extension to a n-species system

Extending the analysis presented above to a  $n$ -component system is rather straightforward. Let us call  $C_\alpha^i$  the concentration of the species  $i$  in the compartment  $\alpha$  ( $\alpha = 1, 2$ ). The concentration of all species in compartment  $\alpha$  can be defined as a vector  $\mathbf{C}_\alpha = [C_\alpha^1, C_\alpha^2, \dots, C_\alpha^n]$ , and satisfies the Master equation :

$$\partial_t C_\alpha^i = I_\alpha^i - J_{\alpha \rightarrow \beta}^i + J_{\beta \rightarrow \alpha}^i \quad (3.6)$$

where  $J_{\alpha \rightarrow \beta}^i$  is the mean flux of the species  $i$  from the compartment  $\alpha$  to the compartment  $\beta$ , and  $I_\alpha^i$  is a net source and sink term including both the presence of external fluxes of species  $i$  in and out of compartment  $\alpha$ , and chemical transformation involving species  $i$  in compartment  $\alpha$ .

For a closed system (no source and sink term), the total concentration for the  $i$ -th specie is fixed :  $C_{tot}^i = C_\alpha^i + C_\beta^i$ . All the equations may thus be written for the fractions  $\phi_\alpha^i = C_\alpha^i / C_{tot}^i$ , satisfying  $\phi_1^i + \phi_2^i = 1$ . Then  $\phi_2 = \mathbf{1} - \phi_1$  becomes implicit and the master equation is now written only as a function of  $\phi \equiv \phi_1$  :

$$\partial_t \phi^i = -j_{1 \rightarrow 2}^i(\phi, \mathbf{1} - \phi) + j_{2 \rightarrow 1}^i(\mathbf{1} - \phi, \phi) \quad (3.7)$$

with the normalized fluxes  $j_{\alpha \rightarrow \beta}^i = J_{\alpha \rightarrow \beta}^i / C_{tot}^i$ . Assuming as before that both compartments follow identical exchange rules,  $\phi_{1/2} = 1 - \phi_{1/2} = [\frac{1}{2}, \frac{1}{2}, \dots, \frac{1}{2}]$  is a stationary solution. The linear stability of the symmetric solution is determined by the Jacobian matrix  $\mathbf{M}$  :

$$M_{i,k} = -2 \left( \partial_{\phi^i} j_{1 \rightarrow 2}^k \right)_{\phi_{1/2}} \quad (3.8)$$

The symmetric state is *unstable*, and spontaneously evolves towards a non-symmetric state if  $\mathbf{M}$  has at least one positive eigenvalue.

In a multi-component system, the fluxes can be written similarly to the main text :

$$J_{\alpha \rightarrow \beta}^i = J_\alpha(\mathbf{C}_\alpha) S_\alpha^i(\mathbf{C}_\alpha) P_{\alpha \rightarrow \beta}(\mathbf{C}_\alpha, \mathbf{C}_\beta) \quad (3.9)$$

The functions  $J_\alpha$ ,  $S_\alpha^i$  and  $P_{\alpha \rightarrow \beta}$  may contain various non-linearities. In particular  $P_{\alpha \rightarrow \beta}$  may involve any combination of pair interactions  $\{S_\alpha^i, C_\beta^j\}$  which can lead to a very rich behaviour. One could in particular describe in this way the transport of proteins directly interacting with the secretion (coat proteins) or the fusion (SNAREs) machinery, themselves directly involved in transport.

### 3.1.3 Application : two species and a free energy

To model complex phenomena with two or more species, we may either build the transport laws from assumption, or derive rates from a free energy. Though the knowledge of such a free energy is not necessarily within our grasp, we show here an example of such a derivation. If we know the energy potential as a function of  $\phi_A$  and  $\phi_B$ , then we can write a set of exchange rates using detailed balance. These rates might not correspond to the biological rates as detailed balance need not be satisfied. However, if we assume the

stationary states to derive from the free energy, then detailed balance will lead to the correct stationary states. It is quite intuitive to build an energy landscape that can show three kind of behaviour : homogenous, phase separation with  $A$  and  $B$  together, or phase separation with separate  $A$  and  $B$ .

One simple form we can take for the free energy of a cisternae is :

$$f(\phi_A, \phi_B) = \alpha (\phi_A^2 + \beta\phi_B^2 + \gamma\phi_A\phi_B) + \phi_A \log \phi_A + \phi_B \log \phi_B \quad (3.10)$$

In which  $\alpha$  and  $\alpha\beta$  describe the interaction of  $A$  with itself and  $B$  with itself respectively : if  $\alpha < 0$ , proteins  $A$  will tend to regroup in the same cisterna, and otherwise proteins  $A$  will tend to spend in as many cisternae as possible.  $\alpha\gamma$  describes the interaction of  $A$  with  $B$ , and a negative value corresponds to an attractive interaction, whereas a positive value leads to a repulsion, and the tendency for  $A$  and  $B$  to segregate in different cisternae. The log terms correspond to the entropy as was mentioned earlier. Examples of similar forms of the energy may be found in [23, 25], and later in chapter 4.

Here,  $f$  is normalized by the activation energy in the system. If  $f$  is normalized by  $k_B T$  (thermally activated system),  $\alpha$  is inversely proportional to the temperature. If there are only two cisternae, the free energy of the first is  $f(\phi_A, \phi_B)$  and the free energy of the second is  $f(1 - \phi_A, 1 - \phi_B)$ , and the state of the whole system can be described merely by the concentrations of  $A$  and  $B$  in the first cisternae. We call  $f_{tot}$  the total energy of the system defined by :

$$f_{tot}(\phi_A, \phi_B) = f(\phi_A, \phi_B) + f(1 - \phi_A, 1 - \phi_B) \quad (3.11)$$

It is shown in the appendix that, as long as we do not consider the fluctuations (if we stay in the mean-field approximation), we can in some case map laws of transport to an energy landscape. The other way round, we can deduce the fluxes from the energy (once again, the fluctuations will not be correctly described), if we assume detailed balance to be satisfied. This is valid if the active ATP-dependent processes activate the events of fission and fusion but do not change the stationary states of the system.

Let us write the rates of exchange, assuming  $A$  and  $B$  to be transported separately.  $W(\phi_A \rightarrow \phi_A + \delta_A, \phi_B)$  is the rate at which an infinitesimal load  $\delta A$  is received by the first compartment from the second. Detailed balance imposes :

$$W(\phi_A \rightarrow \phi_A + \delta_A, \phi_B)P(\phi_A, \phi_B) = W(\phi_A + \delta_A \rightarrow \phi_A, \phi_B)P(\phi_A + \delta_A, \phi_B) \quad (3.12)$$

$$P(\phi_A, \phi_B) = \frac{1}{Z} e^{-f_{tot}(\phi_A, \phi_B)} \quad (3.13)$$

Assuming  $\delta_A$ , the variation of the concentration of a cisterna after fusion or fission of a vesicle, to be small, we can expand the energy around  $\phi_A$  and  $1 - \phi_A$ , and we find :

$$\frac{W(\phi_A \rightarrow \phi_A + \delta_A, \phi_B)}{W(\phi_A + \delta_A \rightarrow \phi_A, \phi_B)} = \exp \left( -\delta_A \frac{\partial f}{\partial \phi_A} \Big|_{\phi_A, \phi_B} - \delta_A \frac{\partial f}{\partial \phi_A} \Big|_{1-\phi_A, 1-\phi_B} \right) \quad (3.14)$$

This is a general result of detailed balance, and gives the ratio of the rates but not the rates themselves. Let us then define a transport rate  $k_0$ , such as :

$$W(\phi_A \rightarrow \phi_A + \delta_A, \phi_B) = k_0 \exp \left( -\delta_A \frac{\partial f}{\partial \phi_A} \Big|_{1-\phi_A, 1-\phi_B} \right) \quad (3.15)$$

$$W(\phi_A + \delta_A \rightarrow \phi_A, \phi_B) = k_0 \exp \left( \delta_A \frac{\partial f}{\partial \phi_A} \Big|_{\phi_A, \phi_B} \right) \quad (3.16)$$

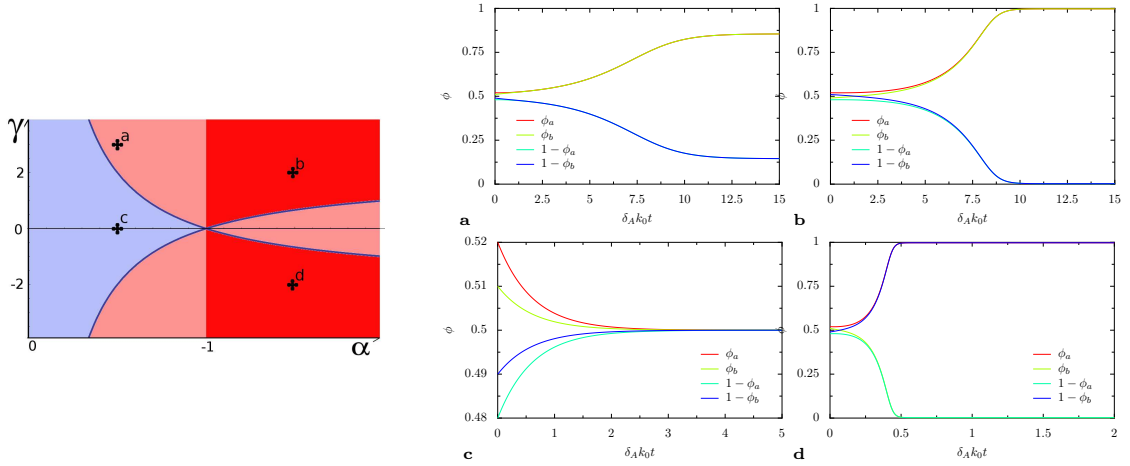


**Figure 3.5:** Left : Partial phase diagram for an exchange model with rates given by detailed balance, with  $f(\phi_A, \phi_B) = \alpha(\phi_A^2 + \phi_B^2 + \gamma\phi_A\phi_B) + \phi_A \log \phi_A + \phi_B \log \phi_B$  as a free energy per cisterna. Light blue corresponds a stable symmetric solution, red is completely unstable and light red corresponds to the symmetric state being a saddle point. Right : density of A and B proteins in both compartments as a function of time for four points on the phase diagram. **a** : ( $\alpha = 0.5, \gamma = 3$ ), and **b** : ( $\alpha = 1.5, \gamma = 2$ ) : A and B are mainly in the same compartment. **c** : ( $\alpha = 0.5, \gamma = 0$ ) : A and B are evenly distributed in the two compartments. **d** : ( $\alpha = 1.5, \gamma = -2$ ) : A accumulates in the first compartment whereas B is mainly in the second compartment.

And therefore :

$$W(\phi_A + \delta_A \rightarrow \phi_A, \phi_B) = k_0 (\phi_A \exp[+1 + \alpha(2\phi_A + \gamma\phi_B)])^{\delta_A} \quad (3.17)$$

$$W(\phi_A, \phi_B + \delta_B \rightarrow \phi_B) = k_0 (\phi_B \exp[+1 + \alpha(2\phi_B + \gamma\phi_A)])^{\delta_B} \quad (3.18)$$

For simplicity, we will later assume  $\beta = 1$  (i.e. we assume the energy to be symmetric with  $A \leftrightarrow B$ ), and  $\delta_A = \delta_B$ . To go further, we need to recall that  $\delta_A$  is small and therefore  $\partial f / \partial \phi_A(\phi_A + \delta_A) \approx \partial f / \partial \phi_A(\phi_A)$ . Finally we renormalize the times by  $1/k_0\delta_A$ , and we can write the fluxes as a function of the rates :

$$J_{1 \rightarrow 2}^A(1 - \phi_A, \phi_B) = W(\phi_A \rightarrow \phi_A - \delta_A, \phi_B) \approx W(\phi_A + \delta_A \rightarrow \phi_A, \phi_B) \quad (3.19)$$

$$J_{1 \rightarrow 2}^B(\phi_A, 1 - \phi_B) = W(\phi_A, \phi_B \rightarrow \phi_B - \delta_B) \approx W(\phi_A, \phi_B + \delta_B \rightarrow \phi_B) \quad (3.20)$$

As we can see from equation 3.16,  $\delta_A$  changes the magnitude of the fluxes but not the stationary states. Since we are interested in the stationary properties of the system, we can enter  $\delta_A$  into the normalization of the energies as we discuss in the appendix 3.5.1. There are now two parameters  $\alpha$  and  $\gamma$ , that can be negative or positive, and their values lead to all possible behaviors for the stable solution.

We can now use the result from section 3.1.2 to study the stability of the symmetric solution. We find that the stationary solution is stable if and only if :

$$\alpha \geq -1 \quad (3.21)$$

$$\gamma^2 \leq 4 \left( \frac{1 + \alpha}{\alpha} \right)^2 \quad (3.22)$$

The symmetric solution can be stable when the log term dominates ( $\|\alpha\| \leq 1$ ) and will be stable if  $\alpha > 0$  ( $A$  molecules, as well as  $B$  molecules, self-repel). Otherwise,  $A$  molecules will tend to accumulate in one compartment, and  $B$  molecules will accumulate either with  $A$  (especially if  $\gamma > 0$ ) or in the other compartment (especially if  $\gamma < 0$ ). The analysis of the symmetric solution enables us to know whether it is stable (see figure 3.5), but does not give more information on final steady state than its symmetry.

Therefore, using the linear analysis of the symmetric state does not yield as much information as minimizing the free energy. If the free energy is known, linear analysis should therefore be employed only if  $f_{tot}$  cannot be minimized. The inverse procedure, mapping a set of laws of transport to a free energy, seems therefore much more promising. We give an example of a such procedure in appendix 3.5.1. Unfortunately, writing a suitable free energy becomes rapidly more complicated and can be non-analytic, especially for many-species system. Moreover, the normalization of the energy is not straightforward (as already glimpsed in this section, in which the energies are normalized by  $\delta_A$ ). The issues of fluctuations, linked to the normalization of the energy, cannot be addressed in a mean-field formulation, and in the next section, we deviate from the mean-field formulation.

### 3.1.4 Influence of a finite vesicle fusion time

If vesicular transport between secreting and receiving compartment (the so-called *step 2* in 3.1.1) is not infinitely fast, vesicles will dwell for some time in the inter-compartment region, and will have a non-uniform distribution of concentration, reflecting the concentration of the emitting compartment at the time of their secretion. While this situation appears much more complex than the one described in section 3.1, we show below, restricting ourselves to a one-species system for simplicity, how a model with inter-compartment dwelling of vesicles can be mapped to the simpler model with immediate fusion of vesicles.

Each vesicle can carry a given amount of proteins, and a vesicle budding from or merging with a compartment will change the concentration of this compartment. Let us call  $C_v$  the resulting change of concentration in the compartment, which can be seen as the load carried by a vesicle. Allowing vesicles to dwell between compartments for a finite time causes the total number of molecules in the compartments to decrease, and hence yields an effective total concentration  $C_{\text{eff}} = C_1 + C_2$  lower than the actual total concentration in the system  $C_{tot}$  :

$$C_{\text{eff}} = C_{tot} - \sum_{i=1}^{N_v} C_v^i \quad (3.23)$$

where  $N_v$  is the number of vesicles between compartments, and  $C_v^i$  the concentration carried by the  $i$ -th vesicle. This sum over all the vesicles is actually a random variable, but its mean can be computed analytically in certain cases. For instance, in the case of a symmetric system, we expect the mean value of  $C_v$  to be computed easily, and therefore we should be able to compute  $C_{\text{eff}}$  in a symmetric system. This will be valid as long as the system is symmetric, and therefore valid until  $C_{\text{eff}} = C_{tot}^*$ , the critical value at which the symmetry is broken. Therefore, we have a chance to know where the symmetric/asymmetric transition occurs.

If the system is symmetric, all vesicles have the same average concentration  $\bar{C}_v$  and :

$$\sum_{i=1}^{N_v} C_v^i \approx N_v \bar{C}_v \quad (3.24)$$

Let us assume that each vesicle in the inter-compartment medium has a rate of fusion  $W_r$  towards any of the compartments. The average number of vesicles in the media is then  $2K_v/W_r$  (where  $K_v$  is the rate of individual vesicle secretion). Moreover, the average vesicle concentration  $\bar{C}_v$  can be written as the maximal concentration  $C_v^{max}$  a vesicle may carry, times the average vesicle saturation fraction  $\bar{S}$  (obtained from Eq.3.3), leading to :

$$C_{\text{eff}} = C_{\text{tot}} - 2 \frac{K_v}{W_r} C_v^{max} \bar{S} \quad (3.25)$$

Finally, the product  $K_v C_v^{max}$  is the number of vesicle leaving a compartment per unit time multiplied by the maximum concentration of each vesicle, and can be identified with  $J_s \equiv K_0 C_s$ . The critical point of a system of total concentration  $C_{\text{tot}}$  with vesicles staying a finite time between the compartments can thus be obtained from the critical point (Eq.3.5) of a system with infinitely fast fusion, but with an effective total concentration  $C_{\text{eff}}^{\text{sym}}$  given by :

$$C_{\text{eff}}^{\text{sym}} = C_{\text{tot}} - 2C_s \frac{K_0}{W_r} \bar{S} \quad , \quad \bar{S} = \frac{C_{\text{eff}}^{\text{sym}}}{C_{\text{eff}}^{\text{sym}} + 2C_s} \quad (3.26)$$

Namely,

$$\frac{C_{\text{eff}}^{\text{sym}}}{C_{\text{tot}}} = \frac{1}{2} - \frac{1+w_r}{w_r} \phi_s + \sqrt{2\phi_s + \left(\frac{1}{2} - \phi_s \frac{1+w_r}{w_r}\right)^2} \quad (3.27)$$

With  $\phi_s = C_s/C_{\text{tot}}$ ,  $w_r = W_r/K_0$ . For a given set  $(\phi_s, w_r)$ , we can therefore know the localization of the symmetric/asymmetric transition, which takes place for  $C_{\text{eff}} = C_{\text{tot}}^*$ . We might also be interested in knowing the concentration in each compartments in the asymmetric state.

To do so, one can compute the effective concentration in a fully asymmetric system, in which one compartment has a concentration  $C_{\text{eff}}^{\text{asym}}$  and the other has a concentration close to zero :

$$C_{\text{eff}}^{\text{asym}} = C_{\text{tot}} - C_s \frac{K_0}{W_r} S' \quad \text{with} \quad S' = \frac{C_{\text{eff}}^{\text{asym}}}{C_{\text{eff}}^{\text{asym}} + C_s} \quad (3.28)$$

The difference between Eq.3.27 and Eq.3.28 being that in the latter case, the empty compartment is sending out empty vesicles, and only vesicles from the first compartment contribute to the depletion effect. We find :

$$C_{\text{eff}}^{\text{asym}}(\phi_s, w_r) = C_{\text{eff}}^{\text{sym}}\left(\frac{1}{2}\phi_s, w_r\right) \quad (3.29)$$

In the case vesicle fusion occurs with a finite rate, we cannot find the stationary solution analytically. We performed a numerical simulation of a system with finite vesicle fusion time and a total concentration  $C_{\text{tot}}$  and compared the location of the critical line with the infinitely fast fusion model, the equations of which we solved numerically. The numerical simulation consists of two compartments of concentrations  $C_1$  and  $C_2$  from which vesicles may bud with a rate  $K_v$ . Each vesicle budding from a compartment  $\alpha$  has a saturation

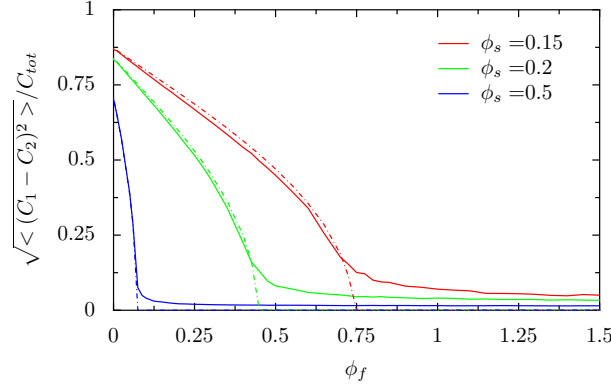


**Figure 3.6:** Root mean square (RMS) of the difference of concentration between the two compartments as a function of  $\phi_f = C_f/C_{tot}$  for various values of  $\phi_s = C_s/C_{tot}$ . Dash-dotted lines represent the mean-field values of the concentration (normalized by  $C_{eff}^{asym}/C_{tot}$  with effective parameters  $\phi_s^{eff} = C_s/C_{eff}^{sym}$  and  $\phi_f = C_f/C_{eff}^{sym}$ ). Solid lines represent the simulated results with vesicles in the inter-compartments medium, with a vesicle fusion rate  $W_r = K_0$ , i.e. up to 40% of the molecules are out of the compartments. The non-zero value of the RMS in the symmetric state is due to fluctuations.

$S(C_\alpha)$ . At each time step, each vesicle may merge with a compartment at a rate  $W_r$ , and the compartment is chosen according to the probability  $P$  described in the main text. The algorithm may be written as follows :

```
#Fusion probability of a vesicle of saturation Sv with the first compartment
def Pf1(Sv,C1,C2)=(Sv*C1+Cf)/( 2*Cf + Sv*(C1+C2) )
#Saturation of the vesicles leaving from a compartment of concentration C
def S(C) = C / (C+Cs)
```

```
#Sves[i] : Saturation of the i-th vesicle
#Nves : number of vesicles
```

```
while t<Tmax :
    t=t+dt
```

```
#Checks if a vesicle leaves the first compartment
if rand(1) < Kv*dt :
    Nves=Nves+1
    Sves[Nves]=S(C1)
    C1=C1 - Cv*Sves[Nves]
```

```
#Checks if a vesicle leaves the second compartment
if rand(1) < Kv*dt :
    Nves=Nves+1
    Sves[Nves]=S(C2)
    C2=C2 - Cv*Sves[Nves]
```

```
#Checks for each vesicle if it merges with a compartment
for i=1 to Nves :
    if rand(1) < Wr*dt :
        if rand(1) < Pf1(Sves[i],C1,C2) :
            C1=C1+Cv*Sves[i]
        else :
            C2=C2+Cv*Sves[i]
```

$$\text{reorder}(\text{Sves}, \text{Nves})$$
$$\text{Sves}[i]=0$$

Comparison with the solution of the infinitely fast fusion model are shown in Fig.3.6. Not only the location of the critical line, but also the actual values of the concentrations in each compartment in the asymmetric steady state, were found to agree very well, even for low vesicle fusion rate (i.e. a large amount of material outside the compartments). This justifies our infinitely fast transport, mean-field approach, as systems with fluctuations and with a finite transport time can be mapped to simpler systems, which we have analytical tools to study.

## 3.2 Compartment differentiation in an open system

The relative simplicity of the model presented in Sec.3.1.1, essentially characterized by two parameters ( $C_s/C_{\text{tot}}$  and  $C_f/C_{\text{tot}}$ , Fig.3.4.a), allows us to address issues of direct biological relevance, such as the presence of external fluxes of material, and the possibility for chemical transformations within the system. Organelles such as the Golgi apparatus are strongly polarized, with distinct entry and exit faces. We investigate the consequences of cooperative transport in such open systems, assuming that the species of interest enters the system through compartment 1, and exits through compartment 2, while exchange between the two compartments proceeds as described previously. Mathematically, this amounts to including a source term  $I_1 = J_{in}$  and a sink term  $I_2 = -J_{out}$  in Eq.3.1 yielding :

$$J \equiv J_{1 \rightarrow 2} - J_{2 \rightarrow 1} = J_{in} - \partial_t C_1 = \partial_t C_2 + K_{\text{off}} C_2 \quad (3.30)$$

where a simple linear relationship was assumed for the out-flux :  $J_{out} = K_{\text{off}} C_2$ , and where the exchange fluxes ( $J_{1 \rightarrow 2}$ ) are still given by Eqs.3.2,3.3,3.4. At steady state, all fluxes must be balanced, including the net flux  $J$  between the two compartments :  $J_{in} = J_{out} = J$ .

### 3.2.1 Qualitative analysis

The dynamical behaviour of the set of equations Eq.3.30 is discussed in some details in Sec.3.2.2, but a qualitative understanding of the open system may be inferred from the results obtained for a closed system. We showed (Fig.3.4b) that the flux  $J_{1 \rightarrow 2}$  cannot exceed a maximum value and decreases upon increasing total concentration beyond a threshold. In an open system, this behaviour may result in the absence of a steady state : if the influx into compartment 1 exceeds the maximum net flux from  $1 \rightarrow 2$ , the concentration  $C_1$  of the entry compartment steadily increases with time, leading to a further decrease of inter-compartment exchange. In the absence of other compensatory mechanisms,  $C_1$  would diverge and  $C_2$  would vanish, leading to a vanishing exit flux. This divergence is probably not realistic, but it illustrates the consequence of such non-linear transport for an open system : beyond a critical influx, the system is essentially blocked, filtering transit proteins at a very low flux. While a such feature has a negative impact on the rate of transport, it strongly increases the residency time of molecules and may prove advantageous to a system such as the Golgi apparatus, whose function is to process and chemically modify proteins.

### 3.2.2 Phase-space trajectories of an open system

We now discuss possible dynamical behaviours of an open systems satisfying the kinetic equation 3.30, where the fluxes between the two compartments are given by Eqs. 3.2,3.3,3.4. Although the exchange rules between the compartments are symmetric, the existence of external fluxes breaks the symmetry of the system, and different concentrations should be expected in the two compartments even for low incoming flux. The critical behaviour at high incoming flux, as depicted in Fig.3.4 for a closed system, has nevertheless a profound impact on the steady states, or the absence thereof.

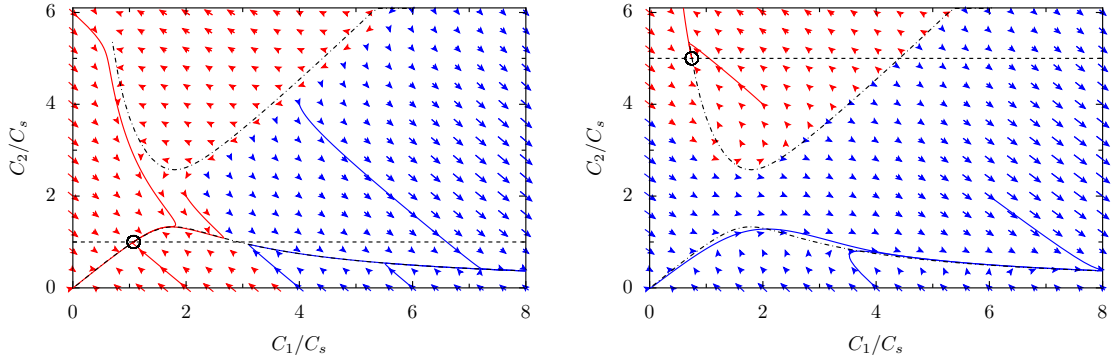


**Figure 3.7:** Phase-space trajectories of system with an exit flux  $J_{\text{out}} = K_{\text{off}}C_2$  ( $K_{\text{off}} = 0.005K_0$ ), and an input flux  $J_{\text{in}} = 0.005K_0C_s$  (left) and  $J_{\text{in}} = 0.025K_0C_s$  (right). Dash-dotted lines represent  $\dot{C}_2 = 0$  and dashed lines  $\dot{C}_{\text{tot}} = 0$ . Red arrows represent initial condition with convergent trajectories whereas blue arrows are for initial conditions yielding a divergence of  $C_1$ .

As discussed above, one expects the flux exchanged between the two compartments to present a maximum value  $J_{\text{max}}$  (necessarily smaller than the maximum possible flux  $K_0C_s$ , see Fig.3.4.b), theoretically leading to a diverging concentration in the first compartment and a vanishing exchange flux if  $J_{\text{in}} > J_{\text{max}}$ . Depending on initial conditions, a non-convergent behaviour might actually also appear for values of  $J_{\text{in}}$  a priori compatible with the existence of a steady-state. For instance, if the initial concentration is very high in the first compartment, the divergent regime may occur for smaller in-flux  $J_{\text{in}} < J_{\text{max}}$ . This can be understood by considering the phase space trajectories of the system.

The coordinates in phase space are the concentrations  $(C_1, C_2)$ , and the steady states (if any) are given by the intersections of the  $\dot{C}_2 = 0$  and  $\dot{C}_{\text{tot}} = 0$  curves. Since  $J_{\text{out}} = K_{\text{off}}C_2$ , the line  $\dot{C}_{\text{tot}} = 0$  is obviously the line  $C_2 = J_{\text{in}}/K_{\text{off}}$ , whereas the curve  $\dot{C}_2 = 0$  has to be computed numerically. If these two lines do not intersect, there is no steady state and  $C_1$  always diverges. If they do intersect, the thus-defined fixed points may be linearly unstable, or may be surrounded by a basin of attraction, as shown in Fig.3.7.

The phase space representation Fig.3.7 can be used to study the consequences of a transient change of the input flux (i.e. a pulse or a block of secretion). Let us consider a system which is in a stable steady state  $(C_1^1, C_2^1)$  for an input flux  $J_{\text{in}}^1$ . If the incoming flux is changed to  $J_{\text{in}}^2$  at time  $t_1$ , the phase space trajectories will be changed, and the system will follow a new trajectory starting from  $(C_1^1, C_2^1)$ . According to this new trajectory, the system will reach a new position  $(C_1^2, C_2^2)$  at a time  $t_2$ . If the flux is then switched back to its original value  $J_{\text{in}}^1$ ,  $(C_1^2, C_2^2)$  will not necessarily be in the attractive region of the stable steady state. Therefore, a transient change of the incoming flux may bring the system out of a stable steady state. In the case of a strong pulse ( $J_{\text{in}}^2 \gg J_{\text{in}}^1$ ) the system may follow a divergent trajectory and the concentration  $C_1$  will increase strongly with time. Formally, whatever the (finite) value of  $(C_1^2, C_2^2)$  after a pulse, the system may reach a stationary regime if the incoming flux  $J_{\text{in}}$  after the pulse is small enough. However, this may take a very long time. The approximation  $C_1 \rightarrow \infty, J_{\text{in}} = 0$  shows this time grows like  $(C_1^2)^2$ .

### 3.3 Consequence of cooperative transport for protein maturation

We now quantify the consequences of the kind of cooperative transport considered here on protein maturation and sorting. We investigate the situation sketched in Fig.3.8, where a molecular species  $A$  enters the system via compartment 1 and is transformed into a species  $B$  by maturation enzymes, before leaving the system via compartment 2. The processing accuracy is defined as the total fraction of the input that exits the system as mature ( $B$ ) molecules :

$$\text{Accuracy} \equiv \frac{1}{A_0} \int_0^\infty dt J_{out}^B \quad (3.31)$$

Where  $A_0 = \int_0^\infty J_{in} dt$  is the total amount of  $A$  molecules to have entered the system and  $J_{out}^B$  is the out-flux of  $B$  molecules. The accuracy thus defined reaches unity when no molecules exit the system without being processed ( $J_{out}^A = 0$ ). A Michaelis-Menten maturation kinetics is chosen in order to account for the limited amount of enzymes in the system. Calling  $A_1$  and  $B_1$  the concentrations of  $A$  and  $B$  in the first compartment, and  $R(A_1)$  the reaction rate in the first compartment, we have :

$$\partial_t B_1 = R(A_1)A_1 = R_0 C_m \frac{A_1}{A_1 + C_m} \quad (3.32)$$

with an identical kinetics in compartment 2. Here,  $R_0$  is the maximal maturation rate and  $C_m$  is the concentration of  $A$  beyond which enzymatic reaction saturates. For simplicity, we assume that the state ( $A$  or  $B$ ) of a molecule influences neither its transport between compartments nor its export from the system, so that Eq.3.30 is still valid for the concentrations  $C_{1,2} = A_{1,2} + B_{1,2}$ . Taking the weights of  $A$  and  $B$  in the fluxes to be their respective weights in the compartments :

$$J^A = \frac{A_1}{A_1 + B_1} J_{1 \rightarrow 2} - \frac{A_2}{A_2 + B_2} J_{2 \rightarrow 1} \quad (3.33a)$$

$$J^B = \frac{B_1}{A_1 + B_1} J_{1 \rightarrow 2} - \frac{B_2}{A_2 + B_2} J_{2 \rightarrow 1}, \quad (3.33b)$$

The following set of kinetic equations is obtained :

$$\dot{A}_1 = J_{in} - R(A_1)A_1 - J^A \quad (3.34a)$$

$$\dot{B}_1 = R(A_1)A_1 - J^B \quad (3.34b)$$

$$\dot{A}_2 = -R(A_2)A_2 + J^A - K_{off}A_2 \quad (3.34c)$$

$$\dot{B}_2 = R(A_2)A_2 + J^B - K_{off}B_2 \quad (3.34d)$$

Normalizing rates with the vesiculation rate  $K_0$  and concentrations with the concentration  $C_s$  at which secretion saturates, Eq.3.34 is controlled by 5 parameters. These are :  $r_0 = R_0/K_0$  and  $C_m/C_s$ , which compare the activity of the maturation enzymes and of the secretion machinery,  $C_f/C_s$ , which defines the threshold for dominant specific fusion (Eq.3.5), and  $k_{off} = K_{off}/K_0$ , which compares exit and exchange rates. The fifth parameter is the normalized amount of material going through the system :  $A_0/C_s$ . For simplicity,

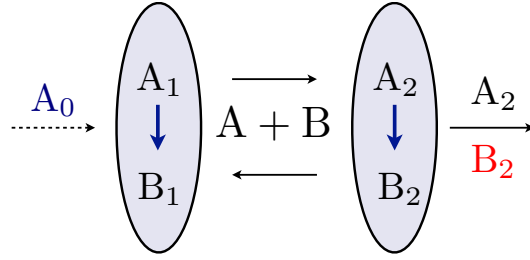


**Figure 3.8:** Sketch of an open system with protein maturation. Particle enter the system through compartment 1, undergo maturation  $A \rightarrow B$  while in the system, are exchange between compartment via cooperative transport, and exit the system via compartment 2.

we investigate a situation similar to the so-called *pulse-chase* procedure[54], where a fixed amount of material is delivered to the system in a finite amount of time (which we assume very small), and set  $A_1(t = 0) = A_0$  and  $J_{in} = 0$  below.

In order to focus on the role of cooperative transport, we further assume that particle export is not a rate-limiting step ( $K_{\text{off}}/K_0 \rightarrow \infty$ , except for the description of the purely linear system, in Sec.3.3.1 below), and we analyze the processing accuracy in terms of a competition between the kinetics of maturation and transport (controlled by 4 parameters). We can compare three situations : purely linear transport, transport with saturation of the carriers, and cooperative transport (with saturation of the vesicles).

### 3.3.1 Processing accuracy for linear transport

In order to quantify the consequences of cooperativity on the processing accuracy of a two-compartment system, we compute the accuracy of a perfectly linear system by linearizing Eqs.3.2,3.3,3.4 when  $A_0 \ll C_m, C_s, C_f$ , yielding :  $J_{1 \rightarrow 2} = K_0 C_1/2$  and  $J_{2 \rightarrow 1} = K_0 C_2/2$ . Choosing  $J_{\text{out}} = K_{\text{off}} C_2$  for simplicity, and the initial conditions  $C_1(t = 0) = C_1(0)$  and  $C_2(t = 0) = 0$ , the kinetic evolution of the vector  $\mathbf{C} = \{C_1(t), C_2(t)\}$  is easily obtained :

$$\mathbf{C}(t) = e^{M_l t} \begin{pmatrix} C_1(0) \\ 0 \end{pmatrix}, \quad M_l = -\frac{K_0}{2} \begin{bmatrix} 1 & 1 \\ 1 & 1 + 2k_{\text{off}} \end{bmatrix} \quad (3.35)$$

where  $k_{\text{off}} = \frac{K_{\text{off}}}{K_0}$ . The matrix  $M_l$  can be diagonalized, and the matrix exponential becomes a regular exponential, and the concentration in the second compartment reads :

$$C_2(t) = \frac{C_1(0)}{2\sqrt{1 + k_{\text{off}}^2}} (e^{\alpha_+ t} - e^{\alpha_- t}) \quad (3.36)$$

with the eigenvalues :

$$\alpha_{\pm} = \frac{K_0}{2} \left( \pm \sqrt{1 + k_{\text{off}}^2} - (1 + k_{\text{off}}) \right) \quad (3.37)$$

The (normalized) probability density that a particle exits the system from the second

compartment at time  $t$  is  $P_{exit}(t) = K_{off}C_2(t)/C_1(0)$  :

$$P_{exit}(t) = K_0 \frac{k_{off}}{\sqrt{1 + k_{off}^2}} (e^{\alpha+t} - e^{\alpha-t}) \quad (3.38)$$

The mean residence time of a particle in the system is thus  $\langle T \rangle \equiv \int_0^\infty dt (t P_{exit}(t)) = 2(1/K_0 + 1/K_{off})$ .

The accuracy of protein maturation ( $A \rightarrow B$ ) and sorting is defined as the fraction of the total quantity of molecules that entered the system to leave as matured molecules (Eq.3.31). It may also be written as :

$$\text{Accuracy} = \int_0^{+\infty} P_{exit}(t) P(B, t|A, 0) dt \quad (3.39)$$

where which  $P(B, t|A, 0)$  is the probability for a molecule to be mature (state  $B$ ) at time  $t$  while starting immature (state  $A$ ) at  $t = 0$ . At the linear level, the maturation kinetics (Eq.3.32) becomes :  $\partial_t B_\alpha = R_0 A_\alpha$ , and  $P(B, t|A, 0) = 1 - e^{-R_0 t}$ . The efficiency of the linear system may then be computed analytically using Eqs.(3.37,3.38,3.39), yielding :

$$\text{Accuracy}|_{\text{linear}} = \frac{2r_0(1 + r_0 + k_{off})}{k_{off} + 2r_0(1 + r_0 + k_{off})} \quad (3.40)$$

with  $r_0 = R_0/K_0$ . Below, we use the limit  $k_{off} \rightarrow \infty$  in order to focus on the effect of cooperative transport and enzyme kinetics on the accuracy of the system. The benchmark to which more complex transport and maturation processes must be compared is thus the linear accuracy  $\text{Accuracy}|_{\text{linear}} \rightarrow 2r_0/(1 + 2r_0)$ . However, since our goal is ultimately to study the consequences of cooperativity, our model of which includes a saturation of the carriers, we are rather interested in comparing the cooperative model to a model with saturation of the carriers but without cooperativity.

### 3.3.2 Processing accuracy without specific vesicular fusion

Saturation of maturation enzymes and transport intermediates ( $C_m, C_s < A_0 \ll C_f$ , with  $A_0$  the initial particle concentration) has mixed effects on the systems processing accuracy. Saturation of inter-compartment transport at high concentration (for  $A_0 \gg C_s$ ) causes the particle residency time of molecules to grow as  $A_0$  (Eq.3.3) while saturation of enzymatic reaction (for  $A_0 \gg C_m$ ) causes the mean maturation time increase linearly with  $A_0$  (Eq.3.32), so the net effect on processing accuracy depends on the precise values of the parameters.

In order to get a feel for the role of the different parameters, we compute the first order correction to the linear processing kinetics studied in section 3.3.1, in the limit of very fast exit from the second compartment :  $k_{off} \rightarrow \infty$ . In this case, the accuracy is controlled by the flux exiting the first compartment, now written  $J_{out} = \frac{1}{2}K_0C_sS(C_1)$  and Eq.3.34 may

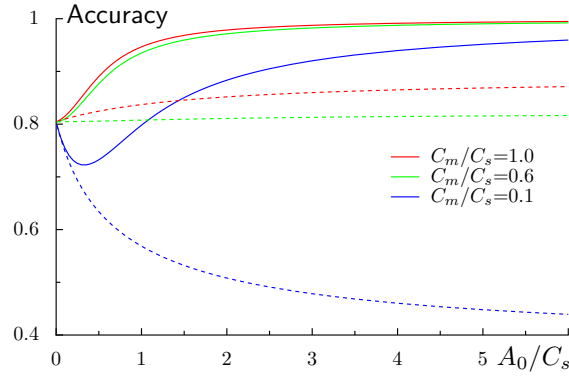


**Figure 3.9:** Accuracy (Eq.3.31) as a function of the initial concentration  $A_0$ , for different saturation ratios  $C_m/C_s$  of maturation and transport. At high concentration, specific vesicle fusion greatly enhance processing accuracy (solid lines, with  $C_f/C_s = 0.1$ ), as compared to random fusion ( $C_f \rightarrow \infty$ , dashed lines) (with  $R_0/K_0 = 2$ , and  $K_{\text{off}}/K_0 = 100$ ).

be rewritten :

$$C = A + B \quad (3.41a)$$

$$\dot{A} = -C_s \frac{1}{2} \frac{A}{C + C_s} - r_0 C_m \frac{A}{A + C_m} \quad (3.41b)$$

$$\dot{B} = -C_s \frac{1}{2} \frac{B}{C + C_s} + r_0 C_m \frac{A}{A + C_m} \quad (3.41c)$$

where the subscript 1 has been dropped in the concentrations, time has been normalized by  $1/K_0$ , and  $r_0 \equiv R_0/K_0$ . Taylor expansion of this set of equation for  $A_0 \ll \min(C_s, C_m)$  yields the first order correction to the accuracy of the linear system (Eq.3.40) :

$$\begin{aligned} \text{Accuracy} = & \frac{2r_0}{1+2r_0} + \frac{A_0}{C_s} \frac{C_m(1+2r_0) - C_s(1+r_0)}{C_m(1+r_0)(1+2r_0)^2} \\ & + \mathcal{O} \left[ \left( \frac{A_0}{C_s} \right)^2 \right] \end{aligned} \quad (3.42)$$

An increase in processing accuracy is thus observed at high concentration if maturation saturates for higher initial concentrations than secretion, according to  $C_m/C_s > (1+r_0)/(1+2r_0)$ . This can be seen in Fig.3.9, which shows the variation of the processing accuracy as a function of the total amount of material to be processed, in the absence of cooperative fusion (dashed lines).

### 3.3.3 Processing accuracy and cooperative transport

Cooperative fusion has a profound influence on the processing accuracy of a compartmentalized organelle responsible for protein maturation and sorting. When combined with saturation of the transport, cooperative fusion leads to a robust increase of the accuracy (see Fig.3.9, solid lines), which can be understood as follows : At high concentration ( $A_0 > C_f, C_s$ ), specific interactions promote backward fusion of vesicles secreted

by the highly concentrated compartment. As the forward fusion probability is very low ( $P_{1 \rightarrow 2} \sim 1/A_0$ , Eq.3.4) the mean residency time increases as  $A_0^2$ , as compared to the linear increase observed in the absence of specific fusion (section 3.3.2). On the other hand, the mean maturation time is still linear in  $A_0$ , so high concentrations lead to a more pronounced increase of the residency time compared to the maturation time, resulting in an increased processing accuracy at high concentration, even if the chemical transformation is performed by a limited amount of maturation enzymes ( $C_m \ll C_s$ ).

### 3.4 Conclusion and outlook

The predicted high processing accuracy displayed Fig.3.9 essentially stems from the increase of the residency time of molecules transiting through the system. In striking contrast with the usual Fick's law of gradient-driven transport, cooperative transport through the compartmentalized system described here is strongly impaired by a large concentration heterogeneity. A strong prediction of our model is that the transport time actually increases with an increasing incoming flux (above a threshold). Pulse-chase experiments on the Golgi seem to show this trend, but data are still too scarce for a direct comparison (see Fig.4.1 in [54]). Although an apparent functional drawback, slow transport through organelles is common. For instance, the typical transport time across the Golgi is of order of 20 minutes [46], whereas diffusion of a membrane protein over an area equal to that of the entire Golgi apparatus (of order  $10\mu\text{m}^2$ ) should be of order one minute (with a diffusion coefficient  $D_2 \sim 0.1\mu\text{m}^2/\text{s}$  [80]).

In this chapter, we showed that organelles constantly exchanging material via transport vesicles may spontaneously adopt different biochemical identities, provided : *i*) the flux of vesicles secreted by an organelle is bounded, and *ii*) there exists a sufficient level of specific vesicle-organelle fusion directed by molecular recognition. In open systems hosting fluxes, these transport properties give rise to a dynamical switch from a linear to a low throughput kinetics above a critical influx. For compartmentalized organelles whose function is to process and export influxes of proteins, such as the Golgi apparatus, this switch allows the export rate to spontaneously adjust to the amount of material to be processed, a definitive functional advantage that may avoid the release of unprocessed material even under high influx. However, in Yeast, and in some lower Eukaryotes, the Golgi apparatus is not stacked, and the maturation rates are much faster [83] (of the order of one minute, as we will see in chapter 4). It could be argued that a pluricellular organism does not need to respond chemically to their environment as fast as unicellular organisms, but requires more quality control as generating offsprings takes longer.

The disruption of the Golgi apparatus has been observed in many neuro-degenerative diseases [96, 97], and in apoptosis [98, 99]. This disruption is caused, in some cases, by the inhibition of Grasp 65 a Golgi stacking factor [49]. Such a disruption is expected to increase the rate of export, because the whole Golgi will contribute to the export (not just the trans-face). It could therefore be argued that the incomplete maturation could cause cell death or disfunction, and Golgi disruption could directly cause apoptosis or the syndromes of neuro-degenerative diseases. However, the inhibition of Grasp 65, and Golgi unstacking, is not lethal, and there must therefore exist additional quality control mechanisms. For instance, the export of molecules likely depends on the state (mature or immature) of the molecule. There is no concluding evidence, as far as we know, that increasing the export by Golgi disruption is the cause of neurodegenerative pathologies or apoptosis [98].

## 3.5 Appendix : From transport rates to an energy landscape

### 3.5.1 Theory

We can wonder under which conditions a set of laws of exchange between compartments, in a closed system, can be mapped to an energy landscape. Let us assume a system described by the proportion  $\phi$  of molecules of interest in the first cisterna. Let  $j_{out}(\phi)$  be the outbound flux from a cisternae of concentration  $\phi$ .

Let us assume the transport between compartments to be mediated by vesicles always carrying the same amount of cargo, called  $\delta\phi$ . When a vesicle leaves the first compartment and joins the second, the proportion of molecules of interest in the first compartment goes from  $\phi$  to  $\phi - \delta\phi$ , and we can write the flux exiting from the first compartment :

$$j_{out}(\phi) = k(\phi)P(\phi)\delta\phi \quad (3.43)$$

where  $k(\phi)$  is a budding frequency from and  $P(\phi)$  is the probability of forward fusion (with the second compartment) of a vesicle leaving the first compartment.

Let us define  $N = 1/\delta\phi$ . There are thus  $N + 1$  states available to the system ( $\phi = 0$ ,  $\phi = \delta\phi$ ,  $\phi = 2\delta\phi$ , ... ,  $\phi = 1$ ). We can therefore describe the state by the number  $n$ , such as  $\phi = n\delta\phi$ . As done in the main text, we consider the fusion of vesicles to be infinitely fast, therefore the only transitions allowed are  $n \rightarrow n + 1$  and  $n \rightarrow n - 1$ . We call  $W_n^+$  and  $W_n^-$  respectively the rates of these transitions.

We call  $P_n(t)$  the probability for the system to be in the state  $n$  at time  $t$ , and  $\mathbf{P}(t)$  the vector  $(P_0(t), P_1(t), \dots, P_N(t))$ . Let us consider a steady state  $\mathbf{P}$ . Because  $\dot{\mathbf{P}} = \mathbf{0}$  at steady state, we find :

$$P_0W_0^+ = P_1W_1^- \quad (3.44)$$

And, for  $n \geq 1$  :

$$W_n^+P_n + W_n^-P_n = P_{n-1}W_{n-1}^+ + P_{n+1}W_{n+1}^- \quad (3.45)$$

By iteration, we find that the detailed balance is satisfied by any stationary solution. We can show that the stationary solution in such a system exists and is unique.

Let us call  $\mathcal{W}$  the evolution matrix of the system such as :

$$\mathbf{P}(t + dt) = \mathcal{W}\mathbf{P}(t) \quad (3.46)$$

Where  $dt$  is a unit time much smaller than the inverses of the rates  $\{W_n^\pm\}$  defined earlier. The evolution matrix therefore verifies :

$$\mathcal{W}(n, n + 1) = W_n^+ dt \quad (3.47)$$

$$\mathcal{W}(n, n - 1) = W_n^- dt \quad (3.48)$$

$$\mathcal{W}(n, n) = 1 - (W_n^+ + W_n^-) dt \quad (3.49)$$

A stationary probability  $\mathbf{Q}$ , if any, satisfies  $\mathbf{Q} = \mathcal{W}\mathbf{Q}$ . The diagonal and subdiagonal values of  $\mathcal{W}$  are strictly positive because of our assumption on  $dt$ , whereas all the other values are zero, and  $\mathcal{W}$  is a non-negative matrix. Because the subdiagonal values are

all strictly positive,  $\mathcal{W}$  is irreducible : there is no non-trivial invariant subspace, i.e. no non-trivial subset  $\mathcal{A}$  such as  $\forall \mathbf{P} \in \mathcal{A}, \mathcal{W}\mathbf{P} \in \mathcal{A}$ .

As  $\mathcal{W}$  is irreducible and non negative, the Perron-Frobenius theorem for positive matrixes can be applied [100] (it could also be noted that  $\mathcal{W}^{N+1}$  is positive hence  $\mathcal{W}$  is primitive). The Perron-Frobenius theorem states that there is a strictly positive eigenvalue that is strictly superior to all other eigenvalues, and that there is a positive eigenvector corresponding to that value. Because  $\|\mathbf{P}\| = 1$ , this eigenvalue is one. Therefore, a stationary solution exists, that is unique (and satisfies detailed balance, as shown above).

From now on, we will use the variable  $\phi = n\delta\phi$  instead of  $n$ , since it is more intuitive. Let us assume an energy  $f_{tot}(\phi)$  such as the stationary probability  $Q(\phi)$  is  $Q(\phi) = \exp(-f_{tot}(\phi))$ . We mentioned that detailed balance is satisfied by any stationary distribution and hence

$$\frac{W(\phi \rightarrow \phi + \delta\phi)}{W(\phi + \delta\phi \rightarrow \phi)} = \exp\left(\frac{f_{tot}(\phi)}{f_{tot}(\phi + \delta\phi)}\right) \quad (3.50)$$

We can expand this energy, and we get :

$$\frac{W(\phi \rightarrow \phi + \delta\phi)}{W(\phi + \delta\phi \rightarrow \phi)} = \exp\left(-\left(\frac{\partial f_{tot}}{\partial \phi}\right)_{\phi} \delta\phi\right) \quad (3.51)$$

If we define an energy  $f(\phi)$  per cisternae such as  $f_{tot}(\phi) = f(\phi) + f(1 - \phi)$ , we find :

$$\frac{W(\phi \rightarrow \phi + \delta\phi)}{W(\phi + \delta\phi \rightarrow \phi)} = \exp\left(-\left(\frac{\partial f}{\partial \phi}\right)_{\phi} \delta\phi + \left(\frac{\partial f}{\partial \phi}\right)_{1-\phi} \delta\phi\right) \quad (3.52)$$

We assumed the vesicles to bear a constant quantity of molecules  $\delta\phi$ , and therefore  $W(\phi \rightarrow \phi + \delta\phi)\delta\phi = j_{out}(1 - \phi)$ . We then find :

$$j_{out}(\phi) = k_w \delta\phi \exp\left(\left(\frac{\partial f}{\partial \phi}\right)_{\phi} \delta\phi\right) \quad (3.53)$$

In which  $k_w$  is a constant rate. And eventually :

$$\frac{\partial f}{\partial \phi} = \frac{1}{\delta\phi} \log\left(\frac{j_{out}(\phi)}{k_w \delta\phi}\right) \quad (3.54)$$

$$f_{tot}(\phi) = f(\phi) + f(1 - \phi) \quad (3.55)$$

We can see that the constant  $k_w \delta\phi$  disappears in  $f_{tot}$ , which can be expressed as :

$$f_{tot}(\phi) = \frac{1}{\delta\phi} \int_0^{\phi} \log[j_{out}(\psi)] d\psi + \frac{1}{\delta\phi} \int_0^{1-\phi} \log[j_{out}(\psi)] d\psi \quad (3.56)$$

In this section, we were able to built an effective energy from the transport equations. To do so, we assumed the transport to be mediated by vesicles able to carry a discrete amount of cargo,  $\delta\phi$ . We also assumed that the evolution of the system was probabilistic. These assumptions differ from the assumptions generally made in Chapter 2, in which the vesicles could carry a continuous amount of cargo (from 0 to  $C_s$ ), and in which we mainly discussed the mean-field approximation of this system. Let us now discuss whether the system described in section 3.1.1 can be mapped to an energy landscape as described above.

### 3.5.2 Application

Let us consider the system described in section 3.1.1 of this chapter. We call  $C_{tot} = C_1 + C_2$  the total concentration in the system and we renormalize all concentrations by  $C_{tot}$ , so that :  $\phi = C_1/C_{tot}$ ,  $\phi_s = C_s/C_{tot}$ ,  $\phi_f = C_f/C_{tot}$ . Let us recall the transport laws in the system :

$$\partial_t \phi = j_{out}(1 - \phi) - j_{out}(\phi) \quad (3.57)$$

$$j_{out}(\phi) = j_s S(\phi) P_{1 \rightarrow 2}(\phi) \quad (3.58)$$

$$S(\phi) = \frac{\phi}{\phi + \phi_s} \quad (3.59)$$

$$P_{1 \rightarrow 2}(\phi) = \frac{S(\phi)(1 - \phi) + \phi_f}{S(\phi) + 2\phi_f} \quad (3.60)$$

We can take  $j_s = 1$  because the prefactors in  $j_{out}$  are removed by the sum in equation 3.55.

Using equation 3.56, we can find an analytical expression for  $\delta\phi f_{tot}(\phi)$ . We show the result in figure 3.10 for two sets of parameters :

- $\phi_s = 0.5$ ,  $\phi_f = 0.1$  :  $f_{tot}$  shows two minima as a function of  $\phi$  and hence the symmetric state is not stable. This was predicted in section 3.1.1.
- $\phi_s = 0.5$ ,  $\phi_f = 0.5$  :  $f_{tot}$  shows one minima at  $\phi = \frac{1}{2}$  and hence the symmetric state is stable. This was predicted in section 3.1.1.

The critical line  $\phi_f^*(\phi_s)$  can be found by solving  $\partial_\phi f_{tot}|_{\phi=\frac{1}{2}} = 0$  and yields :

$$\phi_f^* = \frac{1}{4\phi_s(\phi_s + 1)} \quad (3.61)$$

This is equivalent to the critical line (equation 3.5) found by analysing the symmetric solution. Finding the stationary solutions is also possible by minimizing the energy with respect to  $\phi$ , which comes down to solving  $j_{out}(\phi) = j_{out}(1 - \phi)$ , and therefore there is no computational gain in describing the system by an energy landscape.

As of now, we did not comment on the value of  $\delta\phi$  and on the temperature (by which the energy is normalized), and therefore we cannot define temperature-driven phase transitions. Clearly,  $\delta\phi$  is not well defined, because in this system the vesicles carry a variable load  $S(\phi) \in [0, 1]$ . Since  $S(\phi)$  changes continuously from 0 to 1, there is no way to define the smallest unit of cargo exchange between the compartments, and the approximation is only valid in the limit  $\delta\phi \rightarrow 0$ . Therefore the mapping to an energy landscape yields the correct shape of the energy but does not yield the scale of the energy. Comparing the fluctuations in the energy landscape formulation and in a model system (out of the mean-field approximation, as was studied in section 3.1.4 of this chapter) can give the scale of the energy.

Though the perspective of mapping a set of transport laws to an energy landscape is very appealing, in practical, finding  $f$  might be difficult analytically. Moreover, this mapping becomes hazardous in the case of many species, as writing detailed balance might not

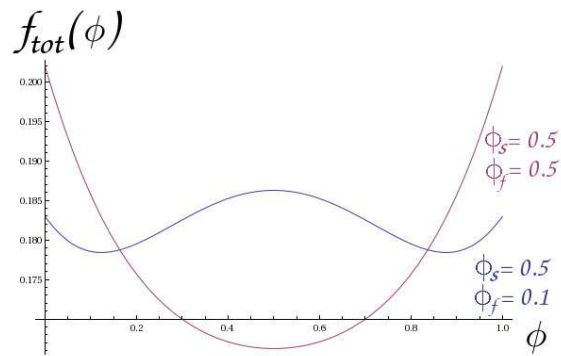


**Figure 3.10:** Total energy  $f_{tot}(\phi)$  (normalized by  $\delta\phi$ ) as a function of  $\phi$  for two sets of parameters. Blue :  $\phi_s = 0.5$ ,  $\phi_f = 0.1$ . The energy shows two wells, which illustrates the stability of the asymmetric state. Red :  $\phi_s = 0.5$ ,  $\phi_f = 0.5$ . There is only one well at  $\phi = \frac{1}{2}$  as the symmetric system is stable.

be possible if some species are cotransported. Moreover, the definition of the temperature is unclear, and no computational gain is obtained when finding the stationary solutions of the system. Therefore, we did not continue in that direction.



## Chapter 4

# Building differentiated compartments

### Introduction

In the previous chapters, we studied various aspects of transport in the cell. In chapter 1, we saw that the composition of the cell membrane was closely related to biological function, including the entry of material in the cell. In chapter 2, we saw that a gradient of chemical composition along an organelle could result in a gradient of energy driving the transport of molecules. We also noticed that the structure of the organelle could influence transport. In chapter 3, we realized that there was a feedback between the identity of organelles and their transport properties, as two compartments could be expected to spontaneously adopt different identity because of cooperative transport. So far, the interactions between organelle identity and structure have not been considered. In this chapter, we show how an organelle can spontaneously divide into sub-compartments of different composition. This research started as we decided to study the transport in the Golgi apparatus, for which, as we mentioned, two models are competing. As cartooned in figure 2.2, in the first model, called vesicular transport, cisternae are assumed to have a fixed position in the stack, and molecules are exchanged between neighboring cisternae by tubular and vesicular transport. In the other model, called cisternal progression, individual cisternae advance through the stack, with cisternae being assembled at the cis face of the Golgi apparatus and disassembled at the trans face.

A strong argument in favor of cisternal maturation was given by Matsuura-Tokita *et al.* [83] and Losev *et al.* [101] in 2006. In Yeast, in which the Golgi cisternae are disseminated in the cell (and hence do not form stacks), the identity of each cisterna changes with time from a typical cis-Golgi identity to a typical trans-Golgi identity. This evolution, which occurs on a timescale of the order of one minute, was observed by fluorescently labeling markers typical of cis Golgi or trans Golgi, as illustrated in figure 4.1.

In the previous chapter, we showed that the existing experiments on protein transport along the stack in the mammalian Golgi apparatus could not demonstrate the validity of the cisternal progression model. These experiments on Yeast seem therefore to be a much stronger argument. However, the very different structure of the Golgi apparatus in Yeast could sap this argument by convincing us that the Yeast Golgi and the mammalian Golgi

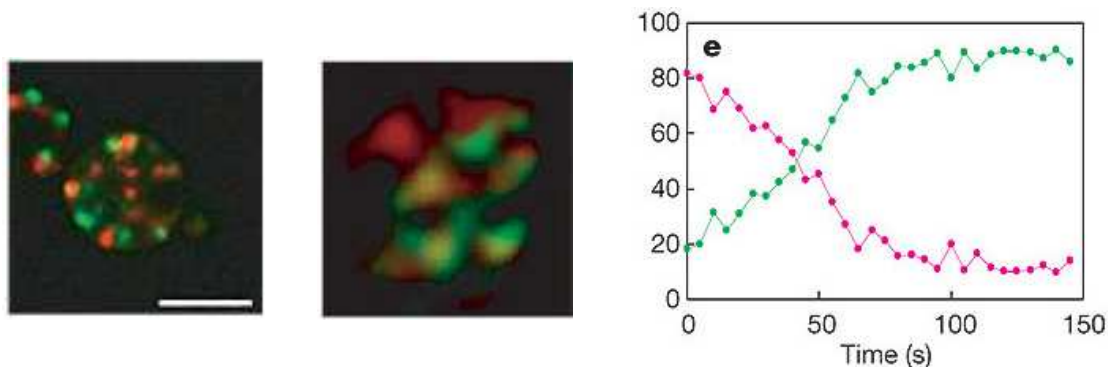


**Figure 4.1:** LEFT : Electron microscopy of a yeast cell with fluorescently tagged Golgi (scale bar  $5\mu m$ ). The red marker, mRFP-Sed5, is a SNARE protein typical of the cis Golgi attached to a red fluorescent molecule, and the green marker, GFP-Sed7, is an enzyme acting on GTPases, typical of the trans Golgi, attached to GFP, a green fluorescent protein. CENTER : Electron microscopy of an individual cisterna (of size  $\approx 1\mu m$ ). RIGHT : evolution of the total fluorescence in one cisterna as a function of time for the red and green markers. Taken from Matsuura-Tokita et al. [83].

are two rather different organelles, though it has been shown that under certain conditions, the Yeast Golgi apparatus can be stacked. As physicists, we are tempted to think that the two different Golgi structures, namely individual cisternae maturing independently and strongly connected cisternae in stacks, could be described in one unified framework. We must then identify one or several control parameters that could dictate Golgi structure.

Maturation in the Golgi apparatus chemically changes lipids and proteins in a specific sequence of reactions, and the products of reaction can have different physical properties than their precursors. It has been shown both in vitro [102], and in vivo [103] that molecules of different physical properties in a membrane will tend to phase separate and form domains of different composition. For instance, ceramids are matured into sphingolipids in the cis Golgi, and ceramids are known to form domains in sphingolipid membranes [104]. We can therefore expect maturation to cause the formation of domains in the Golgi membrane. One can actually see the non-uniform distribution of cis and trans Golgi markers in a yeast cisterna, as illustrated in figure 4.1 (center). In yeast, maturation is very fast (of the order of  $1min$ , as shown in figure 4.1) as compared to maturation in mammals (typically  $\approx 20min$ ), and, provided domains of different lipid composition do form on cisternae, we can expect smaller domains in Yeast Golgi than in mammal Golgi, as faster maturation allows less time for domain growth.

In chapter 1, we saw that membrane domains have the tendency to deformed into curved buds because of line tension, which acts to reduce the length of the interface between membrane regions of different compositions. In this chapter, we will assume that those buds are the precursors of new cisternae, as once detached from the membrane, they form large vesicles of distinct chemical identity. We also showed that domains must reach a critical size  $\lambda_b$  for protrusions to form,  $\lambda_b$  being controlled by the mechanical properties of the membrane. It is very tempting to assume that fast maturation (e.g. in Yeast) results in domains smaller than  $\lambda_b$ , while slow maturation (e.g. in mammals) may allow for domains to grow beyond the critical size  $\lambda_b$ , resulting in connected sub-compartments of different compositions. This hypothesis is illustrated in figure 4.2.

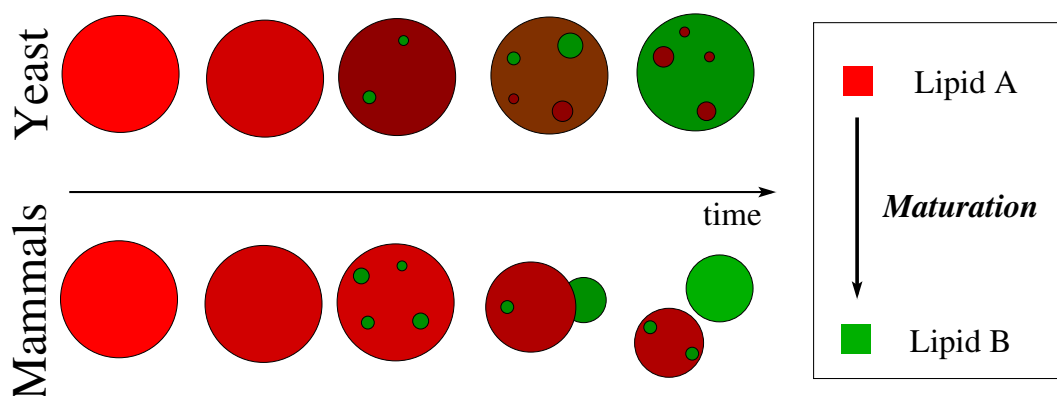


**Figure 4.2:** Illustration of our model for the structure of the Golgi apparatus. In mammals, maturation is slow ( $\sim 20$  min) and large domains of newly synthesized lipids  $B$  can grow. Line tension causes these large domains to form bud, which pinch off the membrane and form new cisternae. In Yeast, in which the Golgi apparatus is usually not stacked, maturation is fast ( $\sim 1$  min) and the domains of  $B$  are too small to form buds, and no new cisterna appears.

In a first section, we will see how maturation of lipids in the Golgi apparatus can cause the formation of lipid domains, which in turn can form large buds. We will then see how the rate of maturation can control the existence of those domains (and hence, following our hypothesis, control the stacking of the Golgi) as there is a competition between the kinetics of domain growth and the kinetics of chemical maturation.

## 4.1 Thermodynamics of phase separation in a membrane

In this section, we will understand why different lipid species  $A$  and  $B$  in a membrane will tend to form domains. Each molecule of  $A$  and  $B$  in the membrane is assumed to interact with its nearest neighbors only. We can use an Ising-like formalism to describe the system, in which two adjacent molecules are either similar (with no cost in energy), or different (with an energetic penalty  $J$ ). In the context of lipid membranes, the interaction energy may come from many sources, including mismatch between the length of lipid tails (introduced in chapter 2), or the tendency of each lipid to form different phases, as described in [105]. In the whole chapter, we will assume the system to be isotropic.

The total composition energy of the system hence writes :

$$\mathcal{H}_\phi = \frac{1}{2} \sum_{i,j} J_{ij} [s_i (1 - s_j) + s_j (1 - s_i)] \quad (4.1)$$

In which  $s = 0$  for a  $A$  molecule and  $s = 1$  for a  $B$  molecule, and  $J_{ij} = J$  if the molecules  $i$  and  $j$  are neighbors and  $J_{ij} = 0$  otherwise. We call  $V_i$  the set of nearest neighbors to the site  $i$ , and  $z = \text{card}(V_i)$  the number nearest neighbors a site has. Alternatively, we can re-write the Hamiltonian as :

$$\mathcal{H} = zJ \sum_i s_i - \frac{J}{2} \sum_i s_i \sum_{j \in V_i} s_j \quad (4.2)$$

We will see that this model predicts a phase separation (the formation of domains enriched in  $A$  or  $B$ ) if  $J$  is above a threshold.

### 4.1.1 Mapping to a free energy

Though a great way to run simulations, a discrete model such as this makes the analytical solving of problems uneasy (Onsager received the Nobel prize for solving the Ising model in two dimensions, whereas the three dimensional Ising model has not been solved explicitly). However, it has been shown that this discrete model could be mapped to a continuous free-energy [23]. To do so, we can introduce  $\phi(\mathbf{x}_i, t) \in [0, 1]$ , the time average of  $s_i$ , in which  $\mathbf{x}_i$  is the position of the site  $i$ .  $\phi$  is the time average on a timescale  $\tau$  much larger than the transition time ( $0 \rightarrow 1$  or  $1 \rightarrow 0$ ) of a site. We also assume  $\phi$  to vary smoothly in space, i.e. on lengthscales larger than  $a$ , the distance between two nearest neighbors. In the following, we call  $\overline{X}$  the time average of the observable  $X$ , and we can write :

$$\phi(\mathbf{x}_i, t) = \overline{s_i} \quad (4.3)$$

We can introduce  $\delta_i$  :

$$\delta_i = s_i - \phi(\mathbf{x}_i, t) \quad (4.4)$$

Because  $s_i$  is 0 or 1, the identity  $\phi(\mathbf{x}_i, t) = \overline{s_i^2}$  can also be written. As a result, we find :

$$\overline{\delta_i^2} = \phi(\mathbf{x}_i, t) - \phi(\mathbf{x}_i, t)^2 \quad (4.5)$$

We can compute the time-average of the Hamiltonian in equation 4.2 :

$$\overline{\mathcal{H}} = zJ \sum_i \phi(\mathbf{x}_i, t) - \frac{J}{2} \sum_i \overline{(\phi(\mathbf{x}_i, t) + \delta_i) \sum_{j \in V_i} (\phi(\mathbf{x}_j, t) + \delta_j)} \quad (4.6)$$

As  $\phi$  is already an averaged variable, the time average in equation 4.6 only concerns the  $\delta_i, \delta_j$ . By definition,  $\overline{\delta_i} = 0$ , and equation 4.6 can be re-written as :

$$\overline{\mathcal{H}} = zJ \sum_i \phi(\mathbf{x}_i, t) - \frac{J}{2} \sum_i \sum_{j \in V_i} \phi(\mathbf{x}_i, t) \phi(\mathbf{x}_j, t) - \frac{J}{2} \sum_i \sum_{j \in V_i} \overline{\delta_i \delta_j} \quad (4.7)$$

The term last term describes the correlation in the fluctuations at site  $i$  with the fluctuations of neighboring sites. Since we assumed the system to be isotropic, we can expect this term to be proportional to  $z$ , the number of nearest neighbors, times the average correlation  $\overline{\delta_i \delta_j}$ , in which  $j$  is one of the closest neighbors to  $i$ . Obviously,  $\|\overline{\delta_i \delta_{j \in V_i}}\| \leq \overline{\delta_i \delta_i}$ , as a site cannot be more correlated with a neighbor than with itself. Recalling  $\overline{\delta_i \delta_i} = \phi(\mathbf{x}_i, t) - \phi(\mathbf{x}_i)^2$ , we can therefore write :

$$- \frac{J}{2} \sum_{j \in V_i} \overline{\delta_i \delta_j} = \frac{zJ}{2} \sum_i \alpha (\phi(\mathbf{x}_i, t) - \phi(\mathbf{x}_i)^2) \quad (4.8)$$

with  $\alpha = \frac{\overline{\delta_i \delta_{j \in V_i}}}{\overline{\delta_i \delta_i}}$  and  $-1 \leq \alpha \leq 1$

We can also re-write the second term in equation 4.7. We assumed that  $\phi$  changes smoothly in space (i.e. on lengthscales larger than  $a$ , the distance between two nearest neighbors), and we can therefore expand  $\phi(\mathbf{x}_j, t)$  around  $\phi(\mathbf{x}_i, t)$ . The linear term in  $a$  will not contribute as the left and right neighbors (respectively top and bottom neighbors) will yield opposite contributions and hence cancel each other. Therefore, only the constant term  $\phi(\mathbf{x}_i, t)^2$ , the quadratic term in  $a^2$  and higher order even terms will remain. Let us call  $d$  the number of dimensions of the system. At second order in  $a$ , the second term from equation 4.7 yields :

$$- \frac{J}{2} \sum_i \sum_{j \in V_i} \phi(\mathbf{x}_i, t) \phi(\mathbf{x}_j, t) \approx - \frac{J}{2} \sum_i \left[ z\phi(\mathbf{x}_i, t)^2 + \frac{z}{2d} a^2 \phi(\mathbf{x}_i, t) \Delta \phi(\mathbf{x}_i) \right] \quad (4.9)$$

We can now write this contribution as an integral over space rather than a sum, since we are assuming  $\phi$  to change on lengthscales larger than  $a$ . We take benefit of the integration to integrate by part the laplacian term and we find :

$$- \frac{J}{2} \sum_i \sum_{j \in V_i} \phi(\mathbf{x}_i, t) \phi(\mathbf{x}_j, t) \approx - \frac{J}{2a^2} \int_S \left[ z\phi^2 - \frac{z}{2d} a^2 \|\nabla \phi\|^2 \right] d^2x \quad (4.10)$$

We can now write  $\overline{\mathcal{H}}$ , from equation 4.7 as a space integral using equations 4.8 and 4.10 :

$$\overline{\mathcal{H}} = \frac{J}{2} \int_S \|\nabla \phi\|^2 d^2x - \frac{zJ}{2a^2} (1 - \alpha) \int_S \phi(1 - \phi) d^2x \quad (4.11)$$

with  $0 \leq 1 - \alpha \leq 2$

To write the free energy of the coarse-grained system, we also have to consider the configurational entropy of the system [23]. Using the typical Gibbs entropy, we find :

$$\mathcal{F} = \int_S d^2\mathbf{r} \left[ V[\phi(\mathbf{r})] + \frac{1}{2} \zeta \|\nabla \phi\|^2 \right] \quad (4.12)$$

$$V[\phi] = \frac{1}{2a^2} K \phi(1 - \phi) + \frac{k_B T}{a^2} [\phi \log \phi + (1 - \phi) \log(1 - \phi)] \quad (4.13)$$

$\mathcal{F}$  is the free energy of the coarse-grained system. The mapping to the discrete Hamiltonian of equation 4.1 is assured by setting  $\zeta = \frac{z}{2d}J$  and  $K = zJ(1 - \alpha)$ . The continuous model can be understood as follows :

- $\phi$  represents the density local of  $A$
- $1 - \phi$  represents the local density of  $B$
- The term in  $\zeta$  describes the penalty in creating gradients of concentration in the system.
- The term in  $K$  describes the repulsion between  $A$  and  $B$ .
- The contribution proportional to  $k_B T$  represents the entropy.

Phase separation in systems with a free energy similar to 4.12, called Landau free energy, have been intensely studied theoretically (see [106] for a review). Let us consider a system of typical size  $L$ . In Eq.4.12, the term  $V(\phi)$  is a bulk term and grows like  $L^2$  whereas  $\zeta \|\nabla\phi\|^2$  is an interface term and grows like  $L$  for a fully phase separated system. Therefore,  $\zeta$  plays no role in the phase transition in the limit  $L \rightarrow \infty$  (i.e. the thermodynamic limit). In such an infinitely large system, it can be shown [107] that there exists a critical value  $K_c$  such as for  $K > K_c$  it is energetically favorable to form one or many domains enriched in  $A$  and one or many domains enriched in  $B$ . Because of the entropy, it costs more to form domains of a species which is rare in the system. Therefore,  $K_c$  is a function of  $\bar{\phi}$ , the mean value of  $\phi$  in the system. The line  $K_c(\bar{\phi})$  in the phase diagram is called the *binodal* line.

However, in the regime in which the heterogeneous system is thermodynamically favorable, the phase separation will not always be observed. Indeed, if infinitesimal heterogeneities due to thermal fluctuations do not spontaneously grow, the homogeneous phase will be metastable as it will take a long time for large enough domains to nucleate. Therefore, we will not study the metastable domain of the phase diagram, but the domain in which at least some infinitesimal fluctuations will grow. This domain is called the *spinodal* region. The binodal and spinodal domains are illustrated in figure 4.3.

### 4.1.2 Spinodal decomposition

We mentioned that in an infinitely large system (thermodynamic limit), the phase transition is dictated by the bulk term  $V(\phi)$ . Neglecting the interface cost, it will always be favorable for the system to phase separate if  $V$  has a double well structure [107]. Deriving  $V$  (Eq. 4.13) twice with respect to  $\phi$  shows that there is a transition at :

$$K^* = \frac{k_B T}{\bar{\phi}(1 - \bar{\phi})} \quad (4.14)$$

For any  $K > K^*$ ,  $V(\phi)$  has a double well structure and the phase separation is thermodynamically favorable. In the following, we will show that  $K^*$  is the spinodal line, and for

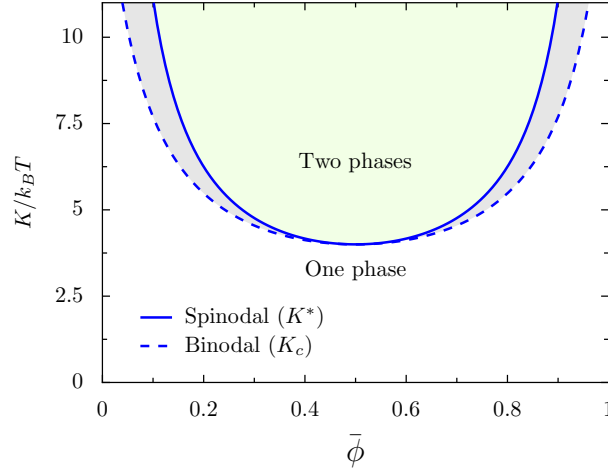


**Figure 4.3:** Phase diagram of a system described by the free energy 4.12. In the binodal region (light gray), the homogenous system is metastable whereas in the spinodal region (light green), infinitesimal fluctuations spontaneously grow to make the system heterogeneous.  $\bar{\phi}$  is the mean value of  $\phi$ , the local order parameter, in the system. The spinodal line is given by  $K^* = \frac{k_B T}{\bar{\phi}(1-\bar{\phi})}$ .

$K > K^*$  at least some infinitesimal perturbation will spontaneously grow. We can also extend this result to a finite-size domain, by studying the time evolution of fluctuations of different wavelengths. In the absence of maturation, the order parameter  $\phi$  is conserved and its evolution is given by the Cahn-Hilliard equation [108, 109, 110] :

$$\partial_t \phi = -a^2 \nabla \cdot \mathbf{j} \quad (4.15)$$

$$\mathbf{j} = -\frac{1}{\eta} \nabla \mu \quad (4.16)$$

$$\mu = \frac{\delta \mathcal{F}}{\delta \phi} \quad (4.17)$$

In which  $1/\eta$  is the mobility,  $\mu$  is the chemical potential and  $\mathbf{j}$  is the flux of the order parameter.  $\delta \mathcal{F}/\delta \phi$  is the functional derivative of  $\mathcal{F}$  with respect to  $\phi$ . We will usually assume the dynamics to be slow enough so that  $1/\eta = D/k_B T$  (Einstein's relation), in which  $D$  is the diffusion coefficient. Using the definition of  $\mathcal{F}$  in equation 4.12, we find :

$$\partial_t \phi = \frac{1}{\eta} \left[ k_B T \nabla \cdot \left( \frac{\nabla \phi}{1-\phi} \right) - \frac{K}{2} \Delta \phi^2 - a^2 \zeta \Delta^2 \phi \right] \quad (4.18)$$

We can have both analytical and numerical insight of the behaviour of this system. Let us discuss the evolution of a small perturbation of amplitude  $\epsilon \bar{\phi}$  and wavevector  $\mathbf{q}$ . The perturbed order parameter profile is  $\phi = \bar{\phi} (1 + \epsilon e^{i\mathbf{q}\mathbf{r} + i\omega t})$ , with  $\epsilon \ll 1$ , and  $\bar{\phi}$  being the mean value of  $\phi$  in the system. Inserting this equation in Eq. 4.18, we find :

$$i\omega = \frac{1}{\eta} \mathbf{q}^2 \left[ \left( K \bar{\phi} - \frac{k_B T}{1-\bar{\phi}} \right) - a^2 \zeta \mathbf{q}^2 \bar{\phi} \right] \quad (4.19)$$

$i\omega$  is the rate of growth of the perturbation, which will be amplified if  $i\omega > 0$ . There is a critical  $K^*$  below which no instability appears, and above which fluctuations of the order

parameter may grow, with a fastest growing mode  $q_{max}$  :

$$K^* = \frac{k_B T}{\bar{\phi}(1 - \bar{\phi})} \quad (4.20)$$

$$|\mathbf{q}|_{max} = \frac{1}{a} \sqrt{\frac{1}{\zeta} (K - K^*)} \quad (4.21)$$

The criterion for spontaneous phase separation in an infinite system is thus  $K > K^*(\bar{\phi})$ . The line  $K^*(\bar{\phi})$  is called the spinodal line and is represented in figure 4.4. As we mentioned,  $\zeta$  does not play a role for an infinite system. In a finite system, the effect of  $\zeta$  can be retrieved by noting that there is a cutoff for  $q$  :  $|q|_{min} \approx 2\pi/L$ , as modes with a wavelength larger than the size  $L$  of the system cannot exist.

If the growth of a mode  $\mathbf{q}$  is suppressed by the gradient penalty  $\zeta$ , than any mode  $\mathbf{p}$  such as  $|\mathbf{p}| > |\mathbf{q}|$  will be suppressed as well. Hence, spontaneous growth of fluctuations will not occur if  $i\omega(|q|_{min}) < 0$ . Therefore, the spinodal line  $K^*(\bar{\phi})$  in a finite-size system is :

$$K^* = \frac{k_B T}{\bar{\phi}(1 - \bar{\phi})} + \zeta \left( \frac{2\pi a}{L} \right)^2 \quad (4.22)$$

This is true only for large system, as the entropic term is an approximation for  $L \gg a$ . After this introduction to phase separation in a membrane, we can return to the biological situation of interest in order to understand how maturation can cause such a phase separation.

### 4.1.3 Maturation-induced domain growth

In the case of a membrane undergoing chemical maturation  $A \rightarrow B$ , the mean composition of the membrane,  $\bar{\phi}$ , will change continuously from 0 to 1. Therefore, if  $K > 4k_B T + \zeta(2\pi a/L)^2$ , the system will cross twice the spinodal line, as illustrated in figure 4.4 :

- At first, as there are hardly any  $B$  molecules in the membrane, the system does not phase separate. The spinodal line is reached when there are enough  $B$  molecules in the system (at  $\bar{\phi} = \phi_a$ ).
- At some point, there are not enough  $A$  molecules in the system for the phase separation to be stable anymore, and domains will evaporate after the spinodal line is crossed a second time, at  $\bar{\phi} = \phi_b$ .

Therefore, the system will have only a finite time (depending on the maturation rate) to form domains of  $A$  or  $B$ . Because the time available for the phase-separation is finite, we might not see a unique domain of size  $\sim L$ . We rather expect to see several smaller domains. In chapter 1, section 1.1.4, we saw that line tension  $\sigma$  can cause domains to form buds, if the domain interface energy is larger than the bending energy of the membrane, of order  $8\pi\kappa$ , with  $\kappa$  being the bending modulus of the membrane. We mentioned that circular domains of radius  $R$  will deform into buds if :

$$4\frac{\kappa}{\sigma} < R < 2\frac{\sigma}{\gamma} \quad (4.23)$$

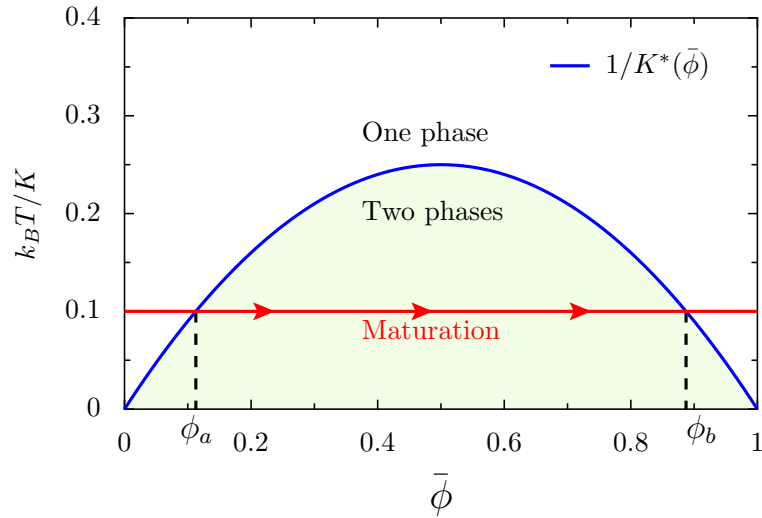


**Figure 4.4:** Phase diagram of a system described by the free energy 4.12. In the case of maturation,  $\bar{\phi}$  increases from 0 to 1 continuously and, if  $K > 4kT$ , the critical line will be crossed twice (at  $\bar{\phi} = \phi_a$  and  $\bar{\phi} = \phi_b$ ). In this case, the system will spend a finite time in the phase-separating (spinodal) region of the diagram.

In which  $\gamma$  is the tension of the membrane. These inequalities reflect that domains will form buds if they are large enough to overcome the bending modulus, but small enough not to be kept flat by surface tension. In the case of chemical maturation, the system will tend to phase separate only during a given time. If we assume that domain growth is slow compared to budding (which we will show in section 4.2) the real issue is whether domains large enough to form buds ( $R > 4\kappa/\sigma \approx 200nm$ , assuming  $\kappa \sim 10k_B T$  and  $\sigma \sim 0.2k_B Tnm^{-1}$ ) will have enough time to grow, and the upper bound  $R < \sigma/2\gamma$  will likely play no role, as long as  $\sigma/2\gamma$  is larger than  $2\kappa/\sigma$ , i.e. if  $\gamma < 10^{-6} J.m^{-2}$ . This is a very low value of the tension, and while it is possible for biological membranes to decrease their surface tension by using pumps and transport channels, the observation of complete buds in model membranes such as giant unilamellar vesicles could be prevented by surface tension.

Having established the requirements for domain growth and budding, we now need to study the kinetics of domain growth in order to know if, for biological rates of chemical maturation, domains large enough to bud ( $\approx 200nm$ ) will have time to grow.

## 4.2 Kinetics of domain growth

In this section, we study the growth of domains in a two-component membrane. We will first study the kinetics of phase separation in the absence of chemical maturation, and then we will see how those kinetics can, in certain approximations, be extended to a membrane with chemical maturation.

### 4.2.1 Lifschitz-Slyozov-Wagner theory

Lifschitz and Slyozov, and independently Wagner, showed that the dynamics of phase separation should follow a particular scaling law [109, 110]. Their work was extended and compared to numerical simulations (see [106] for a review) for a wide variety of models. We present here a discussion valid for systems in dimension  $d > 2$ . The case  $d = 2$  is a critical case for which the power laws are expected to be only marginally valid [111, 106]. Other possible dynamical models will be mentioned later, for instance including the role of hydrodynamics. The demonstration presented here is a reproduction of the demonstration by A.J. Bray in [106].

Let us recall the free energy of the system :

$$\mathcal{F} = \int_S ds \left[ \frac{1}{2} \zeta (\nabla \phi)^2 + V(\phi) \right] \quad (4.24)$$

Let us call  $V'(\phi) = \partial V / \partial \phi$ . Since  $\phi$  is conserved we can still write :

$$\partial_t \phi = -\nabla \cdot \mathbf{j} \quad (4.25)$$

$$\mathbf{j} = -\frac{D}{k_B T} \nabla \mu \quad (4.26)$$

$$\mu = \frac{\delta \mathcal{F}}{\delta \phi} = -\zeta \nabla^2 \phi + V'(\phi) \quad (4.27)$$

In which all lengths are normalized by  $a$  ( $a \sim 1nm$ ), the size of a molecule  $A$  or  $B$ , and all energies by  $k_B T$ . In addition, all times are normalized by  $\Theta = a^2 / D$  (of order  $10^{-6}s$ ). Unless specified otherwise, all the quantities in the following will be dimensionless according to this normalization.

As gradients are penalized by  $\zeta$  we expect a system in the spinodal region to form domains of sharp interface. In the following, we will call  $\phi_1$  the mean value of  $\phi$  in a domain and  $\phi_0$  the average of the order parameter in the bulk (outside the domains). As the interface are expected to be sharp, we introduce the notion of domain wall, the interface of a domain with the bulk. The equation for  $\mu$  (4.27) can be written along the coordinate  $z$  normal to a domain wall :

$$\mu = V'(\phi) - \zeta \left( \frac{\partial \phi}{\partial z} \right)_t C - \zeta \left( \frac{\partial^2 \phi}{\partial z^2} \right)_t \quad (4.28)$$

In which  $C$  is the curvature of the domain wall. For a spherical domain of radius  $R$  in  $d > 2$  dimensions,  $C = (d - 1) / R$ .

We may multiply this equation by  $\partial\phi/\partial z$ , which is sharply peaked at the interface (as gradients are penalized by  $\zeta$ ), and integrate it from the center of the domain to infinity. We get the (general) Gibbs-Thomson boundary condition at the interface :

$$\mu_1 \Delta\phi = \Delta V - C\sigma \quad (4.29)$$

$$\sigma = \int_0^\infty \zeta \left( \frac{\partial\phi}{\partial z} \right)_t^2 dz \quad (4.30)$$

In which  $\Delta\phi$  and  $\Delta V$  are the variation across the interface of the order parameter and of the potential respectively.  $\mu_1$  is the value of the chemical potential at the interface, and  $\sigma$  is the line tension. It does correspond to the phenomenological definition we used for surface tension, as it is the energy per length of domain wall.

In the following, we will always assume the concentration profiles to be quasi-stationary, i.e.  $\nabla^2\mu = 0$ . Using the boundary condition (Eq. 4.29), we find :

$$r < R \Rightarrow \mu(r) = \mu_1 = \frac{1}{\phi_0 - \phi_1} \left( V(\phi_0) - V(\phi_1) - \frac{\sigma}{R} \right) \quad (4.31)$$

$$r > R \Rightarrow \mu(r) = V'(\phi_0) + (\mu_1 - V'(\phi_0)) \left( \frac{R}{r} \right)^{d-2} \quad (4.32)$$

In which  $\phi_1$  is the concentration inside a domain,  $\phi_0$  is the bulk concentration at infinity, and  $V' = \partial V/\partial\phi$ . The growth or evaporation of a domain depends on the balance of the fluxes entering or exiting the domain. Formally, for a domain of size  $R$  ; it reads :

$$\dot{R} = \frac{[j]_{R-\delta R}^{R+\delta R}}{\phi_0 - \phi_1} = \frac{\left[ -\frac{\partial\mu}{\partial z} \right]_{R-\delta R}^{R+\delta R}}{\phi_0 - \phi_1} \quad (4.33)$$

Therefore :

$$\dot{R} = \frac{d-1}{2R(\phi_0 - \phi_1)} (\mu_1 - V'(\phi_0)) \quad (4.34)$$

Replacing  $\mu_1$  by its value, and setting  $V(\phi_1) = 0$  as reference, we find :

$$v(R, t) = \dot{R} = \frac{\sigma(d-1)}{R(\phi_1 - \phi_0)^2} \left( \frac{V(\phi_0) + V(\phi_0)(\phi_1 - \phi_0)}{\sigma} - \frac{1}{R} \right) \quad (4.35)$$

Which can be written :

$$\dot{R} = \frac{\sigma(d-1)}{R(\phi_1 - \phi_0)^2} \left( \frac{1}{R_c} - \frac{1}{R} \right) \quad (4.36)$$

$$R_c = \frac{\sigma}{V(\phi_0) + V(\phi_0)(\phi_1 - \phi_0)} \quad (4.37)$$

We find that domains smaller than  $R_c$ , the critical domain size, will evaporate in the bulk whereas larger domains will grow. For small domains,  $R^2\dot{R} \sim -\sigma t$  and hence their evaporation shows a scaling  $R \propto -t^{1/3}$ . To show a similar law for growth, one has to consider an assembly of domains. If a scaling law is assumed for the distribution of domain, the only growth law maintaining the scaling is  $R_c \propto t^{1/3}$ . To show this, the steps are to assume a scaling for  $n(R, t)$  :

$$n(R, t) = f(R/R_c(t)) \quad (4.38)$$

The continuity equation then reads :

$$\partial_t n + \partial_R [v(R)n(R)] = 0 \quad (4.39)$$

Injecting 4.35 and 4.38 in 4.39 yields :

$$R_c^2 \dot{R}_c = A\sigma \quad (4.40)$$

And therefore :

$$R_c \propto (\sigma t)^{1/3} \quad (4.41)$$

Because we assumed a scaling  $n(R, t) = f(R/R_c(t))$ , the size of domains is distributed around  $R_c$ , and  $R_c$  is a good measure of the mean domain size. This argument shows that the mean radius of domains  $\langle R \rangle \approx R_c$  in a bulk will grow like  $t^{1/3}$  if

- The domains are well separated
- The mean size of the domains is much larger than the interface length
- The dynamics is quasi-stationary

It is important to note here that domains larger than  $R_c$  grow by evaporation of smaller domains. We can use this remark to estimate the minimum times at which we can estimate the scaling to be valid. It costs an energy  $2zJ$  to exchange one molecule in the bulk with one molecule in a domain. As domain growth as described by Lifschitz, Slyozov and Wagner is limited by evaporation of small domains, it is limited by the rate  $\exp(-8J/k_B T) D/a^2$  (assuming  $z = 4$ ) at which molecules exit a domain. We therefore cannot expect the scaling before a time  $\exp(8J/k_B T) a^2/D$  [111].

Equation 4.32 shows that the above demonstration is valid for a system in a dimension  $d > 2$  only. For  $d = 2$ , we may expect this scaling to be marginally valid, with possible log corrections [111, 106]. We performed numerical simulations to confirm this scaling.

## 4.2.2 Numerical simulations

To compute the dynamics of such a system, we performed some numerical simulations. At first, we simulated a continuous system, but since it derives from the discrete system, it is more advantageous to simulate a discrete system, which reduces computational time by a few orders of magnitude.

The Metropolis algorithm has widely been used to study the kinetics of phase separation (see for instance [111, 112, 113]). For large times (i.e. for many Monte Carlo steps per site) the dynamics are statistically convincing, and the Lifschitz-Slyozov-Wagner scaling has been observed using the Metropolis algorithm [111, 113]. Other algorithms can be used, for instance by randomly choosing one rate of transition (among all possible transitions, with the probability of a transition being proportional to its rate) and incrementing the time by the inverse of the chosen rate. These algorithms are known as continuous-time

Monte Carlo [114], and have been used to study spin-exchange models [115]. The famous Gillespie algorithm [116], widely used in computational biology, is of this class.

We mainly used the Metropolis algorithm, as we will realize later that it allows a very easy implementation of maturation (and as a Gillespie algorithm yields the same results). In the next section, we detail the Metropolis algorithm we used, and how to find the domain size from the results of the simulation.

### Algorithm

For numerical convenience, we worked with  $s = \pm 1$  instead of 0 and 1. As a result, the Hamiltonian is :

$$\mathcal{H} = -\frac{1}{2} \sum_{m,n} \frac{J_{mn}}{2} s_m s_n \quad (4.42)$$

We used a square lattice with  $J_{mn} = J$  for nearest neighbors and  $J_{mn} = 0$  otherwise. We call  $L_x$  and  $L_y$  the system sizes on the  $x$  and  $y$  axis respectively, and  $s[i, j]$  is the type of molecule at the position  $i, j$ , with  $i \in \{1, 2, \dots, L_x\}$  and  $j \in \{1, 2, \dots, L_y\}$ .  $s$  is  $-1$  for a  $A$  molecule and  $1$  for a  $B$  molecule.  $t$  is the Monte-Carlo time, the number of computation steps per site. The algorithm reads :

```

def Eint(i, j) = - J s[i, j](s[i+1, j] + s[i-1, j] + s[i, j+1] + s[i, j-1])/4

for t in 1 to T :
    # t -> t+1
    for n in 1 to Lx * Ly :
        #New step

        #Chooses one site at random
        i=random(1 to Lx)
        j=random(1 to Ly)
        #Chooses one neighbour at random
        move=random(1 to 4)
        if move==1 : x=i , y=j+1
        else if move==2 : x=i , y=j-1
        else if move==3 : x=i+1, y=j
        else if move==4 : x=i-1, y=j

        #If the neighbours are different ,
        # we compute the energy of the exchange
        if S[i, j] != S[x, y] :
            Eold = Eint(i, j) + Eint(x, y)
            s[i, j] = -s[i, j]
            s[x, y] = -s[x, y]
            Enew = Eint(i, j) + Eint(x, y)
            DeltaE = Enew - Eold

        #Implementation of the Metropolis algorithm
        if DeltaE >0 :
            if random(0 to 1) > exp(-DeltaE):
                #The change is refused
                s[i, j] = -s[i, j]

```

$$s[x, y] = -s[x, y]$$

### Size of domains

After implementation of the Metropolis algorithm, we analysed the data. To know the size of domains, we compute the correlation length of the system. The pair correlation function can be written [117] :

$$G(\mathbf{R}) = \int_S d^2\mathbf{r} \psi(\mathbf{r})\psi(\mathbf{r} + \mathbf{R}) \quad (4.43)$$

$$\psi(\mathbf{r}) = \phi(\mathbf{r}) - \bar{\phi} \quad (4.44)$$

There are various definitions of the correlation length using the pair correlation function, including the first zero of  $G(\|r\|)$  [111]. In this case, computing the values of  $G$  takes a computational time  $\propto S^2$ . Alternatively, the correlation length can be found by computing the first moment of the structure factor  $\mathcal{S}$  [118], which is defined as the Fourier transform of the pair correlation function  $G$  :

$$\mathcal{S}(\mathbf{q}) = \int_S d^2\mathbf{R} G(\mathbf{R}) e^{i\mathbf{q}\cdot\mathbf{R}} \quad (4.45)$$

Using Eq. 4.43, this can be rewritten :

$$\mathcal{S}(\mathbf{q}) = \int_S d^2\mathbf{R} \psi(\mathbf{R}) \int_S d^2\mathbf{r} \psi(\mathbf{r}) e^{i\mathbf{q}\cdot(\mathbf{r}+\mathbf{R})} \quad (4.46)$$

And therefore, with  $\tilde{\psi}$  the Fourier transform of  $\psi$  :

$$\mathcal{S}(\mathbf{q}) = \tilde{\psi}_{-\mathbf{q}} \tilde{\psi}_{\mathbf{q}} \quad (4.47)$$

Which can be written :

$$\mathcal{S}(\mathbf{q}) = \|\tilde{\psi}_{\mathbf{q}}\|^2 \quad (4.48)$$

The computation of  $\mathcal{S}$  therefore only implies the computation of a Fourier transform, which takes a time of order  $S \log S$ . After computing  $\mathcal{S}$ , the correlation length can be found :

$$L_c = \frac{1}{q_c} \quad (4.49)$$

$$q_c = \frac{\int d^2\mathbf{q} \|\mathbf{q}\| \mathcal{S}(\mathbf{q})}{\int d^2\mathbf{q} \mathcal{S}(\mathbf{q})} \quad (4.50)$$

The integrals being replaced by sums, this takes a computational time of order  $S$ , which makes using the structure factor the fastest way to find the correlation length. Let us note that since we computed  $\mathcal{S}$ , we can do a Fourier transform to get  $G$  and alternatively find  $L_c$  by finding the first zero of  $G$ . If we compute  $q_c$ , we can also note that because the  $\mathcal{S}(\mathbf{0})$  does not contribute in  $q_c$ , we can use  $\mathcal{S}(\mathbf{q} \neq \mathbf{0}) = \|\tilde{\phi}_{\mathbf{q}}\|^2$ . In our simulations, we use discrete values for the positions, and hence discrete values for the wave vectors.

This correlation length is usually considered a good measure of domain size [118, 115]. However, this is true if  $\bar{\phi} = \frac{1}{2}$ , since otherwise there are actually two length scales in the system : the size of the (minority phase) domains, and the distance between domains. As of now, we are still in search for a good statistical measure yielding domain size for  $\bar{\phi} \neq 1/2$ .

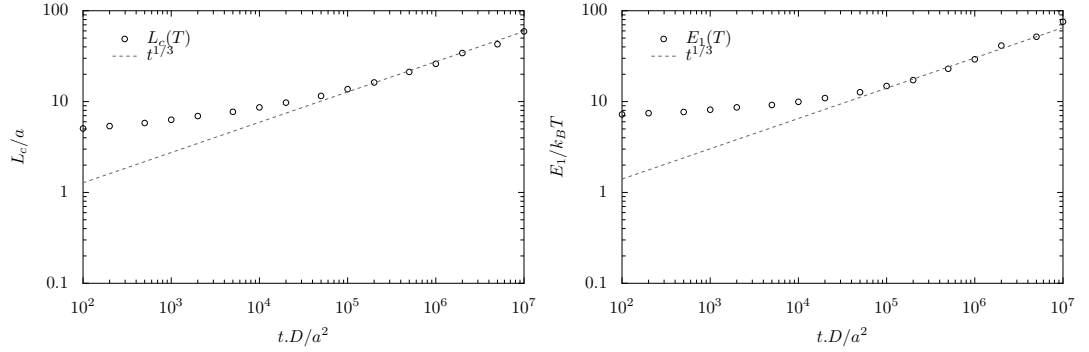


**Figure 4.5:** Monte-Carlo simulations of the correlation length  $L_c$  (left) and the energy per domain  $E_1$  (right) as a function of  $t$  (in units of  $a^2/D$ ,  $t \rightarrow t + 1$  corresponds to one Monte-Carlo step per site on average). The parameters are  $\bar{\phi} = 1/2$ ,  $J = 1.25k_B T$ ,  $L_x = L_y = 150$  (values of the parameters are discussed in section 4.2.3). Similar results were obtained with different system sizes. At late times  $t > \exp(8J/k_B T)a^2/D$ , both  $L_c$  and  $E_1$  follow the  $t^{1/3}$  scaling expected from the Lifschitz-Slyozov-Wagner theory. Results are averaged over 10 simulations.

## Energies

Since we can compute the mean domain size, we also know the approximate number of domains in the system. We can compute the Hamiltonian  $\mathcal{H}$  of the system (equation 4.42), and the energy per domain  $E_1$  can be estimated :

$$E_1 \approx \mathcal{H} \frac{L_c^2}{S} \quad (4.51)$$

In which  $S/L_c^2$  is approximately the number of domains. Since the energy of a domain is mainly due to interfacial effects, we expect  $E_1$  to grow like  $R_c$ , i.e. we expect  $E_1 \propto t^{1/3}$ . The results are shown in figure 4.5. We see that the expected scalings  $R_c \propto t^{1/3}$  and  $E_1 \propto t^{1/3}$  are indeed found, for  $t > 10^5 a^2/D$ . This time is in good agreement with the validity criterion  $t > \tau_J = \exp(8J/k_B T)a^2$  : since we used  $J = 1.25k_B T$ , we did not expect to see the scaling before  $t > 2 \cdot 10^4 a^2/D$ . The values of the parameters are discussed in section 4.2.3.

One of the assumptions of the Lifschitz-Slyozov-Wagner theory is that  $\sigma$ , the line tension, is constant. We can compute a simple estimation of line tension by noting that the energy per domain  $E_1$  is the line tension  $\sigma$  times the contour length  $\mathcal{L}$  of the domains :  $E_1 = \sigma \mathcal{L}$ . Assuming circular domains, we find :

$$\sigma \approx \mathcal{H} \frac{L_c}{2\pi S} \quad (4.52)$$

This method does not yield the exact value of the line tension, which has to be computed with more advanced tools [119, 120]. One of the shortcomings of this method is the assumption that the domains are circular. As illustrated in figure 4.6 (right), it is not the case (except for really long times for which the  $R_c$  is of the order of the system size), and we cannot be confident about the factor  $2\pi$  in equation 4.52.

### 4.2.3 From numerical membranes to biological membranes

In the previous section, we showed how a scaling  $R_c \propto t^{1/3}$  for the mean radius of domains could be obtained. We could run Monte-Carlo simulations of domain growth on a flat membrane, and we realized that the correlation length measured from the static structure factor  $\mathcal{S}$ , a good representation of domain size, did exhibit the same scaling (as shown in figure 4.5). We can identify the Monte-Carlo time  $t$  to the real time in units of  $a^2/D$  as during one Monte-Carlo time  $t \rightarrow t + 1$ , each molecule will move a distance  $a$  on average. We are interested in lipids of size  $a \approx 1nm$  and diffusion coefficient  $D \approx 1\mu m^2 s^{-1}$  [121] moving in a membrane plane during a time 1 – 20 minutes (the maturation time), i.e.  $6 \cdot 10^7 - 10^9 a^2/D$ . In this regime, Monte-Carlo simulations show the Lifschitz-Slyozov-Wagner scaling to be verified.

We have to choose the interaction parameter  $J$  in the simulations. We chose  $J = 1.25k_B T$  as this yields a surface tension  $\sigma \sim 0.2k_B T/a \approx 0.8pN$  (as shown in figure 4.6). This is the typical order of magnitude of line tension in biological membranes [24]. To have access to such large timescales, we performed the simulations on smaller lattices (typically  $150 * 150a^2$ ) than a real cisterna (of order  $1\mu m$ ). Limited simulations on larger systems also show the same behavior. Using  $J = 1.25k_B T$  predicts the scaling to be verified for  $t \gg \exp(-8J/k_B T)D/a^2 \approx 2 \cdot 10^4 D/a^2$ . In the simulations, the scaling is verified for  $t > 10^5 D/a^2$ , in good agreement with the argument mentioned in section 4.2.1 [111].

An interesting point in biological membranes, is that they will not stay flat like, for instance, a simulation grid. Line tension can cause the formation of full buds for large enough domains, but can also deform the membrane for smaller domains. The kinetics of domain growth on non-flat membranes have been studied numerically [122, 123]. In most cases the phase separation of species with different spontaneous curvature has been studied, and such difference in spontaneous curvature can cause even small domains to buckle. Despite this buckling, typical Lifschitz-Slyozov-Wagner kinetics have been observed. Therefore, we can be confident that this scaling should be observed when buckling is driven by line tension. However, we still need to inquire how maturation of membrane components will influence domain growth.

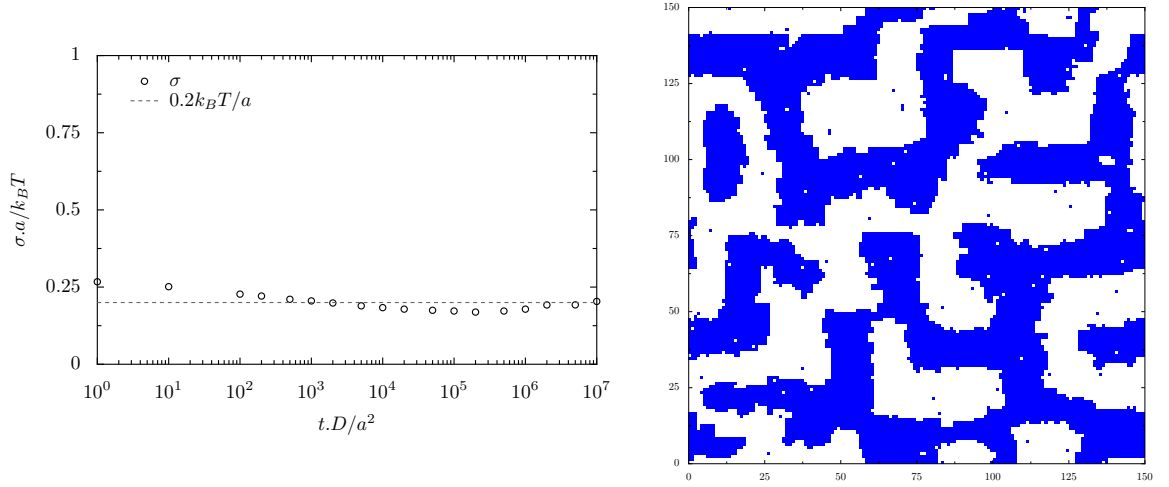


**Figure 4.6:** LEFT : Approximation of the surface tension  $\sigma$  as computed from equation 4.52, as a function of  $t$  (in units of  $a^2/D$ ,  $t \rightarrow t + 1$  corresponds to one Monte-Carlo step per site on average). The surface tension is averaged over ten simulations. RIGHT : An illustration of the system with  $\bar{\phi} = 1/2$  at  $t = 10^5 a^2/D$ . The domains are not circular and exhibit a typical serpentine shape. The correlation length (computed with equation 4.49) is  $14.3 a$ .

### 4.3 Kinetics of domain growth with maturation

To address the issue of the structure of the Golgi apparatus, we need to understand the kinetics of domain growth in membrane in which chemical maturation occurs. Maturation causes domains to grow not only by evaporation of smaller domains (which is fundamental in the Lifschitz-Slyozov-Wagner theory), but also by accretion of newly formed  $B$  molecules to existing  $B$  domains. Surprisingly, numerical simulations [118], showed that in a phase-separating system including a reversible chemical reaction  $A \leftrightarrow B$  of rate  $k$ , the mean size of domains as steady state was proportional to  $k^{-1/3}$  in some regime. In our system of interest, the chemical reaction is irreversible, and domains can only exist transiently. We are interested in knowing the maximum possible size (or rather the maximum value of the energy per domain) these transient domains will reach. We now need to understand theoretically how the growth laws are modified by maturation, and if we can predict a scaling for the maximum domain size as a function of the maturation rate.

#### 4.3.1 Theoretical analysis

Let us consider a maturation  $A \rightarrow B$  at a constant rate  $r$  such as  $\partial_t B = k_r A$ . In terms of  $\phi$  this yields :

$$\partial_t \phi = +k_r(1 - \phi) \quad (4.53)$$

Since the maturation time is of order  $1/k_r$ , using the Lifschitz-Slyozov-Wagner scaling, a naive argument yields that the maximum size of domains  $R_c^{max}$  to grow like  $k_r^{-1/3}$ .

However, this argument should not necessarily hold as the scaling in  $t^{-1/3}$  is derived for a constant  $\bar{\phi}$ , and when the growth of domains is limited by evaporation of smaller

domains. In the case of maturation, domains of  $B$  form as  $\bar{\phi}$  increases, and domains can grow by incorporating  $B$  molecules both newly created by maturation of  $A$  molecules in the bulk, and existing  $B$  molecules released by the evaporation of small domains.

### Influence of $k_r$ on the concentration profile

Let us write the dynamics (equations 4.27 to 4.25), with maturation and, for now, without renormalizing distances and time. The dynamics with maturation then read :

$$\partial_t \phi = -a^2 \nabla \cdot \mathbf{j} + k_r(1 - \phi) \quad (4.54)$$

$$\mathbf{j} = -D \nabla \mu \quad (4.55)$$

$$\mu = \frac{\delta \mathcal{F}}{\delta \phi} = -\zeta \nabla^2 \phi + V'(\phi) \quad (4.56)$$

We would like to compute the order parameter profile in the bulk, around a domain (analog to equations 4.31,4.32), by assuming once more that  $\partial_t \phi = 0$ , i.e. the concentration profile near the interface to be stationary. Unfortunately, there is no analytical solution in most cases. However, we can give some scaling arguments. In section 4.2.1, we showed that the typical lengthscale for gradients of the order parameter around a domain was  $R$ , the size of the domain. In equation 4.56, we thus expect the first term  $\zeta \nabla^2 \phi$  to scale like  $\zeta/R^2$ . In contrast, we expect  $V'(\phi)$  to scale like  $K/a^2$ , and therefore we will neglect the term  $\zeta \nabla^2 \phi$  in the chemical potential. Equation 4.54 now reads :

$$\partial_t \phi \approx -a^2 D \nabla^2 V'(\phi) + k_r(1 - \phi) \quad (4.57)$$

We have to make more restrictive approximations in order to find a solution to this equation. Let us write  $\phi = \bar{\phi} + \delta\phi$ . We now want to assume  $\delta\phi \ll \bar{\phi}$  in order to expand  $V'(\phi)$ . Since we want to solve this equation in the bulk (outside the domains), this approximation is only reasonable if  $\phi_0$ , the value of  $\phi$  in the bulk, is close to  $\bar{\phi}$ , i.e. for  $\bar{\phi} \sim \phi_a$  or  $\bar{\phi} \sim \phi_b$ . In this case we can write :

$$\partial_t \bar{\phi} = k_r(1 - \bar{\phi}) \quad (4.58)$$

$$\partial_t \delta\phi \approx a^2 D V''(\bar{\phi}) \nabla^2 \delta\phi - k_r \delta\phi \quad (4.59)$$

We want to find a growth law in the quasi-stationary regime, i.e.  $\partial_t \delta\phi \approx 0$ . The assumption  $\bar{\phi} \sim \phi_a$  is compatible with quasi-stationarity only if maturation is slow compared to the other dynamics. In the previous chapter, we saw that quasi-stationarity was valid for  $t > \exp(8J)a^2/D$ , and therefore, we can write  $\delta\phi \ll \bar{\phi}$  only if  $k_r \ll \exp(-8J)D/a^2$ . In this case, equation 4.57 can be written :

$$0 \approx V''(\bar{\phi}) \nabla^2 \delta\phi - \frac{k_r}{Da^2} \delta\phi \quad (4.60)$$

A new length scale clearly appears :  $\lambda_r = \sqrt{V''(\bar{\phi}) \frac{Da^2}{k_r}}$ . As long as the sizes of the domains are well below  $\lambda_r$ ,  $k_r$  will play no role in the concentration profile. To see that more clearly, let us note that equation 4.60 can be solved, and yields :

$$\delta\phi \propto \left(\frac{r}{\lambda_r}\right)^{1-\frac{d}{2}} K_{\frac{d}{2}-1} \left(\frac{r}{\lambda_r}\right) \quad (4.61)$$

In which  $K_m(r)$  is the modified Bessel function of the second kind (a solution to  $\nabla_r^2 X = X(r) - m/r^2$  in two dimensions). Because we assumed the laplacian term in 4.56 to be negligible, we know that  $\mu \propto \delta\phi + (\partial V/\partial\phi)_{\bar{\phi}}$ . The Gibbs-Thomson boundary condition (equation 4.29) still applies and we can write for a domain of size  $R$  and composition  $\phi_1$  (compare equations 4.31, 4.32) :

$$r < R \Rightarrow \mu(r) = \mu_1 = \frac{1}{\bar{\phi} - \phi_1} \left( V(\bar{\phi}) - V(\phi_1) - \frac{\sigma}{R} \right) \quad (4.62)$$

$$r > R \Rightarrow \mu(r) = V'(\bar{\phi}) + (\mu_1 - V'(\bar{\phi})) \left( \frac{r}{R} \right)^{1-\frac{d}{2}} \frac{K_{\frac{d}{2}-1}(r/\lambda_r)}{K_{\frac{d}{2}-1}(R/\lambda_r)} \quad (4.63)$$

Let us now find a scaling for  $\lambda_r$ . We can assume that  $V''(\bar{\phi}) \sim K/a^2$  (see equation 4.13), and typically  $K \sim 1$ . Using typical values  $D \approx 10^{-12} m^2.s^{-1}$ ,  $k_r \approx 1 min^{-1}$  (in yeast), one finds :  $\lambda_r > 10\mu m$ , which is two orders of magnitude larger than the critical size of domains to form buds, and  $\lambda_r$  is even one order of magnitude larger than the size of a cisterna. Therefore, in the issue at hand, we can expand the Bessel functions for small values of  $r/\lambda_r$ . Since  $K_m(x \rightarrow 0) \rightarrow x^{-m}$ , we find :

$$r > R \Rightarrow \mu(r) \approx V'(\bar{\phi}) + (\mu_1 - V'(\bar{\phi})) \left( \frac{r}{R} \right)^{2-d} \quad (4.64)$$

Eventually, we find the expression of  $\partial_r \mu$  to be very similar to the expression in the absence of maturation :

$$\partial_r \mu|_{R+\delta R} \propto (\mu_1 - V'(\bar{\phi})) \frac{1}{R} \quad \text{with} \quad \mu_1 = \frac{1}{\bar{\phi} - \phi_1} \left( V(\bar{\phi}) - V(\phi_1) - \frac{\sigma}{R} \right) \quad (4.65)$$

And in the limit  $R \ll \lambda_r$ , we find that the gradient of the chemical potential is unchanged by slow maturation. We also assumed that  $\phi_0$ , the value of  $\phi$  in the bulk is close to  $\bar{\phi}$ . During most of the growth process, this hypothesis does not apply. However, our argument that the maturation lengthscale  $\sqrt{D/k_r}$  is much larger than the sizes of interest should hold.

We therefore expect that as long as  $R \ll \sqrt{D/k_r}$  and  $k_r \ll \exp(-8J)D/a^2$ , we should find the same behavior for  $\mu$  as in the absence of maturation, and therefore we should find :

$$R_c^2 \dot{R}_c \propto \sigma \quad (4.66)$$

However,  $\sigma$  will depend upon time as  $\bar{\phi}$  changes with time.

### Influence of a changing line tension

As we mentioned in section 4.1.2, domain will spontaneously grow only if  $\bar{\phi}$  is between two values  $\phi_a$  and  $\phi_b$ , that correspond to the crossing of the critical line. As was shown earlier (see equation 4.66), we have :

$$\partial_t(R_c^3) \propto A\sigma \quad (4.67)$$

We expect  $\sigma$  to be strictly positive only for  $\phi_a < \bar{\phi} < \phi_b$ . More generally,  $\sigma$  depends on  $\bar{\phi}$  (see equation 4.30), which changes with time because of maturation. We should thus write :

$$R_c^3(t_b) \propto \int_{t_a}^{t_b} \sigma(t) dt \quad (4.68)$$

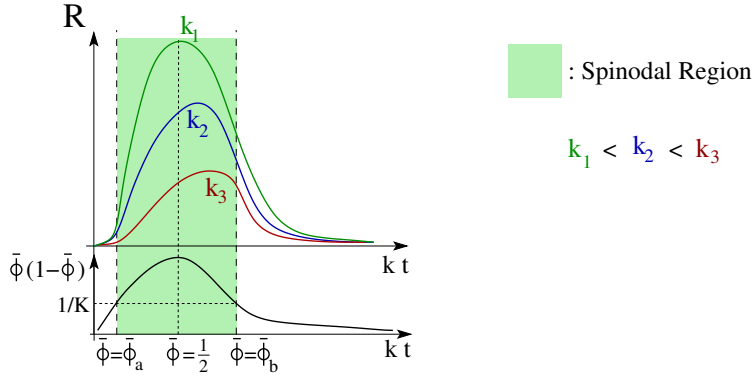


**Figure 4.7:** Cartoon of the expected mean radii of domains as a function of time for increasing chemical maturation rates  $k_1, k_2, k_3$ . For small rates (slow maturation) domain growth follows closely maturation and the maximum domain size is reached for  $\bar{\phi} \approx \frac{1}{2}$ . For large maturation rates, the maximum domain size is reached for  $\frac{1}{2} < \bar{\phi} < \phi_b$ .

In which  $t_a$  and  $t_b$  are the times at which  $\bar{\phi} = \phi_a$  and  $\bar{\phi} = \phi_b$  respectively, i.e. the times at which the phase separation begins, and ends, respectively. Since we are in a quasi-stationary regime,  $\sigma$  does not depend explicitly on time but depends only on the thermodynamic parameters of the system. We indeed realized in section 4.2.2 that in the absence of maturation,  $\sigma$  was constant as long as the Lifschitz-Slyozov-Wagner hypothesis applied. Here, the only thermodynamic parameter changing with time is  $\bar{\phi}$ , and equation 4.68 can be rewritten :

$$R^3 \propto \int_{\phi_a}^{\phi_b} \frac{1}{\bar{\phi}} \sigma(\bar{\phi}) d\bar{\phi} \quad (4.69)$$

Since we assumed  $\dot{\bar{\phi}} = k_r(1 - \bar{\phi})$ , we find :

$$R^3 \propto \frac{1}{k_r} \int_{\phi_a}^{\phi_b} \frac{1}{1 - \bar{\phi}} \sigma(\bar{\phi}) d\bar{\phi} \quad (4.70)$$

The integral is a constant depending only upon the function  $\sigma(\bar{\phi})$  and hence we showed that  $R^3 \propto k_r^{-\frac{1}{3}}$ , assuming the standard Lifschitz-Slyozov-Wagner hypothesis to be verified, and the average domain size to be much smaller than  $\sqrt{D/k_r}$ .

### 4.3.2 Application to domain budding in cisternae

We are interested in knowing if, for a given  $k_r$ , domains large enough to form buds will grow. Up to  $\bar{\phi} = 1/2$ ,  $B$  is the minority species and hence we must consider domains enriched in  $B$  in a bulk enriched in  $A$ . For  $\bar{\phi} > 1/2$ ,  $A$  is the minority species and we expect to see domains of  $A$  in a bulk of  $B$ . Therefore, the previous computation, which focused on the size of domains of  $B$ , will not give the actual sizes of domain in the system for  $\bar{\phi} > 1/2$  : as  $\bar{\phi}$  increases the density of  $A$  vanishes and the domains (of  $A$ ) will get smaller and smaller, until they all evaporate for  $\bar{\phi} > \phi_b$ . Therefore, there will exist a maximum domain size  $R_c^{max}$  on the membrane.

Let us consider a very slow maturation compared to domain growth. As  $\bar{\phi}$  increases from  $\phi_a$  to  $1/2$ , domains of  $B$  grow, and, in the limit of infinitely small maturation,  $B$

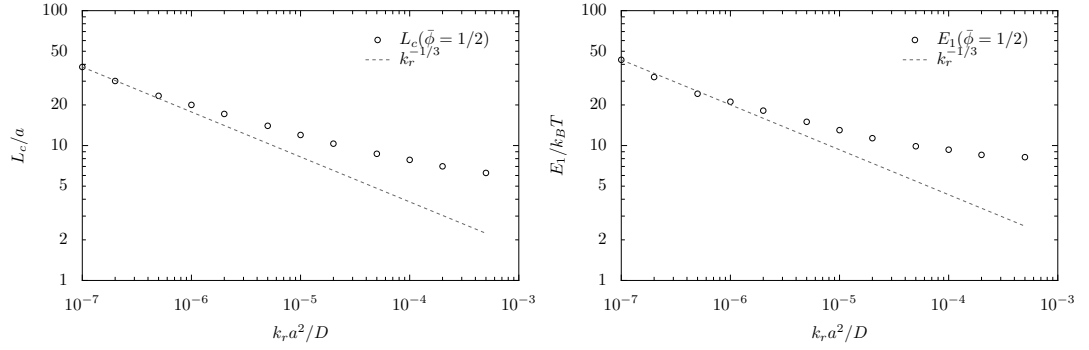


**Figure 4.8:** Monte-Carlo simulations of the correlation length  $L_c$  (left) and the interfacial energy per domain  $E_1$  (right) as a function of  $k_r$ , the chemical maturation rate, in units of  $D/a^2$ .  $R$  and  $E_1$  are shown for  $\bar{\phi} = \frac{1}{2}$ . The only thermodynamic parameter is  $J = 1.25k_B T$ , yielding a line tension  $\sigma \simeq 0.2k_B T/a$ .

forms a unique domain growing only as new  $B$  molecules are formed, until it spans the half of the membrane area at  $\bar{\phi} = 1/2$ . At that time, a domain of  $A$  occupies the other half. As soon as  $A$  becomes the minority species, the domain enriched in  $A$  shrinks. Therefore, if domain growth is much faster than the kinetics of maturation, we expect  $R_c^{max}$  to be reached at  $\bar{\phi} \approx \frac{1}{2}$ . In other limits, the situation is more complex, but we know that domains will evaporate for  $\bar{\phi} > \phi_b$ , and hence we expect  $R_c^{max}$  to be reached for  $\frac{1}{2} < \bar{\phi} < \phi_b$  (in which  $\phi_b$  is the value of  $\bar{\phi}$  for which the spinodal line is crossed the second time). This is illustrated in figure 4.7.

Because of this issue, we could not estimate the scaling of  $R_c^{max}$  except in the limit  $R_c^{max} \approx R_c(\bar{\phi} = 1/2)$ . Moreover, in section 4.2.2, we mentioned that the correlation length is a good measure of domain length for  $\bar{\phi} = 1/2$  only, and  $R_c^{max}$  cannot be estimated numerically with the correlation length.  $R_c(\bar{\phi} = 1/2)$  can be shown to obey the  $k^{-1/3}$  scaling by changing the integration interval in equation 4.70, yielding :

$$R_c^3 \left( \bar{\phi} = \frac{1}{2} \right) \propto \frac{1}{k_r} \int_{\phi_a}^{\frac{1}{2}} \frac{1}{1-\bar{\phi}} \sigma(\bar{\phi}) d\bar{\phi} \quad (4.71)$$

We can verify numerically if this scaling is indeed observed, but we need more tools to determine if the assumption  $R_c^{max} \approx R_c(\bar{\phi} = 1/2)$  is valid.

### 4.3.3 Numerical simulation

We could compare our predictions to the numerical simulation of a phase-separating membrane with maturation. To simulate such a system, we merely have to implement maturation in the algorithm presented in section 4.2.2.

Let us define  $P_{chem} = k_r a^2/D$ , the renormalized rate of chemical reaction, which we expect to be much smaller than 1. At each computation step, we choose a site at random. If it is occupied by an  $A$  molecule, it has a probability  $P_{chem}$  to be matured to a  $B$  molecule. Therefore, in the algorithm presented previously, we add at each new step :

```
#New step
if random(0 to 1) < Pchem :
```

```

#Chooses one site at random
i=random(1 to Lx)
j=random(1 to Ly)
if s[i,j]==-1:
    s{i,j}=1

```

In section 4.2.2, we observed a scaling  $R \propto t^{1/3}$  for  $t > 10^5 a^2/D$ . We therefore expect to see a scaling  $R \propto k_r^{-1/3}$  only for  $k_r < 10^{-5} D/a^2$ . We show here results from numerical simulations including maturation. As the correlation length is a good measure of the domain size only for  $\bar{\phi} = \frac{1}{2}$ , we computed the value of  $R$  for  $\bar{\phi} = \frac{1}{2}$ . The result is shown in figure 4.8.

As we can see in figure 4.8, we find the predicted scaling  $R_c \propto k_r^{-1/3}$  for  $k_r < 10^{-6} D/a^2$ . The scaling appears somehow for larger timescales (smaller  $k_r$ ) than it appears in the absence of maturation. This can be understood as the scaling requires additional assumptions, including small maturation rates.

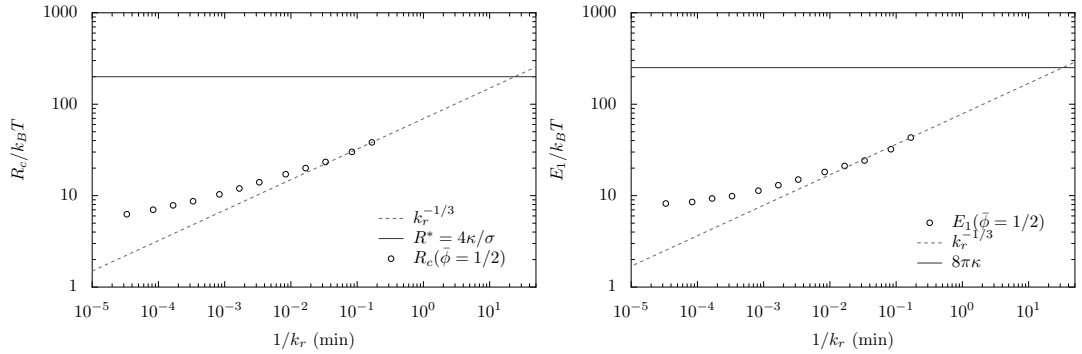


**Figure 4.9:** Extrapolation of the domain size (left) and the energy per domain (right) as functions of the inverse of the maturation rate  $k_r$ . For  $\kappa = 10k_B T$ , a rate of  $0.510^{-9}D/a^2$  is required, i.e.  $k_r \sim 1/30 \text{ min}^{-1}$ . We chose  $J = 1.25k_B T$ , yielding  $\sigma \sim 0.2k_B T/a$ .

## 4.4 Discussion

After studying the kinetics of phase separation in a two-dimensional membrane with conserved order parameter, we focused on phase separation kinetics in a membrane in which one species is generated progressively by a chemical reaction, with a rate  $k_r$ . We showed that in both cases we should expect a scaling of the mean domain size, growing like  $t^{1/3}$  (i.e. like  $k_r^{-1/3}$  in the case of chemical maturation). To show that this expansion of the Lifschitz-Slyozov-Wagner theory did apply to our biological system, we ran a Monte-Carlo simulation where the membrane was represented by a square lattice. Because of computational time constraints, we limited ourselves to small grid sizes (though simulations on larger grids showed qualitatively the same behavior). In order to mimic lipids in the Golgi apparatus, we assumed a grid size  $a \approx 1nm$ , a diffusion coefficient  $D \approx \mu m^2 s^{-1}$ , an interaction energy  $J = 1.25k_B T$  with the nearest neighbors, yielding a line tension of order  $0.2k_B T$ .

Our simulation do exhibit the predicted scaling, though at larger times than in the absence of maturation, which is likely because of the more restrictive hypothesis required for the scaling when maturation takes place. We extrapolated our results to have a scaling of the reaction rate  $k_r$  required for the formation of large enough domains, which can form buds (figure 4.9). We know that buds are thermodynamically favorable for line energies per domain larger than  $8\pi\kappa$ , i.e. for domains of size  $R > 4\kappa/\sigma$ . With our choice of  $D, a, \sigma$ , we find that the maximal reaction rate allowing domain budding is  $k_r^{max} \sim 0.5 \cdot 10^{-9}D/a^2 \approx 1/35 \text{ min}^{-1}$ , which is slightly smaller than the typical the order of magnitude of reaction rates in the mammalian Golgi apparatus. This extrapolation is illustrated in figure 4.9.

According to this extrapolation, a cisterna in the mammalian Golgi apparatus should not form complete bud as the reaction rate is slightly too high ; however the order of magnitude of the estimated maximal reaction rate is quite close to the reaction rate in mammals. Since we only reasoned on orders of magnitude, this result is quite satisfactory. We chose  $\sigma \approx 0.8pN$  at  $\bar{\phi} = 1/2$ , which is not the maximal tension (tensions up to  $3.3pN$  have been measured [24]). As Lifschitz-Slyozov-Wagner theory predicts  $L \propto (\sigma t)^{1/3}$ , and as  $R_c = 4\kappa/\sigma$ , slightly higher line tensions could increase significantly the maximum reaction rate allowing bud formation. Moreover, many factors could actually facilitate budding,

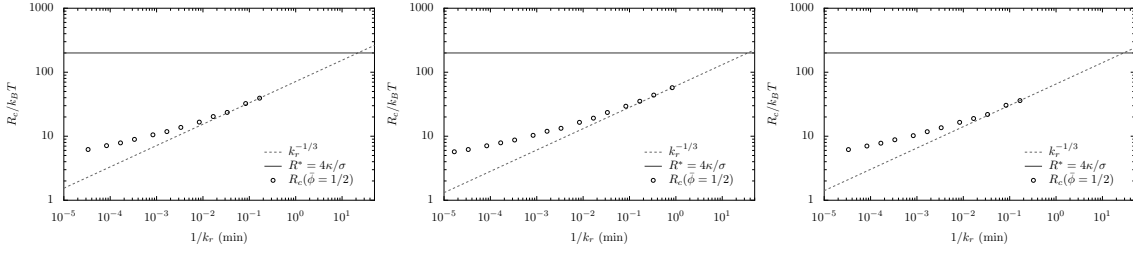


**Figure 4.10:** Extrapolation of the domain size as a function of the inverse of the maturation rate  $k_r$ , for various system sizes. Left :  $L_x = L_y = 128 a$ , center :  $L_x = L_y = 200 a$ , right :  $L_x = L_y = 256 a$ .

For  $\kappa = 10k_B T$ , we find  $20 \text{ min} < 1/k_r^* < 40 \text{ min}$ . We chose  $J = 1.25k_B T$ , yielding  $\sigma \sim 0.2k_B T/a$ . The size of the simulation box seem to little influence the scaling behavior and the maximal maturation rate to form buds.

such as the existence of proteins favoring a non-zero spontaneous curvature.

One might be concerned that the spatial and time scales of our simulations are well below the time and space scales of the actual, biological system. Concerning the time scale, it is no concern as the smallest  $k_r$ , the more valid the approximations leading to the  $k_r^{-1/3}$  scaling. To test whether the grid size could affect the scaling and the maximum reaction rate allowing the formation of buds,  $k_r^*$ , we performed the simulation on various grid sizes. In figure 4.10, we show that for grids of size  $128 * 128$ ,  $200 * 200$  and  $256 * 256$ .  $k_r^*$  does not seem to be affected by the grid size.

We focused each time on the mean domain size at  $\bar{\phi} = 1/2$ , which we called  $R_c(\bar{\phi} = 1/2)$ . Actually, we are interested in the maximum domain size during the maturation,  $R_c^{max}$ , which could take place for  $\bar{\phi} > 1/2$ . We therefore need a computational tool to measure  $R_c$  for  $\bar{\phi} \neq 1/2$ . Since we are interested in domains of size  $R_c \approx 0.2 - 0.4 \mu m$  in cisternae of size  $L \sim 1 \mu m$ , we expect the size of domains to be close to the system size, and because the argument proposed in section 4.3.1, we expect  $R_c^{max} \approx R_c(\bar{\phi} = 1/2)$ .

In figure 4.11 (right), we show a snapshot of the system for  $k_r = 10^{-5} D/a^2$ , at  $\bar{\phi} = 1/2$ . Interestingly, the domains are much more circular than in the absence of maturation. This can be explained as when domains start to form, at  $\bar{\phi} = \phi_a$ , only a few domains will form as few  $B$  molecules are available. Therefore, domains will tend to be far away from each other. As  $\bar{\phi}$  increase, newly formed  $B$  molecules will mostly join existing domains, and therefore domains will be more distinct than in a system starting from  $\bar{\phi} = 0$ . The fact that domains are circular rather than serpentine is encouraging for our goal of comparing the domain size to a critical radius for domains to form bud. Moreover, the expression of  $\sigma \approx E_1/2\pi R_c$  is rather convincing in this case. As we find the same value  $\sigma \sim 0.2k_B T/a$  (as illustrated in figure 4.11, left) as in the serpentine phase (without maturation), we can be confident that our approximation for  $\sigma$  is not dependent on the geometry of domains.

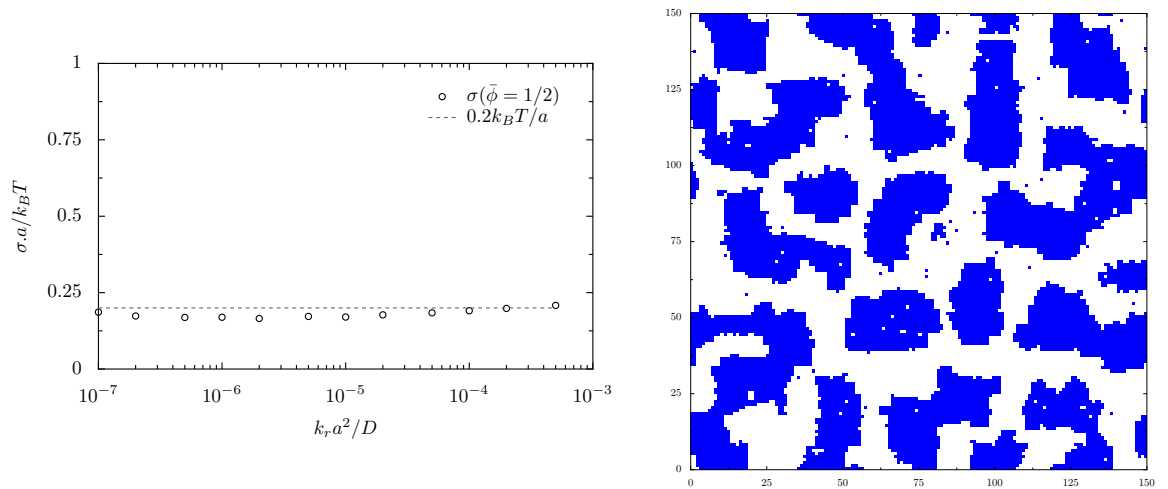


**Figure 4.11:** LEFT : Approximation of the surface tension  $\sigma$  computed from equation 4.52, as a function of  $k_r$  (in units of  $D/a^2$ ). The surface tension is averaged over sixteen simulations. RIGHT : An illustration of the system at  $k_r = 10^{-5} D/a^2$ . In the presence of maturation, the domains are much more circular and the serpentine phase can be seen only partially. The measured correlation length corresponding to this system is  $12.5 a$ .

## Conclusion

In this chapter, we showed that the size of membrane domains in the cisternae of the Golgi apparatus can be controlled by the maturation rate  $k_r$ . Theoretical arguments and simulation indicate that the size of domains grow like  $k_r^{-1/3}$ , for small enough values of  $k_r$ . Using typical values of the diffusion coefficient, the lipid size, and the line tension, we find that the typical reaction time has to be of the order of twenty to forty minutes, which is the typical maturation time in the Golgi apparatus of mammals. On the other hand, maturation is faster in Yeast, the Golgi apparatus of which do not exhibit a stacked structure. It is therefore a convincing argument that the structure of the Golgi apparatus can be controlled by the reaction rate.

However, in the computation of domain growth, we only considered the diffusion of the individual lipid molecules, hence the Lifschitz-Slyozov-Wagner scaling. It has been shown that other scalings can be expected [124]. For instance, at large lengthscales, the hydrodynamic regime in  $t^{1/2}$  should dominate. To know whether the  $t^{1/3}$  is indeed dominant in the membrane, we would be highly interested in experimental comparisons. Since it is possible to fluorescently tag lipids such as ceramids and sphingolipids, we would like to compare our theory to a model experimental system. It could also be of high interest to use more advanced numerical methods. For instance molecular dynamics of the continuous Hamiltonian, solved in Fourier space, have been shown a powerful tool to study phase transitions. Such methods could permit, using the coarse-grained Hamiltonian, the study of large timescales (many minutes) and lengthscales (a few micrometers).

However, we demonstrated a possible mechanism allowing the internal properties of an organelle (here, the maturation rate in the Golgi apparatus) to control its structure. This internal control is the very definition of self-organization, the ability for a structure

or pattern to be created without external control. The sequel is to integrate this self-organization ability into a dynamic system including the fluxes from the endoplasmic reticulum, the exchange between compartments, and the export to the cell.

# Conclusion

“ How many miles to Avalon?  
None, I say, and all.  
The silver towers are fallen. ”

---

Roger Zelzany, **The guns of Avalon**

In this thesis, it appeared clearly that membranes are not passive bystanders in cell life. We realized in chapter 1 that the composition of a membrane can enable it to selectively allow the entrance of certain molecules or bodies. A membrane rich in GM1 will allow the formation of tubules by SV40 viruses, and these tubules will be pinched off and offer viruses a gateway to the cell. Though tubule formation is passive, it is a specific mechanism based on the affinity of SV40 for GM1. The fact that membrane properties influence transport is a very general phenomenon, and is not restricted to the entry of pathogens. In chapter 2, we saw how a gradient of chemical or physical properties along an organelle, the Golgi apparatus, could allow both forward transport, backward transport, and quasi stationary localization. We showed in that chapter that lateral interactions between membrane components can play a role in transport mechanisms : as the mean composition changes gradually in the cisternae, the lateral interactions in the membrane also change along the gradient, and an energy landscape is generated.

Beyond thermodynamics, we may also be interested in the kinetic effects of membrane identity, which can be mapped to an energy landscape only in some cases, and with some difficulties of interpretation. The membrane of organelles contains molecular tags to be recognized by vesicles, including the SNARE proteins, which act as complementary pairs of anchors, enabling the recognition and fusion of a vesicle with a cellular compartment. As those tag molecules are both transported and actors in the transport processes, some non-linear effects appear, yielding to the building and maintenance of intra-cellular gradients. Interestingly, the non-linearities do not only modify the stationary states of the system but also its dynamic behavior, e.g. how an organelle involved in the processing of immature proteins will react to a high influx of molecules to be processed. We could show that the non-linearities caused by molecular recognition allows the organelle to process any incoming flux of molecules without exporting a large amount of unprocessed molecules.

The emergence of compartment identity by non-linear transport including molecular recognition can be seen as a self-organization property, as the compartments do not need a central authority to be heterogeneous. We wanted to go further in this direction by studying how a series of differentiated sub-compartments (namely, the cisternae of the

Golgi apparatus) could emerge from one homogeneous compartment. We show that the structure of the Golgi apparatus could be controlled by the kinetics of chemical reaction in the organelle. The actual biological picture is actually more complex, as the transport properties and the building of the structure of the Golgi apparatus cannot be separated, and we need to reunite in a single model our three approaches to studying the Golgi apparatus. For instance, we are highly interested in adding fluxes to the phase separation model (chapter 4), in order to model the influx from the E.R., the inter-cisternal flux, and the export to the cell. In fact, we would like integrate in a single model all the "bricks" presented in chapters 2, 3 and 4.

The first step towards such an integration has already been done chapter 4, as new cisternae emerge with a different lipid composition than their precursor. This lipid composition is an important part of organelle identity, and moreover the localization of transmembrane protein depends on lipid composition. Some transmembrane proteins control the recruiting of Arg-GTPase, which is involved in turn in the building of COP coated vesicles. Therefore, the system composed of the new cisterna and its precursor will have an asymmetric composition in transport-related species, and we hope to use the tools from chapter 3 to study transport in this system. A conceptual model has been developed by S. Pfeffer [56] including generation of new cisternae, maintenance of cisternal identity and transport controlled by Rab GTPases, an essential component of membrane identity. We would now like to achieve such a model in more formal manner.

The disruption of the Golgi apparatus has been observed in many neuro-degenerative diseases, but location in the causal chain is still unknown. We believe that having a clearer picture of the interactions between structure, dynamics, and function in the Golgi apparatus, as we are *en route* to, is a necessary step in understanding such diseases. It is clear that much is left to unveil, but combining biology and physics seem a promising way to understand this organelle.

On the physics side, though the living cell is a fundamentally out of equilibrium system, we could learn much by using tools from equilibrium thermodynamics, by assuming the kinetics to be close to equilibrium kinetics. However, as we saw in chapter 3, this is not always possible. Reuniting close to equilibrium dynamics to far from equilibrium dynamics cannot be expected to be easy. However, recent works show that equilibrium tools such as the fluctuation-dissipation theorem can be modified to work in out-of-equilibrium systems, and we can hope that a complete picture of the Golgi apparatus can be drawn, using close to equilibrium and out of equilibrium tools in a single framework. The tools and concepts we used in this thesis are not restricted to the study of cellular organelles, and it could be of high interest to use them in the study of self-organization, transport, and identity at the multi-cellular scale. For instance, embryogenesis can be seen as a self-organizing process in which identity appears by symmetry breaking, identity being both generating, and induced by, gradients of growth factors in the embryo.

# Bibliography

- [1] J.L. Goldstein, R.G.W. Anderson, and M.S. Brown. Coated pits, coated vesicles, and receptor-mediated endocytosis. *Nature*, 279(5715):679–685, 1979. [1](#)
- [2] S. Mukherjee, R.N. Ghosh, and F.R. Maxfield. Endocytosis. *Physiological Reviews*, 77(3):759, 1997. [1](#)
- [3] J.L. Goldstein, M.S. Brown, R.G.W. Anderson, D.W. Russell, and W.J. Schneider. Receptor-mediated endocytosis: concepts emerging from the ldl receptor system. *Annual review of cell biology*, 1(1):1–39, 1985. [1](#)
- [4] T.G. Chappell, W.J. Welch, D.M. Schlossman, K.B. Palter, M.J. Schlesinger, and J.E. Rothman. Uncoating atpase is a member of the 70 kilodalton family of stress proteins. *Cell*, 45(1):3–13, 1986. [1](#)
- [5] MT Pho, A. Ashok, and W.J. Atwood. Jc virus enters human glial cells by clathrin-dependent receptor-mediated endocytosis. *Journal of Virology*, 74(5):2288, 2000. [2](#)
- [6] E. Blanchard, S. Belouzard, L. Goueslain, T. Wakita, J. Dubuisson, C. Wychowski, and Y. Rouillé. Hepatitis c virus entry depends on clathrin-mediated endocytosis. *Journal of virology*, 80(14):6964, 2006. [2](#)
- [7] A.P. Bhavsar, J.A. Guttman, B.B. Finlay, et al. Manipulation of host-cell pathways by bacterial pathogens. *Nature*, 449(7164):827–834, 2007. [2](#)
- [8] M. Marsh and A. Helenius. Virus entry: open sesame. *Cell*, 124(4):729–740, 2006. [2](#)
- [9] MM Perry and A.B. Gilbert. Yolk transport in the ovarian follicle of the hen (*Gallus domesticus*): lipoprotein-like particles at the periphery of the oocyte in the rapid growth phase. *Journal of cell science*, 39(1):257, 1979. [2](#)
- [10] S. Mayor and R.E. Pagano. Pathways of clathrin-independent endocytosis. *Nature reviews Molecular cell biology*, 8(8):603–612, 2007. [2](#)
- [11] B. Tsai, J.M. Gilbert, T. Stehle, W. Lencer, T.L. Benjamin, and T.A. Rapoport. Gangliosides are receptors for murine polyoma virus and sv40. *The EMBO Journal*, 22(17):4346–4355, 2003. [2](#), [20](#)
- [12] M.S. Jacewicz, M. Mobassaleh, S.K. Gross, KA Balasubramanian, P.F. Daniel, S. Raghavan, R.H. McCluer, and G.T. Keusch. Pathogenesis of shigella diarrhea: Xvii. a mammalian cell membrane glycolipid, gb3, is required but not sufficient to confer sensitivity to shiga toxin. *Journal of Infectious Diseases*, 169(3):538, 1994. [2](#)

- [13] H. Ewers, W. Römer, A.E. Smith, K. Bacia, S. Dmitrieff, W. Chai, R. Mancini, J. Kartenbeck, V. Chambon, L. Berland, et al. Gm1 structure determines sv40-induced membrane invagination and infection. *Nature cell biology*, 12(1):11–18, 2009. [2](#), [18](#), [20](#)
- [14] S. Tzlil, M. Deserno, W.M. Gelbart, and A. Ben-Shaul. A statistical-thermodynamic model of viral budding. *Biophysical journal*, 86(4):2037–2048, 2004. [2](#)
- [15] Markus Deserno and William Gelbart. Adhesion and wrapping in colloid-vesicle complexes. *Journal of Physical Chemistry B*, 106:5543–5552, 2002. [2](#), [5](#), [17](#)
- [16] M. Deserno and T. Bickel. Wrapping of a spherical colloid by a fluid membrane. *Europhysics letters*, 62:767–773, 2003. [2](#), [5](#), [11](#)
- [17] B.J. Reynwar, G. Illya, V.A. Harmandaris, M.M. Muller, K. Kremer, and M. Deserno. Aggregation and vesiculation of membrane proteins by curvature-mediated interactions. *NATURE-LONDON-*, 447(7143):461, 2007. [2](#), [17](#)
- [18] W. Römer, L. Berland, V. Chambon, K. Gaus, B. Windschiegl, D. Tenza, M.R.E. Aly, V. Fraissier, J.C. Florent, D. Perrais, et al. Shiga toxin induces tubular membrane invaginations for its uptake into cells. *Nature*, 450(7170):670–675, 2007. [2](#), [10](#), [18](#)
- [19] W. Helfrich. Elastic properties of lipid bilayers: theory and possible experiments. *Z. Naturforsch*, 28(11):693–703, 1973. [4](#)
- [20] W. Helfrich and R.M. Servuss. Undulations, steric interaction and cohesion of fluid membranes. *Il Nuovo Cimento D*, 3(1):137–151, 1984. [4](#)
- [21] E. Evans and W. Rawicz. Entropy-driven tension and bending elasticity in condensed-fluid membranes. *Phys. Rev. Let.*, 64(17):2094–2097, Jan 1990. [4](#), [54](#)
- [22] Matthew S. Turner and Pierre Sens. Gating-by-tilt of mechanically sensitive membrane channels. *Physical Review Letters*, 93, 2004. [5](#)
- [23] S.A. Safran. *Statistical thermodynamics of surfaces, interfaces, and membranes*, volume 194. Westview Press Boulder, CO, 2003. [7](#), [72](#), [94](#), [95](#)
- [24] A. Tian, C. Johnson, W. Wang, and T. Baumgart. Line tension at fluid membrane domain boundaries measured by micropipette aspiration. *Physical review letters*, 98(20):208102, 2007. [7](#), [106](#), [113](#)
- [25] T.L. Hill. *An introduction to statistical thermodynamics*. Dover Pubns, 1960. [7](#), [72](#)
- [26] R. Lipowsky. Budding of membranes induced by intramembrane domains. *Journal de Physique II*, 2(10):1825–1840, 1992. [8](#)
- [27] F. Julicher and R. Lipowsky. Domain-induced budding of vesicles. *Physical review letters*, 70(19):2964–2967, 1993. [8](#)
- [28] RC Liddington, Y. Yan, J. Moulai, R. Sahli, TL Benjamin, and SC Harrison. Structure of simian virus 40 at 3.8-Å resolution. *Nature*, 354(6351):278, 1991. [9](#), [20](#)
- [29] W.B. Turnbull, L. Bernie, and S.W. Homans. Dissecting the cholera toxin-ganglioside gm1 interaction by isothermal titration calorimetry. *Journal of the American Chemical Society*, 126(4):1047–1054, 2004. [10](#), [20](#)

- [30] Lionel Foret and Pierre Sens. Kinetic regulation of coated vesicle secretion. *Proceedings of the National Academy of Sciences*, Accepted, 2008. [12](#)
- [31] HA Kramers. Brownian motion in a field of force and the diffusion model of chemical reactions. *Physica*, 7(4):284–304, 1940. [12](#)
- [32] C.B. Hirschberg and M.D. Snider. Topography of glycosylation in the rough endoplasmic reticulum and golgi apparatus. *Annual review of biochemistry*, 56(1):63–87, 1987. [29](#)
- [33] G. Griffiths and K. Simons. The trans golgi network: sorting at the exit site of the golgi complex. *Science*, 234(4775):438, 1986. [29](#)
- [34] Brad J. Marsh et al. Direct continuities between cisternae at different levels of the golgi complex in glucose-stimulated mouse islet beta cells. *Proceedings of the National Academy of Sciences*, 101:5565–5570, 2004. [29](#), [32](#), [52](#), [53](#), [56](#)
- [35] G. van Meer. Lipids of the golgi membrane. *Trends in Cell Biology*, 8(1):29–33, 1998. [29](#)
- [36] S. Munro. The golgi apparatus: defining the identity of golgi membranes. *Current opinion in cell biology*, 17(4):395–401, 2005. [29](#), [67](#)
- [37] S.I. Bannykh, N. Nishimura, and W.E. Balch. Getting into the golgi. *Trends in Cell Biology*, 8(1):21–25, 1998. [29](#)
- [38] J. Lippincott-Schwartz, J.G. Donaldson, A. Schweizer, E.G. Berger, H.P. Hauri, L.C. Yuan, and R.D. Klausner. Microtubule-dependent retrograde transport of proteins into the er in the presence of brefeldin a suggests an er recycling pathway. *Cell*, 60(5):821–836, 1990. [30](#)
- [39] J.S. Bonifacino and R. Rojas. Retrograde transport from endosomes to the trans-golgi network. *Nature Reviews Molecular Cell Biology*, 7(8):568–579, 2006. [30](#)
- [40] K. Sandvig, O. Garred, K. Prydz, JV Kozlov, SH Hansen, and V. van Deurs. Retrograde transport of endocytosed shiga toxin to the endoplasmic reticulum. *Nature*, 358(6386):510–512, 1992. [30](#)
- [41] S. Munro. Localization of proteins to the golgi apparatus. *Trends in Cell Biology*, 8(1):11–15, 1998. [30](#)
- [42] C. Rabouille, N. Hui, F. Hunte, R. Kieckbusch, E.G. Berger, G. Warren, and T. Nilsson. Mapping the distribution of golgi enzymes involved in the construction of complex oligosaccharides. *Journal of Cell Science*, 108(4):1617, 1995. [30](#)
- [43] N. Jourdan, M. Maurice, D. Delautier, A.M. Quero, A.L. Servin, and G. Trugnan. Rotavirus is released from the apical surface of cultured human intestinal cells through nonconventional vesicular transport that bypasses the golgi apparatus. *Journal of virology*, 71(11):8268, 1997. [30](#)
- [44] I. Hara-Nishimura, T. Shimada, K. Hatano, Y. Takeuchi, and M. Nishimura. Transport of storage proteins to protein storage vacuoles is mediated by large precursor-accumulating vesicles. *The Plant Cell Online*, 10(5):825, 1998. [30](#)

- [45] M. Elsner, H. Hashimoto, and T. Nilsson. Cisternal maturation and vesicle transport: join the band wagon!(review). *Molecular membrane biology*, 20(3):221–229, 2003. [30](#)
- [46] G. H. Patterson, K. Hirschberg, R. S. Polishchuk, D. Gerlich, R. D. Phair, and J. Lippincott-Schwartz. Transport through the golgi apparatus by rapid partitioning within a two-phase membrane system. *Cell*, 133:1055–1067, 2008. [31](#), [32](#), [41](#), [42](#), [44](#), [52](#), [85](#)
- [47] M. Poudret, A. Arnould, J.P. Comet, P. Le Gall, P. Meseure, and F. Képès. Topology-based abstraction of complex biological systems: application to the golgi apparatus. *Theory in Biosciences*, 127(2):79–88, 2008. [31](#)
- [48] L. Bonfanti, A.A. Mironov Jr, J.A. Martínez-Menárguez, O. Martella, A. Fusella, M. Baldassarre, R. Buccione, and H.J. Geuze. Procollagen Traverses the Golgi Stack without Leaving the Lumen of Cisternae:: Evidence for Cisternal Maturation. *Cell*, 95(7):993–1003, 1998. [32](#), [42](#), [44](#)
- [49] Yanzhuang Wang et al. *The EMBO Journal*, pages 3279–3290. [32](#), [52](#), [85](#)
- [50] S. Manley, J.M. Gillette, G.H. Patterson, H. Shroff, H.F. Hess, E. Betzig, and J. Lippincott-Schwartz. High-density mapping of single-molecule trajectories with photoactivated localization microscopy. *Nature Methods*, 5(2):155–158, 2008. [32](#), [33](#), [52](#)
- [51] N.B. Cole, C.L. Smith, N. Sciaky, M. Terasaki, M. Edidin, and J. Lippincott-Schwartz. Diffusional mobility of Golgi proteins in membranes of living cells. *Science*, 273(5276):797, 1996. [32](#), [33](#), [52](#)
- [52] W.H. Press, S.A. Teukolsky, W.T. Vetterling, and B.P. Flannery. *Numerical recipes in Fortran; the art of scientific computing*. Cambridge university press, 1993. [34](#), [39](#)
- [53] P. Espanol and P. Warren. Statistical mechanics of dissipative particle dynamics. *EPL (Europhysics Letters)*, 30:191, 1995. [34](#)
- [54] A. Trucco, R. S. Polishchuk, O. Martella, A. Di Pentima, A. Fusella, D. Di Giandomenico, E. San Pietro, G. V. Beznoussenko, E. V. Polishchuk, M. Baldassarre, R. Buccione, W. J. C. Geerts, A. J. Koster, K. N. J. Burger, A. A. Mironov, and A. Luini. Secretory traffic triggers the formation of tubular continuities across golgi sub-compartments. *Nat Cell Biol*, 6(11):1071–1081, 2004. [44](#), [53](#), [81](#), [85](#)
- [55] R.S. Polishchuk, E.V. Polishchuk, P. Marra, S. Alberti, R. Buccione, A. Luini, and A.A. Mironov. Correlative light-electron microscopy reveals the tubular-saccular ultrastructure of carriers operating between golgi apparatus and plasma membrane. *The Journal of cell biology*, 148(1):45, 2000. [46](#)
- [56] S.R. Pfeffer. How the golgi works: A cisternal progenitor model. *Proceedings of the National Academy of Sciences*, 107(46):19614, 2010. [46](#), [118](#)
- [57] A.S. Opat, C. van Vliet, and P.A. Gleeson. Trafficking and localisation of resident golgi glycosylation enzymes. *Biochimie*, 83(8):763–773, 2001. [47](#)
- [58] F. Jülicher, A. Ajdari, and J. Prost. Modeling molecular motors. *Reviews of Modern Physics*, 69(4):1269, 1997. [47](#)

- [59] R. Kubo. The fluctuation-dissipation theorem. *Reports on Progress in Physics*, 29(1):255–284, 1966. [48](#)
- [60] C. Wilson and A. Ragnini-Wilson. Conserved molecular mechanisms underlying homeostasis of the golgi complex. *International Journal of Cell Biology*, Article ID 758230, 2010. [49](#), [66](#)
- [61] J. Derganc. Curvature-driven lateral segregation of membrane constituents in golgi cisternae. *Physical Biology*, 4:317, 2007. [53](#)
- [62] B. Sorre, A. Callan-Jones, J.B. Manneville, P. Nassoy, J.F. Joanny, J. Prost, B. Goud, and P. Bassereau. Curvature-driven lipid sorting needs proximity to a demixing point and is aided by proteins. *Proceedings of the National Academy of Sciences*, 106(14):5622, 2009. [53](#)
- [63] A. Roux, D. Cuvelier, P. Nassoy, J. Prost, P. Bassereau, and B. Goud. Role of curvature and phase transition in lipid sorting and fission of membrane tubules. *The EMBO Journal*, 24(8):1537–1545, 2005. [53](#)
- [64] U. Seifert. Curvature-induced lateral phase segregation in two-component vesicles. *Physical review letters*, 70(9):1335–1338, 1993. [53](#)
- [65] S. Roche, S. Bressanelli, F.A. Rey, and Y. Gaudin. Crystal structure of the low-ph form of the vesicular stomatitis virus glycoprotein g. *Science*, 313(5784):187, 2006. [53](#)
- [66] P.A. Gleeson. Targeting of proteins to the golgi apparatus. *Histochemistry and cell biology*, 109(5):517–532, 1998. [53](#)
- [67] D.K. Banfield, M.J. Lewis, C. Rabouille, G. Warren, and H.R.B. Pelham. Localization of sed5, a putative vesicle targeting molecule, to the cis-golgi network involves both its transmembrane and cytoplasmic domains. *The Journal of cell biology*, pages 357–371, 1994. [53](#)
- [68] J. Burke, JM Pettitt, H. Schachter, M. Sarkar, and PA Gleeson. The transmembrane and flanking sequences of beta 1, 2-n-acetylglucosaminyltransferase i specify medial-golgi localization. *Journal of Biological Chemistry*, 267(34):24433, 1992. [53](#)
- [69] J. Antoinette Killian. Hydrophobic mismatch between proteins and lipids in membranes. *Biochimica et Biophysica Acta*, 1376:401–415, 1998. [54](#)
- [70] Richard J. Webb et al. Hydrophobic mismatch and the incorporation of peptides into lipid bilayers: A possible mechanism for retention in the golgi. *Biochemistry*, 37:673–679, 1998. [54](#)
- [71] J. Fullekrug and T. Nilsson. Protein sorting in the Golgi complex. *BBA-Molecular Cell Research*, 1404(1-2):77–84, 1998. [54](#)
- [72] K. Mitra, I. Ubarretxena-Belandia, T. Taguchi, G. Warren, and D.M. Engelman. Modulation of the bilayer thickness of exocytic pathway membranes by membrane proteins rather than cholesterol. *Proceedings of the National Academy of Sciences*, 101(12):4083–4088, 2004. [54](#)
- [73] C.E. Machamer. Targeting and retention of Golgi membrane proteins. *Current opinion in cell biology*, 5(4):606–612, 1993. [54](#)

- [74] J. C. Rayner and H. R. B. Pelham. Transmembrane domain-dependent sorting of proteins to the ER and plasma membrane in yeast. *EMBO J.*, 16:1832–1841, 1997. [54](#)
- [75] R. Phillips, T. Ursell, P. Wiggins, and P. Sens. Emerging roles for lipids in shaping membrane-protein function. *Nature*, 459:379–385, 2009. [54](#)
- [76] S. Redner. *A guide to first-passage processes*. Cambridge Univ Pr, 2001. [56](#)
- [77] C. W. Gardiner. *Handbook of stochastic methods*. Springer Berlin, 1985. [56](#)
- [78] O. Bénichou, M. Coppey, M. Moreau, P. H. Suet, and R. Voituriez. Optimal search strategies for hidden targets. *Physical review letters*, 94(19):198101, 2005. [56](#)
- [79] J. A. McNew, F. Parlati, R. Fukuda, R. J. Johnston, K. Paz, F. Paumet, T. H. Söllner, and J. E. Rothman. Compartmental specificity of cellular membrane fusion encoded in snare proteins. *Nature*, 407(6801):153–159, 2000. [65](#)
- [80] J. Lippincott-Schwartz, T. H. Roberts, and K. Hirschberg. Secretory protein trafficking and organelle dynamics in living cells. *Annu. Rev. Cell Dev. Biol.*, 16:557–89, 2000. [66](#), [85](#)
- [81] T. Misteli. The concept of self-organization in cellular architecture. *J Cell Biol*, 155:181–185, 2001. [66](#)
- [82] Y. A. Chen and R. H. Scheller. SNARE-mediated membrane fusion. *Nature Reviews Molecular Cell Biology*, 2(2):98–106, 2001. [66](#), [68](#), [69](#)
- [83] K. Matsuura-Tokita, M. Takeuchi, A. Ichihara, K. Mikuriya, and A. Nakano. Live imaging of yeast Golgi cisternal maturation. *Nature*, 441(7096):1007–1010, 2006. [66](#), [85](#), [91](#), [92](#)
- [84] R. Behnia and S. Munro. Organelle identity and the signposts for membrane traffic. *Nature*, 438(7068):597–604, 2005. [67](#)
- [85] Reinhart Heinrich and Tom A. Rapoport. Generation of nonidentical compartments in vesicular transport systems. *J Cell Biol*, 168:271–280, 2005. [67](#), [69](#), [70](#)
- [86] B. Binder, A. Goede, N. Berndt, and H. G. Holzhutter. A conceptual mathematical model of the dynamic self-organisation of distinct cellular organelles. *PloS one*, 4(12):e8295, 2009. [67](#), [69](#)
- [87] Kühnle J, J. Shillcock, O. G. Mouritsen, and M. Weiss. A modeling approach to the self-assembly of the Golgi apparatus. *Biophys. J.*, 98:2839–2847, 2010. [67](#), [69](#)
- [88] N. Van Kampen. *Stochastic Processes in Physics and Chemistry*. Elsevier, 2007. [68](#)
- [89] M. Bremser, W. Nickel, M. Schweikert, M. Ravazzola, M. Amherdt, C. A. Hughes, T. H. Söllner, J. E. Rothman, and F. T. Wieland. Coupling of coat assembly and vesicle budding to packaging of putative cargo receptors. *Cell*, 96(4):495–506, 1999. [68](#), [69](#)
- [90] N. B. Cole and J. Lippincott-Schwartz. Organization of organelles and membrane traffic by microtubules. *Current opinion in cell biology*, 7(1):55–64, 1995. [68](#)
- [91] M. A. Welte. Bidirectional transport along microtubules. *Current Biology*, 14(13):R525–R537, 2004. [68](#)

- [92] J.S. Bonifacino and B.S. Glick. The mechanisms of vesicle budding and fusion. *Cell*, 116(2):153–166, 2004. 68
- [93] I. Jordens, M. Fernandez-Borja, M. Marsman, S. Dusseljee, L. Janssen, J. Calafat, H. Janssen, R. Wubbolts, and J. Neefjes. The Rab7 effector protein RILP controls lysosomal transport by inducing the recruitment of dynein-dynactin motors. *Current Biology*, 11(21):1680–1685, 2001. 68
- [94] J.P. Caviston and E.L.F. Holzbaur. Microtubule motors at the intersection of trafficking and transport. *Trends in cell biology*, 16(10):530–537, 2006. 68, 69
- [95] L. Michaelis and M.L. Menten. Die kinetik der invertinwirkung. *Biochem. Z*, 49(333-369):352, 1913. 69
- [96] J. Hardy. Amyloid, the presenilins and alzheimer’s disease. *Trends in neurosciences*, 20(4):154–159, 1997. 85
- [97] N.K. Gonatas, A. Stieber, and J.O. Gonatas. Fragmentation of the Golgi apparatus in neurodegenerative diseases and cell death. *Journal of the neurological sciences*, 246(1-2):21–30, 2006. 85
- [98] C.E. Machamer. Golgi disassembly in apoptosis: cause or effect? *Trends in cell biology*, 13(6):279–281, 2003. 85
- [99] J.D. Lane, J. Lucocq, J. Pryde, F.A. Barr, P.G. Woodman, V.J. Allan, and M. Lowe. Caspase-mediated cleavage of the stacking protein grasp65 is required for golgi fragmentation during apoptosis. *The Journal of cell biology*, 156(3):495, 2002. 85
- [100] JL Ullman. On a theorem of frobenius. *The Michigan mathematical journal*, 1(2):189–193, 1952. 87
- [101] E. Losev, C.A. Reinke, J. Jellen, D.E. Strongin, B.J. Bevis, and B.S. Glick. Golgi maturation visualized in living yeast. *Nature*, 441(7096):1002–1006, 2006. 91
- [102] C. Dietrich, LA Bagatolli, ZN Volovyk, NL Thompson, M. Levi, K. Jacobson, and E. Gratton. Lipid rafts reconstituted in model membranes. *Biophysical journal*, 80(3):1417–1428, 2001. 92
- [103] K. Simons and E. Ikonen. Functional rafts in cell membranes. *Nature*, 387(6633):569–572, 1997. 92
- [104] J. Sot, L.A. Bagatolli, F.M. Goñi, and A. Alonso. Detergent-resistant, ceramide-enriched domains in sphingomyelin/ceramide bilayers. *Biophysical journal*, 90(3):903–914, 2006. 92
- [105] E.J. Shimshick and H.M. McConnell. Lateral phase separation in phospholipid membranes. *Biochemistry*, 12(12):2351–2360, 1973. 94
- [106] A.J. Bray. Theory of phase-ordering kinetics. *Advances in Physics*, 51(2):481–587, 2002. 96, 100, 102
- [107] P.M. Chaikin and T.C. Lubensky. *Principles of condensed matter physics*. Cambridge Univ Pr, 2000. 96
- [108] J.W. Cahn. On spinodal decomposition. *Acta Metallurgica*, 9(9):795–801, 1961. 97

- [109] I.M. Lifshitz and VV Slyozov. The kinetics of precipitation from supersaturated solid solutions. *Journal of Physics and Chemistry of Solids*, 19(1-2):35–50, 1961. [97](#), [100](#)
- [110] C. Wagner. Theorie der alterung von niederschlägen durch umlösen (ostwald-reifung). *Zeitschrift für Elektrochemie, Berichte der Bunsengesellschaft für physikalische Chemie*, 65(7-8):581–591, 1961. [97](#), [100](#)
- [111] D.A. Huse. Corrections to late-stage behavior in spinodal decomposition: Lifshitz-slyozov scaling and monte carlo simulations. *Physical Review B*, 34(11):7845, 1986. [100](#), [102](#), [104](#), [106](#)
- [112] K. Binder. Kinetic ising model study of phase separation in binary alloys. *Zeitschrift für Physik A Hadrons and Nuclei*, 267(4):313–322, 1974. [102](#)
- [113] J.G. Amar, F.E. Sullivan, and R.D. Mountain. Monte carlo study of growth in the two-dimensional spin-exchange kinetic ising model. *Physical Review B*, 37(1):196, 1988. [102](#)
- [114] M.E.J. Newman and G.T. Barkema. *Monte Carlo methods in statistical physics*. Oxford University Press, USA, 1999. [103](#)
- [115] F. Krzakala. Glassy properties of the kawasaki dynamics of two-dimensional ferromagnets. *Physical review letters*, 94(7):77204, 2005. [103](#), [104](#)
- [116] D.T. Gillespie. A general method for numerically simulating the stochastic time evolution of coupled chemical reactions. *Journal of computational physics*, 22(4):403–434, 1976. [103](#)
- [117] G. Gaspari and S.E. Cohn. Construction of correlation functions in two and three dimensions. *Quarterly Journal of the Royal Meteorological Society*, 125(554):723–757, 1999. [104](#)
- [118] S.C. Glotzer, E.A. Di Marzio, and M. Muthukumar. Reaction-controlled morphology of phase-separating mixtures. *Physical review letters*, 74(11):2034–2037, 1995. [104](#), [107](#)
- [119] K. Binder. Monte carlo calculation of the surface tension for two-and three-dimensional lattice-gas models. *Physical Review A*, 25(3):1699, 1982. [105](#)
- [120] K. Binder, B. Block, S.K. Das, P. Virnau, and D. Winter. Monte carlo methods for estimating interfacial free energies and line tensions. *Journal of Statistical Physics*, pages 1–40, 2011. [105](#)
- [121] G.M. Lee, A. Ishihara, and K.A. Jacobson. Direct observation of brownian motion of lipids in a membrane. *Proceedings of the National Academy of Sciences*, 88(14):6274, 1991. [106](#)
- [122] PB Sunil Kumar, G. Gompper, and R. Lipowsky. Budding dynamics of multicomponent membranes. *Physical review letters*, 86(17):3911–3914, 2001. [106](#)
- [123] P. B. Sunil Kumar and Madan Rao. Shape instabilities in the dynamics of a two-component fluid membrane. *Phys. Rev. Lett.*, 80(11):2489–2492, Mar 1998. [106](#)
- [124] J. Fan, T. Han, and M. Haataja. Hydrodynamic effects on spinodal decomposition kinetics in planar lipid bilayer membranes. *J. Chem. Phys*, 133:235101, 2010. [115](#)

### Abstract

In this theoretical work, we studied the relation between membrane identity, transport and organelle structure in cells. We first study the entry of pathogens such as viruses or toxins in cells. We showed how the chemical and physical properties of the cell membrane can control the entry of molecules or bodies. We then focus on transport in the Golgi apparatus. We see that by an adequate formulation of transport in the Golgi, we can give an accurate interpretation of existing experimental data. We show that differences of identity allow the localization of molecules in one cisterna of the Golgi stack.

Then, we show that we can write general requirements on the transport processes to enable the heterogeneity of compartments. We show that this requirements may have dramatic functional consequences on transport. Eventually, we study the building of new compartments in the cell. We consider one membrane compartment, which we can see as the precursor of the Golgi apparatus, in which the membrane lipids undergo a chemical reaction and are transformed into another lipid species (as occurs in the Golgi apparatus). There can be a competition between the kinetics of phase separation and the kinetics of the chemical reaction which control the structure of the compartment.

### Résumé

Dans ce travail théorique, nous avons étudié les relations entre l'identité d'une membrane (sa composition chimique et ses propriétés physique), le transport lié à cette membrane, et la structure adoptée par cette membrane. Nous avons d'abord étudié l'entrée de pathogènes dans la cellule. Nous avons montré que ce sont les propriétés physiques et la composition de la membrane qui contrôlent l'entrée des pathogènes dans la cellule en contrôlant leur adhésion sur la membrane et leur aggrégation.

Nous nous sommes ensuite tournés vers le transport dans l'appareil de Golgi, où nous montrons qu'une formulation adéquate des processus de transport permet de donner une interprétation précise d'expériences passées. Nous avons montré que des différences d'identité dans les membranes peuvent causer un transport des molécules dans l'appareil de Golgi.

Nous nous intéressons ensuite à la maintenance de cette identité dans des organelles qui s'échangent en permanence des molécules. Nous montrons que cet échange doit avoir des propriétés particulières pour permettre la conservation de l'identité. Ces propriétés du transport ont un grand rôle sur la physiologie de l'organelle, et nous montrons qu'ils peuvent augmenter le rendement de l'appareil de Golgi. Enfin, nous montrons que le changement progressif d'identité dans un organelle peut contrôler la structure même de cet organelle.